NASA
Technical
Paper
1933

November 1981

The Aerodynamics of Bodies in a Rarefied Ionized Gas With Applications to Spacecraft Environmental Dynamics

Nobie H. Stone

NASA

NASA Technical Paper 1933

1981

The Aerodynamics of Bodies in a Rarefied Ionized Gas With Applications to Spacecraft Environmental Dynamics

Nobie H. Stone
George C. Marshall Space Flight Center
Marshall Space Flight Center, Alabama

NASA
National Aeronautics and Space Administration

Scientific and Technical Information Branch

ACKNOWLEDGEMENTS

The author gratefully acknowledges his indebtedness to Professor Shi Tsan Wu, the University of Alabama in Huntsville, for his encouragement and valuable comments throughout the study, and to Professor Uri Samir, Tel Aviv University and the University of Michigan, for his suggestions and comments, which were especially helpful in the discussion of the results available from ionospheric satellites.

TABLE OF CONTENTS

Chapter			Page
I.	INTRODUCTION		1
	A.	Purpose	1
	B.	Statement of the Problem	3
		1. General Characteristics of the Ionosphere	3
		2. Characteristics of the Interaction	4
	C.	Approach	7
II.	A CRITICAL REVIEW OF PREVIOUS INVESTIGATIONS		9
	A.	Theoretical Investigations	9
		1. Mathematical Formulation	9
		a. Kinetic Equations	10
		b. The Continuum Equations	13
		c. Comparison With Classical Gas Dynamics	16
		2. Results of Theoretical Treatments	17
	B.	Available Satellite Data	22
	C.	Laboratory Investigations	24
III.	THE APPROACH AND CONTRIBUTION OF THE PRESENT EXPERIMENTAL STUDY		27
	A.	Potential Contribution of Further Laboratory Studies	27
	B.	Scaling Techniques	28
		1. Derivation of the Vlasov Scaling Laws	28
		2. Method of Applying Scaling Laws	31
	C.	Experimental Methods and Apparatus	33
		1. Vacuum System	35
		2. Plasma Source	36
		3. Spatial Manipulation of Diagnostic Probes and Test Bodies	44

TABLE OF CONTENTS (Continued)

Chapter			Page
	D.	Measurement Techniques	45
	E.	Free-Stream Characteristics	47
IV.	RESULTS OF THE PRESENT EXPERIMENTAL INVESTIGATION		54
	A.	Charged Particle Current Density Variations in the Near and Mid-Wake Regions	55
		1. Experiment A	55
		2. Experiment B	64
		3. Experiment C	69
		4. Experiment D	85
		5. Experiment E	97
	B.	Electron Temperature Measurements in the Near-Wake Region	105
	C.	Vector Ion Flux Measurements in the Near- and Mid-Wake Regions	115
V.	CONCLUSION		130
	A.	Summary of Results and Conclusions	130
		1. Disturbance Envelope	130
		2. Ion Trajectory Focusing by the Plasma Sheath	132
		3. Enhancement of Electron Temperature in the Near-Wake Ion Void Region	133
		4. Axial Ion Peak	133
		5. Deflection of Ion Trajectories in the Mid-Wake Region	136
		6. Diagnostic Applications of the Wake Structure	137
		7. Effects of Ion Thermal Motion	137
		8. Effects of Large R_d Values	138
	B.	Suggestions for Future Research	139
		1. Theoretical	139
		2. Experimental	140
		3. In Situ	141
APPENDIX A — DERIVATION OF THE FLUID EQUATIONS			145
APPENDIX B — A CRITICAL REVIEW OF THE RESULTS FROM FLUID TREATMENTS			150

TABLE OF CONTENTS (Concluded)

Chapter		Page
APPENDIX C	— A CRITICAL REVIEW OF THE RESULTS FROM KINETIC TREATMENTS	163
APPENDIX D	— A CRITICAL REVIEW OF THE RESULTS FROM THE AVAILABLE SATELLITE DATA	196
APPENDIX E	— A CRITICAL REVIEW OF THE RESULTS FROM PREVIOUS EXPERIMENTAL INVESTIGATIONS	218
APPENDIX F	— DIAGNOSTIC INSTRUMENTS AND ANALYSIS TECHNIQUES	258
APPENDIX G	— THE DIFFERENTIAL ION FLUX PROBE	271
REFERENCES		287

LIST OF TABLES

Table	Title	Page
1-1.	General Characteristics of the Ionosphere	5
2-1.	Summary of Theoretical Calculations	21
3-1.	Laboratory and Ionospheric Free Stream Parameters	35
4-1.	Experiment Body and Plasma Parameters after Stone et al. [73]	99
5-1.	Plasma Properties and Scaling Parameters	144
D-1.	Some Details on the Ariel 1, Explorer 31, and Gemini-Agena 10 Spacecraft, after Samir [89]	208
D-2.	Parameters for Figure D-7	208
D-3.	Parameters for Figure D-9, after [14]	208
E-1.	Experimental Conditions	243
E-2.	Scale Factors for the Magnetogasdynamic Interaction	244

LIST OF ILLUSTRATIONS

Figure	Title	Page
1-1.	Typical ion and electron concentrations in the ionosphere for mid-latitude daytime. These values change with the diurnal cycle	4
3-1.	Schematic of the MSFC No. 1 plasma wind tunnel facility	34
3-2.	Kaufman engine schematic after Stone and Reihmann [68]	37
3-3.	Kaufman engine electric potential	39
3-4.	Ion kinetics energy versus acceleration potential after Stone and Reihmann [68]	40
3-5.	Dependence of engine beam current on cathode current after Stone and Reihmann [68]	41
3-6.	Dependence of engine beam current on magnet current after Stone and Reihmann [68]	42
3-7.	Ion density profile in the plasma stream 1.4 m from the Kaufman accelerator, after Stone et al. [69]	43
3-8.	Relative density of slow, charge exchange ions, n_s, to fast, stream ions, n_f, as a function of chamber pressure	48
3-9.	Relative density of slow, charge exchange ions, n_s/n_f, as a function of chamber volume at a pressure of 10^{-5} torr	49
3-10.	Transverse profiles of normalized ion current density, Δ, and flow direction, O, 1.98 m downstream from the Kaufman accelerator. The maximum stream angle at X = 38 cm is 12.8°. Data obtained with a 2.54 cm diameter aperture on the accelerator	51

LIST OF ILLUSTRATIONS (Continued)

Figure	Title	Page
3-11.	Axial profiles of normalized ion current density, electron temperature and the perpendicular (radial) component of ion temperature, $T_{i\perp}$ (calculated from relation by Hester and Sonin [52]). All values are normalized to the value measured at Z = 0 (most distant point from the accelerator)	52
3-12.	Axial variations of R_d, S, Φ_b, and $M_\perp$ resulting from the variations of T_e, J_i (or n_i) and T_i shown in Figure 3-11. Each parameter is normalized by its value at Z = 0	53
4-1.	Ion current density profiles downstream from a conducting sphere (R_o = 3 cm) for $R_d \cong 0.8$, $S \simeq 17$, and $\Phi_b \simeq -5$, data after Stone et al. [74]	57
4-2.	Morphology of converging VB streams and diverging trailing "V" (TV) waves for various values of Φ_b	59
4-3.	Convergence angle of the ion void boundary (determined at its $J_o/2$ point) for various values of Φ_b	60
4-4.	The dependence of the void boundary angle, θ_v, the void boundary streams, θ_{VB}, and the TV wave, θ_{TV}, on Φ_b	61
4-5.	Dependence of the crossing point of the VB streams, $Z^* \equiv Z_\alpha$, on Φ_b	63
4-6.	Axial variation of $\eta = [J(0,z) - J_o]/J_o$ with Z/R_o for the conditions: $R_d \simeq 0.8$, $S \cong 17$, and $\Phi_b \simeq -5$ (Case I) and $R_d \cong 1.2$, $S \cong 5.2$, and $\Phi_b \cong -4.9$ (Case II), after Stone et al. [9]	65
4-7.	Axial position of the ion peak maximum as a function of S for several cases, after Sonin et al. [75]	67
4-8.	Axial ion current density profiles downstream from a conducting sphere for $R_d \cong 4.3$, $S \cong 25.5$, and Φ_b as indicated	70

LIST OF ILLUSTRATIONS (Continued)

Figure	Title	Page
4-9.	Transverse ion current density profiles for the conditions of Figure 4-8 with $\Phi_b = -41$	71
4-10.	Intercept of the leading edge of the axial ion peak with the Z-axis as a function of $\lvert\Phi_b\rvert^{-1/2}$ for Case I-C, ⊙, and Case II-C, Δ	72
4-11.	Variation of axial ion peak intercepts and VB-stream crossing point with $\left[S R_o^{\alpha} / \lvert\Phi_b\rvert^{1/2}\right]$	74
4-12.	Axial ion peak maximum amplitude in J_o as a function of $\lvert\Phi_b\rvert^{-1/2}$, data from Experiment A (B, Case I-C)	76
4-13.	Variation of the normalized maximum amplitude of the axial ion peak, $[J_{max}/J_o]$ with $[S/\lvert\Phi_b\rvert]^{1/2}$, for Case I-C (O) and data from Experiment A (□)	77
4-14.	Variation of the axial ion peak width at half maximum with $\lvert\Phi_b\rvert^{-1/2}$ for Case I-C (O) and data from Experiment A (□)	79
4-15.	Effect of misalignment on axial ion current density profiles and the ability to detect the axial ion peak, (a) a transverse J/J_o profile at the point of maximum enhancement, (b) an axial profile on-axis, and (c) an axial profile displaced $\simeq R_o/2$ off the Z-axis, after Sonin et al. [75] . . .	84
4-16.	Ion current density profiles downstream from a conducting cylinder (8 cm diameter by 8 cm long) oriented with its axis of symmetry normal to the flow direction at Z/R_o = 3.2 for (a) $R_d \simeq 5.4$, $S \simeq 10.8$ and (b) $R_d \simeq 4.25$ and $S \simeq 10.8$. Values of Φ_b for both cases as indicated . . .	87
4-17.	Ion current density profiles in the wake of a long conducting cylinder oriented normal to the flow direction ($2R_o$ = 2.54 cm) at $Z/R_o = 3$ for (a) $R_d = 1.74$, $S = 9.35$ and (b) $R_d = 0.74$, $S = 15.8$. Values of Φ_b are as indicated . . .	88

LIST OF ILLUSTRATIONS (Continued)

Figure	Title	Page
4-18.	Ion current density profiles downstream from the Apollo model. Note that the model was not aligned with the flow direction (of 5° to 10°)	92
4-19.	Ion current density profiles downstream from the Soyuz model	93
4-20.	Schematic showing geometry and orientation of the Apollo and Soyuz models. Inclination of the Apollo model to the flow direction is 5° to 10°	94
4-21.	Ion current density profiles downstream from a conducting sphere for $R_d = 5.7$, $S = 10.6$, and $\Phi_b = -14$ (Case I), after Stone et al. [86]	98
4-22.	Dependence of the sheath width at the critical cross-section of the ost body (X/λ_D) on (Φ_b/S). Open circles represent data for a sphere, solid circles for a ⊥ cylinder, and open triangle a parallel cylinder, after Stone et al. [73]	101
4-23.	Growth of the extent of the disturbed zone ΔW, normalized by R_o/S with normalized distance downstream, after Stone et al. [73]	103
4-24.	Normalized ion current depletion in the trough of the rarefaction wave as a function of axial distance, after Stone et al. [73]	104
4-25.	Transverse profiles of $[T_e(\text{wake})/T_{eo}]$ downstream from a conducting sphere for $T_{eo} \cong 1200°K$, $n_{io} \cong 7.5 \times 10^4/cm^3$, $E_i \cong 5.3$ eV, $P = 4 \times 10^{-6}$ torr, after Samir et al. [77]	107
4-26.	Transverse profiles of $[T_e(\text{wake})/T_{eo}]$ at $Z/R_o = 1.3$ downstream from a conducting sphere at severe chamber pressures for $T_e = 800°K$, $n_{io} \cong 5 \times 10^4/cm^3$, $E_i = 4.5$ eV, and $\phi_s \simeq +0.3$ V, after Oran et al. [76]	109

LIST OF ILLUSTRATIONS (Continued)

Figure	Title	Page
4-27.	Axial profiles of $[T_e(\text{wake})/T_{eo}]$ downstream from a conducting sphere, after Oran et al. [98]	110
4-28.	Comparison of the variation of $[T_e(\text{wake})/T_{eo}] = 1$ with $n_s/n_f = 1$ as determined by Oran et al. [76], with growth of instability (amplitude × frequency) predicted by Gurevich et al. [32]	114
4-29.	Ion current density profiles downstream from a long conducting cylinder for $R_d \cong 1$, $S \cong 7.5$, $Z/R_o \cong 11$, and Φ_b as indicated	117
4-30.	Example DIFP raw data. Profiles show current collected as a function of deflection voltage with no retarding potential, $J(\phi_d, \phi_r = 0)$. Data obtained off axis for the conditions of Figure 4-29 with Φ_b as indicated	118
4-31.	DIFP data showing: (a) normalized sum of peak currents obtained on axis at $Z/R_o = 11.2$ for various values of Φ_b, □, compared with Faraday cup data, O, from Figure 4-29; and (b) the angle and amplitudes of the peaks corresponding to the data in (a)	119
4-32.	Transverse variation of θ and $[J_{peak}/J_o]$ for $Z/R_o \cong 11$, $\Phi_b = -56$: (a) current density profile from Figure 4-29; (b) angle of incidence, θ, variation for two converging streams; and (c) peak height variation	121
4-33.	Variation of θ along Z-axis for the conditions of Figure 4-29. Solid line is the geometric angle subtended by the test body radius	123
4-34.	Variation of the average incidence angle, θ_{av}, with ϕ_b at various positions along the Z-axis for $S \cong 15.8$ (Case I) and $S \cong 9.4$ (Case II)	126

LIST OF ILLUSTRATIONS (Continued)

Figure	Title	Page
4-35.	DIFP data corresponding to Figure 4-30: (a) variation of θ with ϕ_b and (b) corresponding variations of peak amplitudes with θ	127
4-36.	Schematic representation of the flow processes described by the data from Figures 4-30 and 4-35	128
5-1.	Ion behavior within disturbed zone	131
5-2.	An example method for large body in situ plasma flow interaction studies, after Stone and Samir [101]	142
B-1.	Potential profiles at various distances downstream from a small cylinder for $T_i >> T_e$. Note: $b_c z = (z/\lambda_D)^{1/2}/S$, after Rand [4]	161
B-2.	Transverse potential profiles as above, in Figure B-1, but for a half plane, after Rand [4]	161
B-3.	Steady-state wave patterns for $T_e/T_i >> 1$ and (a) $S < 1$; (b) $S > 1$; (c) leading wave front angle versus S with $T_e/T_i >> 1$, after Sanmartin and Lam [10]	162
B-4.	Steady-state wave patterns with $T_e/T_i << 1$ for (a) $S < 1$ and (b) $S > 1$, after Sanmartin and Lam [10]	162
C-1.	Potential field in the vicinity of spherical bodies in a collisionless plasma. All axes are normalized by λ_D except (a) which is normalized by R_o, after Maslennikov and Sigov [16-18]	183
C-2.	Ion trajectories in the vicinity of spherical bodies. Note that (d) is an expansion of some trajectories of (c). All distances are normalized by λ_D, after Maslennikov and Sigov [17]	184
C-3.	Ion density profiles in the plane $Z/R_o = 1.4$ behind a spherical body with $R_d = 0.08$, $S = 1.4$, and Φ_b as shown, after Maslennikov and Sigov [17]	185

LIST OF ILLUSTRATIONS (Continued)

Figure	Title	Page
C-4.	Transverse ion density profiles downstream from a long rectangular cylinder for the conditions: $R_d = 1.5$, $S = 6$, $\Phi_b = -2.75$, $X = x/R_o$. Solid lines are first order solutions, $n_i^{(1)}$, while dashed lines are $n_i^{(0)}$ solutions, after Taylor [20]	185
C-5.	Ion density profiles for the conditions of Figure C-4. $R_d = 1.5$, $S = 6$, (a) $\Phi_b = -2.75$, (b) $\Phi_b = -14$. All profiles are first order, normalized by n_o, after Taylor [12]	186
C-6.	Ion distribution function, $f(v_x/a_i)$, behind a long plate at $X/R_o \simeq 0.4$ and various values of $t = z/S \cdot R_o$, $T_e/T_i = 1$, after Gurevich, et al. [26]	187
C-7.	Ion trajectories (a) and density profiles (b) for $R_d = 1$, $S = 3.5$, and $\Phi_b = -5$, and density contours for $\Phi_b = 0$ (c), long plate body, after Call [12]	188
C-8.	Ion trajectories (a) and potential contours (b), for a disk with $R_d = 1$, $S = 1.1$, and $\Phi_b = 0$, and (c) potential profiles for a long plate under same conditions, after Call [12]	189
C-9.	Equipotential (left) and ion density (right) contours for $R_d = 1.5$, $S = 6$, $T_e/T_i = 1$ and (top to bottom), $\Phi_b = +3$, 0, -1, -2.75, -6, and -40, after Fournier [23]	190
C-10.	Equipotential (a) and ion density (b) contours for $R_d = 1.5$, $S = 6$, $\Phi_b = -2.75$, and (top to bottom) $T_e/T_i = 1$, 2, 10, after Fournier [23]	191
C-11.	Equipotential contours for $S = 6$, $\Phi_b = -2.75$, $T_e/T_i = 1$, and (a) $R_d = 1.5$ and (b) $R_d = 10$, after Fournier [23]	192

LIST OF ILLUSTRATIONS (Continued)

Figure	Title	Page
C-12.	Transverse ion density profiles for R_d = 1, S = 3.5, and Φ_b = -5 for (b) a plate and (c) a disk. (a) shows behavior schematically, after Martin [13]	193
C-13.	Variation of Z_d (open circles), θ_d (triangles-open → plate, closed → disk), and θ_w (square, open → plate, closed → disk) with S. Dashed line shows Mach angle, after Martin [13]	194
C-14.	Effect of Φ_b on Z_d (circles), θ_d (squares), and θ_w (triangles) open → plate, closed → disk. Dashed line shows the Mach angle, after Martin [13]	194
C-15.	Transverse ion density profiles for R_d = 0.2, S = 3.5, and Φ_b = -5. (a) Plate, (b) disk, after Martin [13]	195
C-16.	Effect of R_d on Z_d and θ_d for S = 3.5 and Φ_6 = -9, after Martin [13]	195
D-1.	Spacecraft geometry, dimensions, and instrument locations	209
D-2.	Variation of electron current with angle of attack. Ariel I data from days 116, 117, 118, and 120 in 1962. (Note: Ram direction = 180° in this figure.) After Henderson and Samir [36]	210
D-3.	Normalized electron current, I_e I_o, as a function of angle of attack between the probe normal and the flow direction, θ, for (a) probe in the wake created by the spherical ion probe, and (b) probe in the wake created by the main body of the satellite, after Henderson and Samir [36]	210
D-4.	Variation of electron current, I_e, collected with the probe at space potential, as a function of angle of attack. Explorer 31 data obtained with the surface mounted planar Langmuir probe, after Samir and Wrenn [37]	211

LIST OF ILLUSTRATIONS (Continued)

Figure	Title	Page
D-5.	Variation of $\delta_e \equiv n_e$ (wake) $/ n_e$ (front) with average ionic mass, $[m_i]_{av}$, over the altitude range 520 to 1020 km; data from Explorer 31, after Samir [38]	212
D-6.	Variation of normalized ion density with angle of attack. Measurements of n_i obtained from spherical ion probe; n_e, from the boom-mounted Langmuir probe on Ariel I, after Samir and Willmore [39]	213
D-7.	Variation of normalized current, $I_i(\theta)$ $I_i(\theta=0)$ (solid lines), and normalized electron current (dashed lines) as functions of angle of attack, θ, over the altitude ranges, 700 to 930 km (pass 393); 900 to 600 km (pass 482); and 570 to 520 km (pass 683); Explorer 31 data, after Samir, et al. [86]	214
D-8.	Ion and electron currents collected during the Gemini-Agena 10 maneuvers. (a) Normalized currents (ambient current only approximated) as a function of the separation distance, and (b) currents collected during the Agena yaw maneuver, after Troy, et al. [43]	215
D-9.	Variation of T_e with angle of attack for (a) an O^+-plasma and (b) an H^+-plasma for conditions shown in Table D-3, after Samir and Wrenn [80]	216
D-10.	Variation of electron temperature in the frontal region (open circles) and wake region (closed circles) as a function of altitude, after Samir and Wrenn [80]	216
D-11.	Normalized electron temperature, $T_e(\theta_e)$ $T_e(\theta\ 0)$ as a function of angle between the probe normal and $\vec{B}$, θ_B, for two relative orientations between $\vec{V}_o$ and $\vec{B}$; after Samir and Wrenn [80]	217

LIST OF ILLUSTRATIONS (Continued)

Figure	Title	Page
D-12.	Examples of the classes of angular dependence of electron temperature on angle of attack; (a) at 2700 km altitude with $[m_i]_{av} = 1.1$, (b) at 1600 km altitude with $[m_i]_{av} = 1.6$, (c) at 800 km altitude with $[m_i]_{av} = 3.3$, and (d) at 2400 km altitude with $[m_i]_{av} = 4.4$; all cases in sunlight except (a); after Troy, et al. [42]	217
E-1.	Potential of a flat plate as a function of the angle between the plate and the plasma flow direction, after Meckel [44]	244
E-2.	Transition regions of the ionosphere, after Cox [45]	245
E-3.	Langmuir probe current in the wake of a conducting sphere for a collision dominated plasma, after Cox [45]	245
E-4.	Ion current density profiles downstream from a conducting sphere for several body potentials for a 90 eV ion stream; $V_o = 11$ km/sec, $n_i = 2.1 \times 10^6/cm^3$ (a); $4.9 \times 10^6/cm^3$ (b); and $3.1 \times 10^5/cm^3$ (c). $R_o = 2.54$ cm for all cases, after Hall, et al. [46]	246
E-5.	Electric field enhancement by the sheath at front and rear of a conducting sphere as a function of ion density, data for a 90 eV ion stream, after Hall, et al. [46]	246
E-6.	Normalized ion density profiles downstream from a spherical test body and a conical test body with its apex into the flow. The cone angle was 15°. Data were obtained for a variety of test body potentials, as indicated, after Clayden and Hurdle [47]	247
E-7.	Contours of equal normalized current density (a), (b), and (c) for the indicated conditions. Contours of equipotential, $\Phi = (e\phi/kT_e)$, for the indicated conditions, after Skvortsov and Nosachev [48]	248

LIST OF ILLUSTRATIONS (Continued)

Figure	Title	Page
E-8.	Ion current density profiles (transverse) behind spherical test bodies of different diameters but the same Debye ratio, R_d, for the indicated conditions and distances downstream. Closed circles, R_o = 1 cm, open circles, R_o = 2 cm, after Skvortsov and Nosachev [49] ...	249
E-9.	Transverse profiles of normalized ion current for (a) $\Phi_b S^2 = -0.05$; (b) $\Phi_b S^2 = -0.25$; (c) $\Phi_b S^2 = -0.5$; open circles T_e = 1 eV, closed circles, T_e = 3.1 eV, after Skvortsov and Nosachev [49]	249
E-10.	Schematic of variable potential test body (a); ion current density profiles along the Z-axis (b), after Sajben and Blumenthal [50]	250
E-11.	Transverse profiles of ion current density downstream from a small cylindrical test body for S = 6, R_d = 0.005, and $\Phi_b = -3.5$; (b) axial ion current density profile for same conditions as (a) compared with potential profile predicted by Rand [4]; and (c) transverse ion current density profiles for a small cylinder for S = 28, R_d = 0.2, and $\Phi_b = -3$, after Hester and Sonin [34]	251
E-12.	Calculated and observed ion stream deflection produced by a small cylinder for S = 5.7, R_d = 0.005 and $\Phi_b^{1/2}/S$ as indicated, after Hester and Sonin [34]	252
E-13.	The far wake ion current density distribution for a sphere at floating potential and negatively biased; S = 5.7, R_d = 1.8 (at model), and 0.7 (at position of last trace due to axial variation of plasma stream) with $\Phi_b = -3.5$ (left) and $\Phi_b = -20$ (right), after Hester and Sonin [53]	252

LIST OF ILLUSTRATIONS (Continued)

Figure	Title	Page
E-14.	Ion current density profiles in the wake of a large cylinder for S = 23, R_d = 39, and Φ_b = -50 (a) and Φ_b = 0 (b); and a large sphere for S = 5, R_d = 46, and Φ_b = -3.5, after Hester and Sonin [53]	253
E-15.	Ion current density along the wake axis as a function of test body potential for various ion stream energies, after Knott and Petersen [54]	253
E-16.	The ion current density in the wakes of spherical test bodies for the indicated conditions, P ≅ 1.6×10^{-7} torr, S = 10 (except under the Z_2-axis where S ≅ 6), E_i = 20 eV, T_{eo} = 1400 to 2000°K, X-axis = f(T_e/T_i), Y-axis = f(Φ_b) and Z-axis = f(R_d), after Fournier and Pigache [58]	254
E-17.	Electron current, T_e, as a function of probe potential, Φ_p, (with respect to plasma potential) after Illiano and Storey [57]	255
E-18.	Effects of slow ion concentration (proportional to chamber pressure indicated in the figure) on the near wake structure, after Martin and Cox [60]	255
E-19.	Axial profiles of normalized ion current density for (a) H = 1100 O_e, T = 2700°K, J_o = 30 μA/cm^2 and $V_o/\hat{c}_i$ = 1.95; (b) H = 1900 O_e, J_o = 30 μA/cm^2 and $V_o/\hat{c}_i$ = 2.6. Points = experiment, line (1) = neutral approximation, line (2) = electric field included in theory, after Bogashchenko, et al. [61]	256
E-20.	Positions of relation [J/J_o]-extrema, data from Bogashchenko, et al. [61]	256

LIST OF ILLUSTRATIONS (Continued)

Figure	Title	Page
E-21.	Axial profiles of normalized ion current density downstream from a plate oriented normal to the plasma flow direction for (a) $V_o = 1.5 \times 10^3$ cm/sec, $V_o/\hat{c}_i = 1.4$ and H = 700 (1), 1100 (2), and 1500 O_e (3). (4) are calculated values; (b) $V_o = 1.4 \times 10^5$ cm/sec, $V_o/\hat{c}_i =$ 15, H = 1100 O_e for $2R_o = 3.5$ (1), 5 (2), and 7 mm (3) where (4) gives calculated values and (c) $V_o =$ 1.5×10^5 cm/sec, $V_o/\hat{c}_i = 1.5$, $R_o/R_{L(i)} = 0.45$ for $2R_o = 3.5$ mm, H = 1000 O_e (1); 5 mm, 700 O_e (2); 7 mm, 500 O_e (3); and (4) giving calculated values, after Astrelin, et al. [62]	257
F-1.	Electrostatic (Langmuir) probe	265
F-2.	Semi-log plot of I-V curve	266
F-3.	Faraday cup assembly	267
F-4.	RPA schematic	268
F-5.	RPA characteristic	269
F-6.	Schematic of energy analyzer	270
G-1.	Differential ion flux probe schematic (showing a cut through the instrument in a plane normal to the deflection system slits), after Stone [71]	279
G-2.	Ion current, $I(\phi_d, \phi_r = 0)$, at various angles of attack, θ, for (a) a 10 eV ion stream, and (b) a 20 eV ion stream, after Stone [71]	280
G-3.	Ion current, $I(\phi_d, \phi_r = 0)$, for a fixed angle of attack of 20° and various ion stream energies, E, after Stone [71]	281

LIST OF ILLUSTRATIONS (Concluded)

Figure	Title	Page
G-4.	Critical deflection voltage, ϕ_d^* (at which maximum ion current is collected), as a function of mean kinetic energy, E, at fixed angles of attack, after Stone [71]	282
G-5.	Normalized critical deflection voltage, (ϕ_d^*/E), as a function at angle of attack θ, after Stone [71]	283
G-6.	Error incurred in determining ion kinetic energy as a function of angle of attack, after Stone [71]	284
G-7.	Composite amplitude envelope for ion current peaks, $I(\phi_d^*, \phi_r = 0)$, as a function of angle of attack (normalized to the peak amplitude at $\theta = 20°$), after Stone [71]	285
G-8.	Ion current, $I(\phi_d, \phi_r = 0)$, as a function of deflection voltage in the presence of multiple ion streams created by a long cylindrical body 42 cm upstream with E = 19 eV. (The zero bias voltage case is amplified by a factor of 10), after Stone [71]	286

LIST OF SYMBOLS

$\vec{a}$	Acceleration due to the Lorentz force $\equiv (q/m)\ [\vec{E} + \vec{v} \times \vec{B}/C]$ (dynes).
a_i	Ion acoustic speed $\cong (2kT_e/m_i)^{1/2}$ (cm/sec).
A	Area.
$\vec{B}$	Magnetic induction (gauss).
c	Speed of light (cm/sec).
$\vec{c}$	Random thermal (peculiar) velocity $(\vec{c}) = 0$ (cm/sec).
$\hat{c}$	Most probable thermal speed $\equiv (2kT/m)^{1/2}$ (cm/sec).
$\bar{c}$	Mean thermal speed $(8kT/\pi m)^{1/2}$ (cm/sec).
$C_{V,P}$	Specific heats at constant volume and pressure, respectively.
D	Diffusion coefficient (effective).
e	Electronic charge (e.s.u.).
$\vec{E}$	Electric field (statvolts/cm).
E_i	Net ion energy (due to drift) (eV).
f	Particle distribution function in phase space.
I	Current (statamps).
$\vec{J}$	Current density $(qn\vec{u})$ (statamps/cm^2).
k	Boltzmann's constant (c.g.s. units).
$\vec{k}$	Propagation constant (wave vector) (cm^{-1}).

L	Characteristic body length (cm).
m	Particle mass (gm).
M	Mach number based on particle most probable speed $\equiv (V_o/\hat{c})$.
n	Particle number density, $n(\vec{x},\vec{v},t)$ (cm^{-3}).
P	Hydrostatic pressure $(dynes/cm^2)$.
q	Particle charge (e for electrons, Ze for ions) (e.s.u.).
Q	Total charge on a surface (e.s.u.).
$Q(\vec{v})$	Arbitrary function of particle velocity, $\vec{v}$.
r	Radial coordinate (w.r.t. the wake axis) $\equiv (x^2 + y^2)^{1/2}$ (cm).
R_o	Characteristic body radius (cm).
R_d	Debye ratio $\equiv (R_o/\lambda_D)$.
R_L	Cyclotron (Larmor) radius $\equiv (mv_\perp c/eB)$ (cm).
R_{M_e}	Magnetic Reynolds number $\equiv R_o V_o/\eta$.
S	Ion acoustic Mach number (ion speed ratio) $\equiv (V_o/a_i)$.
t	Time (sec).
T	Temperature (°K).
$\vec{u}$	Mean (drift) velocity ($\cong V_o$ for ions) (cm/sec).
$\vec{v}$	Particle velocity.
V_o	Spacecraft orbital velocity (plasma drift velocity) (cm/sec).
x	Transverse ($\perp$ to V_o) spatial coordinate (cm).
$\vec{x}$	Spatial coordinate vectors, $\vec{x} = (x,y,z)$ with $z\hat{k} \parallel \vec{V}_o$ (cm).
X	Normalized x-coordinate $\equiv (x/\lambda_D)$.
$\vec{X}$	Normalized coordinate vectors.

y — Transverse ($\perp$ to $\vec{V}_o$) spatial coordinate (cm).

Y — Normalized y-coordinate $\equiv (y/\lambda_D)$.

z — Parallel spatial coordinate ($\parallel$ to $\vec{V}_o$) (cm).

Z — Normalized z-coordinate (z/λ_D), also the number of electronic charges on an ion.

Greek Symbols

α — (e/kT), or an arbitrary constant.

β — Speed ratio $\equiv (m_i V_o^2/kT_e)^{1/2} = \sqrt{2}\,S$.

γ — Ratio of specific heats.

δ — Finite difference.

ϵ — 1.6×10^{-12} erg/eV (constant).

η — Magnetic diffusivity (viscosity) of the plasma.

θ — Angle w.r.t. $\vec{V}_o$ (deg).

Θ — Temperature (eV).

λ — Collision mean-free-path-length (cm).

λ_D — Debye length $\equiv (kT_e/4\pi n_o e^2)^{1/2}$ (cm).

ν_c — Effective collision frequency (sec^{-1}).

ρ — Mass density $\equiv nm$ (gm/cm^3).

ρ_c — Charge density $\equiv nq$ ($e.s.u./cm^3$).

σ — Surface charge density ($e.s.u./cm^2$).

τ — Line charge density (e.s.u./cm).

ϕ — Space potential w.r.t. ambient plasma potential; i.e., $\phi_s = 0$ (statvolts).

Φ — Normalized space potential $\equiv (e\phi/kT_e)$.

χ_s	Sheath thickness (cm).
ψ	Velocity potential (cm^2/sec).
ω	Wave frequency (sec^{-1}).
ω_P	Plasma frequency $\equiv (4\pi n_o q^2/m)^{1/2}$ (sec^{-1}).
ω_c	Cyclotron (Larmor) frequency $\equiv (eB/mC)$ (sec^{-1}).

Subscripts

b	Body surface
e	Electrons
i	Ions
o	Ambient (undisturbed flow)
s	Sheath edge
α	Particular constituent of the plasma

CHAPTER I. INTRODUCTION

A. Purpose

Any object placed in space will be immersed in a macroscopically neutral conglomeration of positively and negatively charged particles, as well as neutral particles, generally called a plasma. The space plasma is found throughout the observable universe and, although very tenuous, is an important component of the space environment and enters into many natural phenomena. When some relative motion exists between a body and the surrounding space plasma, a complex interaction occurs which modifies both the electrodynamic characteristics of the body and the flow field of the plasma. Such plasma-electrodynamic interactions occur frequently in nature and take on a wide variety of forms; planetary magnetospheres and comets are well known examples.

The interaction of the ionospheric plasma with orbiting spacecraft (to which this study is limited) is, from the scientific point of view, the only example of a natural plasma flow interaction which is readily available for study in its entirety. The only other readily available interaction is that of the geomagnetic field with the solar wind, which is of such a scale that it must be studied piecewise. From the measurement technology point of view, the ionospheric plasma in the vicinity of the spacecraft is disturbed and does not represent the ambient medium. For example, charged particles are accelerated as they approach the spacecraft so that measurement of the energy distribution and concentration of thermal particles are adversely affected. In this sense, the spacecraft-space plasma interaction is a rather complex example of the classic problem of the measurement perturbing the medium being measured. It there-

fore becomes apparent that a thorough understanding of the physical mechanisms involved in this interaction and their dependences on various plasma and spacecraft parameters (also known as ionospheric aerodynamics) is of fundamental interest from both scientific and technological points of view.

Although it has long been recognized that the spacecraft-space plasma interaction occurs and can adversely affect measurements of the ambient geoplasma, most space missions have involved single satellites which, a priori, could provide only very limited information. Therefore, with the possible exception of the Gemini-Agena 10 and 11 missions, no deliberate and systematic attempt has been made to study the problem in space. As a result, the available in situ data are incomplete in spatial coverage and fragmentary in the sense that seldom were all the necessary measurements made. These data are, therefore, incapable of providing a well grounded understanding of the problem.

In the absence of definitive in situ measurements, a large number of theoretical and ground-based experimental studies have been made. Although much valuable information has been gained from these efforts, both approaches have their limitations and the field of ionospheric aerodynamics is far from being well understood. Not all aspects of the problem have been studied adequately, even within the current experimental and theoretical limitations, and the results of previous studies have not been correlated sufficiently; some are even contradictory.

The present experimental investigation treats specific aspects of the plasma flow interaction with conducting bodies and includes previously unavailable vector ion flux measurements in the zone of disturbance. The underlying objective of the present study is, therefore, to draw the existing information together and integrate it with the results of the present experimental investigation into a unified and definitive parametric treatment of the problem.

B. Statement of the Problem

1. General Characteristics of the Ionosphere. As already stated, the medium in which artificial satellites orbit is a plasma; i.e., it is a gas which is sufficiently ionized that its behavior is dominated by electrostatic interactions rather than hardsphere collisions which characterize the neutral atmosphere. We further note that the ionospheric plasma is considered to be in thermodynamic equilibrium and collisionless on the scale of the orbiting satellite and the disturbance surrounding it.

The ionospheric medium obtains these characteristics primarily from three processes. First, whereas the lower atmosphere is mixed by wind and weather systems and therefore maintains a uniform composition at all altitudes up to approximately 100 km, above this point the low altitude disturbances and solar generated current systems are too weak to produce an effective mixing, molecular diffusion becomes the dominant transport process, and the atmosphere becomes stratified in accordance with Dalton's law; i.e., the various constituents diffuse through each other and become dominant at different altitudes. The upper layers are dominated by lighter constituents while the heavier molecules gravitate to lower altitudes (Figure 1-1). The second process is excitation and ionization of these gas layers, primarily by solar UV. The gases in different layers have different ionization potentials and, therefore, the rate of UV absorption and, hence, ionization is not uniform. The third process is the recombination of the ionized molecules with free electrons. Again, this rate varies with different gases and depends on pressure. The net result is the creation of layers of high ionization at certain altitudes known as the D, E, F_1, and F_2 layers shown in Figure 1-1. Most ionospheric satellites move within or above the F-peaks.

Although it is recognized that the ionosphere is not uniform and that variations in composition, current systems, and other complicating factors do exist, for the purpose of the current study, typical global characteristics in the altitude range 150 to 1200 km will be sufficient. These are provided in Table 1-1. Note that the orbital velocity is me[illegible]e., in between the

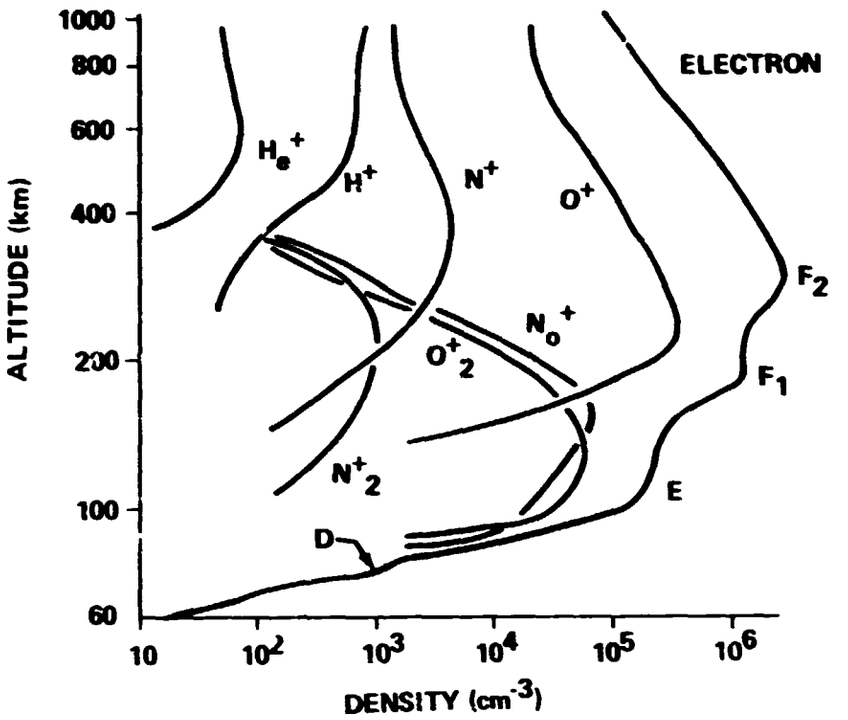

Figure 1-1. Typical ion and electron concentrations in the ionosphere for mid-latitude daytime. These values change with the diurnal cycle.

thermal speeds of the massive ions and the electrons) and the mean-free-path for all collisions is much larger than typical satellite dimensions. Many of these conditions can be created in laboratory synthesized plasma, as discussed in Chapter III.

2. Characteristics of the Interaction. The physics of a body immersed in a quiescent, collisionless plasma is well understood: the body takes on an electric (floating) potential which tends to balance the flux of charged particles to its surface so that no net electrical current flows. The plasma tends to shield itself from this potential by creating a region of unequal ion and electron number density surrounding the body, called the plasma sheath, in which the floating potential on the body is matched to the space potential of the plasma.

When a relative motion exists between a body and its environmental space plasma, an interaction occurs which is far more complex than the simple quiescent case. A redistribution of surface charge occurs on the body and the

TABLE 1-1. GENERAL CHARACTERISTICS OF THE IONOSPHERE*

h (km)	150	200	400	800	1200	3000
V_o (km/sec)	7.83	7.80	7.68	7.47	7.26	6.53
$n_{i,e}$ (cm^{-3})	$3 \cdot 10^5$	$4 \cdot 10^5$	10^6	10^5	10^4	$7 \cdot 10^3$
T_i (°K)	700	1100	1600	2200	2600	5000
T_e (° K)	1000	2000	2800	3000	3000	5000
$\overline{m}_i$ (AMU)	28	24	20	14	10	2
λ_D (cm)	0.40	0.49	0.37	1.20	3.78	5.83
S	10.2	6.6	5.0	4.0	3.5	1.01
m_i	12.2	9.0	6.7	4.6	3.8	1.01
λ_D (cm)	$8 \cdot 10^3$	$5 \cdot 10^4$	$2 \cdot 10^6$	$2 \cdot 10^8$	$4 \cdot 10^9$	$4 \cdot 10^{10}$
$\lambda_{e,i}$	$5 \cdot 10^5$	$1 \cdot 10^5$	$1 \cdot 10^5$	$1 \cdot 10^6$	$1 \cdot 10^7$	$3 \cdot 10^7$

Where, $\lambda_D = 6.9 \sqrt{T_e/n_e}$

$$S = \left[\overline{m}_i V_o^2/2kT_e\right]^{1/2}$$

$$M_i = \left[\overline{m}_i V_o^2/2kT_i\right]^{1/2}$$

* Data from Boyd, in Plasma Diagnostics, Lochte-Holtgreven, W. (Ed.), Wiley Interscience Div., John Wiley and Sons, Inc., New York (1968).

zone of disturbance in the plasma is no longer radially symmetric, regardless of body geometry. When the relative motion between the body and plasma is mesosonic, as it is in the lower ionosphere, several characteristic processes have been found to occur.

Beginning at the body, the plasma sheath on the frontal side may be compressed to some extent by the directed motion of the ions. Immediately behind the body, the more massive particles are swept out leaving a region essentially void of ions and neutrals. Although the electron mobility is sufficiently great to populate the void region from velocity considerations, a negative space charge potential is created by their presence which tends to impede their motion into the region. Hence, the void region which occurs in the wake near the body is highly depleted of all charged and neutral particles.

The way in which the void region is repopulated may result from a variety of mechanisms including focusing of ions into this region by the electric fields in the plasma sheath surrounding the front half of the body, ambipolar diffusion, thermal diffusion, and various plasma oscillations or instabilities. The specific mechanisms which dominate the repopulation process will depend on the various body and plasma parameters. For example, the dominate mechanism for interactions where the body is comparable in size to the sheath thickness would most likely be the electrostatic focusing of ions onto the wake axis by the electric field within the sheath; whereas, for interactions where the body is much larger than the sheath thickness, this effect would be relatively unimportant and some other mechanism such as ambipolar diffusion might be expected to dominate.

Other physical characteristics of the plasma wake include its initial width near the body, the rate at which the disturbance propagates outward downstream from the body, and effects that occur in the wake after the void region has been repopulated. For example, in cases where the electrostatic focusing in the plasma sheath dominates, a region of significant ion number density enhancement has been observed to occur on the wake axis at the crossing point of the deflected ion trajectories. This region of enhanced ion number density is thought, in turn, to create a positive space potential which

further deflects the trajectories of some ions and electrons. Farther downstream, recurring regions of enhanced ion density may occur and propagate outward from the wake axis with a "wave-like" behavior. The generating mechanism for this recurring effect and the exact nature of the associated wave-like structure are not presently known.

The discussion, so far, has dealt only with simple conducting bodies and non-magnetized, collisionless plasmas. Clearly, other complicating factors exist, such as solar UV, secondary electron emission, collisional effects, chemical reactions, and magnetic fields. Since the relative motion between the body and the plasma is supersonic with respect to certain ion plasma waves, a collisionless shock wave may be expected to occur under some circumstances. It is further thought that secondary electron emission may lead to non-monotonical matching in the plasma sheath of the floating potential of the body with the generally more positive space potential of the environmental plasma. Although it is recognized that these effects may possibly occur in space, they are considered as modifications to the basic electrostatic interaction and are, therefore, beyond the scope of the present study which will treat only conducting bodies in a collisionless, unmagnetized, binary plasma.

C. Approach

To accomplish the purpose of drawing the available experimental and theoretical results into a unified treatment, it is necessary to understand the complete meanings and limitations of the previous studies. This involves looking beyond the conclusions reached and into the methods and techniques invoked to arrive at them. A detailed, critical review of previous studies is given in the Appendices to provide the evidence in sufficient detail to constitute a meaningful basis for the conclusions reached. A brief summary and assimilation of the main results are given in Chapter II.

The reviews in Chapter II and Appendices B, C, D, and E also show that not all aspects of the plasma flow interaction previously discussed in B.1 are fully understood. For example, the focusing of ion streams into the ion

void region of the near wake has been presumed on the basis of systematic wave-like variations of ion current density profiles further downstream. However, these measurements are scalar in nature and no deflected ion streams have actually been observed. In addition, quantitative comparisons between the various theoretical treatments and experimental results are essentially nonexistent. This may be due partially to the fragmentary nature of the treatments, but also results from the nature of the experimental measurements. In the past, experiments have depended entirely on measurements of integrated current to arrays of points in space. By "integrated" it is meant that there was little or no distinction as to the flow direction so that the measurements consisted of the total current to a point and were, therefore, scalar rather than vector in nature. Quite clearly, a valid corroboration of the kinetic treatments, where the results are given in terms of distribution functions which remain constant along stream lines, requires experimental vector measurements of the ion flux in addition to the standard measurements. Further, scalar measurements cannot always yield accurate ion density and energy data, particularly within the disturbed flow of the plasma wake, and may be insensitive to processes which depend on the vector nature of the ion flux.

Chapter III provides a discussion of the experimental conditions, methods, and the data analysis techniques for the current investigation while Chapter IV is a detailed analysis of the results. In essence, this experimental study provides a more complete parametric description of the near and mid-wake regions and also gives, in a preliminary way, the much needed description of the vector ion flux behavior in the disturbed flow.

Chapter V is a summary discussion of the results obtained in the context of the physical process found to take place in the flow interaction of a non-magnetized plasma with conducting test bodies. The discussion draws freely from the results of previous studies as well as the current series of experiments. Where possible, the conclusions are extrapolated to describe the expected behavior of the disturbed plasma flow field around bodies orbiting within the ionosphere.

CHAPTER II. A CRITICAL REVIEW OF PREVIOUS INVESTIGATIONS

A. Theoretical Investigations

1. Mathematical Formulation. The theoretical investigation of plasma flows can be approached from two distinct, but related points of view. In the kinetic approach, the flow is considered to result from the net motion of a large collection of particles. This ensemble may consist of several types of particles, each interacting with the other constituents through the appropriate interparticle forces. Therefore, the kinetic approach consists of applying the laws of mechanics to the motion of the individual particles of the ensemble and applying statistical techniques to determine the mean value of the particle motions which are observable on the macroscopic scale. On the other hand, the continuum (or fluid) approach considers a streaming fluid which is divisible into a large number of macroscopic fluid elements. The behavior of each element is taken to represent the average motion of its constituent particles.

Although equivalent macroscopic descriptions of the flow are arrived at through these two approaches, the cumbersome mathematics involving the statistical distribution functions of kinetic theory can be circumvented by the continuum approach. Needless to say, this simplification is achieved at the expense of detailed information on the microscopic state of the plasma. Therefore, a clear understanding of the nature of the two approaches is required when considering their application to a specific problem. In some cases, a clear choice can be made; e.g., it is much more convenient to use the fluid formulation when dealing with a high density, collision dominated medium, while the kinetic approach must be used to describe the behavior of very low density neutral gas flows where no collective behavior occurs and no

meaningful fluid element can be defined. However, in the case of low density plasmas, even though discrete collisions may be unimportant, a collective behavior may occur as a result of long range forces and, hence, the continuum approach may be used — provided that it is not necessary to know the nature of the distribution functions and their behavior in space and time.

Because of the importance of the relationship between the kinetic and continuum approaches and the specific limitations of each to the interpretation of theoretical results, these two approaches will be formulated before discussing the various theoretical treatments reviewed in Chapter II.A.2.

a. Kinetic Equations. Since a plasma consists of a number of different types of particles, including electrons, ions, and neutral molecules, a complete statistical description of the state of the plasma requires a separate function, $f_\alpha(\vec{x},\vec{v},t)$, to describe the distribution of each constituent in six dimensional phase space at some given time. Each of these distribution functions is the solution of a Boltzmann equation of the form:

$$\frac{\partial f_\alpha}{\partial t} + \vec{v} \cdot \frac{\partial f_\alpha}{\partial \vec{x}} + q_\alpha [\vec{E} + \vec{v} \times \vec{B}/C] \cdot \frac{\partial f_\alpha}{\partial \vec{v}} = \left(\frac{\partial f_\alpha}{\partial t}\right)_c \quad , \qquad (2\text{-}1)$$

which describes the rate of change of f_α in space and time. Alternatively, it can be viewed as a statement of the conservation of particles existing in an elemental volume of phase space, $d^3x\, d^3v$.

The Lorentz force, $q_\alpha [\vec{E} + \vec{v} \times \vec{B}/C]$, results from the self-consistent electrostatic and magnetic fields which account for "distant collisions" of particles with long range forces. A collective behavior then results from Coulomb interactions between groups of charged particles. The term on the right-hand side of equation (2-1), $(\partial f_\alpha/\partial t)_c$, accounts for short range, discrete collisions, which may be electrostatic in nature (between two charged particles) or "hard sphere" type collisions.

One of the fundamental assumptions of plasma physics is this ad hoc division of the interactions between groups of particles into long range, collective, and short range, discrete, collisions and the assumption that the former dominates [1].

The Lorentz force is made self-consistent by requiring it to satisfy the Maxwell equations:

$$\nabla \times \vec{B} = \frac{1}{c} \frac{\partial \vec{E}}{\partial t} + 4\pi \vec{J} \tag{2-2}$$

$$\nabla \times \vec{E} = -\frac{1}{c} \frac{\partial \vec{B}}{\partial t} \quad , \tag{2-3}$$

and the Poisson equation:

$$\nabla \cdot \vec{E} = 4\pi \rho_c \quad , \tag{2-4}$$

where $\vec{J}$ is the total current flow and ρ_c is the net charge density.

The current and net charge density, in turn, depend on the distribution functions of the plasma constituents (solutions of the Boltzmann equations) through the relations

$$\vec{J} = \vec{J}_{ext} + \sum_{\alpha} q_{\alpha} \int \vec{v} f_{\alpha} (\vec{x}, \vec{v}, t) \, d^3v \tag{2-5}$$

and

$$\rho_c = \sum_{\alpha} q_{\alpha} \int f_{\alpha} (\vec{x}, \vec{v}, t) \, d^3v \quad . \tag{2-6}$$

Equations (2-1) through (2-4), subject to the definitions (2-5) and (2-6), form the governing equations for plasma flow interactions. This set of partial differential equations is coupled and nonlinear. Clearly, a general, analytical solution is not possible with the presently available mathematical tools. Even a numerical solution would be extremely unlikely as the system of equations stands. Therefore, a number of simplifying assumptions and approximations are generally made in kinetic treatments to obtain a tractable problem.

First, in almost all kinetic treatments, it is assumed that the flow interaction exists in a steady state so that there is no description of time dependent effects. While this obviously has a great impact on the complexity of the equations, its physical justification is questionable. There is, in fact,

experimental evidence that indicates possible wave particle interactions in the wake region. Nevertheless, with some exceptions in which an extremely simplified geometry was evoked [2], this assumption is necessary to obtain a solution.

A second assumption which is generally made is that the magnetic field can be omitted in the first order solutions. There is some experimental justification for this assumption under certain conditions, which will be discussed in a later section. When the plasma contains no magnetic field, the Lorentz force reduces to $q_\alpha \vec{E}$. The assumption that $\vec{B} = \vec{0}$, coupled with the previous assumption that $\partial / \partial t = 0$ eliminates Maxwell equations (2-2) and (2-3), leaving only the Poisson equation (2-4) which the electric field must satisfy. From equation (2-5), we see that the only currents possible are those resulting from external forces, which are generally omitted.

The third major assumption is that the plasma is "collisionless." This means that, although long range, collective interactions will occur and must be considered, the short range, discrete collisions occur so infrequently as to have a negligible effect on the behavior of the plasma. This assumption has a dual impact on the mathematical formulation. First, since the discrete collisions are negligible, we set $(\partial f_\alpha / \partial t)_c = 0$ and equation (2-1) becomes homogeneous (the Vlasov equation). Secondly, since neutral particles can only interact through discrete collisions (which are assumed to be negligible) they can be completely neglected. We, therefore, only require time independent collisionless Boltzmann (or Vlasov) equations for ions and electrons; i.e.,

$$\vec{v} \cdot \frac{\partial f_{i,e}}{\partial \vec{x}} + q_{i,e} \vec{E} \cdot \frac{\partial f_{i,e}}{\partial \vec{v}} = 0 \quad . \tag{2-7}$$

A fifth general assumption, usually made when describing plasma flow interactions of the ionosphere with orbiting spacecraft, is that the flow is mesothermal; i.e., $\bar{c}_i << V_o << \bar{c}_e$ where $\bar{c}_{i,e}$ is the mean thermal speed of ions or electrons and V_o is the orbital speed. The left-hand part of the inequality states that the mean thermal velocity of the ions is negligibly small

compared to the relative motion between the body and the plasma. The ions can therefore be assumed to behave as a monoenergetic stream (no thermal motion). The electrons, on the other hand, have a mean thermal speed much greater than the orbital speed and it can therefore be assumed that they are unaffected by the presence of the body and maintain a Maxwellian distribution. The distribution of electrons is therefore known everywhere (if the self-consistent electric potential is known from the Poisson equation). The ion distribution is known far from the body (in the ambient medium) but must be calculated in disturbed regions. The solution for the ion and electron densities and the electric potential can be approached in several ways, depending on the boundary conditions used at the body and in the undisturbed medium.

The boundary condition at the body generally states that the body is an equipotential surface and that all incident charged particles are neutralized; i.e., no charged particles are reflected from the surface so that, in effect, the ion and electron distribution functions are zero there. In most kinetic treatments, the body potential is assumed to go to zero (to the space potential of the plasma) infinitely far from the body and the resulting electric field is obtained in a self-consistent way by taking into account its effect on charged particles and, conversely, the screening effect of the charged particles on the body potential. In some fluid treatments, the potential is assumed to approach zero at some distance from the body (i.e., a sheath thickness is assumed). The boundary conditions are important since they determine the nature of the flow interaction. They are discussed separately for the various theoretical treatments in Appendices B and C.

b. The Continuum Equations. The set of equations which governs the continuum description of plasma flows consists of conservation equations for mass and momentum, the equations of state, and the Maxwell equations. The conservation equations can be derived by considering the flow of the appropriate physical quantities through macroscopic control volumes. However, they are derived in Appendix A by taking moments of the Boltzmann equation to show more clearly the relationship between the continuum and kinetic descriptions. The continuity equation from Appendix A is of the form:

$$\frac{\partial n_\alpha}{\partial t} + \nabla_\alpha \cdot (n_\alpha \vec{u}_\alpha) = 0 \quad , \tag{2-8}$$

where $\vec{u}_\alpha$ is the average, or drift velocity of the α -constituent. The momentum transfer equation was found to be:

$$\frac{D\vec{u}_\alpha}{Dt} = -\frac{\nabla_x P_\alpha}{m_\alpha n_\alpha} + \frac{q_\alpha}{m_\alpha}[\vec{E} + \vec{u}_\alpha \times \vec{B}/C] - \nu_c \vec{u}_\alpha \quad , \tag{2-9}$$

where

$$D/Dt = \partial/\partial t + \vec{u} \cdot \nabla_x \quad .$$

The electric and magnetic fields are made self-consistent in the continuum formulation by requiring them to satisfy the Maxwell equations (2-2), (2-3), and (2-4). (The remaining Maxwell equations are redundant.) In this case, however, averaged quantities must be used so that the charge and current densities are defined as:

$$\rho_c = \sum_\alpha q_\alpha n_\alpha \tag{2-10}$$

and

$$\vec{J} = \sum_\alpha q_\alpha n_\alpha \vec{u}_\alpha \quad , \tag{2-11}$$

where the summation is over all charge-carrying constituents of the plasma.

The assumptions required in deriving equations (2-8) and (2-9) are that: (1) there is no annihilation or creation of charged particles by discrete collisions (or by other means); (2) the plasma is isotropic; i.e., $c_x^2 = c_y^2 = c_z^2 = \overline{C^2}/3$; and (3) the momentum transferred to and from the α -constituent by discrete collisions can be expressed by an effective collision frequency, ν_c, and takes the form $m_\alpha n_\alpha \nu_c \vec{u}_\alpha$ (more exact forms use the relative velocities of the colliding particles). There is also an implicit assumption that the velocity distribution functions for the various constituents remain locally in near-equilibrium; i.e., in any localized region, the distribution functions change slowly compared to the characteristic time constant for the fluid flow.

This is necessary for average values to be well defined. The assumption used, that no charge is created or annihilated, in effect states that no ionization or recombination reactions are allowed in the plasma on the time scale of the fluid flow. The assumption that the plasma is isotropic implies that either there is no magnetic field or the particles interact frequently enough (through either discrete collisions or collective interactions) so that such quantities as conductivity, temperature, permittivity, and pressure are essentially scalar. The assumption of an isotropic plasma is not essential. However, without this assumption pressure becomes a tensor and equation (2-9) becomes correspondingly more complicated. For the problem at hand, the form of equation (2-9) is generally sufficient.

In the kinetic formulation, the Boltzmann equations for each plasma constituent combined with the Maxwell equations (2-2) through (2-4) and the definitions (2-5) and (2-6) were found to constitute a closed system of equations. However even though the continuum continuity and momentum equations are rigorously derived from the Boltzmann equation, they do not form a closed set when combined with the Maxwell equations. There are $6 + 5\alpha$ variables to be determined (i.e., n_α, P_α, $\vec{u}_\alpha$, $\vec{E}$, and $\vec{B}$) while there are only $6 + 4\alpha$ equations. To obtain closure, one additional equation is required for each of the α constituents.

An additional assumption is therefore required to obtain closure. If the plasma flow velocity is much greater than the mean thermal speed of the ions, then the cold plasma hypothesis can be used; i.e., the plasma ions are assumed to have negligible thermal motion ($T_i = 0$) and as a result of this assumption, the pressure and collisional momentum transfer terms drop out of the momentum equation; i.e., $\nabla_x P = \vec{0}$ and $\nu_c \vec{u}_\alpha = \vec{0}$. (Even though the electrons may have a large thermal motion, they transfer very little momentum during collisions and hence contribute negligible to the above two terms.) If the particles interact frequently enough so that an equilibrium distribution is

maintained, then the local Maxwellian hypothesis may be used. In this case, pressure will always be a scaler and can be related to the number density by:

$$P_\alpha = n_\alpha k T_\alpha \quad , \tag{2-12}$$

where k is Boltzmann's constant and T_α is the temperature of the α-constituent. If the plasma is also assumed to behave as a calorically perfect gas (i.e., the ratio of specific heats is independent of temperature), then equation (2-12) can be simplified to a relation between P_α and n_α; i.e.,

$$P_\alpha = C\rho_\alpha^{\gamma} = C(m_\alpha n_\alpha)^{\gamma} \quad ,$$

where γ is the ratio of specific heats, C_P/C_v, and C is a constant. Therefore,

$$\frac{\nabla P_\alpha}{P_\alpha} = \gamma \frac{\nabla n_\alpha}{n_\alpha} \quad . \tag{2-13}$$

The system of equations (2-2), (2-3), (2-8), (2-9), and (2-13), subject to the definitions (2-10) through (2-12), forms a closed set which is appropriate for describing some types of plasma flow interaction problems. It should be emphasized, however, that along with the specific assumptions listed above, the continuum equations use average values of physical quantities and are, therefore, insensitive to the form of the distribution functions. Therefore, any distribution giving the same average values would produce the same result under this system of equations. We will find that there are cases where the local behavior of the plasma does depend on the form of the distribution function and in such cases, the fluid approach will not provide an adequate description.

c. Comparison With Classical Gas Dynamics. Before reviewing the theoretical results in the next section, it is worthwhile to note some of the similarities between plasma dynamics and classical gas dynamics. Neutral gas flows obey a continuity equation, identical to equation (2-8), and the

Navier-Stokes equation which, with the exception of the electromagnetic force term, is identical to the momentum transfer equation (2-9).

When describing plasma flow interactions with bodies in the earth's ionosphere above 150 km altitude, the particle number densities are sufficiently low to make momentum transfer by discrete collisions negligible; i.e., $\nu_c \to 0$ for all α. Momentum transfer therefore occurs primarily through collective interactions resulting from the electrostatic fields associated with the charged particles and the interaction of charged particles with externally imposed electric or magnetic fields. (Momentum transfer to the body is unimportant since we are primarily concerned with the effect of the body on the plasma medium and not the drag induced on the body. Since the boundary condition used at the surface of the body is that all incident charged particles are neutralized, there is no transfer of momentum to the charged particles in the flow field by direct impact.)

The dominance of long range electrostatic forces creates the possibility for a rapidly moving charged body to exert either an attractive or repulsive force on the ions whereas, in classical gas dynamics, only hard-sphere type collisions are possible; therefore, particles are always repelled when they undergo a collision with either a moving body or other particles. We might, therefore, expect that when the electrostatic force associated with the moving body is repulsive, the plasma flow interaction will be very similar to that of a body moving through a neutral, compressible fluid such as the atmosphere. However, when the force exerted on the ions by the body is attractive, there is no corresponding mechanism in classical aerodynamics and we might expect entirely different phenomena to occur. This will indeed be found to be the case as we review the theoretical and experimental findings in the next few sections.

2. Results of Theoretical Treatments. A detailed discussion of several continuum treatments of the plasma flow interaction problem is given in Appendix B [3-10] while an in-depth discussion of the numerical techniques used and results obtained from a number of kinetic calculations is provided in Appendix C [2], [11-33]. Here, we will summarize only the results which

are most important to the present study. The appropriate appendices should be referred to for further detail and limitations of the results.

An early fluid treatment by Kraus and Watson [3] predicted a trailing ion acoustic Mach cone structure behind very small, negatively charged bodies. It was also found, in this study, that the charge density increased within the Mach cone. Trailing disturbances inclined at the Mach angle with respect to the flow direction have also been predicted by Rand [4,5] for very small diameter cylinders and a half plane and by Sanmartin and Lam [10] for small bodies.

Rand's treatment for small cylinders also predicts (after appropriate modification for $T_e/T_i >> 1$) space charge potential oscillations on the wake axis with a period of $\omega_{pi} Z/V_o$. For the case of the half-plane (or a very large disc) the treatment predicts that ions will be deflected toward the wake axis at the ion acoustic Mach angle. As a result, planes of disturbance will travel both toward the wake axis and out into the ambient plasma. The inclusion of ion thermal motion leads to the conclusion that for $T_e/T_i < 10$, damping of collective wave phenomenon becomes significant at $Z = S \cdot \lambda_D$.

In addition to the prediction of a strong wave front at the acoustic Mach angle, Sanmartin and Lam predict a second wave to develop further downstream. The transverse structure of this second wavefront was predicted to oscillate (described by the Airy function times a sine function). This seems to agree with experimental observations by Hester and Sonin and Fournier and Pigache (Appendix E.1).

The first kinetic treatment of the plasma flow interaction problem to include a self-consistent solution of the space potential, Φ, was made by Davis and Harris [11]. This treatment predicted an ion void region behind medium-sized bodies. Further, the rarefaction of ions was predicted to extend, transversally, beyond the extent of the body. The third main result was the prediction of an axial ion peak some distance downstream from negative bodies. An axial ion peak was also predicted for axisymmetric bodies by Maslennikov and Sigov [16-19], Guerevich et al. [26] and Fournier [23].

In addition to predicting an axial peak, Maslennikov and Sigov also show the deflection of the ion trajectories at the plasma sheath and predict additional deflections due to the positive space charge potential associated with the axial ion peak (Appendix C.2, Figure C-2).

Taylor predicted the axial ion peak to occur for $T_i = T_e$. He further predicted the axial ion peak to split farther downstream and form a trailing "V" structure with a half-angle defined by the ion acoustic Mach angle. These predictions are in agreement with those made on the basis of a fluid treatment by Rand [4] and Sanmartin and Lam [10].

In addition to an ion void, Call [12] predicted the region behind the body to be highly depleted of electrons as well. He also predicted the ion streams, deflected by the plasma sheath at the body for large, negative Φ_b to cross the wake axis and create an additional wave-like structure which does not form a Mach line, but depends on Φ_b. This effect was found only for cylindrical bodies. Call found that axisymmetric bodies focus the ions onto the axis more effectively, forming an ion peak of greater amplitude. Apparently, the increased space potential associated with this higher peak prevents the above penetration by the converging ion streams. Call also predicted an oscillatory structure along the Z-axis for axisymmetric bodies but not for cylinders. This is not in agreement with the predictions of Rand [4] and Fournier [23] and the observations of Hester and Sonin [34], where such a structure was found for cylindrical bodies (Appendix E.1.g).

The work by Call was extended by Martin [13] into a parametric study. In addition to the above predictions, Martin's results show the parametric dependence of the angle of the deflected ion streams, θ_d, the half-angle of the trailing "V" structure, θ_w, and the crossing point of the deflected ion streams on the Z-axis, Z_d, on the parameters R_d, S, and Φ_b. In particular, he predicts the crossing point to have a dependence of the form:

$$[Z_d/\lambda_D] \sim S(R_d/\Phi_b)^{1/2} \quad .$$

This prediction will be discussed in the context of experimental results in Chapter IV.

Gurevich et al. [26] predicted the axial ion peak amplitude to decrease with decreasing T_e/T_i. Specifically, it was found to vanish at $T_e/T_i = 1$ (not in agreement with Taylor) but it still occurred for $T_e/T_i = 4$. This is in agreement with the predictions of Liu and Hung [28,29] for a large sphere and those of Fournier [23] for a long cylinder, where the axial structure vanished for $T_e/T_i = 1$ (for small Φ_b) but was found to occur for $T_e/T_i = 2$. In addition, Fournier's results show the effect of decreasing T_e/T_i to be opposed by increasingly negative Φ_b, so that for a sufficiently negative body potential the axial structure reappears.

Fournier also studied the potential field around the body for a variety of conditions. His findings include the depression of the equipotential contours in the frontal region by the ion motion, a tendency of the contours to become circular for high negative values of Φ_b, the extension of the potential field far into the ambient plasma for $\Phi_b > 0$, and the existence of a negative "potential well" in the ion void region for large negative bodies. A potential well was also found by Liu [2] and Parker [21].

A far-wake ion density structure which agrees with experimental observations of Hester and Sonin (Appendix E.1.g) has been predicted by Woodroffe and Sonin [30] and by Könemann [33]. The treatment by Könemann uses a Greens function formulation based on the potential calculations by Sanmartin and Lam [10].

Finally, the void-filling process has been investigated by Gurevich et al. [32] for plasmas with mixed ion composition. It is predicted that, for proper ratios of heavy and light ion concentrations, a two-stream type instability is generated at the ion void boundary. This mechanism could possibly explain the observation of enhanced electron temperatures in the wakes of ionospheric satellites (discussed below).

The results of the above fluid and kinetic treatments are summarized in Table 2-1. Additional theoretical reviews have been made by Chopra [35] and Liu [1].

TABLE 2-1. SUMMARY OF THEORETICAL CALCULATIONS

Comments	B	Far Wake		Mid-Wake			Near Wake		Effects Included						Effects / Authors
		"Waves"	Axial Sec.	ϕ-Barrier	Trailing "V"	Axial Prp.	ϕ-Well	n_i-Void	T_e/T_i	S	R_d	$\lvert\phi_b\rvert^1$	$\lvert\phi\rvert$	X-ing Traj.	
		"							arb.	$\gg 1$	$\ll 1$	$\ll 1$	$\ll 1$		Kraus / Watson
$R_d \ll 1$ — cylinder $\gg 1$ — 1-2 plane $T_e, T_i \gg 1$ — extension of theory for x = 0		"	"			Exp. ϕ			$\ll 1$ ($\gg 1$)	$\gg 1$	$\ll 1$ $\gg 1$	$\ll 1$	$\ll 1$		Hand
Axial ϕ-peak suggested for $T_e, T_i \ll 1$			ϕ (ϕ_b 0)			short for $\phi < 0$			$\gg 1$	$\gg 1$	$\gg 1$	$\gg 1$	arb.	No	Lam Greenblatt
		"							$\gg 1$	$\gg 1$ $\ll 1$	$\ll 1$	$\ll 1$	$\ll 1$		Sanmartin-Lam
Peak-head Space Charge						n_i		"	$\gg 1$	$\gg 1$	10, 25	$\gg 1$	arb.		Davis-Harris
Orbiting Ions			ϕ	All cases	Suggested	n_i ϕ	$R_d < 1$ $\phi_b = -1$	"	$\gg 1$	1.1 1.4 7.5	0.05 1 20	0 to 3-	arb.	Yes	Maslennikov Sigov
						n_i	$\phi_b = -1$	"	1	0	1.5	2.5	arb.		Taylor
Rarefaction Mach Cone						n_i		"	$\frac{1}{4}$	$\gg 1$	$\gg 1$		$\ll 1$		Gurevich et al.
	Some cases		ϕ	"		n_i	$R_d \geq 1$ ϕ_b 0	"	$\gg 1$	1.1 6	0.2 to 25	0 to 40	arb.	No	Call
			r_i			"	"		1 2 10	1 6 10	1.5 to 10	$(\sim 2)^1$ to -40	arb.	Not probable	Fournier
		"			"	n_i		"	$\gg 1$	3.5	0.2 1	-5	arb.	No	Martin

Note 1. ϕ_b always negative except - 3 by Fournier.

B. Available Satellite Data

The most useful in situ data have come from the Ariel I, Explorer 31, Gemini-Agena 10, and the Atmospheric Explorer (AE-C) missions. The details of the satellite geometry, orientation, instrument locations, and orbital data are given in Appendix D along with a more detailed review and discussion of the results. The instruments used included Langmuir probes of various geometries (to measure T_e, n_e and ϕ_s) planar, gridded retarding potential analyzers (RPA's) (to measure E_i, T_i and n_i) and a cylindrical retarding ion mass spectrometer (to determine m_i). A general discussion of these instruments is given in Appendix F. In this section, the main results obtained from these missions will be briefly stated.

Observations of electron current variations with angle of attack have been made on all of the above missions. The Ariel I data show the electron density in the ion void region to be depleted by a factor of 10^{-2} below its ambient value in the altitude range of 400 to 700 km (where 0^+ is the major ionic constituent) [36]. Similar data were obtained from the Explorer 31 satellite over a wider range of altitude and hence plasma conditions. These results agree with the Ariel I findings and, in addition, show the depth of the electron depletion in the near wake to be directly proportional to the ionic mass [37,38].

The behavior of the ion current as a function of angle of attack was studied on the Ariel I satellite at a radial distance of $2R_{Ariel}$ from the center, and on the AE-C satellite at about $1.6R_{AE}$ from its center. The Ariel I measurements [39] show the ion current to be depleted by a factor of 3, compared to 100 for the electrons under similar conditions. This discrepancy may be the result of (1) the increased distance downstream at which the ion measurements were made, (2) the existence of a positive space potential and, hence, an ion-rich medium, or (3) the effect of the -6 volt potential applied to the spherical ion probe which made these measurements.

The ion current data obtained from a cylindrical Langmuir probe on the AE-C satellite were used to conduct a parametric study of the effects of R_d, T_e, and m_i on the void filling process [46,47]. These studies show that the ion current density in the near wake has an exponential dependence on R_d and a linear dependence on S. The presence of hydrogen ions was found to greatly accelerate the void filling process; i.e., for an 0^+-plasma, the ion current density in the void was depleted by factors of 100 at T_e = 1000°K and 30 at 3000°K while for a 50% oxygen, 50% hydrogen plasma, the ion current depletions were only by factors of 6 and 2.3 for T_e = 1500° and 3000°, respectively.

Measurements of electron concentration were also made by boom-mounted probes at $5R_{Ariel}$ from the center of the Ariel I satellite [36]. These measurements show a distinct axial electron density peak in the wakes of both the main body of the satellite and its spherical ion probe and, therefore, tend to confirm the laboratory and theoretical predictions of axial ion peaks. No such peak was found, however, in the wake of the Gemini 10 capsule (Appendix D).

Measurements made on the Explorer 31 [37,42] and Gemini-Agena 10 [43] missions have indicated an elevated electron temperature in the near wake. Both missions show enhancements as large as 1.8 times the ambient electron temperature. A detailed study of the Explorer 31 data revealed no significant dependence of this effect on the geomagnetic field [42]. Apparently, then, this is strictly a plasma wake phenomenon and may be the result of a potential well in the ion void region, or possibly wave particle interactions set up by oscillations at the wake boundaries.

Finally, the Ariel I data provide some indirect evidence for the existence of oscillations or instabilities at the ion void boundaries. Unexplainably high currents were obtained at the modulation frequency of the ac probe (Appendix D.2.c and Appendix F). These current levels could be explained by plasma oscillations in the range of the ion plasma frequency. Such oscillations may explain the elevated electron temperatures observed in the wake.

C. Laboratory Investigations

A detailed discussion of the numerous laboratory investigations and their results is given in Appendix E [34,44-64]. The various diagnostic instruments and analysis techniques used are discussed briefly in Appendix F. Below is a brief statement of some of the results obtained from these investigations which apply to the present study.

Early investigations by Hall, Kemp, and Sellen [46] clearly show the ion void region and the axial ion peak for a spherical test body. The ion current density was measured at a number of stations across the wake for a wide range of body potentials, revealing a distinct dependence of the axial ion peak on Φ_b. More detailed measurements of the ion peak, including both transverse and axial profiles for a variety of potentials, were published a year later by Clayden and Hurdle [47]. These measurements, in addition to showing the dependence on Φ_b, show the axial ion peak to rise rapidly behind the body and trail off slowly, extending beyond $20R_o$ downstream. Similar results were found for a sphere and a conical body oriented with its apex into the flow.

Experiments conducted by Skvortsov and Nosachev [48,49] show a rarefaction wave that forms an ion acoustic Mach cone which is in agreement with several theories discussed above. These data also show the axial ion peak to move toward the test body as Φ_b becomes more negative, in general agreement with the theoretical predictions of Martin [11].

A second experiment was conducted to study the accuracy of parametric scaling. Measurements taken for constant values of R_d, S, and Φ_b, obtained at different values of T_e, show little variation while a significant variation appears in some cases when only the ratios R_d and Φ_b/S^2 were preserved.

The experiments by Hester and Sonin [34, 51-53] were made with long cylinders and spheres of various R_d values. These studies show that no appreciable void region occurs for small cylinders but that a sequence of axial peaks occur on the wake axis, in general agreement with the (modified) predictions of Rand [4]. Further, these peaks divide and form trailing "V" structures. The first of these peaks behaves as the crossing ion streams,

predicted theoretically by Call [12]; however, it is not clear what mechanism is involved in the remaining structures. An ion rarefaction wave was also observed, in general agreement with Rand [4].

For bodies in the range $1 \leq R_d \leq 10$, Hester and Sonin observed that an ion void formed and an axial ion peak occurred. The axial ion peak for spherical bodies was very high and no oscillating structure was observed downstream as in the case of the small cylinder. The peak divided into a trailing "V" structure as in other studies. The amplitude of the axial ion peak was greatly diminished for bodies in the range $R_d \simeq 40$. However, it did occur for sufficiently negative values of Φ_b and formed at lower values for spheres than cylinders.

In addition to confirming most of the above results, the experiments by Fournier and Pigache [56-59] involved a detailed study of the effects of an effective ion thermal motion (the motion was not Maxwellian).

These experiments confirm the direct proportionality of the wake structure amplitude to the T_e/T_i ratio as predicted by the theoretical treatments discussed above. Ion current density profiles taken with $T_e/T_i \simeq 100$ showed a striking axial ion peak, as in most of the above studies. The amplitude of the peak was diminished at $T_e/T_i = 10$ and vanished completely at $T_e/T_i = 1$ (with the test body roughly at floating potential for all cases). There was no significant variation in the peak amplitude with R_d; although, Φ_b influenced it very strongly, as expected.

Finally, in addition to the above experimental studies of the electrostatic interaction, several experimental investigations of the flow interaction in the presence of a magnetic field were reviewed [61-64]. All of these experiments were made with the embedded B-field parallel to the plasma flow direction.

The net result of the parallel magnetic field is the generation of axial ion current density oscillations along the wake axis with a period proportioned to $(Z\omega_{ci}/2\pi V_o)$. In addition, the amplitudes of the oscillations were found inversely proportional to $R_o/R_L(i)$. Evaluating these parameters for typical ionospheric conditions shows that such oscillations would be very small in

amplitude and that the period would extend far beyond the mid-wake zone. Therefore, it is concluded that the omission of the geomagnetic field in the study of the near and mid-wake regions of small to medium sized bodies is justifiable.

CHAPTER III. THE APPROACH AND CONTRIBUTION OF THE PRESENT EXPERIMENTAL STUDY

A. Potential Contribution of Further Laboratory Studies

In Chapter II, we have reviewed the previous theoretical, in situ and laboratory investigations. While this review shows that a great deal of progress has been made toward understanding the basic spacecraft-space plasma interaction over the past two decades, it has also revealed several unanswered questions of a very fundamental nature. For example, does the interaction have a steady-state behavior or, if not, what is its temporal nature and how does this manifest itself in measurable quantities? Does an enhancement of electron temperature actually occur in the void region and if so, what is the casual mechanism? Does the complex wake structure observed in cold, laboratory plasmas occur in the ionosphere, or is it diffused by thermal ion motion? What is the relation between the wave like structure predicted by the kinetic treatments of Call, Martin, and Woodroffe and Sonin, and the fluid treatment by Sanmartin and Lam; do they result from the same physical mechanism, or is the similarity of the predicted wake structure purely fortuitous? Do the orbital and deflected ion trajectories, predicted by Maslennikov and Sigov, actually occur and if so, what is their macroscopic effect?

Several areas of disagreement have also been revealed. For example, why did an axial ion flux enhancement apparently occur in the wakes of the Ariel I satellite and its spherical ion probe but was not found in the wake of the Gemini-10 capsule? Is the disturbance envelope defined by a Mach cone, as suggested by Rand and others, or is it related to other parameters, as

suggested by Hester and Sonin? Is the length of a body in the flow direction important, as suggested by Schmitt, or is the cross-sectional geometry the only controlling factor, as predicted by Taylor and Call? Is there a fundamental difference between the two-dimensional and axisymmetric flow interactions, as suggested theoretically by Call and experimentally by Hester and Sonin, or is the observed difference due to other factors, as suggested by Könemann?

The present experimental program addresses several of the above questions. In some cases, this has been possible by carefully designing the experiment around standard, existing diagnostic instruments. However, in a few cases, differential vector measurements were required which were not suitably provided by any of the known probing techniques. It was, therefore, necessary to develop a new diagnostic instrument specifically for this purpose. This and other aspects of the experimental methods used will be discussed in the remainder of this section.

B. Scaling Techniques

1. Derivation of the Vlasov Scaling Laws. The dimensionless parameters which must be invariant in order to obtain similitude between two flow interactions of different scale sizes can be derived formally from the governing kinetic equations discussed in Chapter II.A.1.a. Assuming magnetic fields to be negligible, the governing equations reduce to a Boltzmann factor for the electron density, a Vlasov equation for the ion distribution function and the Poisson equation which relates the self-consistent electric potential to the net charge density; i.e.,

$$n_e = n_o \exp\left[\frac{e\phi}{kT_e}\right] \tag{3-1a}$$

$$\frac{\partial f_i}{\partial t} + \vec{v} \cdot \hat{\nabla} f_i - \frac{q_i}{m_i} \hat{\nabla}\phi \cdot \frac{\partial f_i}{\partial \vec{v}} = 0 \tag{3-1b}$$

and

$$\hat{\nabla}^2\phi = -4\pi\,[q_i n_i - e n_e] \quad . \tag{3-1c}$$

The simulation parameters are obtained by nondimensionalizing the set of equations (3-1) and requiring the equations to remain invariant in form when the scale size is changed. This will occur if the coefficients of each term, which are the parameter groups, remain invariant. Let:

$$x = R_o X \qquad t = t/\omega \qquad v = V_o u \qquad f_i = n_o F$$

$$\phi = P\Phi \qquad q_i = eZ \qquad m_i = m_p M \qquad n_{i,e} = n_o N_{i,e}$$

$$\hat{\nabla} = \nabla/R_o \quad .$$

Substituting this transformation into equations (3-1a, b and c), we obtain

$$N_e = \exp\left[\Phi\left(\frac{eP}{kT_e}\right)\right] \tag{3-2a}$$

$$\left(\frac{\omega R_o}{V_o}\right)\frac{\partial F}{\partial t} + \vec{u}\cdot\nabla F_i - \left(\frac{ZeP}{m_p M V_o^2}\right)\nabla\Phi\cdot\frac{\partial F_i}{\partial \vec{u}} = 0 \tag{3-2b}$$

and

$$\nabla^2\Phi = -\left(\frac{4\pi e n_o R_o^2}{P}\right)[ZN_i - N_e] \quad . \tag{3-2c}$$

The equations (3-2) will remain invariant if we require $P = kT_e/e$ and the following parameter groups to remain constant:

$$Z \equiv \text{number of charges per ion} \tag{3-3a}$$

$$\Phi = \left[\frac{e\phi}{kT_e}\right] \tag{3-3b}$$

$$\left[\frac{\omega}{V_o/R_o}\right] \tag{3-3c}$$

$$\left[\frac{Ze\mathcal{P}}{m_p M V_o^2}\right] = \frac{ZkT_e}{m_i V_o^2} = \left(\frac{Z}{2}\right) S^{-2} \tag{3-3d}$$

$$\left[\frac{4\pi e n_o R^2}{\mathcal{P}}\right] = \left(\frac{4\pi m_o e^2}{kT_e}\right) R_o^2 = \left(\frac{R_o}{\lambda_D}\right)^2 = R_d^2 \quad . \tag{3-3e}$$

Hence, the dimensionless ratios R_d, S, and Φ arise naturally from the governing equations. Substituting them into the equations gives some additional insight into their effect. Equations (3-2) can now be written in the form:

$$N_e = \exp(\Phi) \tag{3-4a}$$

$$\left(\frac{\omega}{V_o/R_o}\right) \frac{\partial F_i}{\partial t} + \vec{u} \cdot \nabla F_i + \frac{Z}{2} [S^{-2}] \vec{E} \cdot \frac{\partial F_i}{\partial \vec{u}} = 0 \tag{3-4b}$$

$$\nabla^2 \Phi = -R_d^2 (ZN_i - N_e) \quad . \tag{3-4c}$$

Note that the potential field has its greatest effect on the electron density distribution [equation (3-4a)] and that it arises due to charge separation [equation (3-4c)]. Further, the effect of the charge separation is directly proportional to the Debye ratio; i.e., for a given set of plasma stream characteristics, the larger the body, the more pronounced is the effect of the charge separation. This is reasonable since the region of charge separation will increase in size with R_d and E is given by the integral of ρ_c over this region. In equation (3-4b) we see that the effectiveness of the electric field in deflecting ion trajectories is inversely proportional to the square of S. Again, this is reasonable since the magnitude of $\vec{E}$ depends on the thermal energy of the electrons [equations (3-3b), (3-4a), and (3-4c)] and S is a measure of the kinetic energy of the ions relative to the thermal energy of the electrons. The remaining parameter group, $(\omega R_o/V_o)$, indicates that if temporal effects are to be included, then the ratio of the frequency of any such effects to the transit time required for an ion, moving at the flow velocity, to cross the disturbance must be preserved. It also shows that only phenomena with frequencies higher than the transit time will be important.

The effects of the boundary at the test body are twofold. First, the potential on the boundary, Φ_b, is defined by the requirement that $q_i n_i \bar{c}_i = e n_e \bar{c}_e$ and therefore may be considerably greater than unity in magnitude. In space, it may also become positive, depending on the secondary photoemission characteristics of the body and the solar UV intensity. In the laboratory, Φ_b, is normally allowed to be the floating potential or controlled by an external power supply. In any case, the effect on the electrons in the sheath region will be very large [equation (3-4a)]. For large Φ_b, ion trajectories will also be greatly disturbed [equation (3-4b)].

The second effect of the test body boundary is to absorb all incident charge. This means that the distribution function in the disturbed region may be significantly perturbed. Therefore, R_d (which has the form of a Knudsen number) becomes a measure of the disturbance amplitude. For $R_d << 1$, there will be essentially no charge separation and the Poisson equation can be linearized as in Appendix B.2. However, for $R_d >> 1$, the charge separation, and hence Φ, can significantly disturb the plasma in the near region, and a simple, single fluid continuum approach cannot be used (Chapter II.A.1.b).

2. Method of Applying Scaling Laws. In principle, it should be possible to obtain any arbitrary combination of the dimensionless scaling parameters R_d, S, and Φ_b by appropriate choices of the physical variables n_o, T_e, V_o, and R_o. Unfortunately, this is not the case since, in practice, several of these variables are subject to experimental limitations. The test body size must be smaller than the plasma stream, therefore, placing an upper bound of R_s (the plasma accelerator radius) on the body radius, R_o. Further, due to the nature of ion accelerators, it is difficult to obtain high number densities in low energy streams. Therefore, in the range of a few eV. which is appropriate for ionospheric conditions, n_o is directly proportional to V_o^2.

Now consider the dependence of the scaling parameters on these variables and the resulting effect of the above restrictions; i.e.,

$$S^2 = \frac{m_i V_o^2}{2kT_e} \sim \frac{V_o^2}{T_e}$$

$$R_d^2 = \frac{R_o^2}{(6.9)^2 T_e/n_o} \sim \frac{n_o R_o^2}{T_e}$$

$$\Phi_b = \frac{e\phi_b}{kT_e} \sim \frac{\phi_b}{T_e} .$$

The above limits impose no constraint on Φ_b since ϕ_b is independent of all other variables and can be adjusted to any desired value by an external voltage source. Similarly, R_d can be made arbitrarily small and S arbitrarily large by making R_o small and V_o large, respectively. However, R_d cannot be made arbitrarily large while making S small. As stated above, R_o must be less than the beam radius. Any further increase of R_d must be accomplished by increasing n_o and/or decreasing T_e. Note, however, that this is inconsistent with small S which requires small V_o (and therefore small n_o) and/or large T_e. The conditions of large R_d and small S are therefore mutually exclusive in the laboratory and can only be approached within certain practical limits established by the experimental facilities.

The ranges of R_d, S, and Φ_b attainable in the MSFC Space Plasma Simulation Facility are given in Table 3-1. (Physical details of the facility will be given in the next section.)

As a result of the practical constraints on R_d and S, it will be possible to correctly scale very few of the wide range of conditions possible for orbiting satellites or diagnostic instruments in the ionospheric plasma according to the strict Vlasov scaling laws developed above. In recent years, however, a concept known as qualitative scaling has evolved which allows a considerable relaxation of the rigid Vlasov laws [65]. Under qualitative scaling, parameters much greater (or smaller) than unity are required to remain so but are not required to maintain the same order of magnitude. Parameters which are of order unity are scaled as closely as possible; i.e.,

$$P_{space}\begin{cases} >> 1 \\ << 1 \\ \sim 1 \end{cases} \Longrightarrow \qquad P_{Lab}\begin{cases} >> 1 \\ << 1 \\ \simeq P_{space} \end{cases} .$$

In qualitative scaling, the emphasis is on reproducing the correct physical processes for study, rather than the exact interaction morphology.

The series of experiments discussed in Chapter IV apply a variation of the above concept which we will call "partial qualitative scaling." The difference is that no attempt will be made to scale parameters which, from physical arguments, can be shown to have very little or no effect on the physical mechanism under investigation. For example, in the ionosphere, the magnetic field is unimportant in determining the nature of the near and mid wake regions, as shown in Chapter II.C and Appendix E.2. In the case of the temperature ratio, T_e/T_i, no means for correctly controlling T_i exists. (Recall that in Chapter II.C efforts to control T_e/T_i were discussed but found to produce non-Maxwellian ion temperatures.) Therefore, this parameter is not scaled. In this case, the omission is not justified and must be viewed as a fundamental limitation of the experiments.

C. Experimental Methods and Apparatus

The facilities required to synthesize the ionospheric plasma in a laboratory environment comprise what can simply be described as a plasma wind tunnel. It consists basically of a cylindrical vacuum chamber, a plasma source which produces an axial stream, a system of diagnostic probes (described in Chapter III.D), and a manipulator to position probes and test bodies.

The plasma wind tunnel facility at NASA MSFC was established for the purpose of studying and evaluating diagnostic probing devices and techniques [24] and is well suited to ionospheric simulation experiments. A schematic of the facility is shown in Figure 3-1 and the range of plasma stream parameters provided, compared with typical ionospheric values, is given in Table 3-1.

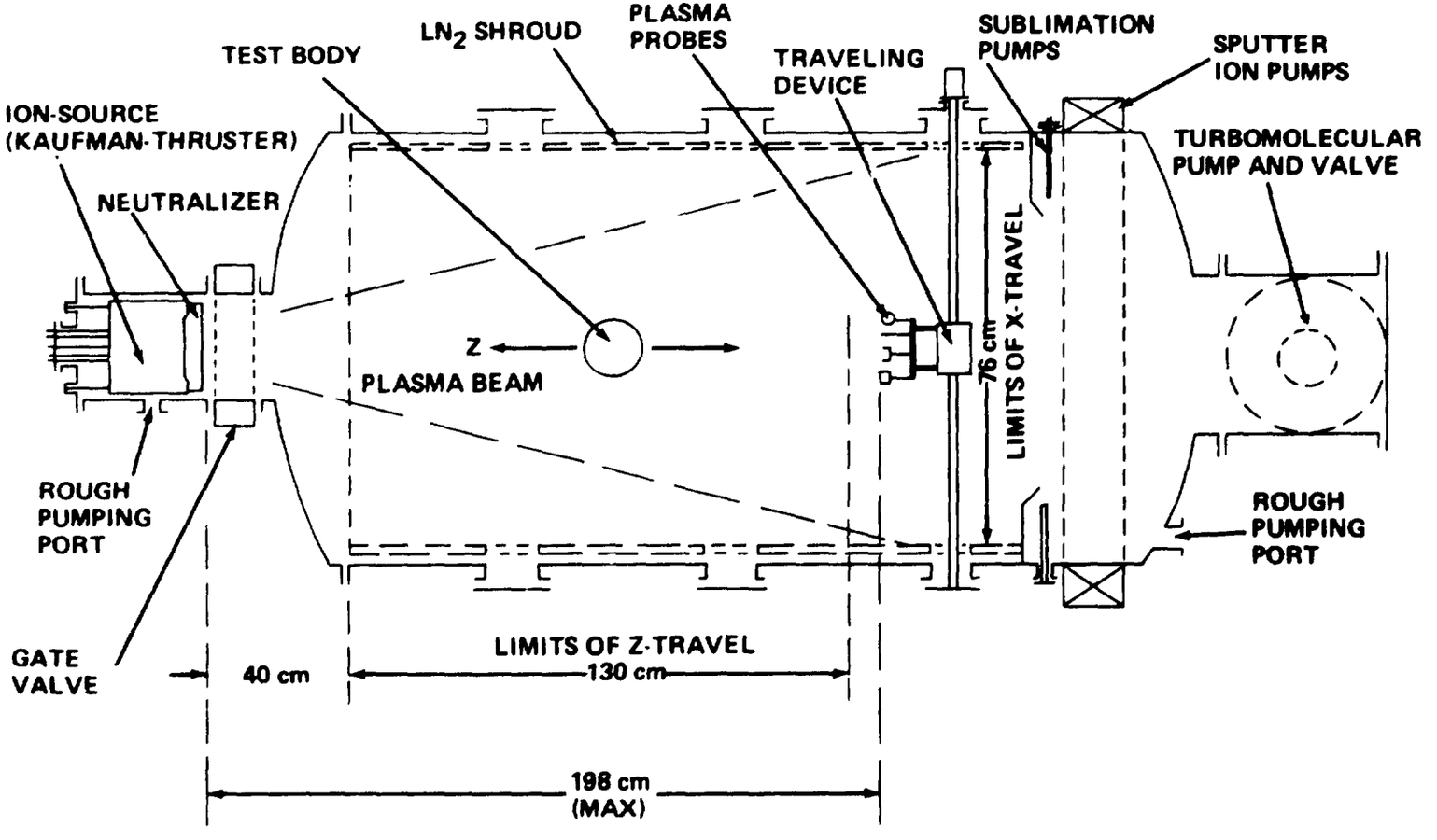

Figure 3-1. Schematic of the MSFC No. 1 plasma wind tunnel facility.

TABLE 3-1. LABORATORY AND IONOSPHERIC FREE STREAM PARAMETERS

Parameters	Ionosphere at 300 km	Laboratory
Velocity (km/sec) — V_o	7.73	9 to 500*
Density (ions/cm^3) — n_o	$\approx 10^6$	10^3 to 10^6
Electron temperature (° K) — T_e	$\approx$ 2400°	1 to 10×10^3
Mean-free-path (cm) — λ	$\approx 10^5$	> 300
Ion composition	0^+, N^+	N_2^+, H_2^+
Average ion mass (AMU) — m_i	20	28, 2
Debye length (cm) — λ_D	$\approx$ 0.5	0.2 to 20
Ion acoustic Mach No. — S	$\approx$ 6	1 to 650
Normalized body potential — Φ_b	$\approx$ -5	Externally controlled
Debye ratio — R_d	$\approx$ 10 to 10^3	1 to $\approx$ 25

* For N_2^+-ions.

1. Vacuum System. The vacuum system provides an ultraclean 6× 4 ft cylindrical working volume in which experiments can be performed with access provided at the front and rear of the chamber. Access for viewing and mechanical or instrument feedthroughs is provided by a number of ports on the top and sides. An additional port in the center of the front door provides a mounting point for the plasma beam source which is normally a modified Kaufman ion thruster. All pumping is done at the rear of the chamber, opposite the ion source.

Initial rough pumping of the chamber to 1×10^{-3} torr is accomplished with a 150 cfm Roots blower which is backed by a 50 cfm mechanical roughing pump. Backstreaming of pump oil is prevented by a liquid nitrogen (LN_2) trap located between the roughing system and the chamber. The ultrahigh vacuum

pumping system consists of differential sputter ion pumps used in conjunction with a titanium (T_i) sublimation pump, a turbomolecular pump, and an open ended 6 × 3-1/2 ft LN_2 shroud, which may be removed to obtain additional working volume. The ion pumps are rated at 1200 liter/sec (for N_2) and are mounted radially as an integral part of the chamber wall. Titanium is sublimed onto the rear wall of the chamber, providing a 26,000 liter/sec pumping capacity for nitrogen, while the turbomolecular pump is rated at 1500 liter/sec for nitrogen. It has the additional advantage that it pumps all gases effectively whereas the sputter ion and T_i sublimation pumping systems are limited to active gases (i.e., N_2, O_2, etc.) and the LN_2 shroud pumps only condensible gases (effectively limited to water vapor).

The ultimate pressure of the chamber, when clean-dry and empty, is approximately 1×10^{-11} torr. Experiments, which are generally conducted during the Kaufman engine discharge, are carried out with a background pressure of 1×10^{-7} to 1×10^{-5} torr, depending on the conditions desired. (It should be noted that at 1×10^{-5} torr, the ion mean-free-path is 5 m, which is sufficient to ensure the existence of a collisionless medium.)

An ultrahigh vacuum system necessitates stringent material requirements, requires rather long turnaround times, and limits plasma composition to ions of active gases (as a result of the selective pumping characteristic of sputter ion and titanium sublimation pumps). However, there are very significant gains in experimental capabilities, especially in diagnostic probe studies where surface conditions have a very definite and poorly understood effect on probe operation.

2. Plasma Source. The plasma beam is generated by a 15-cm. Kaufman-type electron bombardment ion thruster mounted in a stainless steel appendage (Figure 3-2). With certain modifications, the Kaufman thruster has proven to be very well suited for use as a plasma beam source because of its wide range of control over the beam parameters. A detailed discussion of this type source was given by Reader [66], and more recently by Le Vaguerese and Pigache [67].

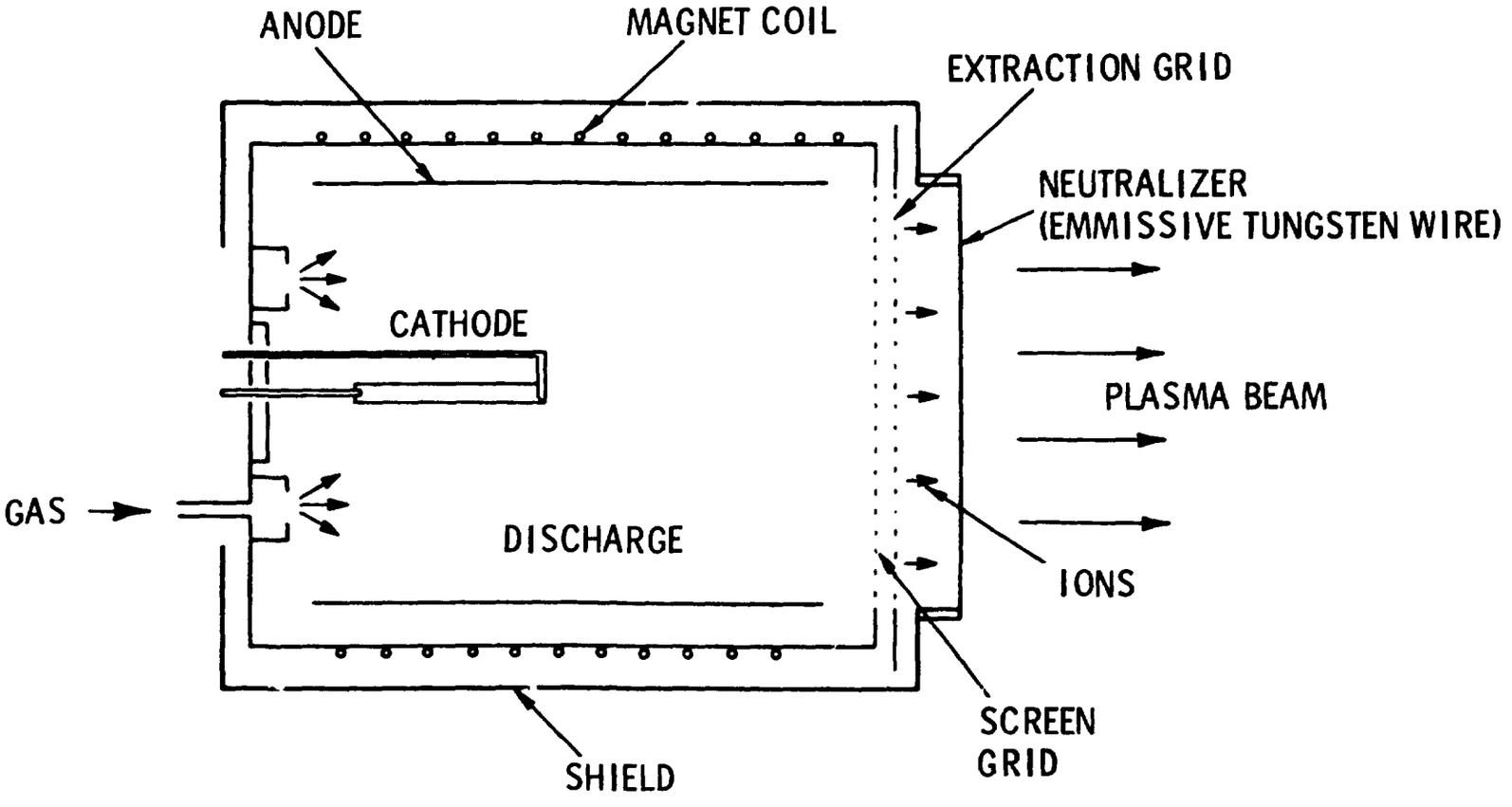

Figure 3-2. Kaufman engine schematic after Stone and Reihmann [68].

During operation, a stream of neutral gas is fed into the thruster's cylindrical discharge chamber, where the gas molecules are ionized by the impact of energetic electrons which are emitted from a tungsten ribbon cathode and accelerated through a potential drop to the hollow anode. Ionization of the gas is enhanced by an axial magnetic field which increases the electron path length. Ions are extracted from the discharge chamber by a voltage between the screen and extraction grids. Acceleration of the extracted ion beam down the axis of the chamber is accomplished primarily by a positive bias on the thruster. However, the kinetic energy of the ions in the beam is also affected by the voltage between the cathode and anode. The plasma in most of the discharge chamber is close to the anode potential so that a positive potential exists between ions in this region and the screen grid (Figure 3-3). This contributes to the total ion acceleration (determined by 127° electrostatic energy analyzer) as shown in Figure 3-4. Finally, an electron current from an emissive tungsten wire located in the exhaust of the thruster is injected into the extracted and accelerated ion beam, thus forming a macroscopically neutral, drifting plasma. It is usually possible to adjust the source so that plasma potential is very close to chamber ground.

The orientation of the thruster within the bell jar appendage is adjustable in two dimensions so that proper alignment of the plasma beam along the chamber axis can be attained. Because of the relatively small atomic mass of the gases to be used in ionospheric or solar wind simulation (N_2 or H_2), both the thickness and hole diameter of the perforated extraction plate had to be decreased to 0.508 mm. This modification matches the throughput of the engine to the pumping speed of the vacuum system so that the proper pressure for efficient ionization can be maintained within the discharge section of the thrust, while pressure in the experimental working area of the vacuum chamber remains low enough to maintain a collisionless medium. Figures 3-5, 3-6, and 3-7 indicate the functional behavior of the thruster.

The total beam current is given in Figure 3-5 as a function of the cathode current, discharge potential, and chamber pressure (directly proportioned to pressure in the discharge sections of the thruster). The magnet

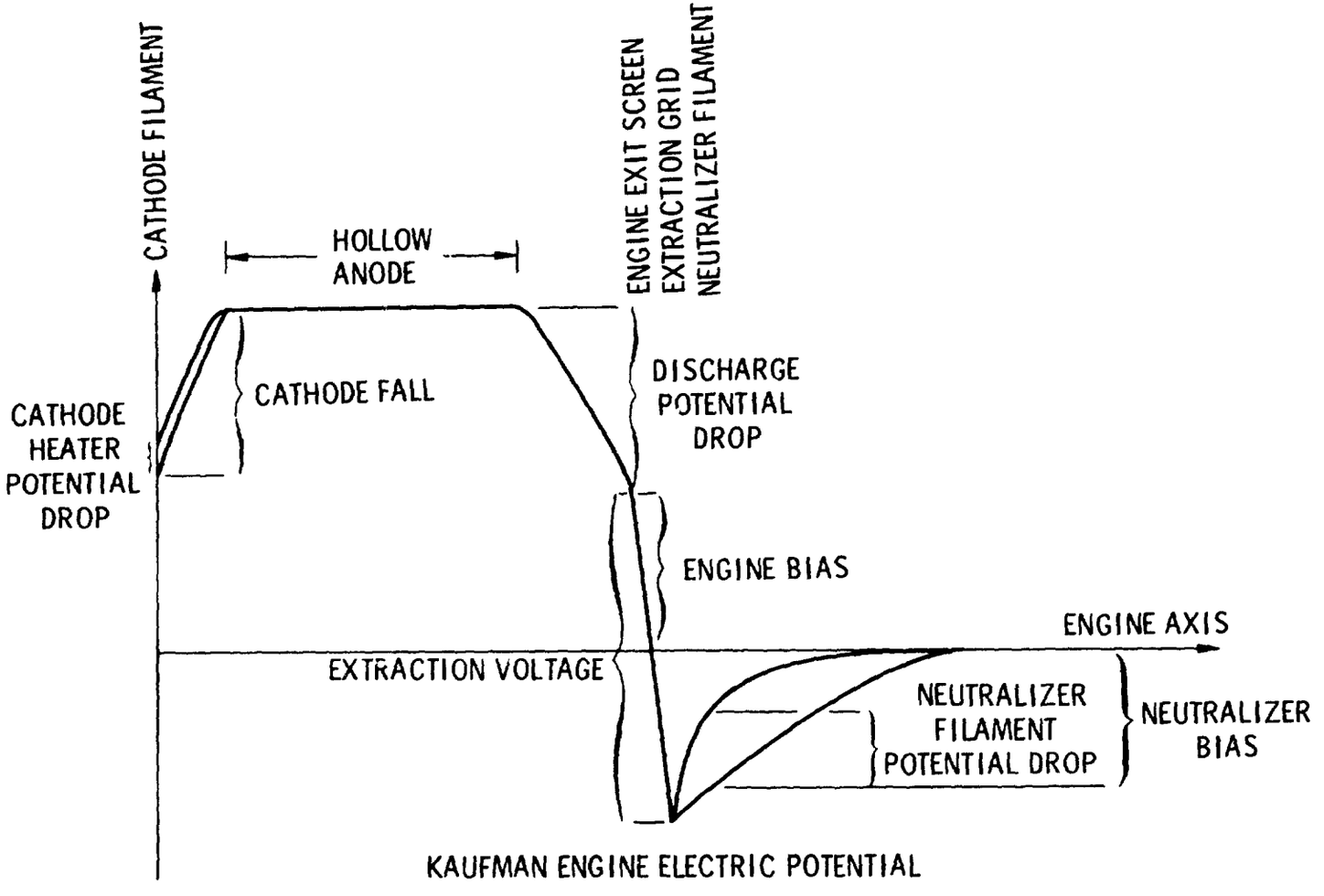

Figure 3-3. Kaufman engine electric potential.

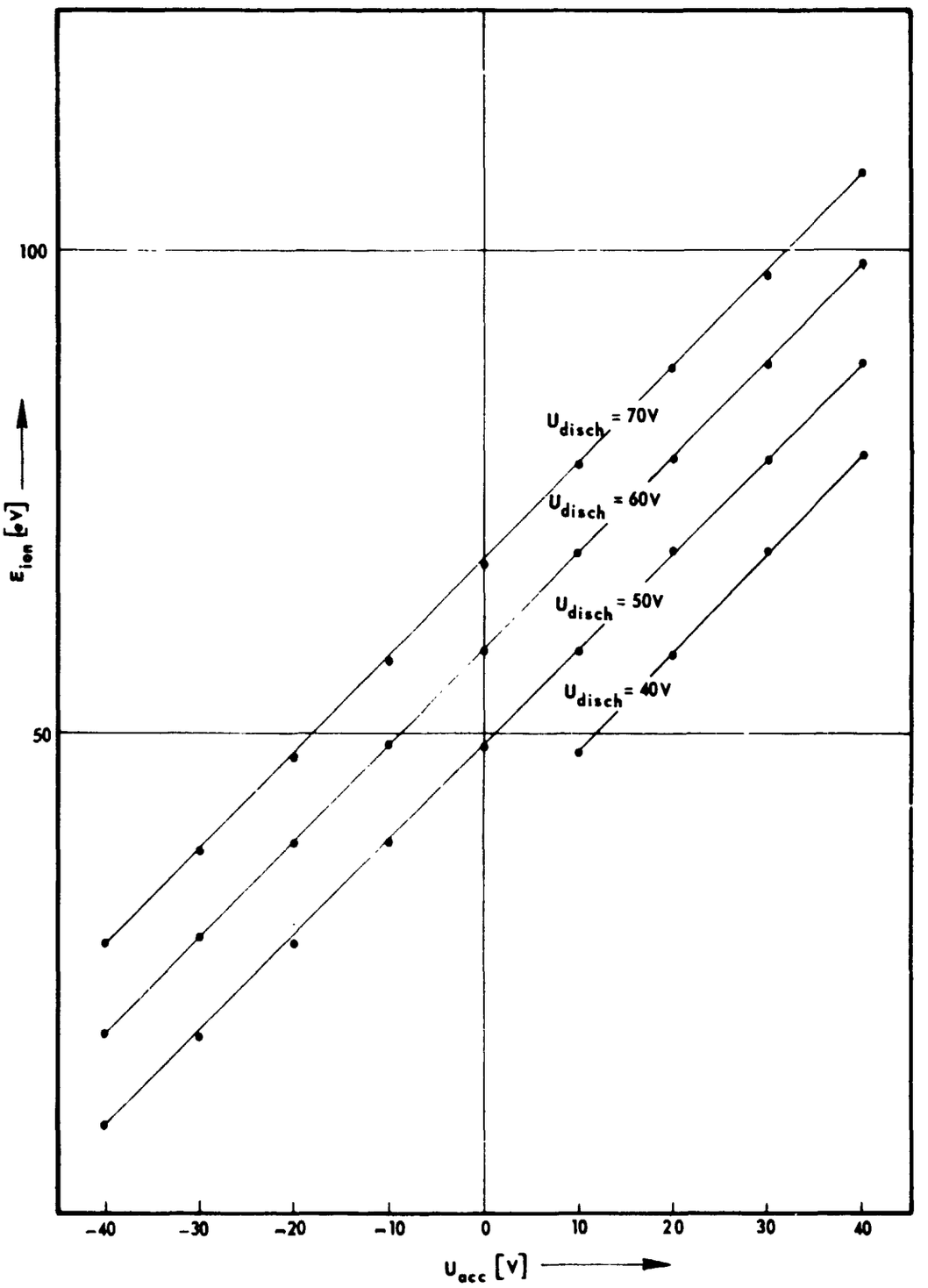

Figure 3-4. Ion kinetics energy versus acceleration potential after Stone and Reihmann [68].

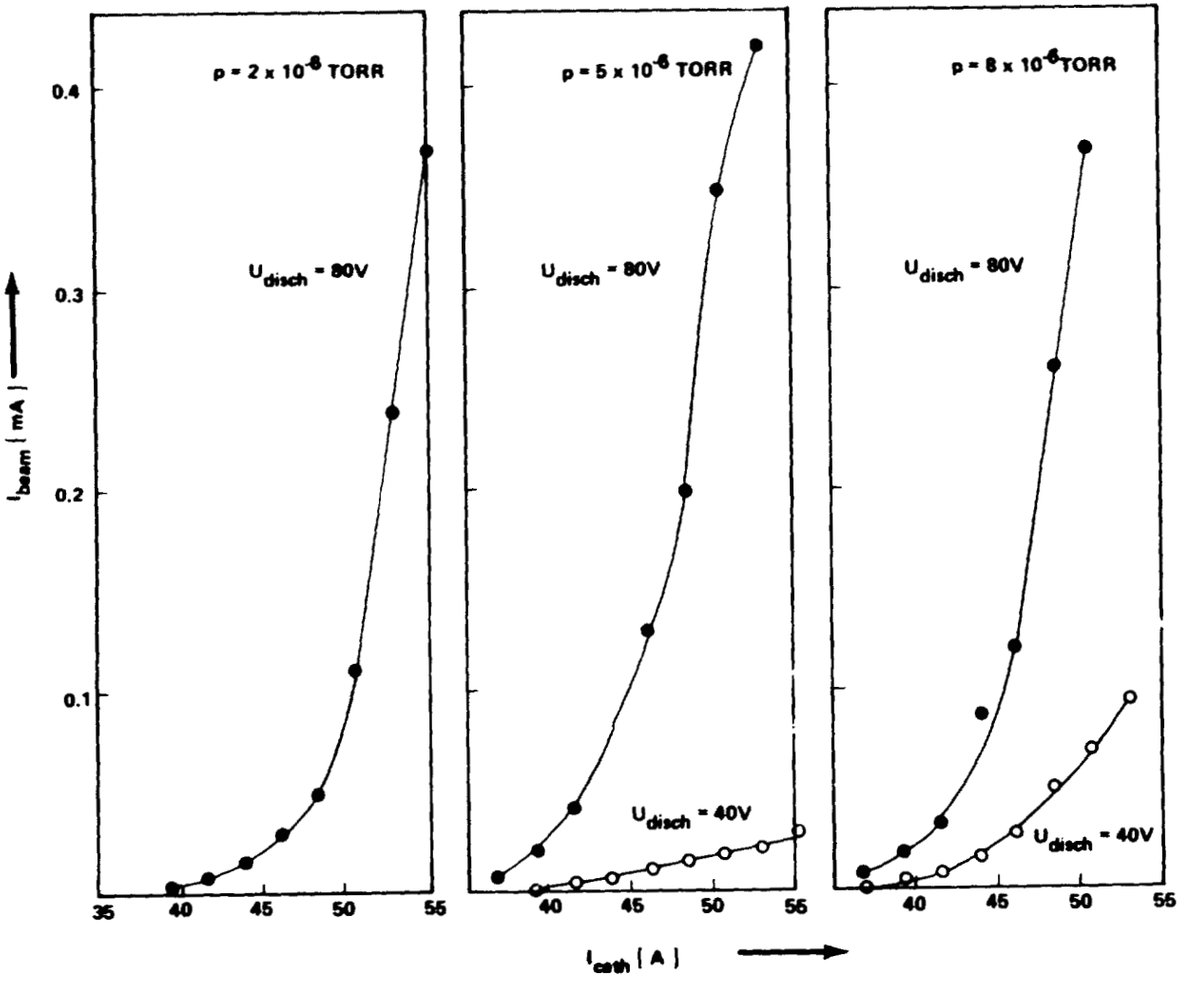

Figure 3-5. Dependence of engine beam current on cathode current after Stone and Reihmann [68].

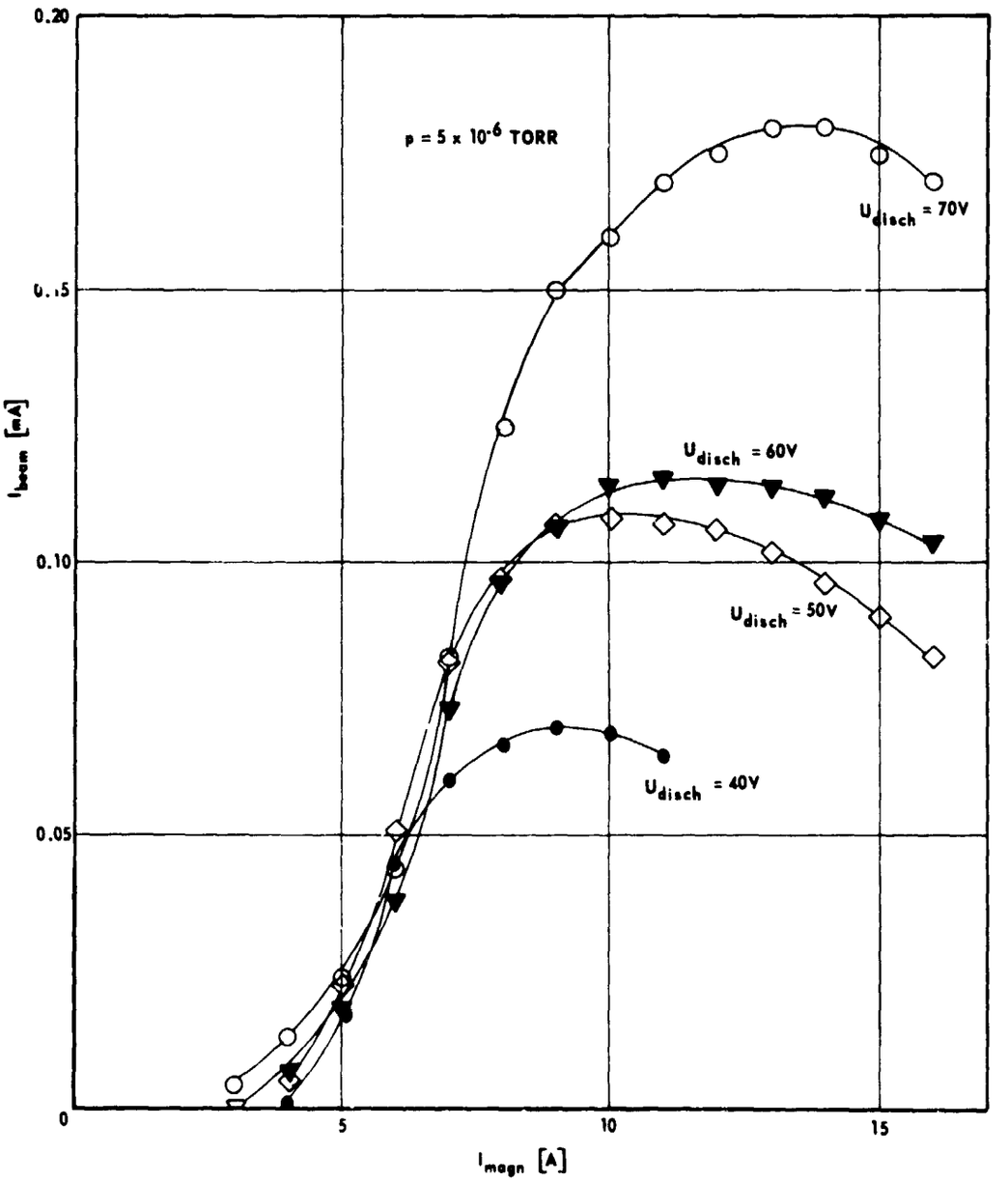

Figure 3-6. Dependence of engine beam current on magnet current after Stone and Reihmann [68].

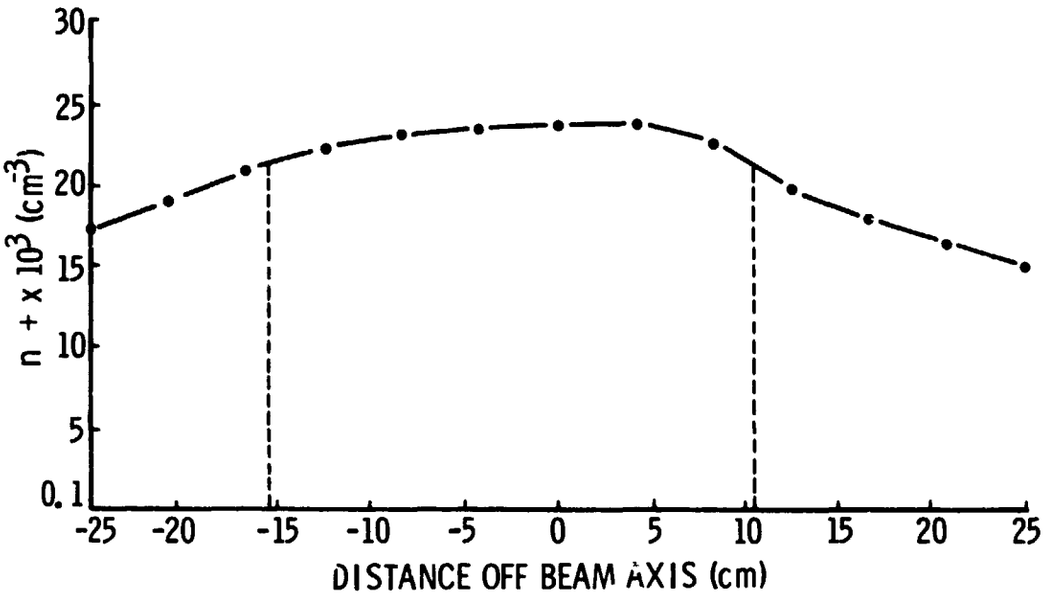

Figure 3-7. Ion density profile in the plasma stream 1.4 m from the Kaufman accelerator, after Stone et al. [69].

current was held constant in all cases at a value that optimized thruster performance. It can be seen that an increase in cathode current produces an exponential type increase of the total beam as a result of enhanced thermionic emission of the cathode in accordance with the Richardson Law. However, it also results in a shorter cathode lifetime, caused by faster evaporation of the filament material. Likewise, a variation of discharge voltage from 40 to 80 volts increases total beam current by a factor of 3 to 6; however, the sputtering rate of the cathode grows by at least an order of magnitude. It should also be noted that at high discharge voltages, the total beam current is not substantially affected by variations in pressure, while at lower voltages a pressure drop results in a considerable decrease in beam current. At 40 volts and 2×10^{-6} torr, the discharge could not be ignited.

The dependence of the total beam current on the magnet current (proportional to the axial magnetic field of the thruster) and discharge voltage is shown in Figure 3-6 for a constant cathode current of 50 amps and a pressure of 5×10^{-6} torr. All of these plots display maxima or plateau regions.

Increasing magnet current beyond the point of maximum beam current results first in a decrease of the total beam current, and finally in oscillations in the discharge which become unstable.

The ion current density of the plasma beam, measured by a gridded Faraday cup located 1.4 m downstream from the thruster, is shown in Figure 3-7 for an ion drift energy of 20 eV. Defining the points at which the current density is 90% of its maximum value to be the useful limits of the beam, the divergence angle is found to be 5.25°. This provides a region which is 26 cm in diameter with a uniform current density (10% variation) for conducting experiments. For a 48 eV beam, the divergence angle decreases to 4.5°, or a workable beam diameter of 23.5 cm. Hence, for more energetic beams, the working area would be smaller, approaching the 15 cm diameter of the source.

The electron temperature in the plasma beam (determined by a cylindrical Langmuir probe oriented perpendicular to the flow) is variable from the order of an electron volt to less thar 2000°K, depending on: (1) the location of the emissive neutralizer wire in the beam, (2) the voltage drop across the wire, and (3) the bias potential applied to the wire. A more detailed coverage of this topic is provided by Sellen [70].

3. Spatial Manipulation of Diagnostic Probes and Test Bodies. The disturbed flow field surrounding a test body emersed in the streaming plasma is currently mapped in two dimensions with either Cartesian or polar coordinate systems. The cartesian coordinate system has been found most useful. It consists of an axial and a transverse mapper. The axial mapper allows any one of three test bodies (or probes) to be lowered into the plasma stream and moved along the chamber (Z) axis. All bodies may be raised to obtain free-stream conditions. The total axial travel is 1.7 m, beginning at the position of the transverse mapper, up to 1.98 m downstream from the plasma source. The transverse mapper is capable of carrying a full complement of instruments (Langmuir Probe, Faraday cup(s), RPA, and DIFP). It moves the instruments in the transverse (X) direction from one side of the chamber to the other. The total transverse movement is 1.07 m. A control system automatically repositions the test body along the Z-axis while the transverse

mapper pauses at one of its end points. The transverse mapper then automatically reverses its direction and moves the instruments back across the chamber. In this way, transverse profiles of the various quantities measured by the instruments are obtained at a series of positions along the Z-axis, downstream from the test body.

It is also important to measure the properties of the ambient plasma stream. This can be done prior to and after the measurements of the disturbed zone by instruments on the X and Z mappers with the test body removed from the stream. (The test body can be raised out of the stream with the plasma source operating so that ambient conditions do not change.) It is also necessary to monitor the ambient plasma stream during the mapping maneuvers so that any drift of the stream conditions will be observed and accounted for. This is accomplished by a second, fixed set of monitoring probes.

The data obtained during the mapping maneuvers can be recorded by XY-plotters, by oscilloscopes and subsequent photographs, or by an automatic digital recording system (ADRS) which stores the data on magnetic tape for subsequent reduction by the Univac 1108 computer. The format of the ADRS is flexible so that functional testing and calibration data for flight instrumentation can be tailored to the format of the actual telemetered flight data, thereby providing an advance test of the data reduction software.

D. Measurement Techniques

The following is a very brief discussion which indicates the particular technique used to provide a given measurement in the present study. A more detailed discussion of the diagnostic instruments and analysis techniques is provided in Appendix F.

In the present study, the electron temperature and density and the plasma potential are determined from Langmuir probe i-v curves. Spherical probes as well as guarded cylindrical and guarded disc probes have been used. The method of analysis (most data were recorded by XY-plotters) is to plot $\ln I$ - vs - ϕ_p. The electron density, n_e, and the plasma potential, ϕ_s, are

determined by the breakaway point (Appendix F). The temperature is given by the slope of the linear portion of the plot, which also serves as an indication of the degree to which the electrons are characterized by a Maxwellian distribution.

The ion density, n_i, is measured by shielded Faraday cups and planar RPA's. In both cases, if the velocity of the particles is know, then n_i follows from the magnitude of the current collected (Appendix F).

The ion flow velocity and temperature (parallel to the flow direction) are determined by a planar RPA and a 127° Electrostatic Energy Analyzer (EEA). The velocity is determined from the RPA data by the inflection point of the current cut-off. Ion temperature is obtained by fitting the data with a theoretical expression. [For digitally recorded data obtained from the ADRS, both V_o and T_i can be determined by fitting the data with the planar RPA equation (Appendix F)]. The ion velocity is determined from the EEA data by the location of the peak point, since the EEA output is essentially the derivative of the RPA output. Note that ion speed is easily obtained in the laboratory since ionic mass is known.

The direction of the ion velocity is measured by the Differential Ion Flux Probe (DIFP) [71]. This instrument was developed as part of the present study specifically for laboratory plasma flow interaction experiments where large trajectory deflections occur and multiple streams must be analyzed simultaneously. The details of this measurement are provided in Appendix G. It should be noted that this instrument also provides an accurate determination of the magnitude of the ion velocity vector, even in regions where the ions have been strongly deflected. In such regions, the planar RPA is inaccurate since it only measures the component of velocity parallel to its normal and without angular information; this can lead to large errors. The EEA is not effective since it is highly collimated and would not see ions at large angles of incidence.

E. Free-Stream Characteristics

It is important to realize the true conditions under which experiments are conducted and the resulting limitations that arise. Laboratory plasma streams are not perfectly uniform and isotropic; they suffer from stream divergence, anisotropic (and sometimes non-Maxwellian) ion thermal motion, charge exchange interactions with residual, neutral gas, and absorption of charge at the chamber walls. These limitations must be considered in arriving at the experimental results by accounting for them in the analysis and/or minimizing them in the experiment.

In terms of stream divergence and charge exchange interactions (which create a slow, nondrifting ion population from the residual gas in the vacuum chamber), the MSFC Space Plasma Simulation Facility has been found to be one of the best available [72]. The slow ion problem becomes more severe with increasing vacuum chamber volume and increasing residual gas pressure as shown in Figures 3-8 and 3-9. The 1.2 m diameter by 2.4 m long chamber used at MSFC is moderate in size and the ultrahigh vacuum system, using a combination of pumps, is capable of reducing ultimate pressures to $\sim 10^{-10}$ torr and working pressures (with the ion accelerator operating) into the range of 5×10^{-6} to 1×10^{-7} torr. The combination of these two factors makes the slow ion population negligible. This conclusion is supported by the fact that, when chamber pressure is below 5×10^{-6} torr, no direct evidence of slow ions has been found in the planar Langmuir probe, RPA, or 127° EEA data and no indirect evidence is indicated by effects on the ion wake. Further, an estimate of the density of slow ions relative to fast, stream ions, n_s/n_f, can be made for this facility from existing data obtained in other facilities, as indicated in Figures 3-8 and 3-9. An estimated value for $P = 1 \times 10^{-5}$ torr is found from the data of Figure 3-9 and the known chamber volume. This value (indicated by MSFC No. 1) is extrapolated into the working pressure range in Figure 3-8, assuming all curves have the same slope. The estimated range of n_s/n_f values within the working pressure range are seen to be below 0.03, which

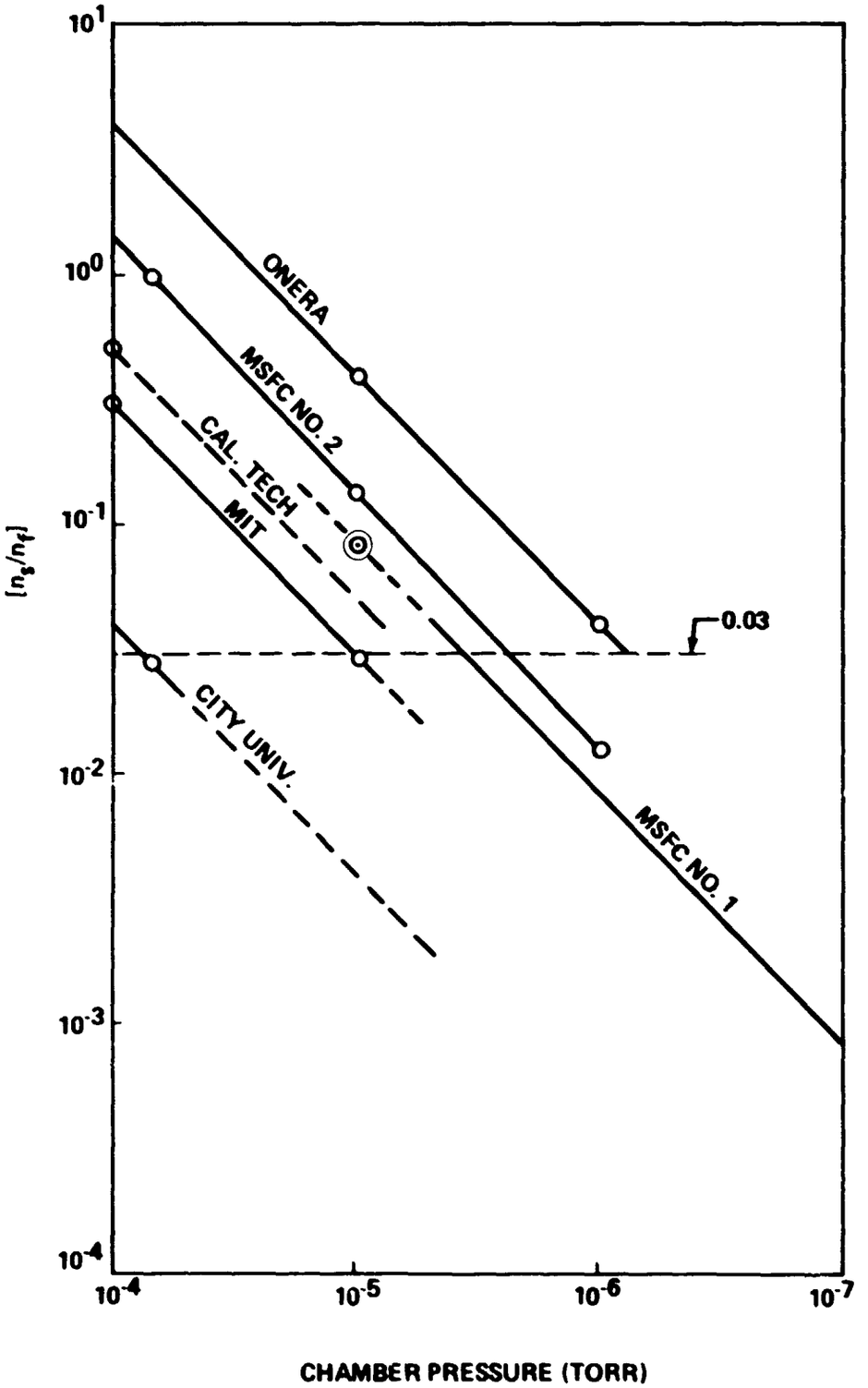

Figure 3-8. Relative density of slow, charge exchange ions, n_s, to fast, stream ions, n_f, as a function of chamber pressure.

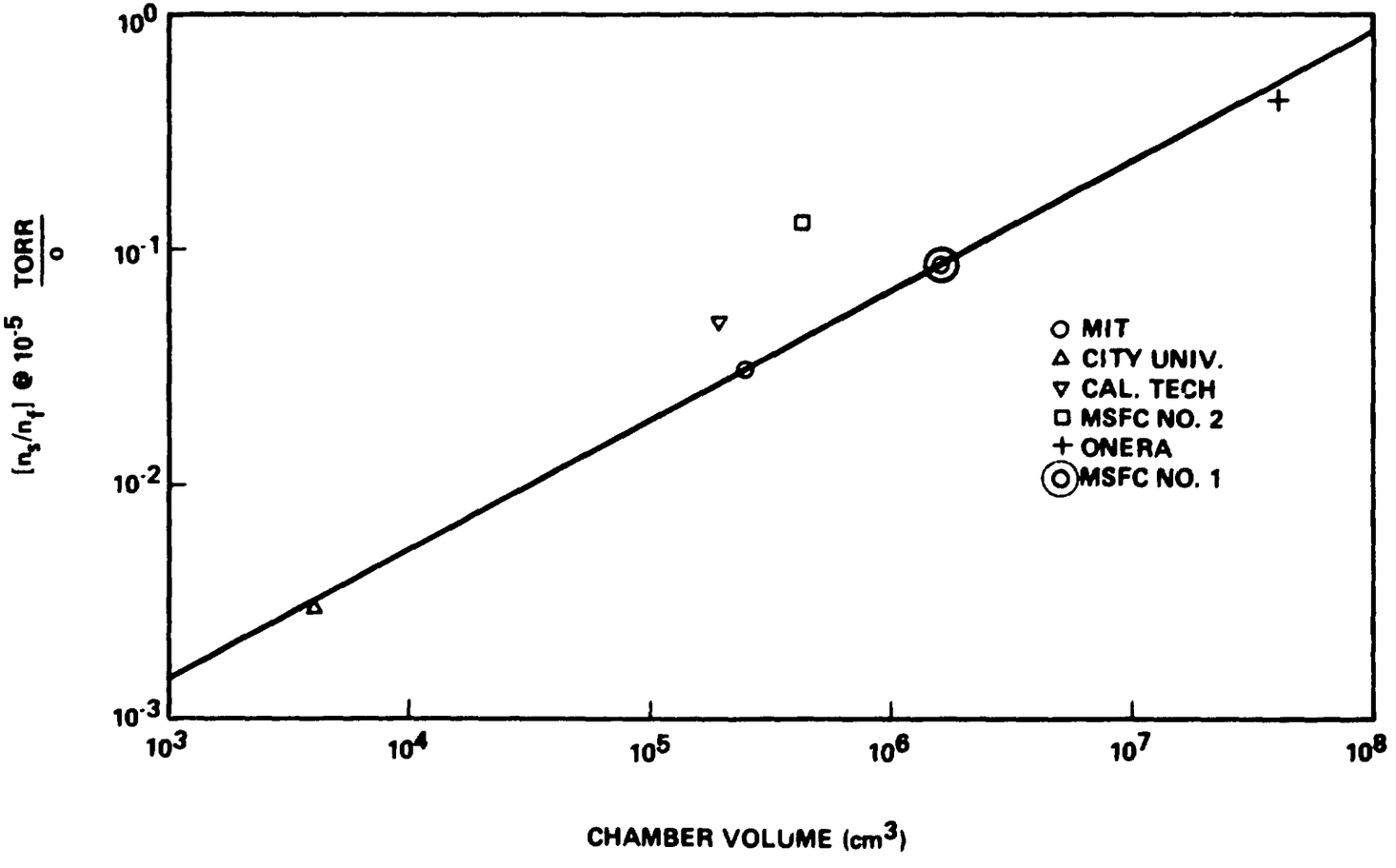

Figure 3-9. Relative density of slow, charge exchange ions, n_s/n_f, as a function of chamber volume at a pressure of 10^{-5} torr.

was found to be the maximum acceptable value for ion wake investigations [76]. Note that the facility designated MSFC No. 2 is a smaller chamber described elsewhere [78].

The plasma stream divergence depends on both the initial divergence due to the acceleration process (i.e., the ratio of the transverse velocity component to the component parallel to the chamber axis) and the space charge potential within the stream (due to imperfect neutralization). These effects become more pronounced as the accelerator diameter and the beam energy decrease. A 48 eV N_2^+-plasma stream from the 15 cm diameter accelerator was found to diverge 1.75° (defined by the points at which the current density falls 10%), thereby providing a working stream diameter of 23.5 cm, at Z = 1.4 m downstream, in which the stream current density varies less than 10% [68]. For lower beam energies, the current density becomes more uniform over larger cross-sectional areas, but the streamline divergence increases. A cross section of the current density for a 20 eV N_2^+-plasma stream, obtained with a 2.5 cm diameter aperture on the Kaufman engine, and the corresponding streamline directions at Z = 1.4 m are shown in Figure 3-10. The offset is the result of deflection by the ambient geomagnetic field. These data demonstrate the disadvantage of small aperture plasma sources.

Stream divergence and charged particle absorption by the chamber walls also affect the axial dependence of current density. This is shown in Figure 3-11, where the current density has been normalized by the value measured on the chamber axis at the position of the instruments carried by the transverse mapper. Also shown in Figure 3-11 is the axial variation of measured electron temperature, T_e, and calculated effective transverse ion temperature $[T_{i\perp}]_{eff}$, based on the approximate expression derived by Hester and Sonin (Appendix E.1.g):

$$\bar{C}_{i\perp} = \frac{4V_o}{3\pi} (R_s/Z) \quad ,$$

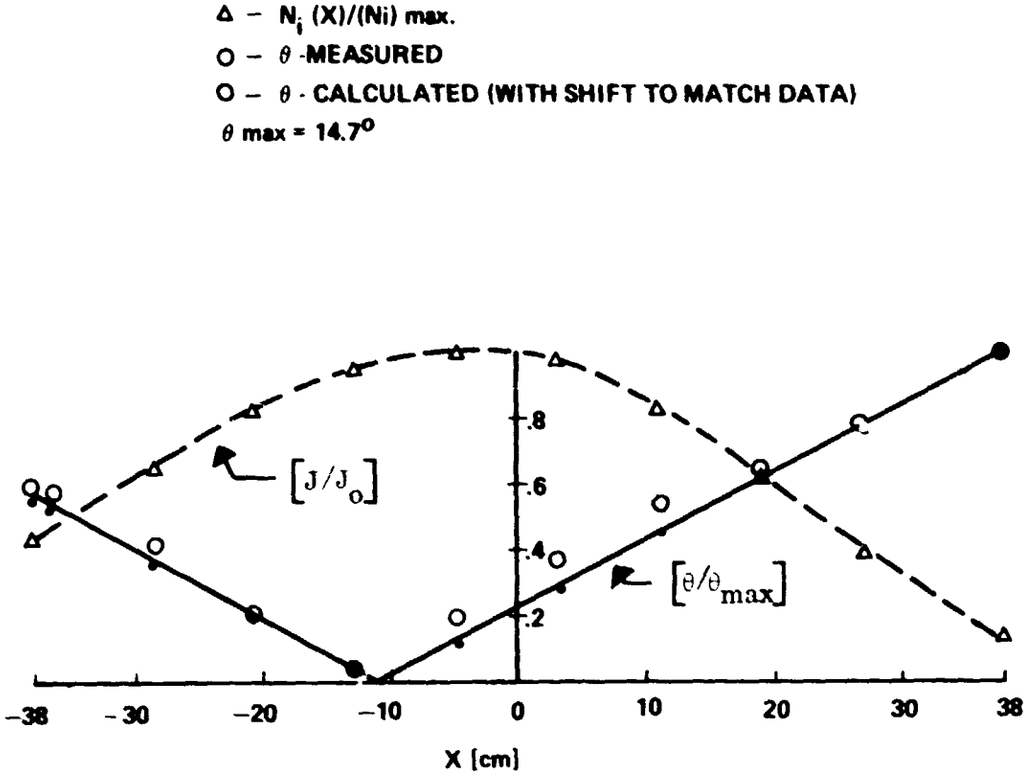

Figure 3-10. Transverse profiles of normalized ion current density, Δ, and flow direction, O, 1.98 m downstream from the Kaufman accelerator. The maximum stream angle at X = 38 cm is 12.8°. Closed points indicate calculated values corrected for geomagnetic deflection. Data obtained with a 2.54 cm diameter aperature on the accelerator.

where R_s is the accelerator radius. Since the mean thermal speed is given by $(8kT_i/\pi m_i)^{1/2}$, it is possible to estimate the effective transverse ion temperature by:

$$[T_{i\perp}]_{eff} = \left(\frac{2m_i V_o^2 R_S^2}{9\pi k}\right) Z^{-2} = \left(\frac{4e}{9\pi k}\right) \phi_{acc} R_s^2 Z^{-2} \quad ,$$

where ϕ_{acc} is the potential through which the ions have been accelerated. The effect of the axial variations shown in Figure 3-11, on the parameters R_d, S, M_1, and Φ_b are shown in Figure 3-12, where, again, the parameters

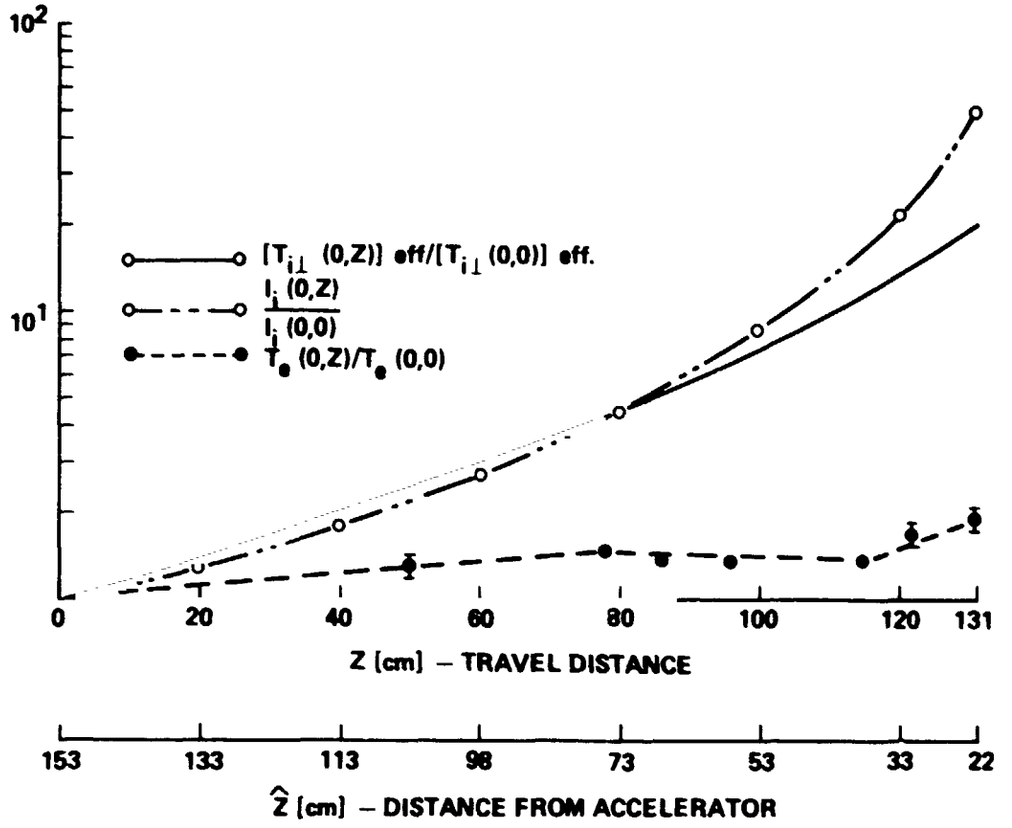

Figure 3-11. Axial profiles of normalized ion current density, electron temperature and the perpendicular (radial) component of ion temperature, $T_{i\perp}$ (calculated from relation by Hester and Sonin [52]). All values are normalized to the value measured at Z = 0 (most distant point from the accelerator).

are normalized by their values on the chamber axis at the position of the transverse mapping probes (1.7 m downstream). Note that the variations are reasonably small except near the accelerator.

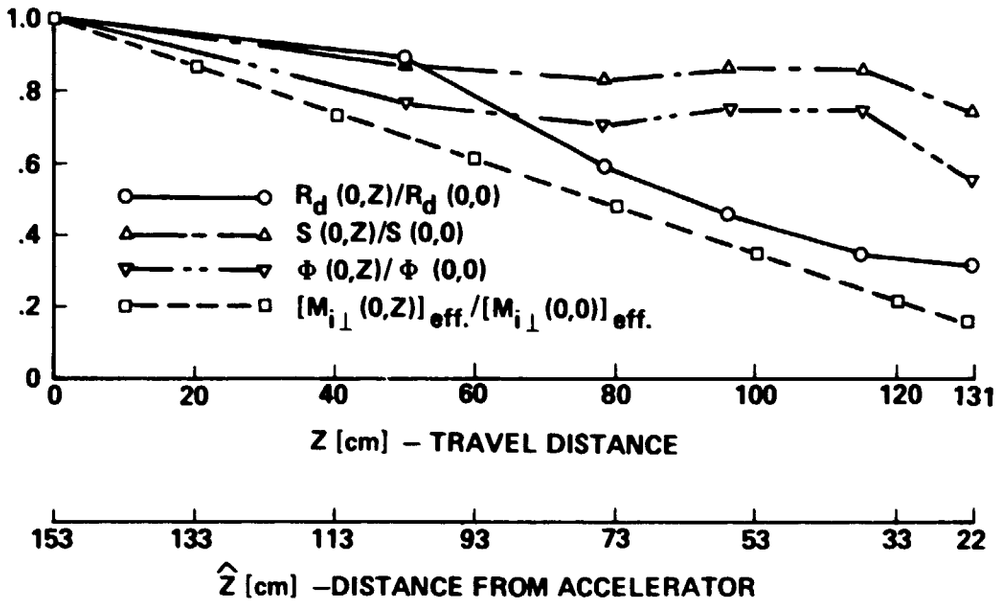

Figure 3-12. Axial variations of R_d, S, Φ_b, and $M_\perp$ resulting from the variations of T_e, J_i (or n_i) and T_i shown in Figure 3-11. Each parameter is normalized by its value at Z = 0.

CHAPTER IV. RESULTS OF THE PRESENT EXPERIMENTAL INVESTIGATION

The objectives of the experimental investigations at MSFC are to (1) supplement the available in situ data, (2) determine the flow interaction mechanisms and their parametric dependences, (3) develop experimental methods and specialized diagnostics required for active experiments in space, and (4) evaluate some of the simplifying assumptions used in theoretical treatments.

The in situ data hint at a very complex wake structure, but are insufficient to support any conclusive results (Chapter II.B.). When the ionospheric conditions can be appropriately simulated, the laboratory investigations offer additional insight into the nature of the interaction by providing a detailed mapping of the entire zone of disturbance (limited to the mid-wake for large bodies), a high degree of control over individual plasma parameters, idealized test bodies, a wide variety of diagnostic instruments (measurement of the complete set of variables) and relatively short turnaround times.

The ability to independently control the plasma and test body variables permits a parametric study of the plasma flow mechanisms. Experiments of this type have been conducted in the hope that the results of such a study can be extrapolated to other regions of parameter space, including those appropriate for the interaction of the ionosphere with orbiting bodies.

It has long been realized that the standard plasma diagnostic instruments were not completely adequate for plasma flow interaction studies since they either collect current from all directions, thereby providing a scalar measurement of the integrated flux, or their results depend on the angle of attack which must be assumed or obtained from other sources (such as satellite orientation). Even the relatively new ion drift meter - RPA [71],

which measures the angle of attack, requires parallel flow. However, in the plasma wake, the highly disturbed flow is not parallel and the flow direction cannot be ascertained from the orbital parameters and the satellite orientation. The complete characterization of such disturbed flows requires the direction as well as the magnitude of the ion flux. The third objective is, therefore, to develop a technique for making high resolution vector ion flux measurements and to substantiate the previously assumed need for such measurements and their potential impact on previous results.

Each of the experiments discussed below may apply to more than one of the above objectives. Therefore, they will be grouped according to the nature of the measurements made; i.e., variations of the charged particle current densities within the near and mid-wake regions, electron temperature variations within the near wake region, and vector ion flux measurements in the near and mid-wake regions.

A. Charged Particle Current Density Variations in the Near and Mid-Wake Regions

1. Experiment A. The first experiment was conducted to investigate the detailed behavior of the ions in the near and mid-wake regions downstream from a conducting spherical test body biased at various potentials [74]. The sphere had a radius of 3 cm and was mounted on the axial mapper and could be either allowed to float, electrically, or biased at an arbitrary potential. Ion current density profiles were obtained downstream from the test body with a small [0.32 cm diameter aperture] Faraday cup mounted on the transverse mapper. The housing and entrance grid of the Faraday cups were maintained at chamber ground while the second grid was biased -22.5 volts so that only ion current was admitted into the collector cup (Appendix F). Note that the grounded housing does not affect the collected ion current since plasma potential was near ground (± 0.4 volt which is small compared to the 20 eV ion drift energy). The chamber pressure was maintained below 4×10^{-6} torr during the experiments so that slow ion concentration should have been negligible

(Chapter III.E.). The ambient plasma stream conditions were monitored by a second Faraday cup of the same type (j_i) and a cylindrical Langmuir probe (T_e, n_e, and ϕ). The beam energy was determined to be 20 ± 1 eV from the accelerator calibration (Figure 3-4). The plasma stream was found to have $T_e \simeq 850°K$, $n_{e,i} \simeq 3 \times 10^3$ cm^{-3}, and $\phi_f = -0.35$ volt (with respect to chamber ground). The scaling parameters are, therefore,

$$R_d \simeq 1 \pm 0.2 \quad , \quad S \simeq 16.5 \pm 1 \quad \text{and} \quad T_e/T_i >> 1 \quad ,$$

where it was assumed that $T_i \simeq 300°K$ in agreement with the values calculated in Chapter III. Profiles of the ion current density in the wake were obtained at various distances downstream over the range $1.07 \leq Z/R_o \leq 35.3$ Five runs were made with the above scaling parameters held reasonably constant while applying the negative potentials of 0.35 (floating), 1.5, 3, 6, and 9 volts to the body. These correspond to $-\Phi_b = 5$, 20.1, 41, 82.2, and 123, respectively.

An example of an ion current density map obtained with the body at floating potential (-0.35 volt) is shown in Figure 4-1. The ion void and mid-wake regions are shown in great detail. At the position of the closest profile ($Z/R_o = 1.07$) there is no measurable ion current in the void. This observation must be qualified, however, since the acceptance angle of the Faraday cup was limited to ±33° and, therefore, ions deflected into the region at higher angles would not be detected. Proceeding downstream, the wake begins to fill with ions. The ion void is completely filled at $Z/R_o = 15.8$, although the flow remains very obviously disturbed as indicated by the two peaks. At this point, an axial enhancement in the ion current density begins to form and reaches its maximum value at $Z/R_o \simeq 20.7$. Beyond the maximum position, the ion peak begins to split into two peaks which travel away from the Z-axis. The ultimate diffusion of the disturbance back into the ambient plasma stream was not observed due to the finite length of the vacuum chamber.

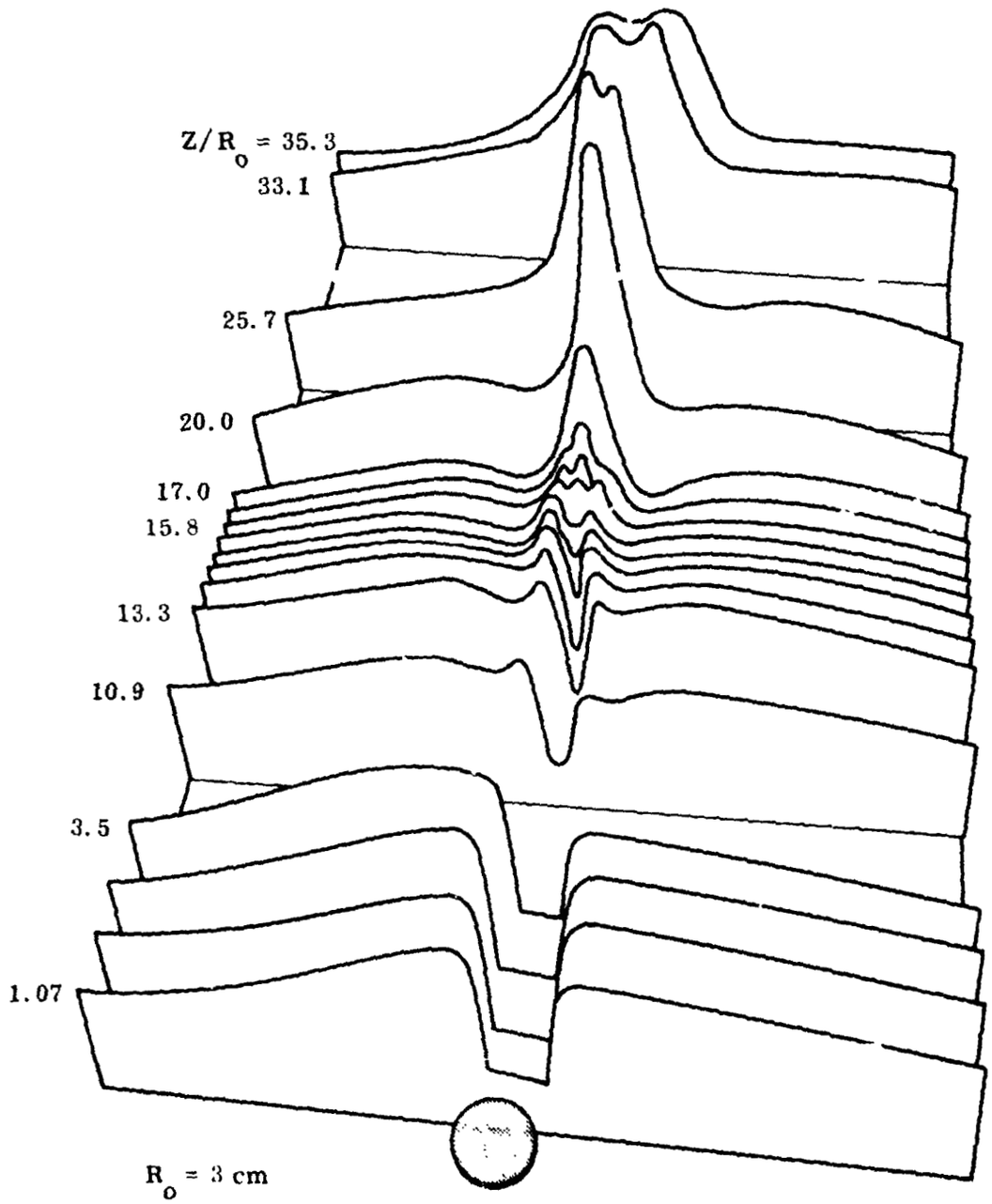

Figure 4-1. Ion current density profiles downstream from a conducting sphere (R_o = 3 cm) for $R_d \cong 0.8$, $S \approx 17$, and $\Phi_b \simeq -5$, data after Stone et al. [74].

Observing the profiles more closely, it can be seen that as the ions move toward the Z-axis to fill in the void region, an ion rarefaction wave is created on either side of the void and propagates away from the axis. It is shown clearly by the profiles between X/R_o = 10.9 and 17.0, but becomes obscured in the mid-wake region by the shoulders of the axial ion peak. This feature will be investigated in more detail in a later experiment.

In the near wake, it can also be seen that the ions moving into the void region form a small ion enhancement on each side between the void and the ion rarefaction wave. This effect is hinted at in the current profile calculations by Maslennikov and Migov (Appendix C.2, Figure C-3). Here the detailed behavior of these peaks is shown as they progress downstream. They persist longer than the void filling process, which is completed at $Z/R_o \simeq 15.8$, and seem to merge between $Z/R_o = 15.8$ and 17.0. Within experimental error, this point is a Mach number, S, of radii downstream, which is consistent with the theoretical calculations by Taylor (Appendix C.3). This would indicate that the peaks are the "converging streams," discussed by Taylor, which are deflected into the wake by the electric fields within the plasma sheath. However, even though Taylor's results show the converging stream effect definitively in the mid-wake region and beyond, there is no indication of the streams in the near wake as shown here.

The wave-like structures in the near wake which propagate inward along the boundaries of the void region will be called Void Boundary (VB) streams, while those which propagate outward, beginning at the axial ion peak, will be called Trailing V (TV) waves. The term "wave" is used here as a convenience and is not intended to indicate that these features necessarily result from collective interactions.

The morphology of the two types of standing wave-like structures is given in Figure 4-2 by plotting the positions of the wave peaks in each transverse current density profile on the XZ-plane for each value of Φ_b used. For example, the points designated as resulting from $\Phi_b = -5$ show the locations of the wave peaks seen in Figure 4-1. Similar information is given in Figure 4-3 for the ion void by plotting the width of the region corresponding

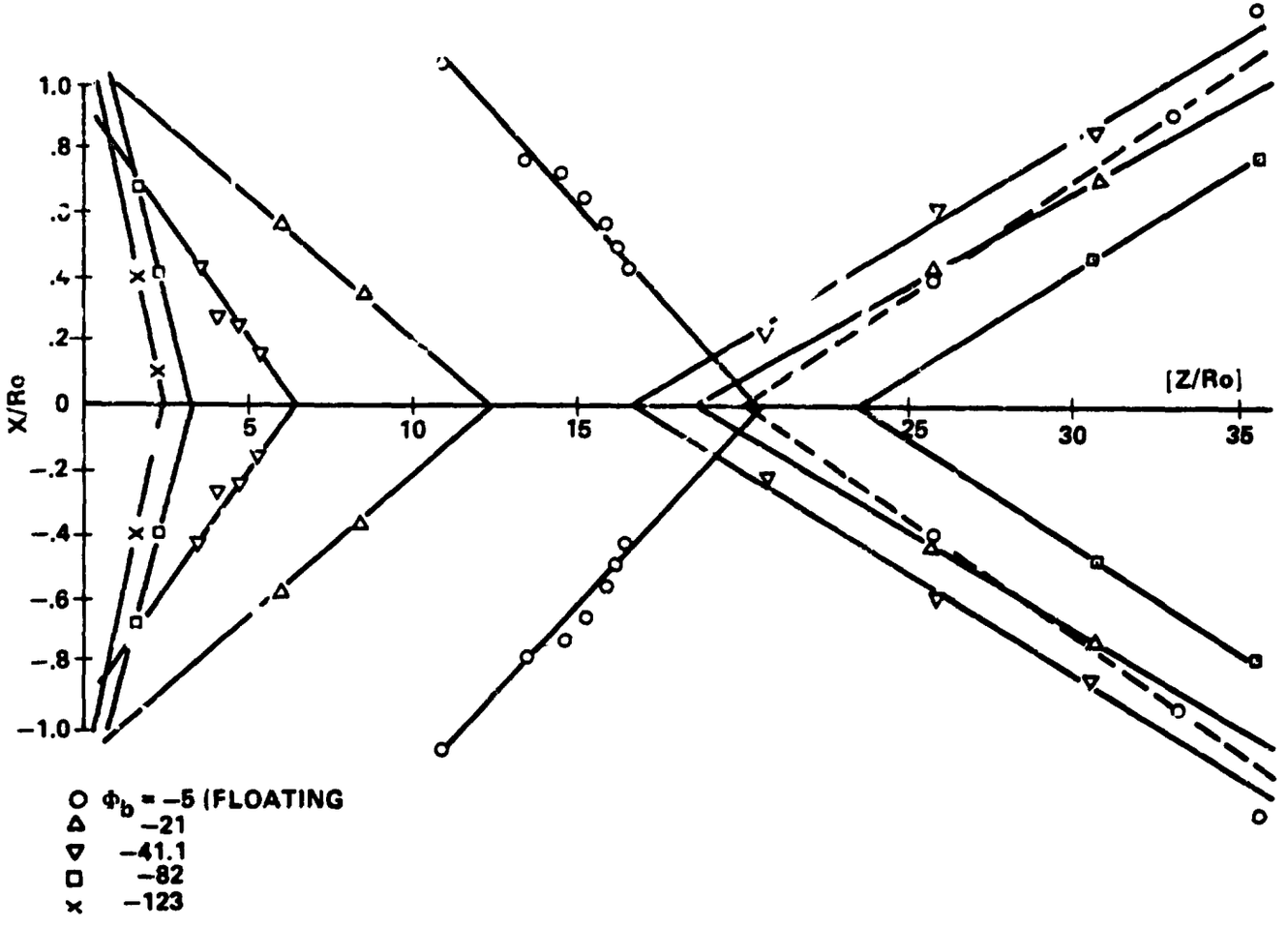

Figure 4-2. Morphology of converging VB streams and diverging trailing "V" (TV) waves for various ues of Φ_b. After Stone [99].

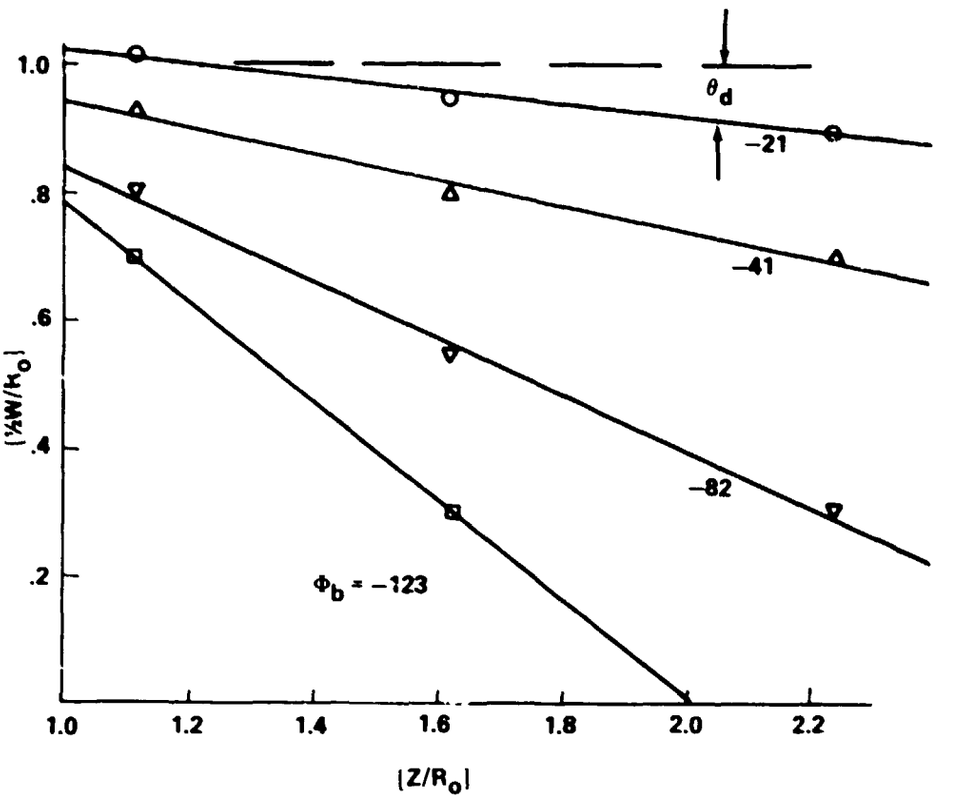

Figure 4-3. Convergence angle of the ion void boundary (determined at its $J_o/2$ point) for various values of Φ_b. After Stone [99].

to a current density of $J_o/2$ for each profile where the void boundaries are well defined (i.e., before the VB streams begin to merge).

It is immediately apparent that all of the TV waves, shown in Figure 4-2, have approximately the same inclination to the Z-axis, while the VB streams have widely varying inclinations, depending on the value of Φ_b. Figure 4-3 shows that the void boundary behaves similarly to the VB streams. This behavior is shown explicitely by Figure 4-4 in which the angles of inclination of the void boundary, the VB streams, and the TV waves are plotted against Φ_b. The angle of the TV waves does not depend on Φ_b, but remains constant at approximately the Mach angle, $\theta_s = \sin^{-1}(1/S)$, indicating wave-like behavior. However, both the void boundary and the VB streams are directly proportioned to Φ_b which is consistent with a true ion stream behavior.

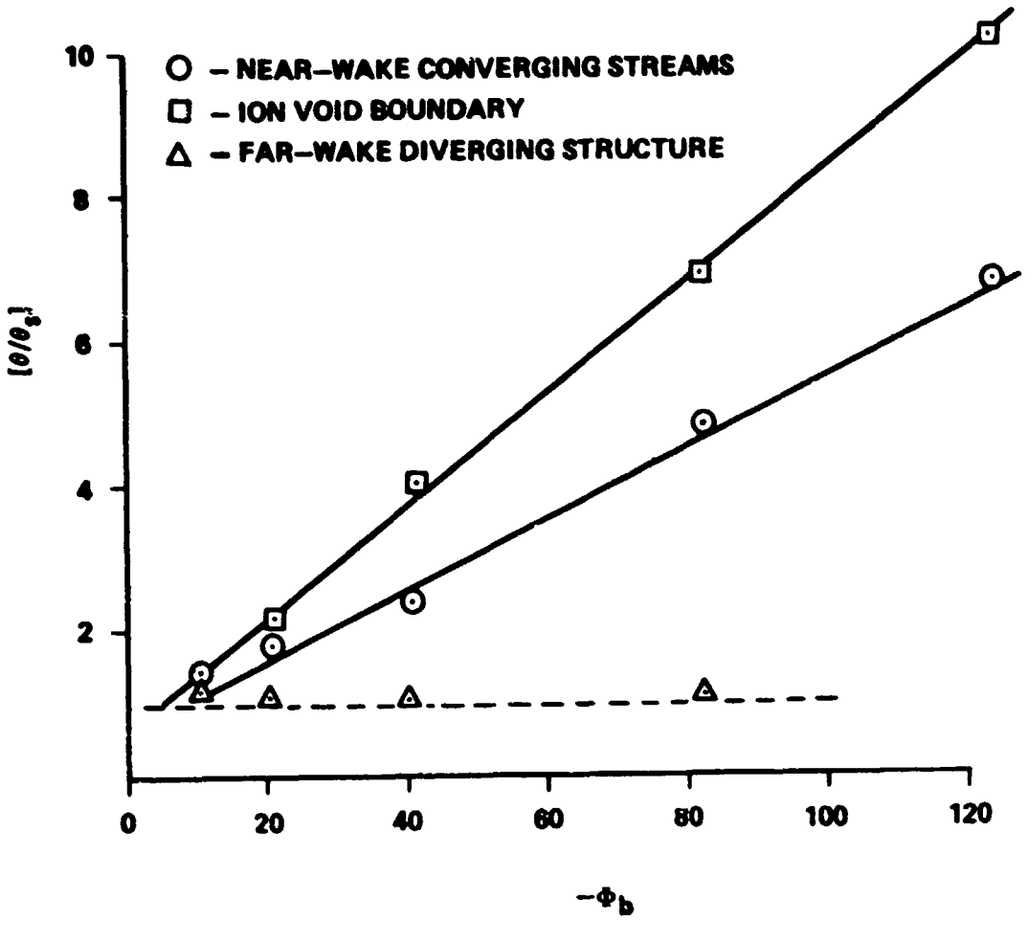

Figure 4-4. The dependence of the void boundary angle, θ_v, the void boundary streams, θ_{VB}, and the TV wave, θ_{TV}, on Φ_b. After Stone [99].

This corroborates the theoretical calculations by Martin (Appendix C.7, Figure C-14) although his result is based on the behavior of the deflected ion streams (apparently the VB streams) after they pass through the axial ion peak, essentially unaffected, and diverge downstream (Appendix C.7, Figure C-12). The behavior of the VB streams corresponds exactly to the behavior of the deflected streams found by Martin except that they are not observed to penetrate the axial ion peak; i.e., no structure with a corresponding angle of inclination to the Z-axis is found emerging on the downstream side of the axial ion peak. The only wave-like structures found beyond the axial ion peak are the TV wav hich correspond exactly to Martin's second wave-like structure characterized by θ_w (Appendix C.7, Figure C-14).

The inclination of the void boundary, θ_v, also shown in Figure 4-4, demonstrates that, even in the nearest vicinity of the test body, the void-filling process is affected primarily by ion deflection due to the value of Φ_b and any thermal or ambipolar diffusion processes, which do not depend on Φ_b, must be of secondary importance. Notice that θ_V and θ_{VB} have the same dependence on Φ_b but differ in slope by a constant. The similarity in Φ_b-dependence could result from the leading edge of the VB stream moving into the void to produce the observed closing of the void boundaries onto the Z-axis. The fact that the inclination of the void boundary is greater than the VB stream peak inclination may be explained by the first ion streams deflected into the wake passing closest to the body and being deflected toward the wake axis by a stronger electric field (and therefore at a greater angle) than the streams that become bunched into the VB-streams.

In Figure 4-5, the apex of the VB streams, determined by extrapolating the points in Figure 4-2 to the Z-axis, are plotted against $|\Phi_b|^{-1/2}$. This is in exact agreement with the Φ_b-dependence predicted theoretically by Martin (Appendix C.7, Figure C-14) and is in general agreement with an earlier experimental estimation of an "exponential" dependence by Stone et al. [74].

The large error bar on the point at $|\Phi_b|^{-1/2} = 0.425$ in Figure 4-5 is due to variation of the floating potential along the chamber axis (Chapter III.E). This effect is also apparent in Figure 4-4. Notice that both VB stream and TV wave structures are linear for all values of Φ_b with the exception of $\Phi_b = -5$, which is the floating potential. Both types of structure are highly nonlinear for this case. This is primarily the result of the axial density variation (Chapter III.E) so that when Φ_b is fixed by an external potential, the ratios, S and Φ_b, remain relatively constant since T_e and V_o do not change appreciably with Z.

In summary, the detailed effects of Φ_b on the near and mid-wake regions have been shown to corroborate the theoretical predictions of Martin precisely. This is made possible because the format in which Martin

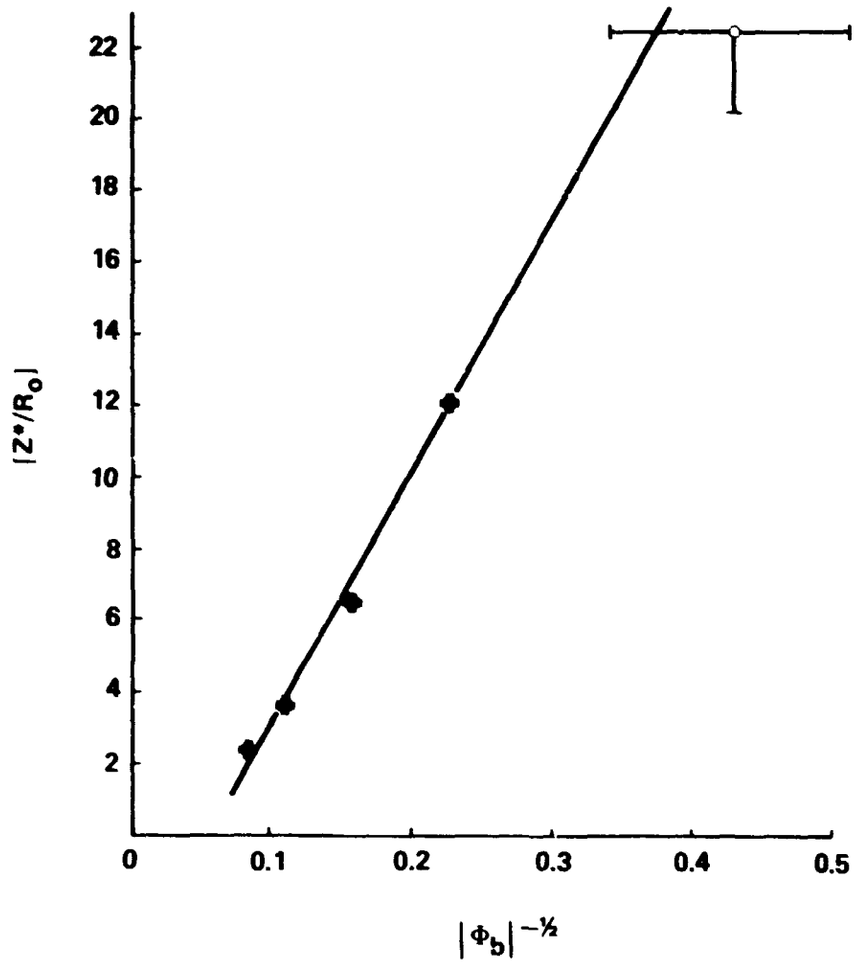

Figure 4-5. Dependence of the crossing point of the VB streams, $Z^* \equiv Z_d$, on Φ_b. After Stone [99].

presented his results is well suited to comparison with experimental measurements. Unfortunately, however, Martin did not present ion trajectory information in conjunction with the current density profiles, so that the exact nature of the wave-like structure cannot be determined from his results. Neither can it be determined from the present experimental measurements. The nature of the wave-like structures and why, if they are ion streams, does "bunching" of the ion trajectories occur to form an enhancement (as in the VB streams) are questions which require vector ion flux measurements.

2. Experiment B. The purpose of the second experiment was to investigate the detailed behavior of the near and mid-wake regions downstream from an electrically floating, conducting spherical test body for a variety of acoustic Mach numbers [69]. To accomplish this, an additional set of ion current density profiles was obtained, similar to those shown in Figure 4-2, but for a much lower drift velocity and, therefore, ion acoustic Mach number. The current density profiles, ambient stream current density, and the electron temperature were measured by the same Faraday cups and Langmuir probe described in Experiment A, above.

The data for a floating test body, brought over from Experiment A, will form Case I and the additional data set obtained in the present experiment will form Case II. The plasma flow conditions were

$$R_d \simeq 0.8 \quad , \quad S \simeq 17, \quad \text{and} \quad \Phi_b \simeq -5$$

for Case I and

$$R_d \simeq 1.2 \quad , \quad S \simeq 5.2, \quad \text{and} \quad \Phi_b \simeq -4.7$$

for Case II.

Figure 4-6 shows the axial variation of normalized ion current density, η, with normalized distance downstream from the center of the test body, Z/R_o, for Cases I and II. The test body for Case II was a conducting sphere with $R_o = 3$ cm as in Case I. The normalized ion current density, η, was obtained by measuring the current density on the Z-axis, $J(0,z)$, and the current densities in the undisturbed plasma stream on either side of the disturbed zone which were averaged to give an effective ambient value, $[J_o]_{av}$. The normalized axial ion flux was then defined as $\eta = (J(0,Z) - [J_o]_{av})/[J_o]_{av}$. Therefore, depletions of ion current density will be represented by negative values, while enhancements will be represented by positive values.

The axial current density profiles of Figure 4-6 show that a maximum value is reached at $Z/R_o = 16$ to 20 for Case I and at $Z/R_o = 4.5$ to 5.5 for Case II. This variation in the location of the maximum axial ion current

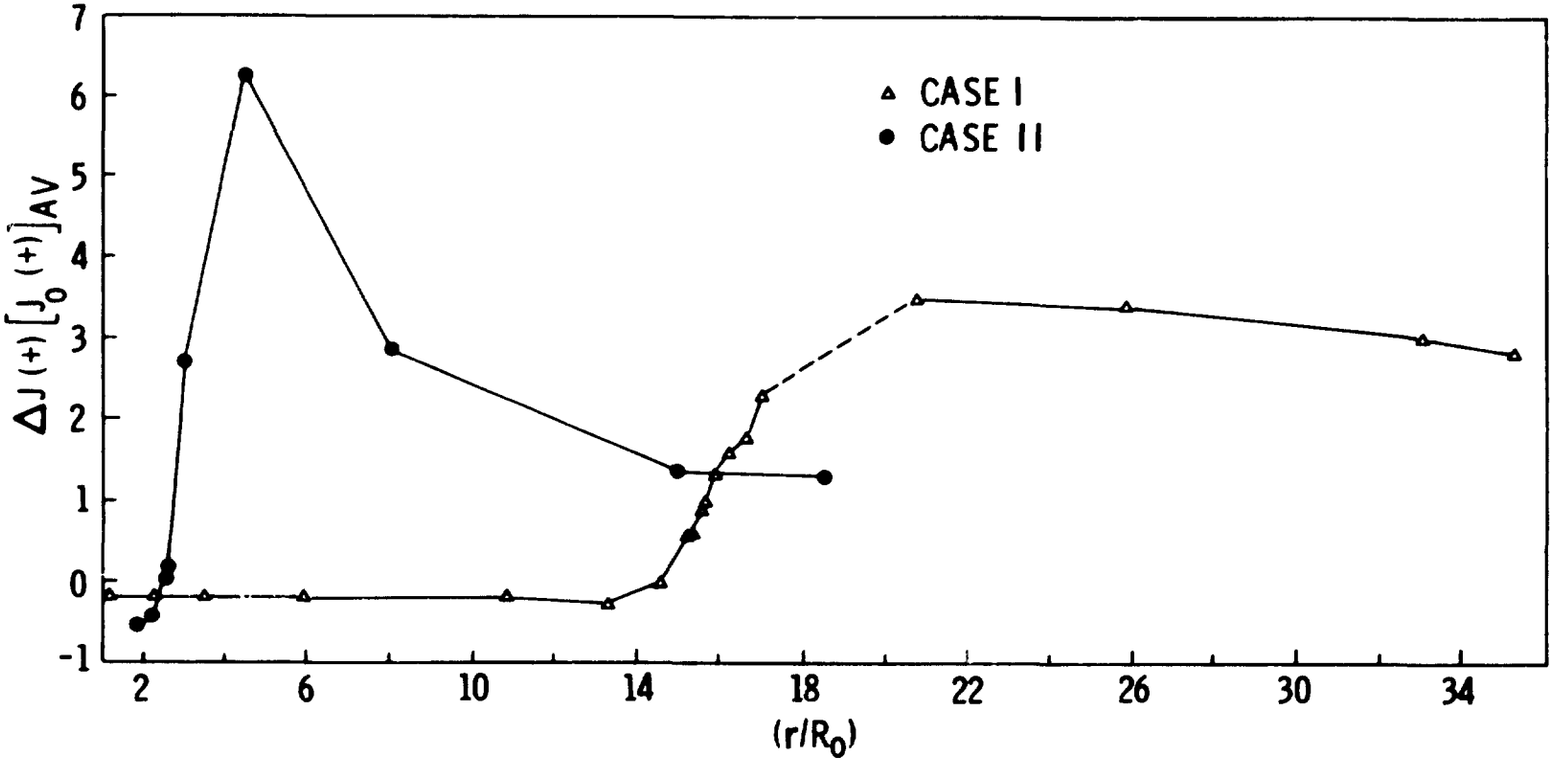

Figure 4-6. Axial variation of $\eta = [J(0,z) - J_o]/J_o$ with Z/R_o for the conditions: $R_d \simeq 0.8$, $S \cong 17$, and $\Phi_b \simeq -5$ (Case I) and $R_d \cong 1.2$, $S \cong 5.2$, and $\Phi_b \cong -4.9$ (Case II), after Stone et al. [69].

density enhancement must be due to differences in the experimental conditions. Note that since both cases use the same test body and since R_d and Φ_b are approximately the same for both cases, the only significant difference is in the ion acoustic Mach number, S. In both cases, within experimental error, the maximum enhancement occurred at a Mach number of radii downstream; i.e., at $Z = S \cdot R_o$. This result directly confirms the prediction by Taylor that the converging ion streams would merge to form an axial enhancement in ion density at approximately $S \cdot R_o$ (Appendix C.3).

To further confirm this result, the positions of the maximum axial ion current density enhancements obtained for Cases I and II, along with similar data obtained from several published sets of current density profiles, were plotted against the ion acoustic Mach number, as shown in Figure 4-7. In several cases it has to be assumed that the test body was maintained at or near the floating potential. Also, some of the results were obtained for circular plates rather than spherical test bodies. However, all bodies were conductors and all had a circular cross-section taken normal to the flow direction. The large error bars in the spatial dimension are the result of a limited number of transverse profiles and therefore a coarse determination of the axial profile (as shown in Figure 4-6 for the present experiment).

Figure 4-7 clearly demonstrates the dependence of the location of the maximum axial ion current density enhancement on the ion acoustic Mach number, and thus further confirms the theoretical result obtained by Taylor. However, more fundamentally, it attests to the fact that an axial ion current enhancement has been found to occur in the wakes of axisymmetric bodies over a wide range of the plasma flow parameters and in a number of different experimental facilities. This result is in accord with the theoretical results obtained by Maslennikov and Sigov, Cali, Martin, Taylor, Fournier, and others (Appendix C). It is simply explained by the action of the self-consistent electric field, existing in the sheath of the test body, on the free-streaming ions. The ions, as a result of the attractive force, are focused onto the wake axis. The amount of deflection and hence the distance

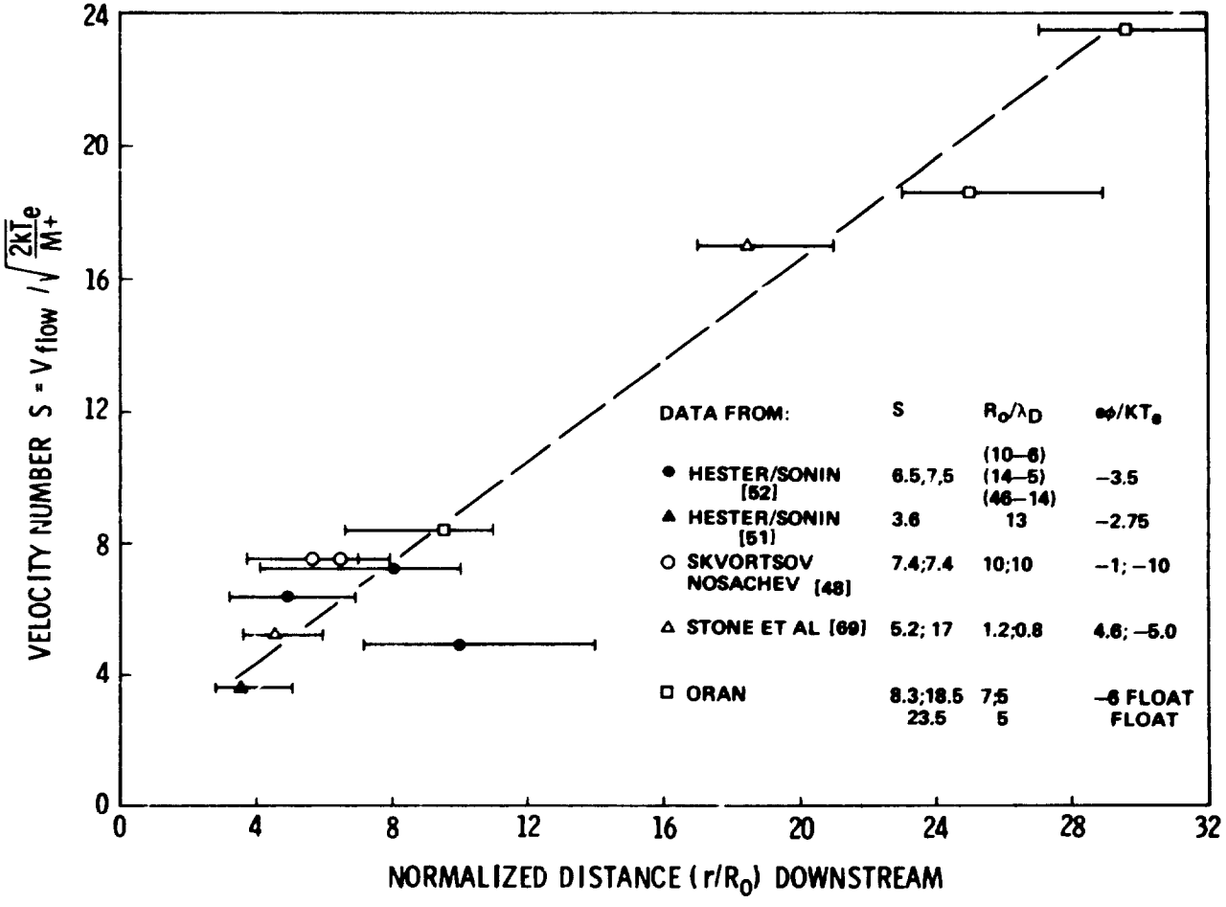

Figure 4-7. Axial position of the ion peak maximum as a function of S for several cases, after Samir et al. [75].

downstream at which the deflected ions converge on the wake axis to form an ion current peak depend on the ratio of the kinetic energy of the ions to the electric field strength in the sheath. However, for a floating body, the body potential becomes increasingly negative until a sufficient number of electrons are repelled to equalize the total ion and electron currents collected. The floating potential is therefore dependent on the kinetic energy of the electrons. The governing ratio is therefore

$$\left(\frac{1}{2} m_i V_o^2\right)/kT_e \equiv S^2 \quad .$$

It is appropriate here to discuss some of the in situ results from the Ariel I satellite. Recall that an axial electron current enhancement was observed by the boom-mounted probe in the wake of the main satellite as well as the spherical ion trap (Chapter II.B). The distance downstream at which the electron current profiles were obtained was $5\ R_o$ for the main body and $30\ R_o$ for the spherical ion trap, which was negatively biased to $\Phi_b \sim -35$. The ion acoustic Mach number at 400 to 800 km attitude is 4.5 to 5. The observation of the enhancement in the wake of the main body is therefore corroborated by the above result since this is approximately the $S \cdot R_o$ point at which the theory of Taylor and now the laboratory results predict that the maximum enhancement should occur.

The conditions at which the enhancement was observed behind the spherical ion trap are not closely approximated by any of the above data; i.e., Figure 4-2 shows results for the appropriate range of body potentials but S is too large while Case II (Figure 4-6) has an appropriate value of S but Φ_b is not sufficiently negative. However, Figure 4-2 shows that one effect of Φ_b becoming highly negative can be to cause the axial ion current enhancement to persist further downstream. Also, from Figure 4-6, it appears that the axial enhancement will still exist at $Z/R_o = 30$, even though Φ_b is small. Also recall that the satellite data were averaged over 10° increments of rotation (Appendix D.2.a). This would, assuming the structure propagates out at an ion acoustic Mach angle, permit two data points on the

axial enhancement 30 R_o downstream from the ion trap. While this is sufficient to reveal the existence of the enhancement, it would not allow observation of the splitting effect found here. Therefore, the creation of an enhancement at $Z/R_o = 5$ downstream from the Ariel I spherical ion trap, and the persistence of this peak out to the point of observation at $Z/R_o = 30$, is in accord with above experimental observations. The possible effects of finite ion thermal motion, which is not present to a sufficient extent in the above experiments, will be discussed in Experiment C below.

3. Experiment C. The third experiment was designed to provide additional insight into the nature and parametric behavior of the axial ion current density enhancement and, particularly, to shed some light on the perplexing question as to why an enhancement was observed in the wakes of the Ariel I satellite and the Ariel I spherical ion trap but was not found in the wake of the Gemini 10 capsule. To accomplish this, the experimental apparatus was improved by motorizing the axial mapper. This allowed continuous axial, as well as transverse, profiles of the wake characteristics to be obtained.

A set of axial profiles of ion current density obtained downstream from a 15 cm diameter conducting spherical test body for a variety of Φ_b values is shown in Figure 4-8. These measurements were made with a Faraday cup located directly behind the test body; i.e., on the Z-axis. The scaling parameters for the profiles of Figure 4-8 are $R_d = 4.3$, $S = 25.5$ with Φ_b taking on the values -20, -40.7, -61.1, -81.5, and -163. This will be referred to as Case I-C.

Note that the axial ion peak moves toward the test body as Φ_b becomes increasingly negative. This presumably is the result of stronger ion focusing, as was found in Experiment A. In addition, the peak height is seen to increase with more negative Φ_b. The third effect to note is the development of a second break point on the leading (upstream) edge of the axial ion peak for highly negative Φ_b. This suggests that the axial ion current peak is created by more than one process, as mentioned in connection with Figure 4-1 in Experiment A, and further, these processes must depend differently on the

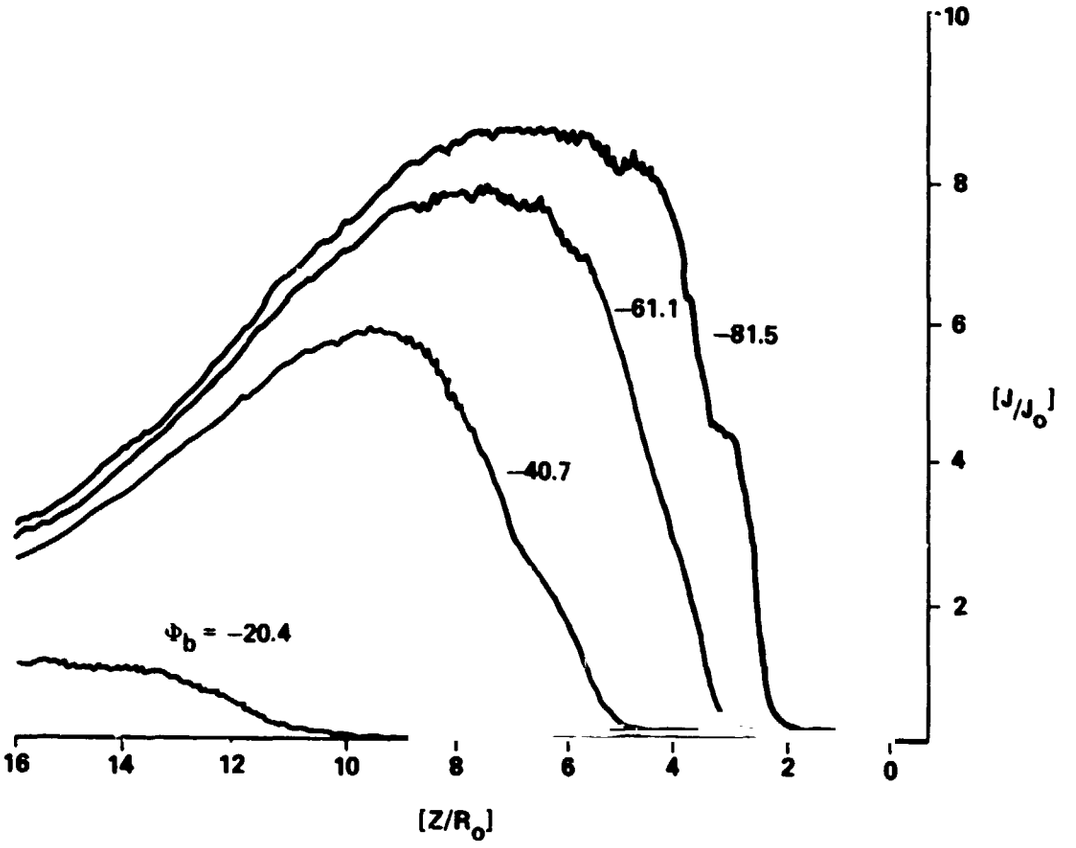

Figure 4-8. Axial ion current density profiles downstream from a conducting sphere for $R_d \cong 4.3$, $S \cong 25.5$, and Φ_b as indicated. After Stone [100].

normalized test body potential, Φ_b. This would explain the tendency for the axial peaks created by different processes to separate at large Φ_b.

A set of transverse profiles of $[J_i/J_o]$ obtained with $\Phi_b = -41$ is shown in Figure 4-9. These profiles correspond to the axial profile obtained at the same voltage in Figure 4-8. Note the striking similarity to the wake morphology shown in Experiment A (Figure 4-1). The void filling process and subsequent development of the axial ion peak are compressed into a smaller range on the Z-axis, as expected since $\Phi_b = -5$ in Figure 4-1 and -40.7 here, while the difference in the ion acoustic Mach numbers is not so great. The exact dependence on R_d, S, and Φ_b will be investigated further in the present experiment. Finally, no splitting of the axial ion peak to form a trailing "V"

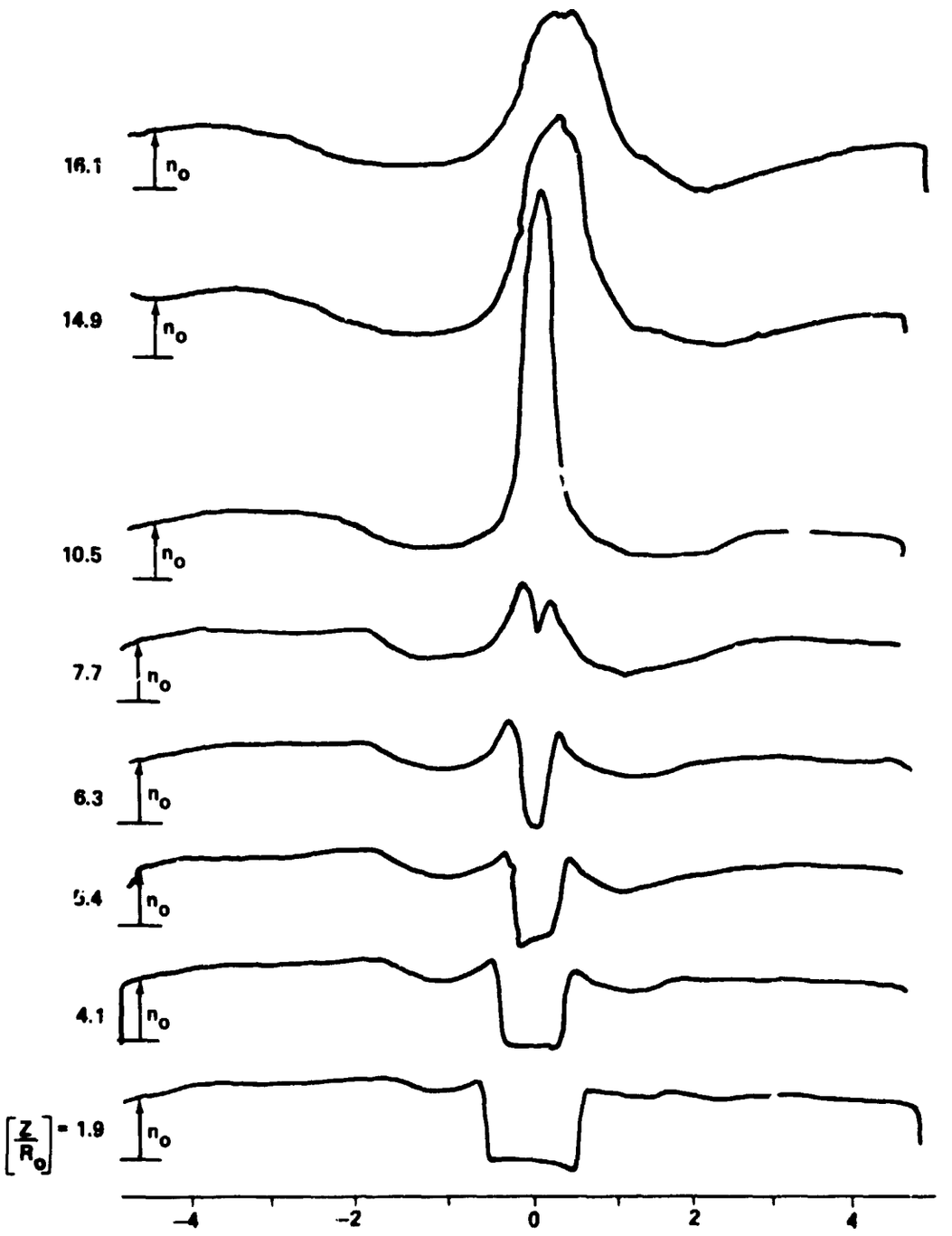

Figure 4-9. Transverse ion current density profiles for the conditions of Figure 4-8 with $\Phi_b = -41$. After Stone [100].

wave is observed. However, the measurements do not extend sufficiently far downstream so that the lack of this effect here is not significant.

A set of axial profiles, similar to those shown in Figure 4-8, were obtained for a second set of scaling parameters: $R_d = 1.72$, $S = 22.8$, and $\Phi_b = -29$, -87, -116, and -232, which will be referred to as Case II-C. The intercept of the leading edge of the axial ion peak for Cases I-C and II-C are plotted against $|\Phi_b|^{-1/2}$ in Figure 4-10. (The intercept is defined by a linear extension of the leading edge below the first break point to the Z-axis.) Each set of points falls on a straight line (as would be expected from Experiment A). However, the lines defined by the two sets of data are offset, indicating a dependence on other parameters.

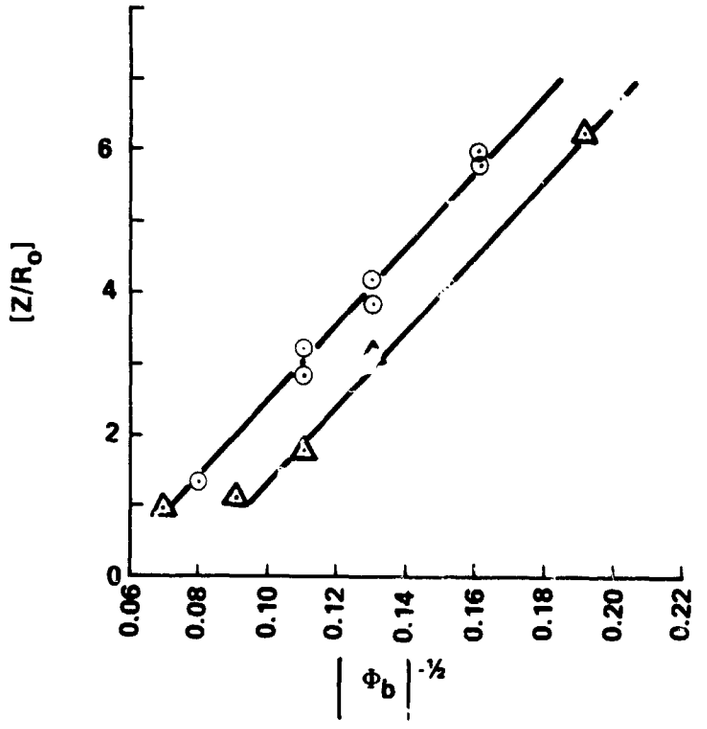

Figure 4-10. Intercept of the leading edge of the axial ion peak with the Z-axis as a function of $|\Phi_b|^{-1/2}$ for Case I-C, ⊙, and Case II-C, Δ.
After Stone [100].

Since S and R_d have different values in the two cases, the dependence on each one can be investigated. Recall from Experiment B that a linear dependence on S would be expected. Therefore, R_d remains the only parameter which can be used to collapse the two sets of points in Figure 4-10 onto a single curve. For this to occur, we allow R_d to have a variable exponent, α, and require:

$$\left(\frac{S R^{\alpha}}{|\Phi_b|^{1/2}}\right)_1 = \left(\frac{S R_d^{\alpha}}{|\Phi_b|^{1/2}}\right)_2 ,$$

where the subscripts 1 and 2 refer to Cases I-C and II-C, respectively. Solving for the parameter, α, we have:

$$\alpha = \frac{\ell n \left[\frac{S_2}{S_1}\left|\frac{\Phi_{b1}}{\Phi_{b2}}\right|^{1/2}\right]}{\ell n \left[R_{d1}/R_{d2}\right]} = 0.02359 ,$$

where the values of S and R_d are given for the two cases and the ratio $|\Phi_{b1}/\Phi_{b2}|^{1/2}$ is found from the curves of Figure 4-10.

In Figure 4-11, the intercepts of the leading edge of the axial ion peaks with the Z-axis, normalized by R_o, are plotted against $\left[S R_d^{\alpha} / |\Phi_b|^{1/2}\right]$ for Cases I-C and II-C. The two sets of data from Figure 4-10 now lie on a single straight line. To further test this finding, the VB-stream intercepts for Case I-C (these data were not available for Case II-C) were obtained, as in Experiment A, and plotted, along with the intercepts obtained in Experiment A. These two sets of points also lie along a common straight line. The curves corresponding to the VB stream and axial current peak intercepts lie on different lines because they represent different effects. The VB-stream intercepts are based on the positions of the peak density of the VB streams. This intercept would therefore occur slightly downstream from the first break point on the axial profiles (Figure 4-8). The intercept of the leading edge of

C - 2

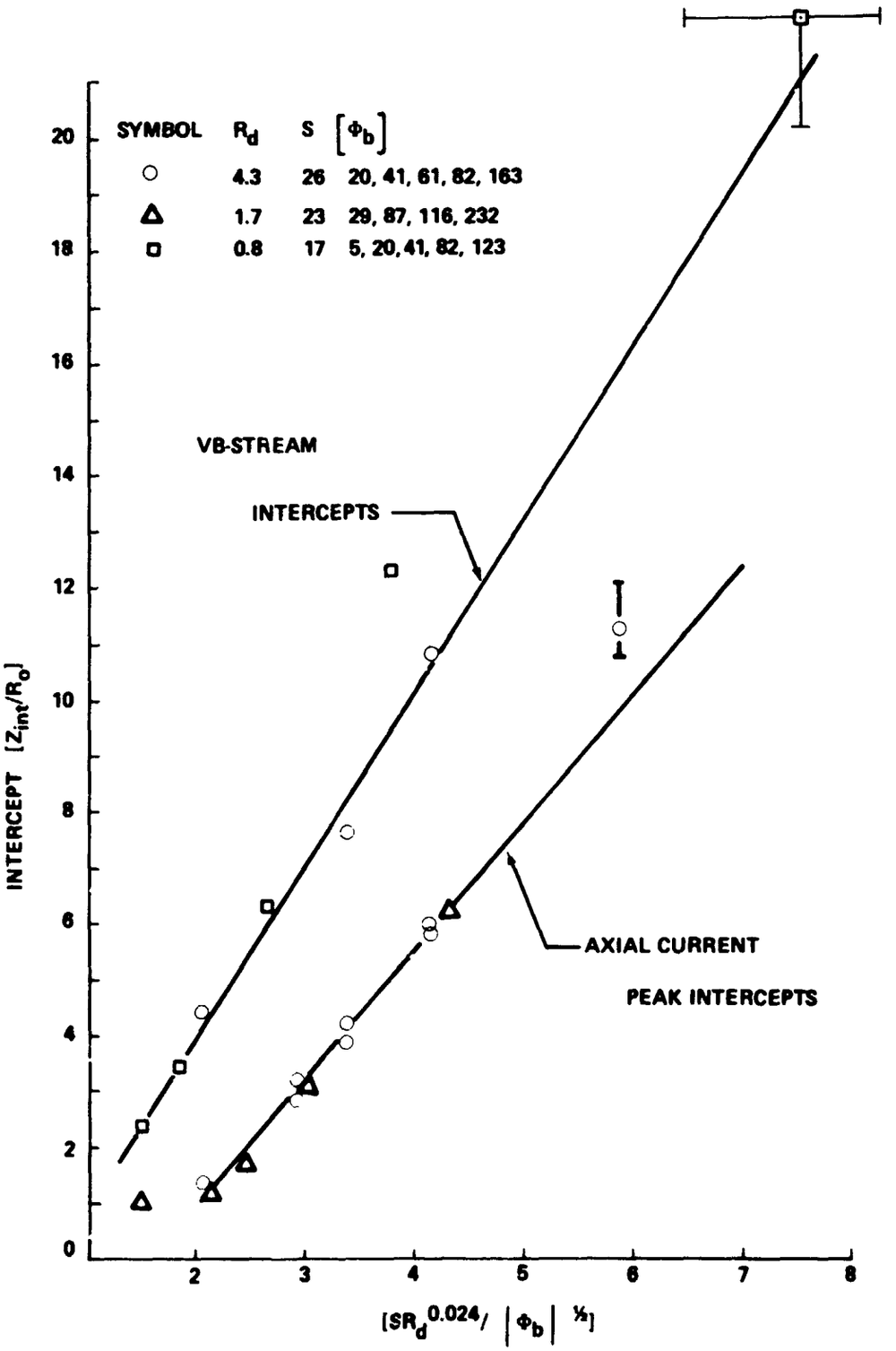

Figure 4-11. Variation of axial ion peak intercepts and VB-stream crossing point with $\left[S R_o^{\alpha} / |\Phi_b|^{1/2}\right]$. After Stone [100].

the axial ion peak would correspond to the edge of the VB streams advancing into the void region, not the peak position.

The above finding is in agreement with the results of Martin's calculations for the S and Φ_b dependence of Z_d/R_o, but does not agree with his conclusion as to the form of the R_d dependence (Appendix C.7). The relation developed by Martin for the dependence of the crossing point location, when normalized by R_o, is

$$\left[\frac{Z_d}{R_o}\right] \sim \frac{S}{|\Phi_b|^{1/2} R_o^{1/2}} \quad .$$

The present experimental results do not agree with this expression. As pointed out in the previous discussion, this expression ignores the distance over which the electric potential is assumed to decrease. When this was included, the expression became:

$$\left[\frac{Z_d}{R_o}\right] \sim \frac{S}{|\Phi_b|^{1/2} R_d^{\xi+1/2}} \quad ,$$

where ξ is a constant. The present experimental results can be made consistent with this expression by requiring $(\xi + 1)/2 = \alpha$ so that $\xi = -0.949$. The average electric field experienced by the deflected ions is therefore related to the body potential by

$$E_{eff.} \sim \Phi_b R_d^{-0.949} \quad .$$

In Figure 4-12, the maximum amplitude of the axial ion peak, compared to the ambient current density, is shown to be inversely proportional to $|\Phi_b|^{-1/2}$. The best fit lines for the data points obtained from Case I-C and Experiment A are offset. This offset was found to vanish when the amplitude is also assumed to be proportional to S, as shown in Figure 4-13, where the two sets of data have collapsed to a single straight line.

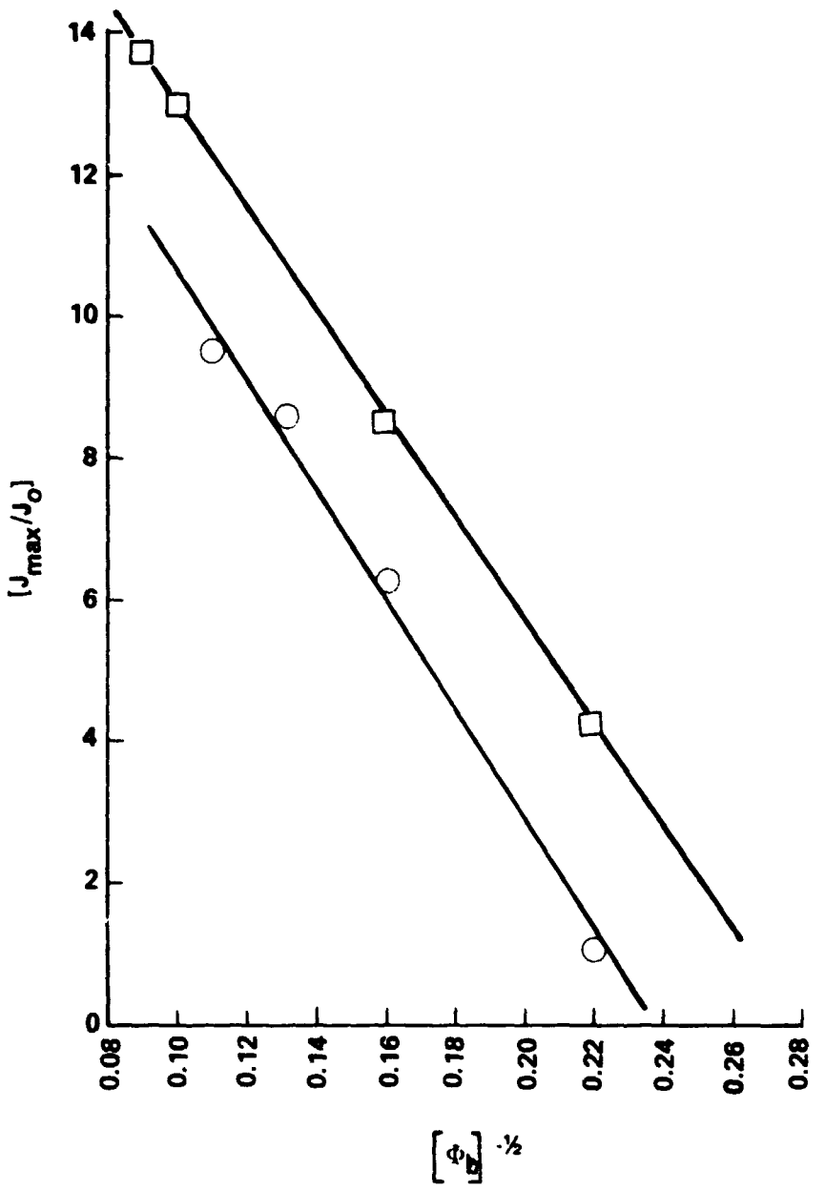

Figure 4-12. Axial ion peak maximum amplitude in J_o as a function of $|\Phi_b|^{-1/2}$ for data from Experiment A (□) and Case I-C (○).

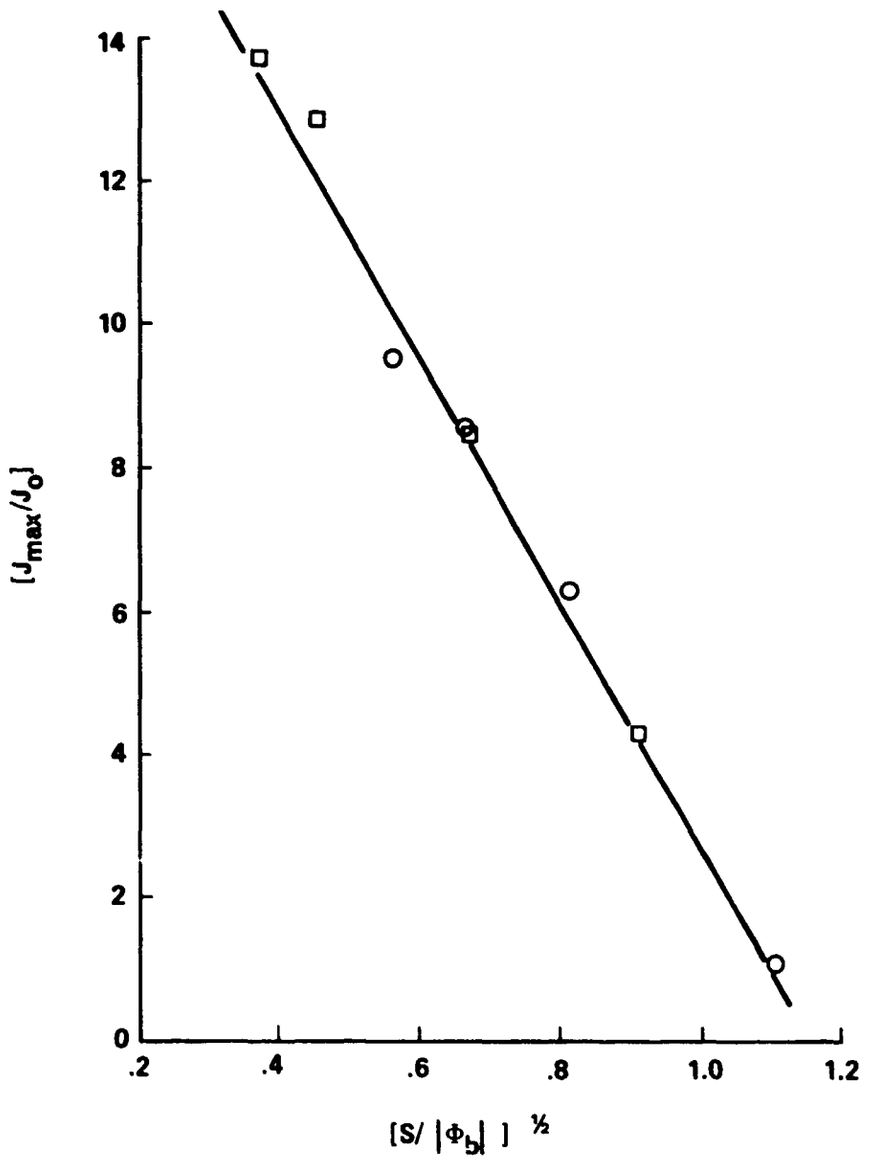

Figure 4-13. Variation of the normalized maximum amplitude of the axial ion peak, $[J_{max}/J_o]$ with $[S/|\Phi_b|]^{1/2}$, for Case I-C (O) and data from Experiment A (□).
After Stone [100].

The $[J_{max}/J_o]$ ratio was not found to depend on R_d (at least not strongly). This is a surprising result since, from simple geometric arguments, the amplitude of the axial peak would be expected to depend on the area of the annular cross-section focused onto the Z-axis and therefore on R_o. However, such an argument assumes simple superpositioning of the ion streams at the intercept point on the Z-axis and does not account for any interaction with the spacecharge potential created there, or dispersion of the streams during transit from the deflection point to the axis. Evidently, the space charge potential is sufficiently strong to repell oncoming ions from the Z-axis, therefore, limiting the peak height to a value proportional to the x-component of ion momentum which is, in turn, proportional to Φ_b which produced their deflection.

There are two competing effects involving R_d. The $[J_{max}/J_o]$ ratio must depend on the ratio of the initial area of the annulus crossed by the ion streams at the body, to the area to which they are focused on the Z-axis. The area of an annulus of thickness dx is proportional to its radius R_d. On the other hand, dispersion of the streams is proportional to the distance traveled in reaching the Z-axis which is, in turn, proportional to R_d and S. It is reasonable, then, that the R_d dependence of these two opposing effects may cancel, leaving only an S-dependence. This appears to be the observed effect in the data as shown by Figure 4-13.

The parametric dependence of the axial ion peak width was also investigated. These results are shown in Figure 4-14, in which the peak width at its midpoint (in amplitude), normalized by R_o, is plotted against $|\Phi_b|^{-1/2}$. This is a very tedious measurement and the measurement error can be expected to be rather large. However, the data points from both Case I-C and Experiment A fit a single straight line reasonably well. The peak width, W_p, is seen to be directly proportional to $|\Phi_b|^{-1/2}$, which is opposite to the dependence of the peak height. Although the inverse variation of W_p and J_{max} with each other as Φ_b changes might suggest a preservation of the total current in the axial ion current density peak; this is not the case. This can be

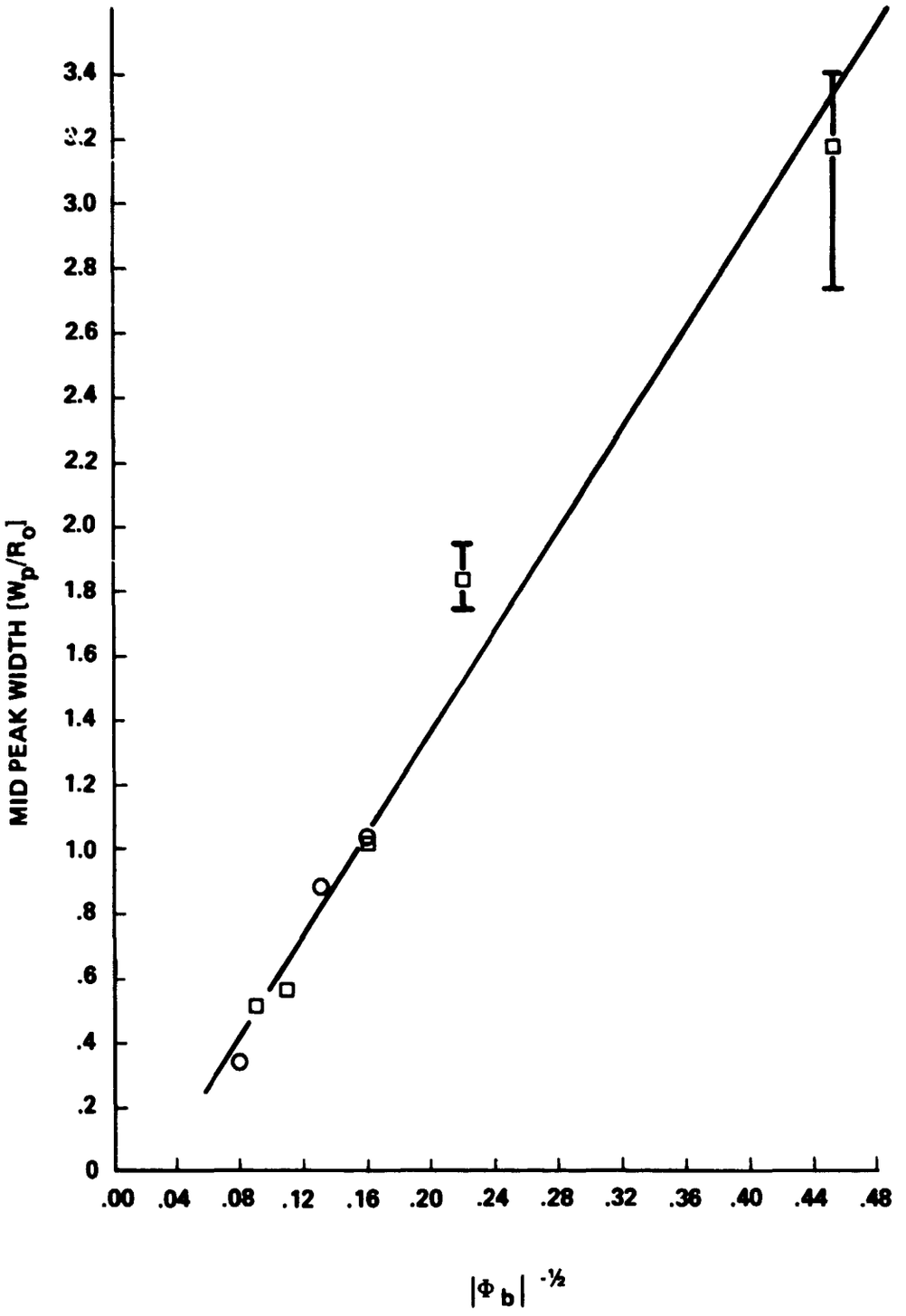

Figure 4-14. Variation of the axial ion peak width at half maximum with $|\Phi_b|^{-1/2}$ for Case I-C (O) and data from Experiment A (□). After Stone [100].

seen by the fact that J_{max} also depends on S while W_p depends only on Φ_b. Therefore, for constant Φ_b, J_{max} varies with S while W_p remains constant. For example, the data in Figures 4-13 and 4-14 show that for $\Phi_b = -41$, the product $(J_{max}/J_o) \times (W_p/R_o)$ is 8.6 for S = 17 and 6.3 for S = 25.

The fact that (W_p/R_o) depends only on Φ_b is reasonable since the peak width should be determined by the distance from the Z-axis at which ions are deflected by the space charge potential. This, in turn, depends only on the momentum of the ions (due to V_x) and the amplitude of the potential barrier formed by the space charge. The tendency for the ion current density peak to form a potential barrier is opposed by the electrons, which strive to neutralize the positive space charge potential. The responsiveness of the electrons is inversely proportional to their thermal motion, characterized by kT_e. The x-component of ion velocity, on the other hand, depends on Φ_b. Therefore, the parameter Φ_b, for this effect, is proportional to the ratio of the normal component of ion momentum to the magnitude of the space charge potential barrier.

Finally, it must be pointed out that the observed parametric dependences shown in Figures 4-11, 4-13, and 4-14 may not apply over other ranges of the indicated parameter groups. For example, Figure 4-13 indicates that the peak amplitude vanishes at $[S/\Phi_b]^{1/2} \simeq 1.16$. However, in Experiment A, a strong peak ($J_{max}/J_o \simeq 2.9$) was observed for the condition $[S/\Phi_b]^{1/2} = [17/5]^{1/2} = 1.84$. In addition, Fournier and Pigache have observed peaks of $[J_{max}/J_o] \simeq 2$ for $[S/\Phi_b]^{1/2} = [10.6/3]^{1/2} = 1.88$ (Appendix E.1.i.). Clearly, these data points are exceptions to the trend shown in Figure 4-13. In the case of Experiment A, the only difference was apparently the body bias Φ_b. The remaining data points from Experiment A are shown in Figure 4-13. Therefore, the linear dependence of Figure 4-13 must be altered in the vicinity of $[S/\Phi_b]^{1/2} \sim 1.1$.

A possible explanation of this change in behavior is that as Φ_b becomes small, the negative space charge in the ion void region becomes the dominant focusing mechanism. Hence, the formation of the peak would then become independent of Φ_b and would still occur. This explanation is

supported by the observation of axial ion peaks by Hester and Sonin in the wakes of small cylinders with $\Phi_b \simeq +3$ (Appendix E.1.g). It can be expected that such a peak, created by the negative space charge potential in the ion void region, would vanish when S and/or R_d become large enough that the deflected streams become diffuse before reaching the Z-axis.

Although the exact differences in the experimental conditions for the present data and that of Fournier and Pigache (i.e., slow ion concentration, stream divergence, and normal ion temperature) are not known, it is interesting to note that the above parametric dependence is apparent in their data. Referring to Figure E-16 of Appendix E.1.i, the Z-axis represents data with the same values of S and T_e/T_i. Moving up the Z-axis, R_d changes from 6 to 25 to 45. Note that the peak width remains about a radius wide at its midpoint as expected from Figure 4-14. Also, the axial ion peak amplitude does not change significantly. However, moving out the Y-axis, Φ_b changes from -3 to -100. This change is accompanied by a striking increase in peak height, as would be expected from the present results shown in Figure 4-13.

We note that measurements of electron density, made with a cylindrical Langmuir probe in the wake of a conducting sphere in the MSFC No. 2 facility [76,77], show an axial electron density enhancement roughly coinciding with the axial ion peak described above. No detailed study of the electron peak has been made.

The parametric behavior of the axial ion peak revealed by this experiment can be used to provide additional insight into the apparent contradiction between the Ariel I and Gemini-Agena 10 data. (Recall that an axial electron peak was observed in the Ariel I and Ariel I spherical ion trap wakes but was not observed in the wake of the Gemini capsule, see Appendix D, Figure D-8.)

As already stated in Experiment B, the observation of an axial electron peak in the Ariel I data at $5R_{Ariel} \sim S.R_{Ariel}$ is consistent with experimental results. Further, Figure 4-8 shows the axial ion peak to persist far downstream so that in view of the similarity of ion and electron peaks mentioned

above, the observation of an electron peak in the wake of the Ariel I spherical ion trap at $5R_{Ariel} >> R_{probe}$ is not unexpected.

The fact that an axial peak was not observed in the wake of the Gemini 10 capsule must result from one of the following possibilities: (1) sufficient ion thermal motion existed to completely suppress any axial enhancement, (2) the wakes of large spacecraft ($R_d \gtrsim 10^2$) are not subject to the converging stream behavior responsible for creating axial peaks, and (3) an axial peak existed in the Gemini 10 wake but was not observed [75].

The laboratory results, together with the results obtained from the Ariel I data under very similar plasma flow conditions, do not support the first possibility. Notice that the Z_2-axis of Figure E-16 in Appendix E.1.i shows data obtained by Fournier and Pigache for $T_e/T_i \cong 1$. Compared with the data of the Z_1-axis for $T_e/T_i \cong 10$, an inverse dependence of the axial peak amplitude on T_e/T_i is clearly demonstrated. However, three points should be made concerning the temperature dependence of these data. First, even though the axial peak height is shown to decrease with decreasing T_e/T_i and vanish at $T_e/T_i \leq 1$, we note that a distinct peak remains at $T_e/T_i = 10$ and that in the ionosphere, $T_e/T_i = 2$, not unity. Therefore, a peak, possibly on the order of the ambient plasma, could still be expected to occur based on these data. This conclusion is also supported by the theoretical calculations of Gurevich, Pitaevskii, and Smirnova which show a slight axial ion peak for $T_e/T_i = 4$ (Appendix C.4). Further, the calculations by Fournier show slight axial disturbance for $T_e/T_i = 2$ (Figure C-10, Appendix C.6). Secondly, the value of S on the Z_1-axis is about twice its value on the Z_2-axis. Figure 4-13 (obtained for $T_e/T_i >> 1$) shows that the effect of increasing S is to decrease the peak height. Therefore, if there were no change in S from the Z_2 to the Z_1-axis, an even greater peak height would be expected for $T_e/T_i \cong 10$ on the Z_1-axis, relative to the data for $T_e/T_i \cong 1$ on the Z_2-axis where the value of $S \cong 5$ is appropriate for the ionospheric conditions. Thirdly, the experimental results were not obtained for a Maxwellian or random motion of the ions. The value of T_i is therefore not a true temperature but represents an

effective temperature based on the mean ion motion normal to the flow direction. This may produce a more severe effect than a true thermal ion motion.

Concerning the second possibility, no theoretical or experimental work is presently available for $R_d > 10^2$ which would apply directly to the case of the Gemini capsule ($R_d \simeq 500$). However, as previously stated, the present study shows the peak height to be independent of R_d (Figure 4-13). This conclusion is supported by the data obtained by Fournier and Pigache shown in Figure E-16 of Appendix E.1.i, which qualitatively extends the result out to $R_d \cong 50$. Therefore, since the experimental data show no dependence of the peak height on R_d for over an order of magnitude, it is reasonable to expect it to remain independent of R_d for the case of the Gemini capsule as well.

Since neither of the first two possibilities appear likely, we must consider why, if an axial peak existed, it was not observed. There are two possible reasons: (1) the maximum peak amplitude was less than ambient in which case it could only be revealed by transverse profiles which were not taken and (2) the peak was sufficiently narrow that it was simply missed due to alignment error in the axial profile.

As concluded above, if an axial peak existed from the available results of both theory and experiment, it would be expected to have an amplitude no greater than the ambient plasma. This is precisely the type peak observed in the Ariel I data. Further, these peaks were observed by transverse profiles made by the boom probe sweeping through the wake region at $Z \cong 5\, R_{Ariel}$. Therefore, the first possible reason for nonobservation of an existing peak is very plausible.

Concerning the second possible reason for nonobservation of an existing peak, Figure 4-14 shows the peak width to vary from several radii to less than a radius, depending on the body potential, Φ_b. The conditions for the Gemini-Agena 10 and Ariel I observations were similar ($\Phi_b \simeq -5$) and would place the expected peak width at approximately 3 radii. As stated above, the peak height is expected to have been no greater than the ambient plasma. However, Figure 4-15 shows explicitly that, even when the axial peak is

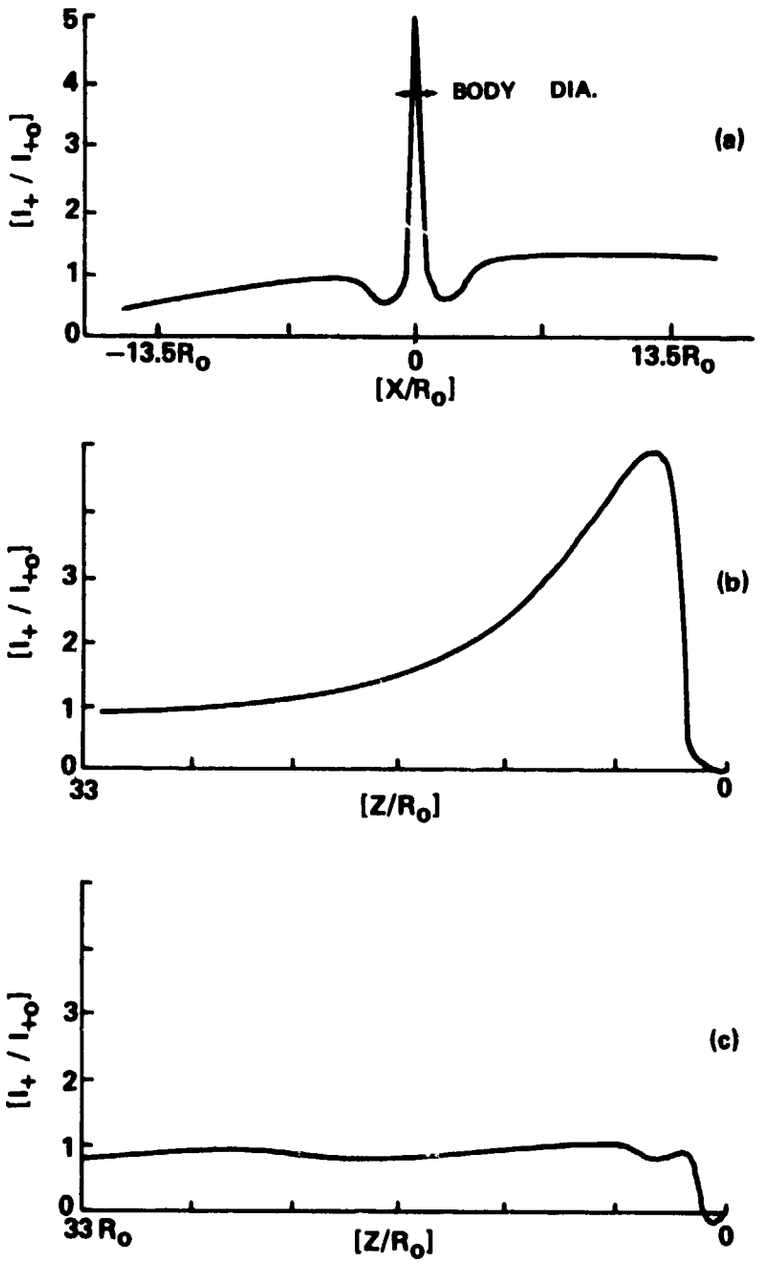

Figure 4-15. Effect of misalignment on axial ion current density profiles and the ability to detect the axial ion peak, (a) a transverse J/J_o profile at the point of maximum enhancement, (b) an axial profile on-axis, and (c) an axial profile displaced $\approx R_o/2$ off the Z-axis, after Samir et al. [75].

considerably greater than ambient, a small displacement of an axial profile of 1 to 2 R_o is sufficient to prevent its observation. For the case of the Gemini capsule where the peak width is expected to have been approximately 3 radii, it follows that a displacement of 1.5 to 2 R_{Gemini} would have resulted in the same effect. Misalignment errors of this size are entirely consistent with the known misalignment on the Gemini-Agena 10 mission [75].

4. Experiment D. The purpose of the measurements in this section is to demonstrate some of the effects of body geometry on the mid-wake structure over the available range of parameter space. The initial measurements for this purpose were made in the MSFC No. 2 facility. The details of the facility, the experimental setup, and the results of two sets of measurements are described elsewhere [78,79].

In the first set of measurements, the mid-wakes of a conducting sphere and a short cylinder with its axis of symmetry oriented perpendicular to the XZ-plane were investigated [78]. The cylinder was studied over the parameter range $(S, R_d) \cong (7, 12)$, $(12, 13)$, $(7, 22)$, and $(12, 25)$ with ϕ_b having values of -4, -2, -1, and -0.4 volts for each case. The same voltages were applied to the sphere for the parameter range $(S, R_d) \cong (7, 13)$, $(13, 12)$, and $(13, 25)$.

The main conclusions obtained from the first measurement set are:

(1) The location of the axial ion peak at $Z = SR_o$, as discussed in Experiment B, is further confirmed for spherical bodies, but may depend on body geometry to some extent.

(2) The peak amplitude was found to be directly proportional to ϕ_b and λ_D, but to be relatively independent of S.

(3) The initial width of the disturbance at the test body varies with λ_D but is independent of S.

(4) If an axial structure occurs in the mid-wake of spherical bodies, it was observed to be in the form of a single peak for all cases whereas the axial structure for the cylinder, oriented perpendicular to the flow, was always a multiple peak or plateau for the cases observed.

(5) The axial peak in the wake of spherical test bodies may be several J_o in amplitude whereas the peak height behind the perpendicular cylinder was never observed to rise significantly above ambient.

In the second set of measurements, the mid-wake was studied for a sphere, two disks of different diameters, a cone with its apex pointed into the flow, a short cylinder mounted with its axis of symmetry parallel and with it perpendicular to the flow direction, and a square plate oriented normal to the flow. The additional conclusions obtained from these measurements are: (1) the previous conclusion concerning a single peak for spheres and multiple peaks for perpendicular cylinders is extended to include all bodies with circular and square cross-sections normal to the flow direction, and (2) the cross-sectional geometry of the body parallel to the flow direction does not appear to alter the basic morphology of the mid-wake structure, but may affect its amplitude and location on the $[Z/R_o]$ axis.

The conclusion concerning the location of the axial ion peak at $S \cdot R_o$ has already been discussed in Experiment B and the dependence of peak amplitude was shown explicitly in Experiment C. Upon closer examination of the first data set, a dependence of the peak height on S was observed and found to be in agreement with the inverse $S^{1/2}$-dependence found in Experiment C. Also, the dependence of peak height on λ_D was found to apply primarily to the normal cylinder.

The conclusion that the peak height depends strongly on λ_D (and therefore R_d) appears to be a direct contradiction of the results of Experiment C and those of Fournier and Pigache (Appendix E.1.i, Figure E-16) where no R_d dependence was found.

Additional measurements (Figures 4-16 and 4-17) have been made in the MSFC No. 1 facility to attempt to resolve this apparent contradiction. Ion current density profiles of the wake of a short (8 cm diameter by 8 cm long) cylinder oriented with its axis of symmetry normal to the XZ-plane (and hence the flow direction) are shown in Figure 4-16. The acoustic Mach number, S, is constant for all cases. The only difference in the (a) and (b)

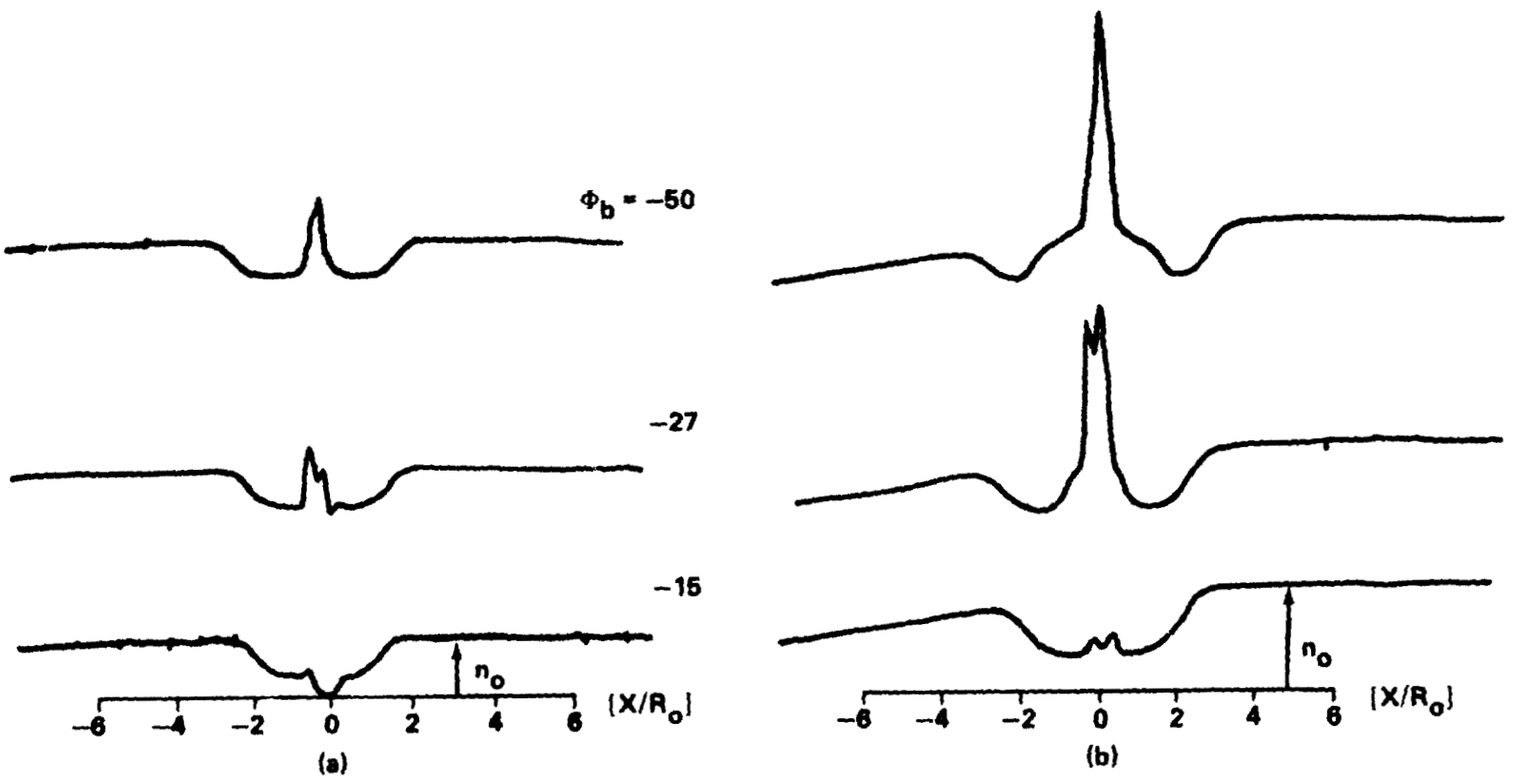

Figure 4-16. Ion current density profiles downstream from a conducting cylinder (8 cm diameter by 8 cm long) oriented with its axis of symmetry normal to the flow direction at $Z/R_o = 3.2$ for (a) $R_d \cong 5.4$, $S \cong 10.8$ and (b) $R_d \cong 4.25$ and $S \cong 10.8$.

Values of Φ_b for both cases are indicated.

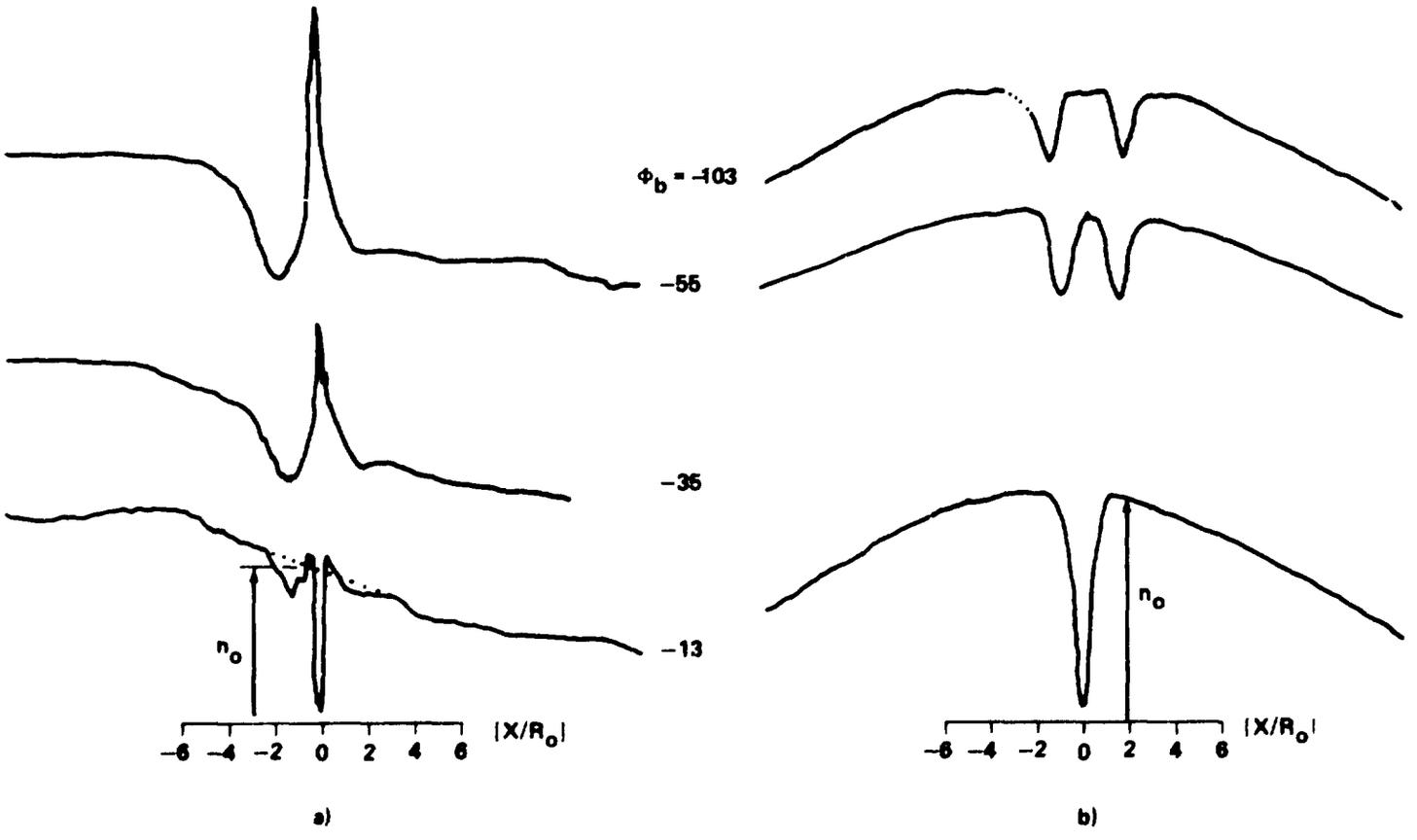

Figure 4-17. Ion current density profiles in the wake of a long conducting cylinder oriented normal to the flow direction ($2R_o$ = 2.54 cm) at Z/R_o = 3 for (a) R_d = 1.74, S = 9.35 and (b) R_d = 0.74, S = 15.8. Values of Φ_b are as indicated.

profiles is a change in the Debye ratio R_d, from 5.4 for (a) to 4.25 for (b). A very strong inverse dependence of the peak height, $[J_p/J_o]$, on R_d is indicated, in agreement with the Oran et al. data [78]. Note that the behavior shown in Figure 4-16 approaches that of a spherical test body (Figure 4-9) for large negative values of Φ_b.

In Figure 4-17, the same types of profiles are given for a 2.54 cm diameter cylinder oriented with its axis of symmetry normal to the XZ-plane, which is sufficiently long to eliminate end effects (i.e., it essentially spands the plasma stream). This case, therefore, represents a completely two-dimensional problem. The Debye ratio, R_d, decreases from 1.74 in (a) to 0.74 in (b) while the ion acoustic Mach number, S, increases from 9.35 to 15.8. Note that there is now a strong decrease in $[J_p/J_o]$ from the conditions in (a) to those in (b). If this is the result of R_d-dependence, then it is the inverse of the dependence indicated in Figure 4 . Since this seems unlikely, we assume that the mid-wake structure for the long cylinder is relatively independent of R_d and has an inverse dependence on S which is consistent with the results for spherical bodies in Experiment C.

We now have a rather confusing picture of the behavior of the mid-wake axial ion peak height: (1) a very weak or no dependence on R_d for spherical bodies, indicated by Experiment C and Fournier and Pigache, (2) a strong inverse R_d dependence for short, normally oriented cylinders (or any square cross sectional body), indicated by Figure 4-16 and Oran et al., and (3) probably a very weak, or no R_d dependence for long, normally oriented cylinders, indicated by Figure 4-17. Although additional data are needed to carry out a complete parametric study as was done in Experiment C, the present data are sufficient to suggest the following explanation which is consistent with all available data and is based simply on the behavior of the plasma sheath. The hypothesis, briefly stated, is that body geometry is important to the intermediate wake structure only when the plasma sheath thickness is relatively small compared to the body dimensions (R_d greater than some value).

The plasma sheath thickness is directly proportional to Φ_b and inversely proportional to R_d. Therefore, for small Φ_b and/or large R_d, the sheath thickness is small compared to the test body dimensions and, therefore, conforms closely to the test body geometry. For spherical bodies, this is not particularly important. However, for nonspherical, and particularly nonaxisymmetric bodies, this results in a decrease of the axial ion peak height since all deflected ions are not focused onto the Z-axis. As Φ_b increases and/or R_d decreases, the plasma sheath expands outward from the test body and takes on an increasingly spherical geometry. This increases the effective spherical symmetry of the test body and correspondingly increases the axial ion peak height.

Specifically, for test bodies with square cross-sections, the focused ion streams will converge to a pair of orthogonal line segments approximately the length of the test body dimensions. This is consistent with the broad plateau regions observed in the mid-wakes of such bodies by Oran et al. [78] and shown in Figure 4-16(a) ($\Phi_b = -27$). As Φ_b increases and/or R_d decreases, the mid-wake takes on a behavior consistent with that of spherical test bodies. Note that in Figure 4-16(a) (larger R_d) the sheath is slower to acquir spherical symmetry ($\Phi_b \cong -50$) than in Figure 4-16(b) (smaller R_d) where a single, above ambient axial ion peak consistent with spherical test body behavior is reached at $\Phi_b \sim -27$. Recall that, from the Oran et al. data, the S-dependence (which should not depend on the sheath behavior) for bodies with square cross-sections was found to be consistent with that found for spherical test bodies in Experiment C.

The above hypothesis is also consistent with the data for the long cylinder. For an infinitely long body, the sheath geometry will not change from that of the body as it increases in thickness. Therefore, no strong R_d dependence is expected for this case. We have already noted above, that the axial ion peak for the long cylinder (Figure 4-17) increases while R_d decreases. This behavior apparently defies any logical explanation and, further, is inconsistent with the R_d-dependence clearly established by the

data of Figure 4-16. This change in the axial ion peak must, therefore, result from variation of S. If so, $[J_p/J_o]$ is inversely proportional to S, which is consistent with the results of Experiment C as well as the Oran et al. data.

The measurements by Oran et al. using a disk showed the peak height to have a weak, inverse dependence on R_o for fixed λ_D (and therefore to be inversely proportional to R_d). This observation is also consistent with the above hypothesis. Although axisymmetric, the disk does not extend downstream and therefore, for large R_d, ions are exposed to the sheath field for a short distance near the disk edge. As R_d decreases, the sheath expands, becomes more spherical, and therefore acts on the deflected ions for a greater distance. For any given Φ_b, as R_d decreases, the peak is drawn in closer to the test body, the deflected ion streams travel a shorter distance and therefore diffuse less, resulting in a slight increase in peak height. This effect is also demonstrated by an increase in Φ_b and it was found that the peak heights of the disks approached that of the sphere at $\phi_b = -4$ volts.

Finally, for spherical test bodies, there will be no geometric change of the sheath regardless of the values of Φ_b and R_d. Opposing effects of increases in annular area (for deflected ions) and the diffusion of the deflected ion streams (both of which depend directly on R_d) result in a very weak R_d-dependence as found in Experiment C.

So far, all measurements have involved geometrically simple bodies (i.e., spheres, disk, plates, cones, or cylinders). A few satellites have approximated these simple geometries. For example, the Ariel I, excluding its booms, was roughly spherical and the Explorer series satellites are cylindrical, similar to the cylindrical bodies used in the above studies. However, in practice, the effects of solar petals and booms must be considered and more advanced spacecraft such as the Apollo series, the Russian Soyuz, and the Space Shuttle are geometrically complex. The data shown in Figures 4-18 and 4-19 for the test bodies shown in Figure 4-20 are intended to provide a very qualitative example of the effects which may occur for geometrically complex bodies.

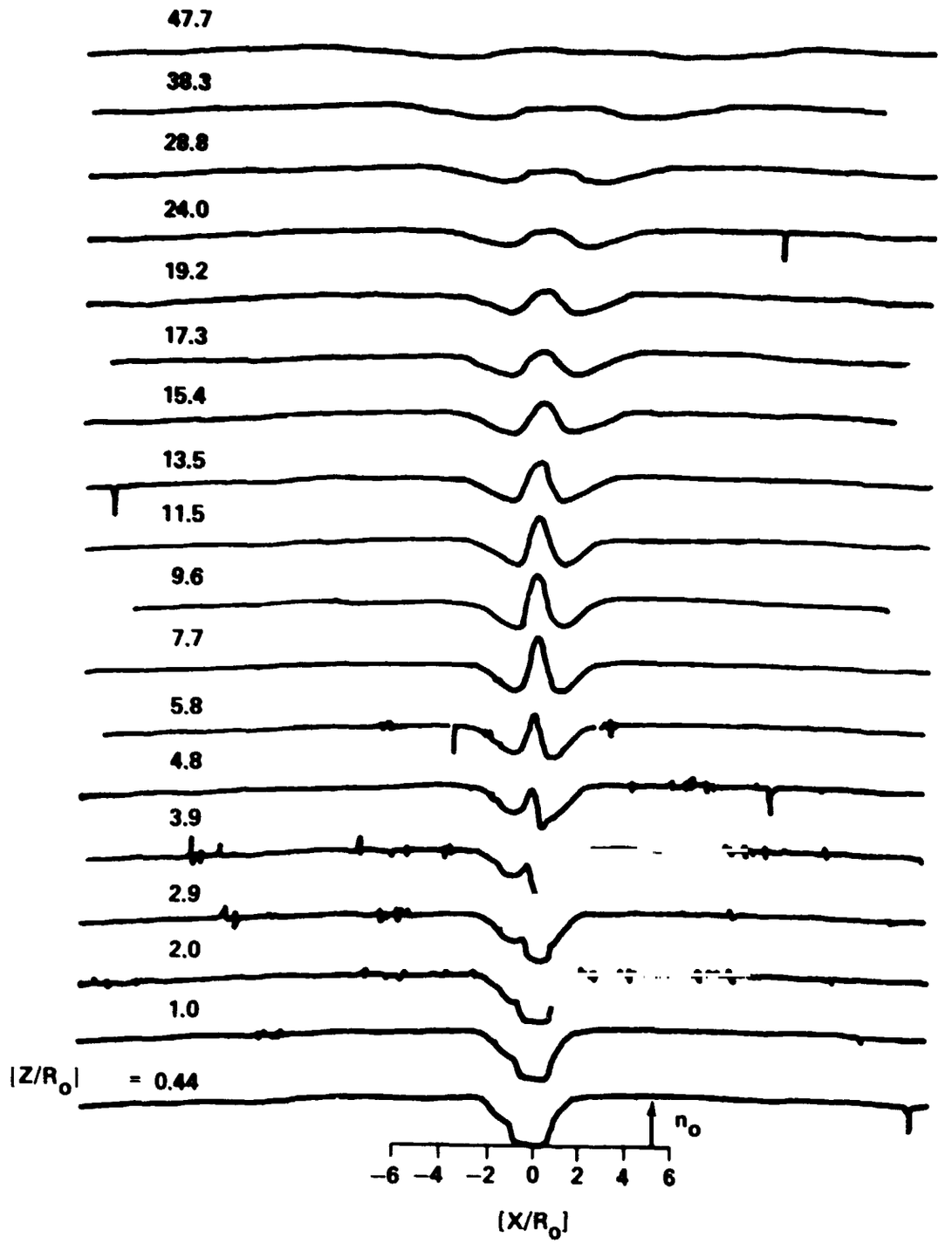

Figure 4-18. Ion current density profiles downstream from the Apollo model. Note that the model was not aligned with the flow direction.

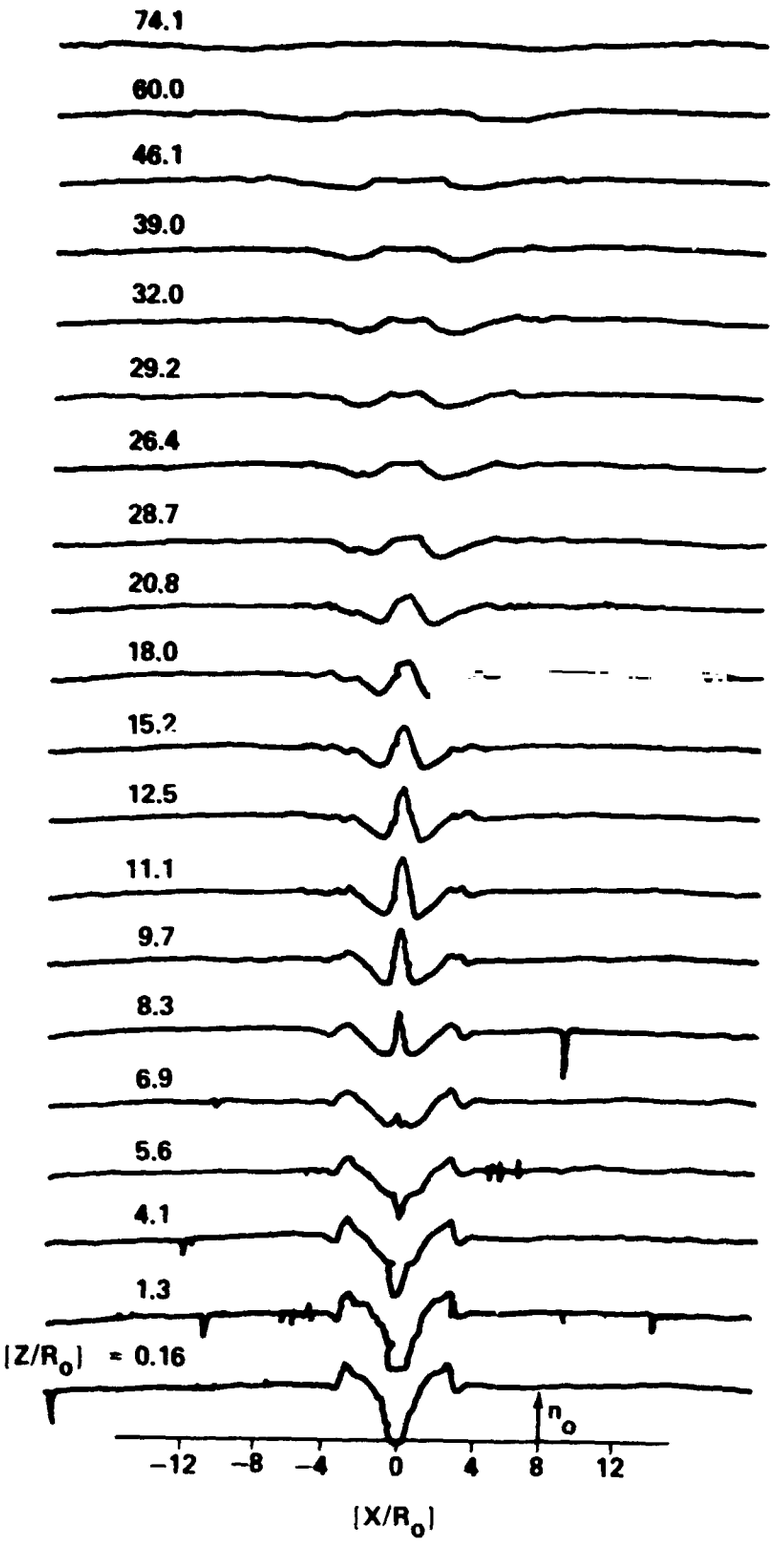

Figure 4-19. Ion current density profiles downstream from the Soyuz model.

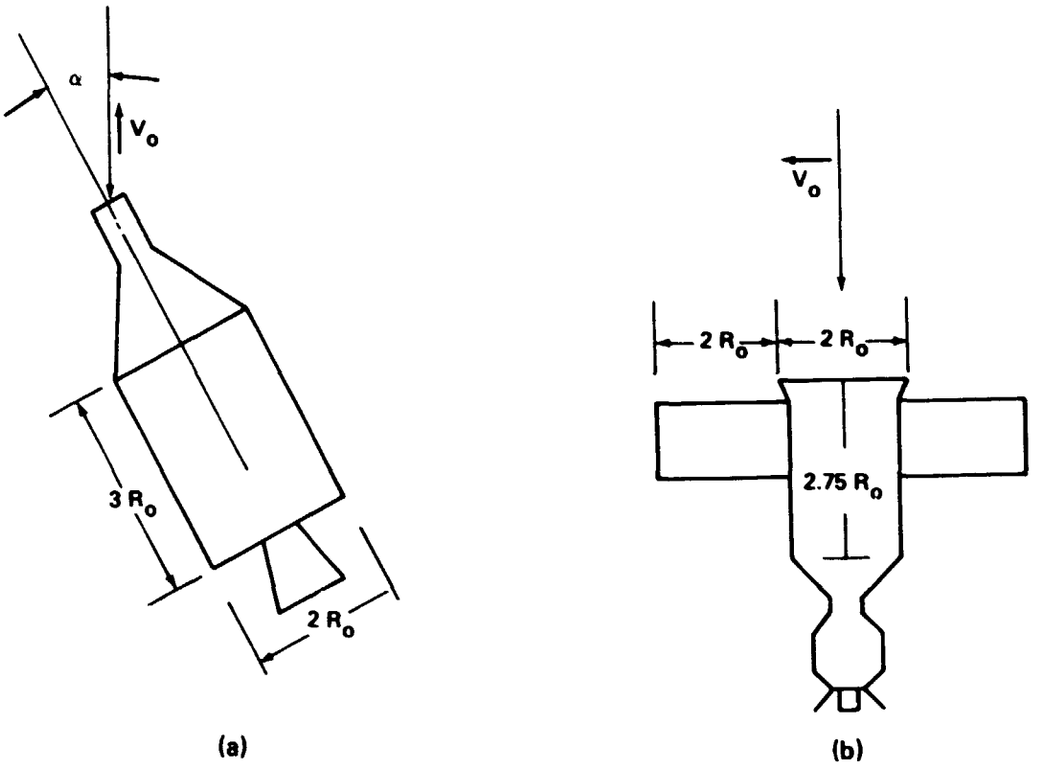

Figure 4-20. Schematic showing geometry and orientation of the Apollo and Soyuz models. Inclination of the Apollo model to the flow direction is 5° to 10°.

The two bodies, shown schematically in Figure 4-20, were scale models of the Apollo and Soyuz spacecraft, with radii of 2.85 and 1.95 cm, respectively. The plasma stream consisted of 20eV N_2^+-ions with 2073°K electrons and a density of $1 \times 10^5/cm^3$. The resulting flow parameters are $S \cong 10.6$, $\Phi_b \cong -3.6$, and $R_d \cong 3$ and 2 for the Apollo and Soyuz models, respectively. The corresponding parameters for these vehicles at 200 km altitude are $S = 7$, $\Phi_b = -5$, and $R_d = 300$ to 500. Because of the discrepancy in the R_d parameters and the fact that extrapolation of results to such high values is not justified on any currently available experimental or theoretical

results, the data must be considered in a very qualitative nature. However, they do demonstrate effects of complex body geometry which may carry over into the spacecraft-ionospheric interaction.

Figure 4-19 shows transverse ion current density profiles in the wake of the Apollo model with its axis of symmetry rotated slightly (5 to 10°) from the flow direction. For all intensive purposes, the Apollo model is approximately a short cylinder, which according to Oran et al. [79] behaves essentially like a sphere when aligned with the flow. However, we observe here that the slight rotation has produced an asymmetry in the wake that persists until it diffuses into the ambient stream at $Z \cong R_o \cong 50$.

In the near wake, this asymmetry manifests itself in the form of an expanded void and a dominant VB stream on the left side. The left side corresponds to the most upstream end of the model and the behavior is, therefore, simply explained by the fact that the wake on this side has roughly $5\ R_o$ greater distance to develop than the right side of the wake, which is behind the most downstream end of the model. It is interesting that the asymmetry carries over into the far wake, where the disturbance extends further on the right side. This would indicate that the right side of the far wake is influenced by the left side of the near wake, consistent with a crossing stream behavior. Therefore, although Experiment A shows that the TV streams form approximately a Mach cone, they must be influenced to some extent by the near wake converging streams. This casts some doubt as to whether they are true collective wave phenomena.

Figure 4-18 shows the wake generated by the Soyuz model. The ion density profiles for this test body are distinctly different from all others previously discussed. The Soyuz itself is approximately a cylinder aligned with the flow direction. However, the effect of the solar panels is very evident.

Since the cross-section the solar panels present to the plasma stream is essentially a line (thickness/λ_D << 1 and length/$\lambda_D \cong 4$) and since, on the basis of this experiment, its Z-dimension is not expected to alter the basic

morphology of its wake, it can be expected to generate a disturbance similar to the long, very small diameter cylinders investigated by Hester and Sonin (Appendix E.1.g, Figure E-11). The small diameter cylinders were found to create a very small (if any) void region and their axial ion peaks to persist several thousand radii downstream. The main body of the Soyuz model, on the other hand, would be expected to produce a disturbance similar to a medium-sized body with axial symmetry; i.e., a significant void region, a mid-wake axial ion peak, and a trailing V structure in the far wake.

These expectations agree with the data in Figure 4-18. Note that no void is observed behind the solar panels, at $Z/R_o \cong 0.16$, which have already produced an axial ion peak while the void created by the main body has not been filled. Progressing downstream, the peaks produced by the solar panels are seen to begin to divide at $[Z/R_o] \cong 8.3$, while the axial ion peak of the main body is just beginning to form. At $[Z/R_o] = 20.8$, the dual solar panel peaks have propagated some distance apart while the axial peak of the main body is just beginning to divide. Further downstream, the main body peak tends to form a trailing V structure.

Apparently, the net disturbance created by this rather complex test body is formed by linear superposition of the component wakes. If this is correct, it will greatly simplify the analysis of the ionospheric disturbances generated by geometrically complex spacecraft, such as the Space Shuttle. The present data are insufficient to properly test the linear supposition hypothesis. However, this can be done by investigating the characteristics of the wake constituents (i.e., the behavior of J_{max}/J_o, the propagation angles of the converging and diverging streams, etc.) and comparing these with the parametric behavior of the independent test body components established above.

It should again be pointed out that due to the large difference in R_d for spacecraft and the laboratory models, the nature of the wakes generated in the two cases may be different. However, the actual thickness of solar panels or the Space Shuttle wings and stabilizers are such as to place them in the R_d

range investigated in laboratory studies where an axial peak was observed. The value of R_d for the Space Shuttle main body, on the other hand, is larger than any value investigated in the laboratory and the disturbance of such large bodies remains unknown. However, even if the interaction in space is significantly different, the effects of mixed wakes, such as linear superposition of the constituent wakes, may remain valid.

5. Experiment E. The purpose of Experiment E is to investigate the overall envelope of the zone of disturbance and its amplitude (excluding the axial ion peak). All of the previous experiments have dealt almost exclusively with some aspect of the behavior of the ion streams deflected by the electric field in the plasma sheath. Here, we will be concerned primarily with the behavior of the rarefaction wave left by the displaced ion streams (see Figure 4-21 for a definition of terms). The scaling parameters have been picked to closely match those of diagnostic instruments in the ionosphere in order to show the type of interference that might occur between instruments [73].

The data presented below were obtained for a spherical body in Case 1, a cylindrical body oriented with its axis of symmetry perpendicular to the flow in Case 2, and a cylindrical body oriented with its axis of symmetry parallel to the flow in Case 3. The data consist of ion current density profiles taken with a Faraday cup with a 0.32 cm diameter, electrically floating aperture. Body diameters, for comparison, were $\geq$ 4 cm.

The details of the three cases are given in Table 4-1. Cases 1 and 2 consist of three sets of data each, corresponding to different values of Φ_b. The ion acoustic Mach number, S, is essentially the same and the Debye ratio, R_d, is similar to within 30 percent for all cases, whereas Φ_b varies greatly. Therefore, the primary difference between the cases will be the geometry of the test bodies and their normalized potentials.

For comparison, the corresponding parameters for the ionosphere at altitudes of 150 and 200 km have also been listed in Table 4-1. The Mach number range is seen to compare favorably with values obtained in the laboratory. The values of λ_D in the laboratory are also similar (within about 50%)

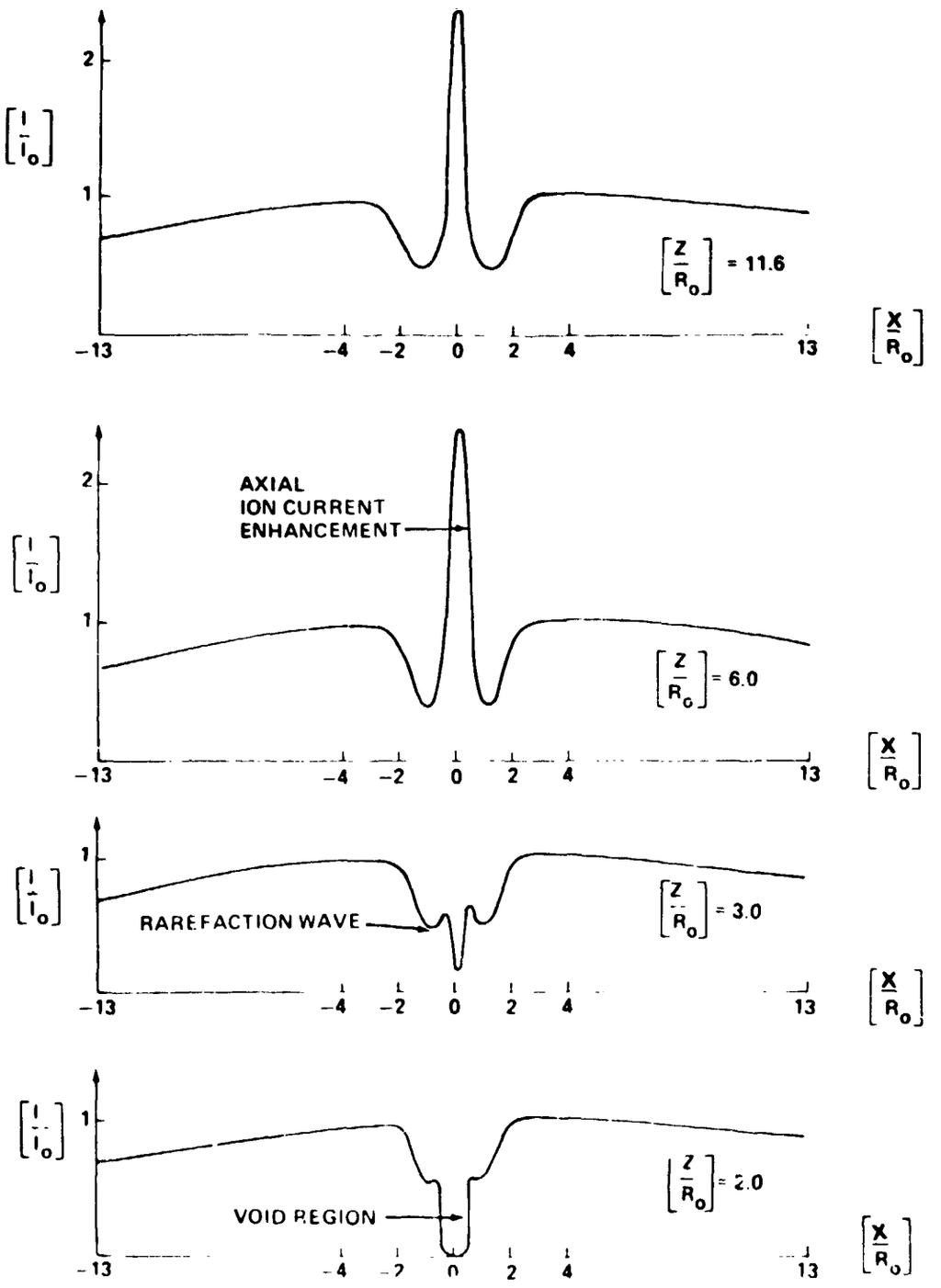

Figure 4-21. Ion current density profiles downstream from a conducting sphere for $R_d = 5.7$, $S = 10.6$, and $\Phi_b = -14$ (Case I), after Stone et al. [86].

TABLE 4-1. EXPERIMENT BODY AND PLASMA PARAMETERS AFTER STONE et al. [73].

Case No.	Body			Plasma Stream				Dimensionless Parameters		
	Geometry	Orientation (Flow = 0°)	Rel. Bias (Volts)	E* (eV)	T_e (°K)	$\eta_{i,e}$ (cm^{-3})	λ_D* (cm)	$S = \left[\frac{E}{T\ (in eV)}\right]^{1/2}$	$R_D^* = [R_o/\lambda_D]$	$\Phi_b^* = (e\phi_B/kT_e)$
1	Sphere	—	-2.6 -4.6 -8.6	20.4	2116	2.1×10^5	0.7	10.6	5.7	-14 -25 -47
2	Cylinder	90°	-2.6 -4.6 -8.6	20.4	2116	2.1×10^5	0.7	10.6	5.7	-14 -25 -47
3	Cylinder	0°	-0.69	20	2110	2×10^5	0.71	10.5	4.0	-3.8
Equivalent Ionospheric Conditions			at 150 km				0.4	10	1.5	~-5
			at 200 km				0.5	6.5	3	~-5

* Where E = Energy corresponding to mean ion velocity ($1/2\ m_i\ v_o^2$)

λ_D = Debye length

R_o = Effective body radius

ϕ_B = Body potential relative to local plasma potential

to those in space. By scaling the body size to obtain the same values of R_d, we find that the laboratory experiment roughly simulates bodies of 3 to 6 cm in diameter. The geometries of the three cases and the corresponding scale sizes in the ionosphere are therefore appropriate for commonly used diagnostic probes such as spherical and planar ion traps, retarding potential analyzers, and spherical Langmuir probes.

In considering the data from the above experiment in the context of its application to future Spacelab experiments, two aspects of the problem of probe interference will be addressed: (1) the spatial extent of the zone of disturbed plasma around an instrument and (2) the possible nature and magnitude of disturbances within this zone.

The spatial extent of the disturbed zone is determined primarily by two factors: the initial width of the disturbance at the widest or "critical" cross-section of the body and the rate of growth as it moves downstream from the body. The initial width consists of the width (or effective diameter) of the body ($2R_o$) and the thickness or width of the plasma sheath on each side ($2X$). The unknown factor is the sheath thickness X, which is determined by subtracting $2R_o$ from the initial width of the disturbance, W_o; i.e., $X = (W_o - 2R_o)/2$. W_o is found from the experimentally determined width at a number of points downstream by a linear extension back to the position of the critical or largest cross-section of the body. For the sphere of Case 1 and the perpendicularly oriented cylinder of Case 2 this occurs $1R_o$ upstream from the rear surface. For the parallel cylinder of Case 3 it occurs at the leading surface, $2R_o$ from the rear. In analyzing the data, the location of the critical cross-section is always taken to be the origin for the Z-axis, where Z is the distance downstream.

Figure 4-22 shows the sheath thickness, determined in the previous method and normalized by the Debye length, X/λ_D, plotted as a function of the normalized body potential divided by the ion acoustic Mach number, S. The large error bars result from the extrapolation process used to find the initial width of the disturbance W_o. This figure shows roughly how the sheath

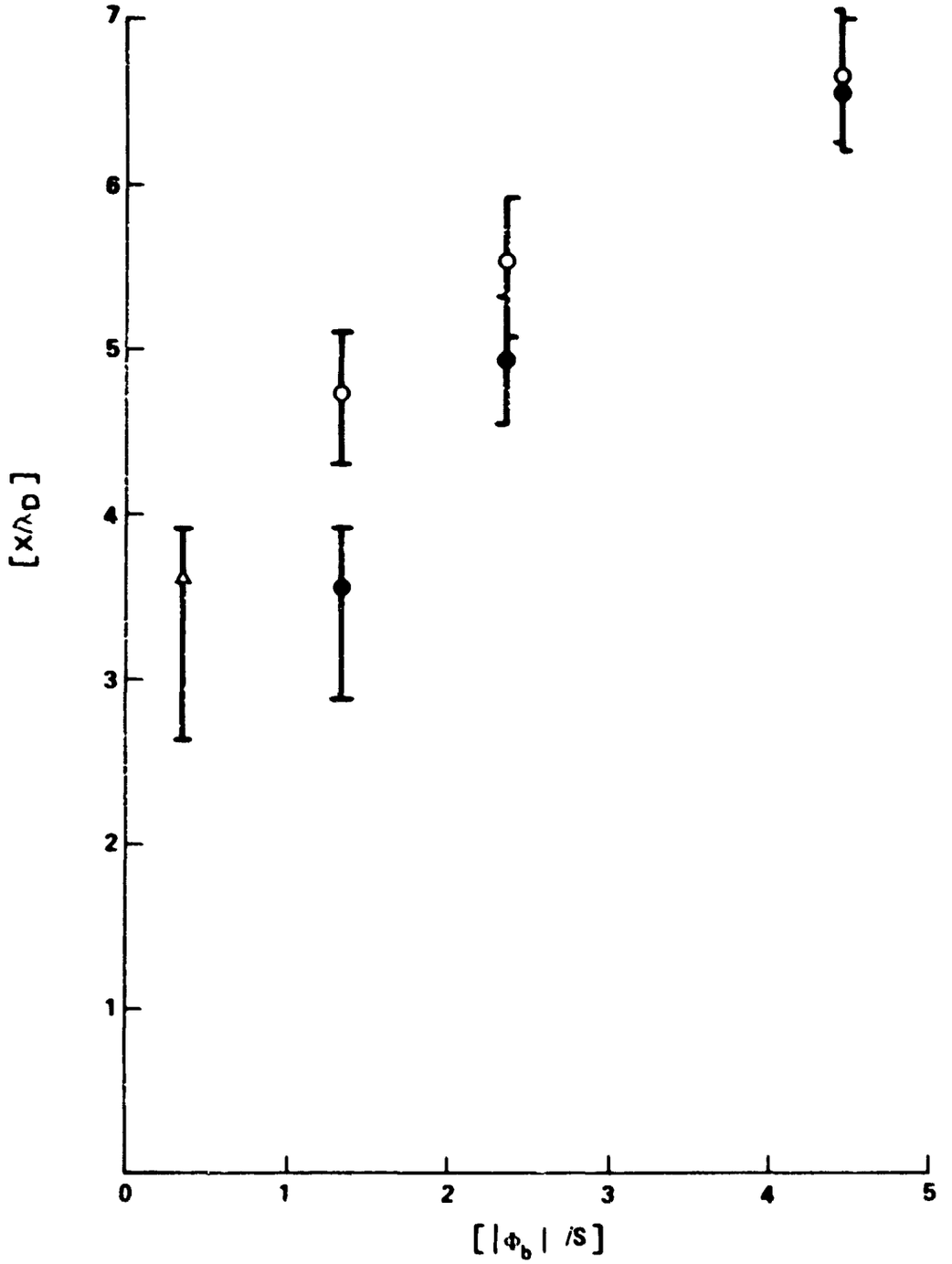

Figure 4-22. Dependence of the sheath width at the critical cross-section of the test body (X/λ_D) on (Φ_b/S). Open circles represent data for a sphere, solid circles for a 1 cylinde , and open triangle a parallel cylinder, after Stone et al. [73].

thickness can be expected to increase in terms of λ_D as a function of increasing $|\Phi_b|$'S. It should be pointed out that while, in the past, low-altitude satellites have generally experienced $|\Phi_b|$ values of less than 10, large potentials may be encountered on the Space Shuttle as a result of its size (and hence large $\vec{V} \times \vec{B}$ emf's), differential charging and nonidealized surface conductivities, and the operation of other experiments which may have an impact on spacecraft charging.

Figure 4-23 shows the rate at which the disturbed zone grows as a function of distance downstream. This is determined by subtracting the initial width W_o from the width measured at a given position downstream, $W(Z)$, or $\Delta W = [W(Z) - W_o]/2$. This shows that when the growth is normalized by R_o and multiplied by the ion Mach number, the dependence is a linear function of (Z/R_o). This indicates that the rarefaction wave propagates outward from the initial disturbance at approximately the ion acoustic speed and the boundaries of the disturbance are defined by a Mach angle $\theta_S = \sin^{-1}(1/S)$. Further, since all seven sets of data obtained over a wide range of $|\Phi_b|$ fall on the same line, Figure 4-23 indicates that the disturbance growth rate is independent of body potential (although the initial size is a function of $|\Phi_b|$, as shown by Figure 4-22). This is in general agreement with theoretical predictions by Martin [13] for wakes of small bodies.

We will now address the possible nature and magnitude of the disturbance to provide some indication of the severity of the impact on measurements made within such a disturbed zone. Figure 4-24 shows the ion current density in the trough of the rarefaction wave, normalized by the local ambient current density, as a function of distance downstream from the body. Interference from other structures in the wake, such as the current enhancement on the wake axis seen in Figure 4-21, makes detailed analysis of the wave depth questionable. However, Figure 4-24 serves to point out quite adequately that at rather large distances downstream the most extensive structure of the disturbed zone, the rarefaction wave, produces reductions of up to a factor of 3 in the measured current density.

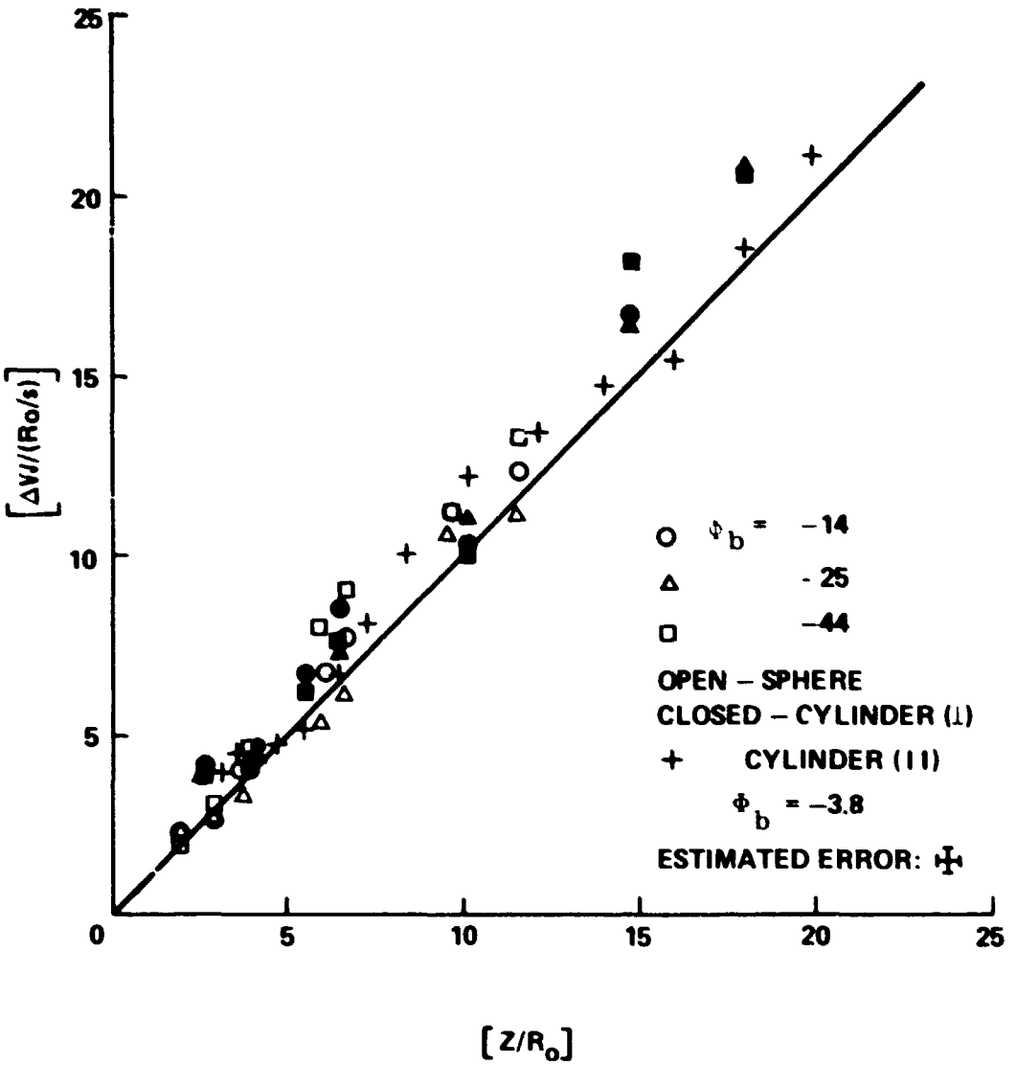

Figure 4-23. Growth of the extent of the disturbed zone ΔW, normalized by R_o/S with normalized distance downstream, after Stone et al. [73].

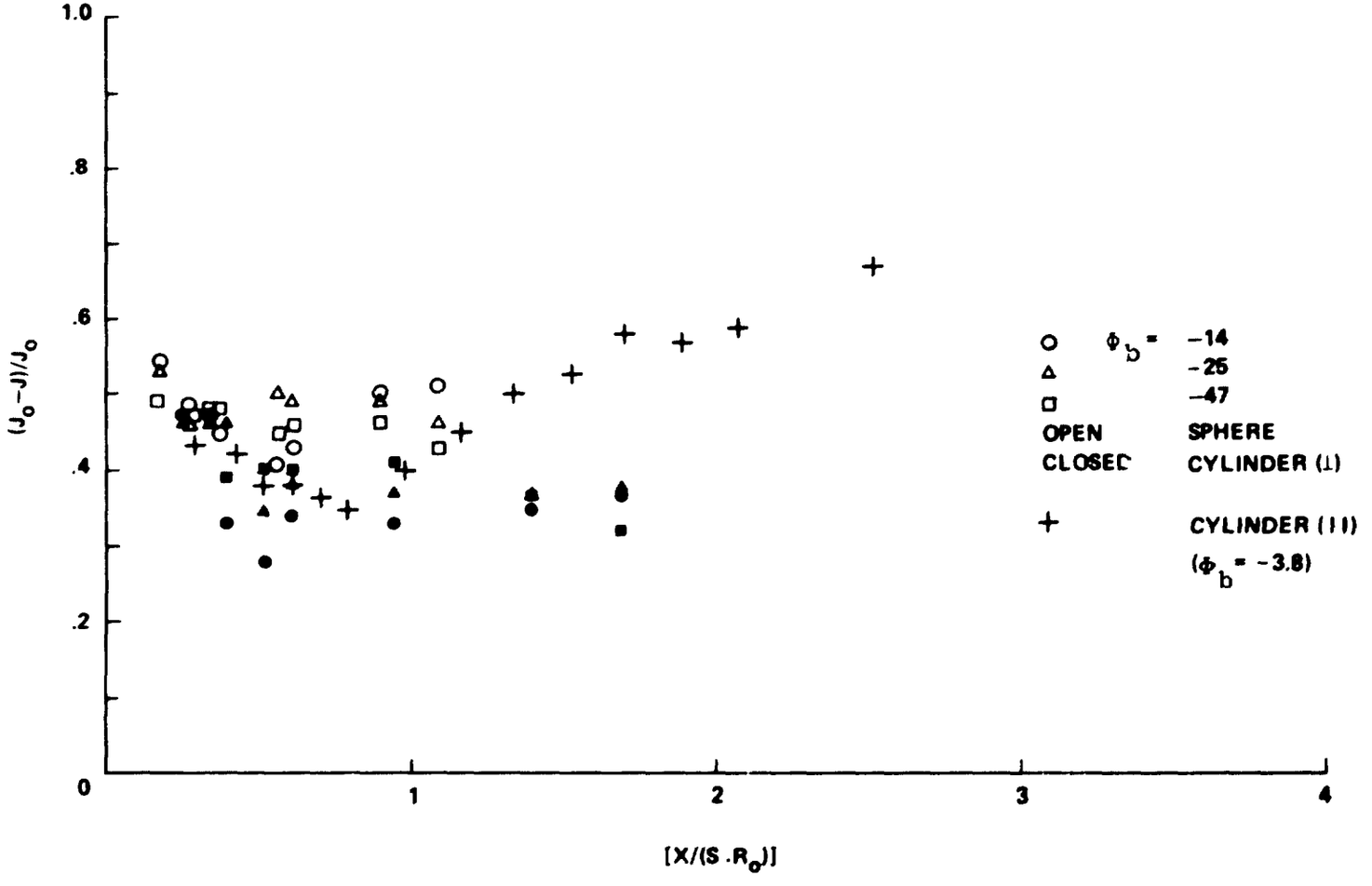

Figure 4-24. Normalized ion current depletion in the trough of the rarefaction wave as a function of axial distance, after Stone et al. [7[illegible].

As was previously stated, laboratory simulation experiments dealing with the perturbations created by instruments or instrument assemblies to be used on large space platforms such as Spacelab are inherently incomplete and inexact, and the limitations of such studies should be remembered. Specifically, in the present work, no attempt was made to scale the temperature ratio (T_e/T_i) properly. However, if fairly large potentials are anticipated in the neighborhood of instruments (as may be the case for Space Shuttle/Spacelab experiments), the above limitation may not be crucial, as indicated by the experimental results by Fournier and Pigache (Appendix E.1.i) and the theoretical predictions by Fournier (Appendix C.6). (It should be emphasized that the experiments discussed here have application only to possible interference between instruments and do not apply to the disturbance created by the Space Shuttle itself. Presumably, instrument packages will be removed from the disturbed plasma zone around the orbiter.) On the other hand, the potential contribution of such laboratory investigations to the planning of future low-energy particle measurements is clearly shown. By carrying out parametric investigations in the laboratory it should be possible to assess the magnitude and extent of the perturbations created by various instruments. This will be helpful in avoiding the possibility of locating other instruments in the zone of disturbed plasma created by a given probe. This possibility is expected to be an important consideration in the design of multiprobe ensembles, such as subsatellites and boom-mounted or ejectable diagnostic packages to be used on future Space Shuttle/Spacelab missions.

B. Electron Temperature Measurements in the Near-Wake Region

The purpose of this experiment is to investigate the behavior of the temperature of electrons in the near-wake region to better understand the in situ observations of T_e-enhancements in the wake of the Explorer 31 satellite by Samir and Wrenn [80] and Troy et al. [42] and in the wake of the Gemini-10 capsule and Agena wakes by Troy et al. [43] (Appendix D.2.b).

The data for this experiment were obtained in the MSFC No. 2 facility downstream from an 8 cm diameter conducting sphere in an Ar^+-plasma. The measurements were made with a stainless steel, cylindrical Langmuir probe 1.5 cm long and 0.1 cm in diameter. The probe surface was bombarded with a high energy ion stream before each set of measurements was taken to remove surface contamination. In addition, the characteristics of the probe were checked before and after each run to insure that no hysteresis developed (i.e., the effect of nonuniform potential on the probe collecting surface).

It is recognized that the electron distribution in the near-wake region may not be Maxwellian. However, the T_e values shown were obtained by fitting a straight line to a plot of $\ell n\,(I_e)$ - vs - ϕ_p in the conventional manner (Appendix F). The point at which the data break away from the line is taken to occur at the plasma potential, ϕ_o. The length of the linear portion of the data is taken as a test for a Maxwellian distribution. Typically, the data were linear over 1.5 decades for both ambient and wake measurements. (The current collected by the probe was amplified in the wake region to compensate for the decrease in current level.) Experimental error for T_e-determination was $\leq 20\%$.

Figure 4-25 shows an example of a set of transverse $[T_e(\text{wake})/T_{eo}]$-profiles at various distances downstream from the center of a body at floating potential ($\phi_b \cong -0.3$ volt). Note that $T_{eo} = T_e$ (freestream). Enhancements of T_e significantly above the experimental error are shown in the near wake, downstream to $Z/R_o \leq 3.5$ and out to $X/R_o \cong \pm 1$. Since $S \cong 7$ for these data, the point at which the T_e enhancement vanishes coincides roughly with the point at which the converging VB streams cross the Z-axis and fill the ion void. Further, the transverse extent of $X/R_o \cong \pm 1$ roughly coincides with the radial boundaries of the ion void. It therefore appears that the T_e enhancement is confined to the ion void in the near-wake region. It is also interesting that the magnitude of the T_e enhancement (~ 2) is of the same order as the maximum enhancements observed in ionospheric wakes (Appendix D.2.b).

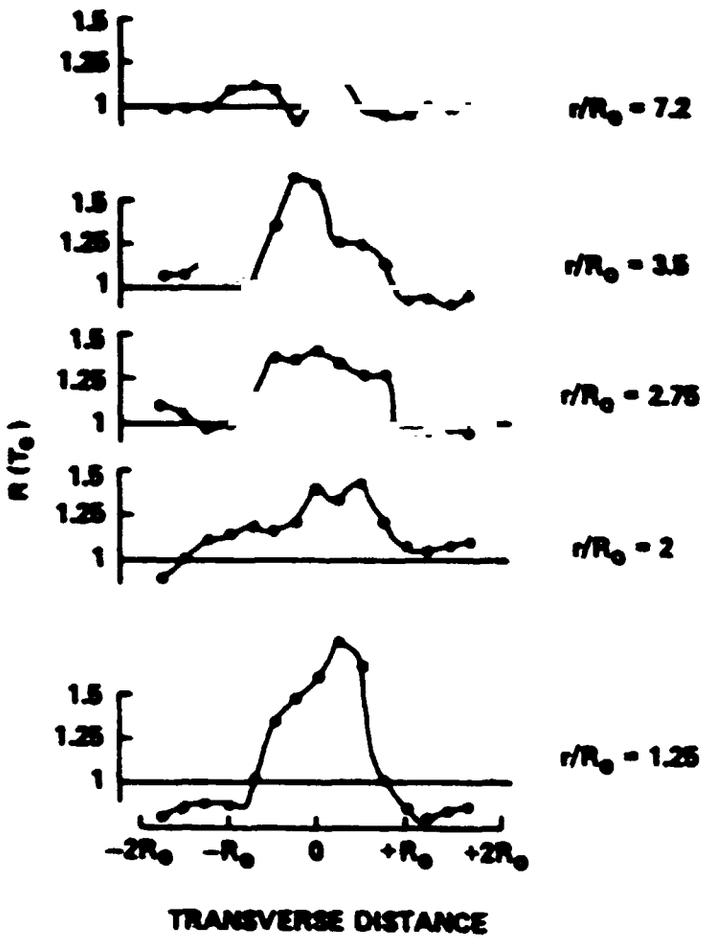

Figure 4-25. Transverse profiles of $[T_e(\text{wake})/T_{eo}]$ downstream from a conducting sphere for $T_{eo} \cong 1200°K$, $n_{io} \cong 7.5 \times 10^4/cm^3$, $E_i \cong 5.3$ eV, $P = 4 \times 10^{-6}$ torr, after Samir et al. [77].

Transverse $[T_e(\text{wake})/T_{eo}]$ profiles were also taken at a fixed distance downstream ($Z/R_o \cong 1.3$) for chamber pressures, ranging from 4×10^{-6} to 2.5×10^{-5} torr, to determine the possible effects of slow, charge exchange ions (Chapter III.E). These data, shown in Figure 4-26, indicate an inverse dependence of $[T_e(\text{wake})/T_{eo}]$ on chamber pressure, and hence slow ion concentration, n_s/n_f. The dependence is obviously nonlinear, increasing more rapidly with P at lower pressures, but $[T_e(\text{wake})/T_{eo}]$ appears to be monotonically increasing with decreasing pressure (or n_s/n_f) over the range studied. This would seem to support the hypothesis of Samir and Wrenn that a potential well in the near wake may be involved [80]. Slow ions have no preferred direction and are, as a result, not swept out by the test body as are the plasma stream ions. They tend to diffuse into the ion void region and neutralize the negative space charge created there; or if a potential well were created (where the space charge potential is more negative than Φ_b), the slow ions would tend to decrease or eliminate it. Therefore, if the T_e enhancement in the wake is produced by a potential well (through either wave-particle interactions within the well or selective three-dimensional screening of the incoming electrons), an inverse dependence on the slow ion concentration (and hence chamber pressure) would be expected, as shown in Figure 4-26.

Evidence for the existence of a potential well in the near wake has been found theoretically by Fournier [23], Call [12], Taylor [20] Maslennikov and Sigov [17], and Parker [21] (Appendix C) and experimentally by Illiano and Storey [57] (Appendix E). Although the Illiano-Storey data revealed no valid T_e enhancement, it should be noted that the measurements were taken with a button collector which occupied a small area on the equator of a conducting spherical test body which could be rotated. It appears that both the button collector and the test body were swept and current was collected either from the button collector, alone, or the entire sphere. This would not correctly reproduce the conditions of the Ariel I and Explorer 31 surface probes, where the spacecraft remained at floating potential. Therefore, while the observation of a potential well is significant, the lack of a T_e enhancement is by no means conclusive.

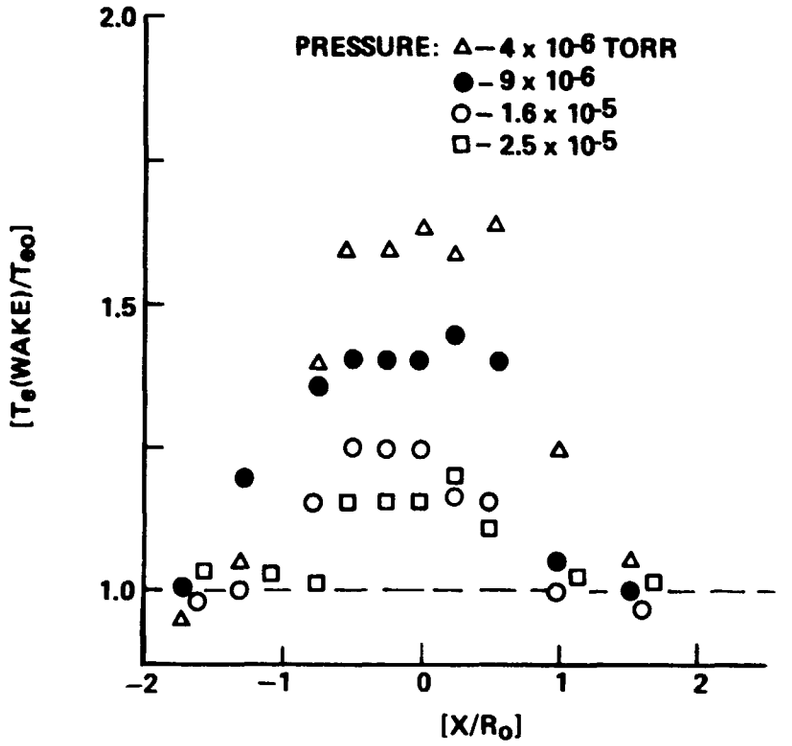

Figure 4-26. Transverse profiles of $[T_e(\text{wake})/T_{eo}]$ at $Z/R_o = 1.3$ downstream from a conducting sphere at several chamber pressures for $T_e = 800°K$, $n_{io} \cong 5 \times 10^4/cm^3$, $E_i = 4.5$ eV, and $\phi_s \cong +0.3$ V, after Oran et al. [76].

In Figure 4-27, axial profiles of the $[T_e(\text{wake})/T_{eo}]$ ratio are plotted for three sets of conditions. In Figure 4-27(a), the plasma stream conditions and chamber pressure are similar to those of Figure 4-26. Note that the T_e enhancement becomes greater near the test body as Φ_b becomes increasingly negative, but that its extent downstream decreases. This, again, is consistent with the behavior of the ion void region which is shortened for highly negative Φ_b as a result of VB stream focusing. In Figures 4-27(b) and (c), the main differences from part (a) are an increase in T_{eo} (approximately a factor of 2)

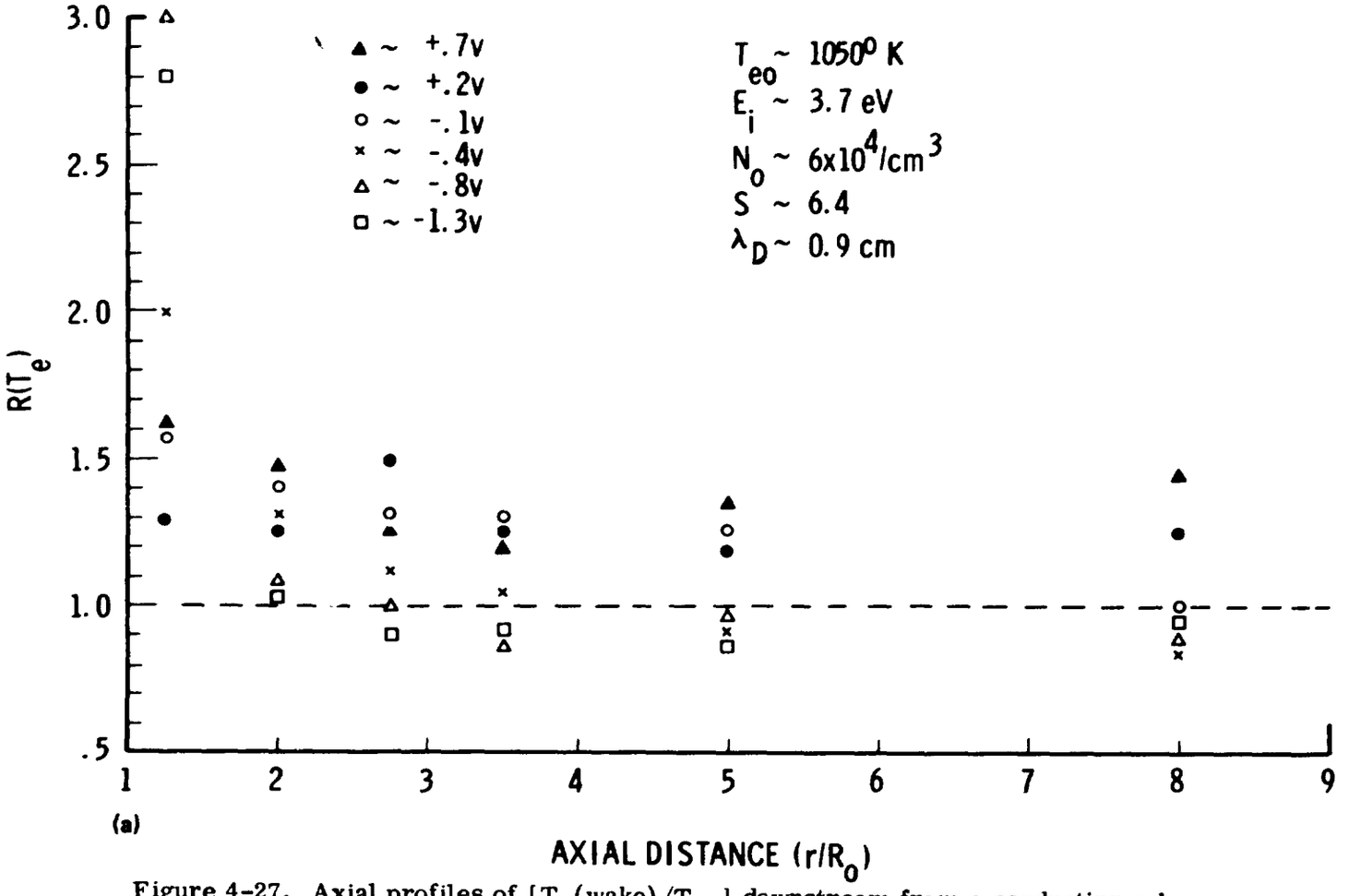

Figure 4-27. Axial profiles of $[T_e(\text{wake})/T_{eo}]$ downstream from a conducting sphere, after Oran et al. [98].

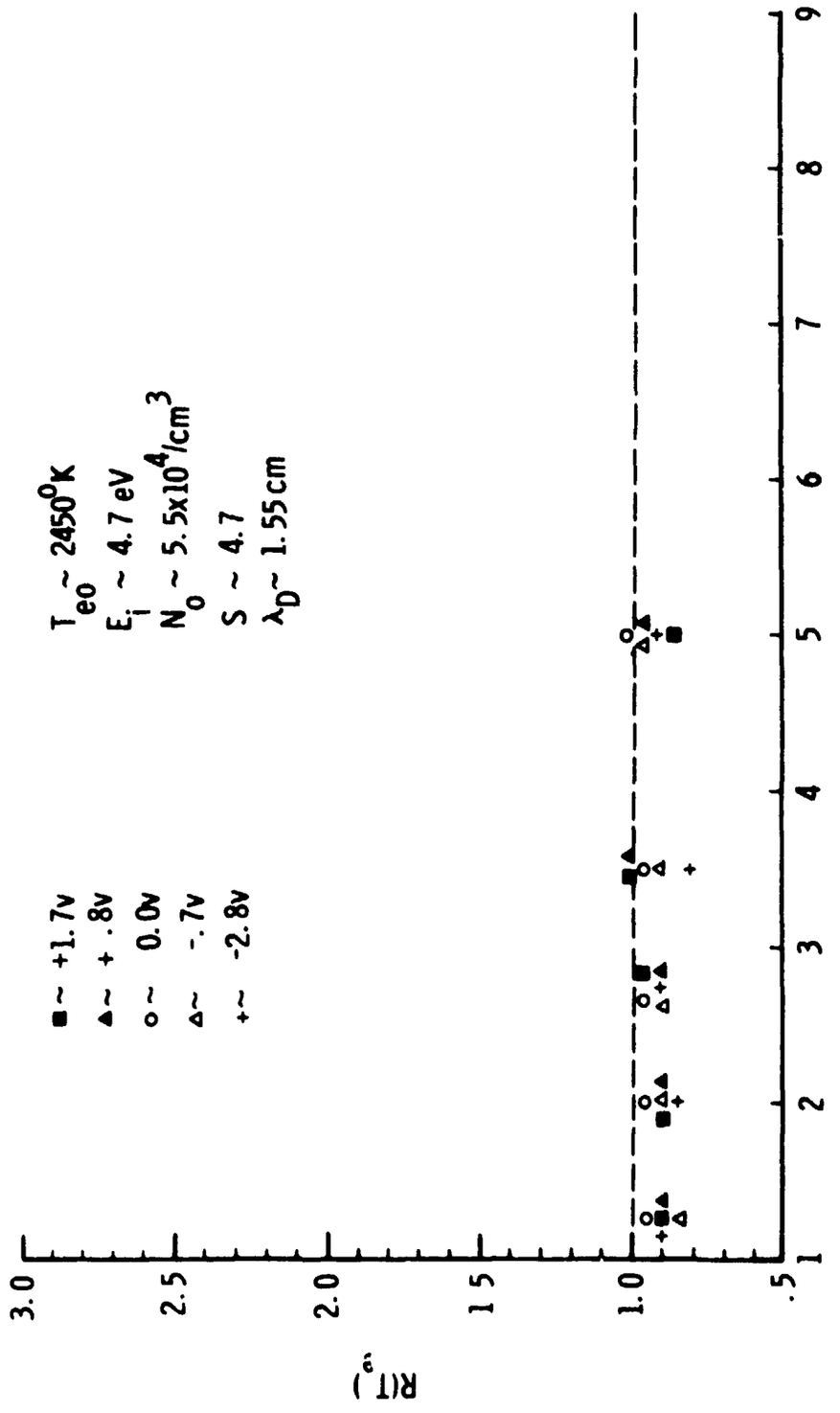

Figure 4-27. (Continued)

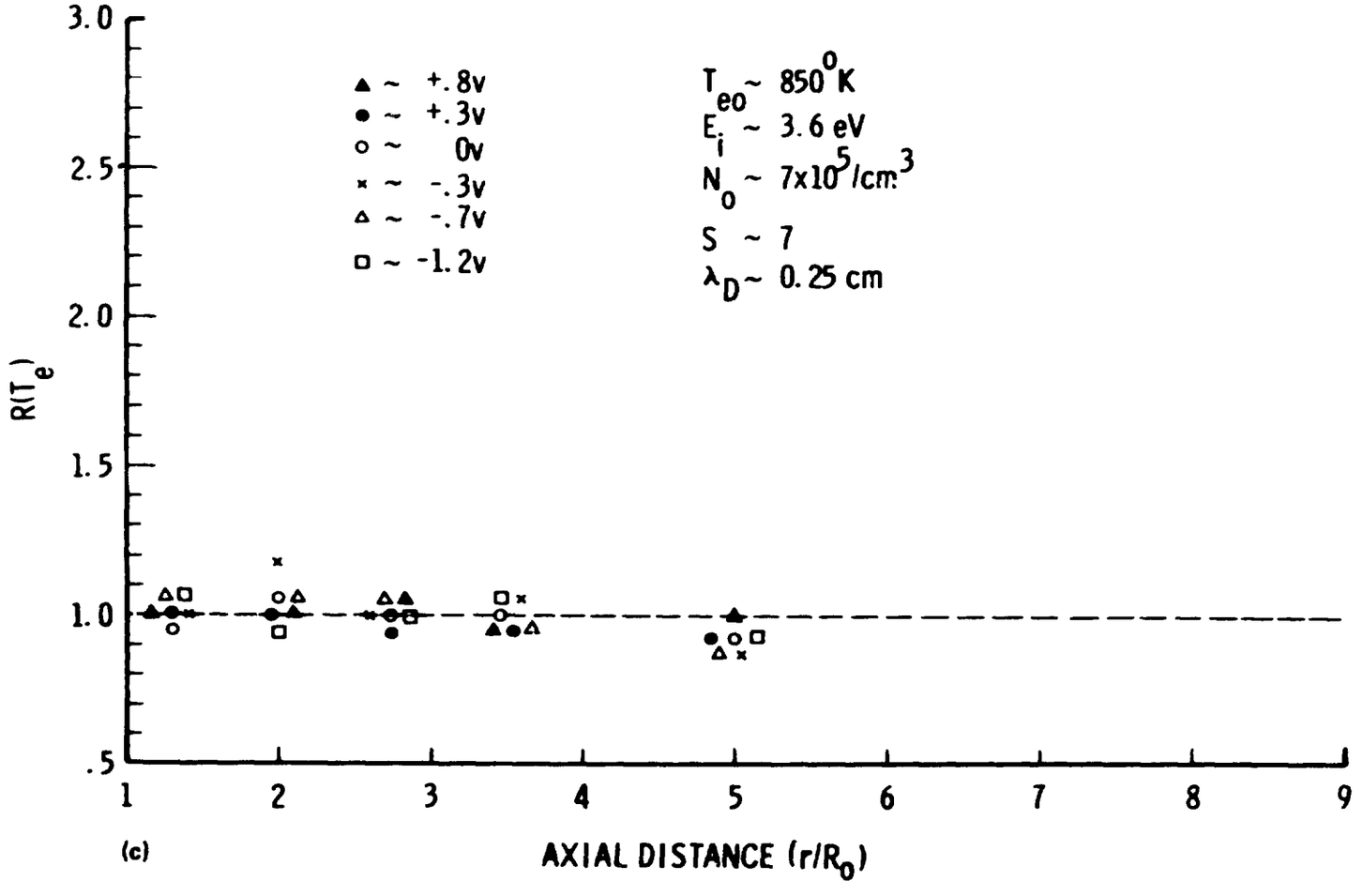

Figure 4-27. (Concluded)

and an increase in n_{io} (approximately an order of magnitude), respectively. In neither case is there any evidence of a T_e enhancement, indicating the enhancement to vanish with increasing T_{eo} and n_{io}.

Although not known when this work originally was published, Gurevich et al. [32] have theoretically studied the expansion of a mixed ion composition plasma into a vacuum (directly analogous to expansion of the ambient plasma stream into the near-wake, ion-void region). In this study, it was found that the electric field set up by the ambipolar diffusion process accelerated light ions to higher velocities than the heavy ion constituents, therefore initiating essentially a two-stream instability when the ratios of light and heavy ion concentrations were within certain limits (i.e., obviously two streams cannot exist when the percentage of heavy ions is 0 or 100).

Based on the Gurevich et al. results, one might expect a similar two-stream instability to occur as a result of the fast, plasma stream ion passing through the slow charge exchange ion population. Further, the results of Gurevich et al. should indicate the n_s/n_f ranges in which this instability can occur. Figure 4-28 shows a plot of the $[T_e(\text{wake})/T_{eo}]$ values shown in Figure 4-26 at $x = 0$ plotted against n_s/n_f values corresponding to the indicated pressure (Chapter III, Figure 3-8). The dashed line represents values of oscillation amplitude, predicted by Gurevich et al., multiplied by its frequency. (We assume that this product should be proportional to any effect of the waves on the particle populations.) Note that the occurrence of instabilities and their dependence on n_s/n_f corresponds roughly to the behavior of $[T_e(\text{wake})/T_{eo}]$ observed by Oran et al.

We can therefore postulate that (1) the two-stream instability occurred throughout the plasma stream, creating a small population of electrons with an enhanced temperature, (2) that the concentration of the new electron population was small so that they were masked by the ambient electrons when measurements were made in the freestream, and (3) that they were observed in the wake due to the negative space change potential, which screened out

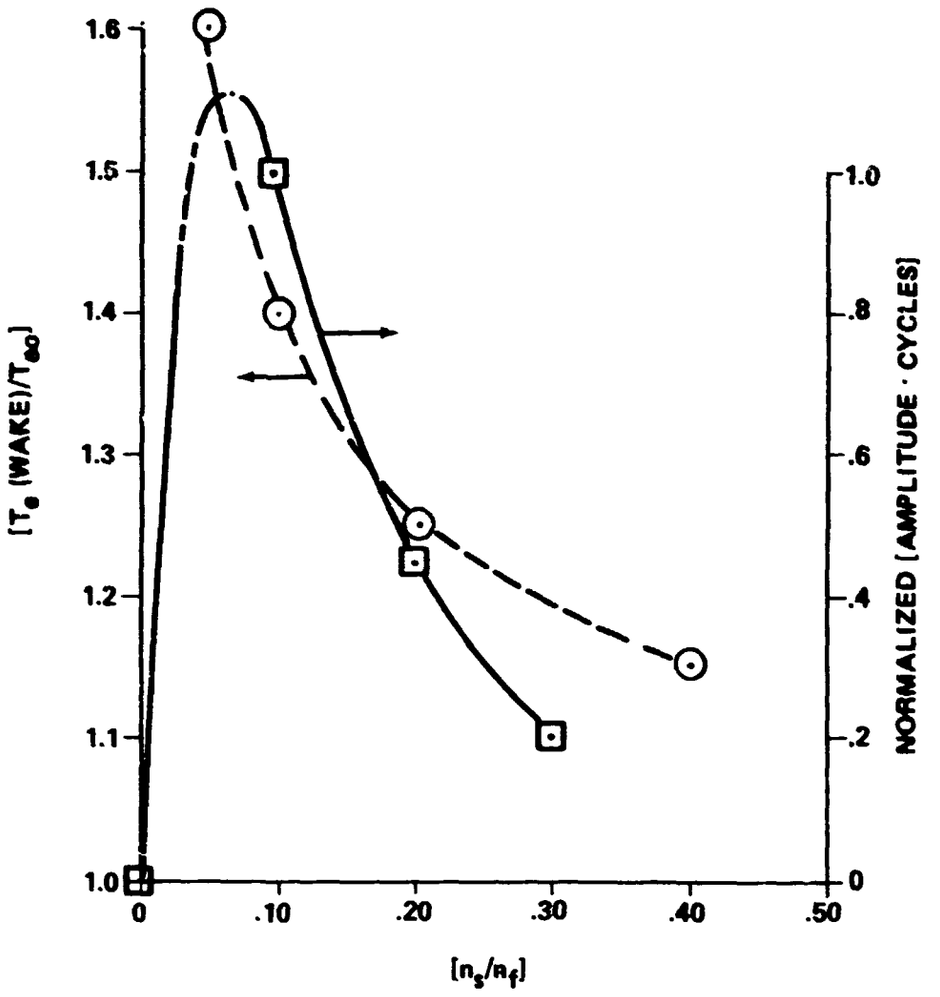

Figure 4-28. Comparison of the variation of $[T_e(\text{wake})/T_{eo}]$ with n_s/n_f as determined by Oran et al. [73], with growth of instability (amplitude × frequency) predicted by Gurevich et al. [32].

most of the ambient electrons, leaving a higher relative concentration of the new electron population which was more energetic and therefore more effectively penetrated the potential barrier.

If this hypothesis is correct, it detracts from the Oran et al. results in their application to in situ observations of the T_e enhancement since the enhancement will have been produced throughout the chamber but observed

only in the wake. Such an effect clearly does not apply to the ionosphere since there is no corresponding slow ion population moving with orbiting spacecraft. However, in this context, the Oran et al. results take on a new importance in that they (1) point out an important electron energizing mechanism which is operative in plasma chambers, and (2) they indicate that the Gurevich et al. effect does occur and, therefore, point the way to a new set of experiments in which mixed composition plasma streams are studied.

The validity of the above hypothesis seems to be supported by the fact that no clear T_e enhancements have ever been observed in the MSFC No. 1 facility (where there is no significant slow ion population), despite extensive and carefully conducted measurements. Further, it helps explain the inverse dependence of the T_e enhancement on T_{eo}, shown in Figure 4-27. If the ambient plasma-stream electrons are indeed heated by a wave-particle interaction, then it is expected that the more energetic the initial electron population, the less dramatic will be the degree of enhancement. This seems reasonable, since the response of the freestream electrons to the wave-generated electric fields should be inversely proportional to their kinetic energy and hence the temperature of the initial population.

C. Vector Ion Flux Measurements in the Near- and Mid-Wake Regions

All of the previous experiments have involved only scalar measurements; i.e., the magnitudes of J_i, J_e, T_e, E_i, and ϕ_s. In these experiments the entire flow field was measured and the flow direction inferred from systematic variations in the ion current density profiles. The limitations of this technique are well known. In the near-wake region where ion streams may be deflected through large angles, Faraday cup and RPA measurements of J_i and E_i will suffer a considerable error since they measure only the component of ion velocity normal to the probe face. Further, recall that it was not possible in previous experiments to distinguish between ion streams and true plasma

waves, created by collective interacti , since no information was available concerning the flow direction of the ions forming the observed wave-like structures. In the present experiment, the Differential Ion Flux Probe (DIFP) [71] will be used to obtain point-by-point measurements of both the ion flux magnitude (current density) and direction in the near- and mid-wake regions of a long conducting cylindrical test body 2.50 cm in diameter (Appendix G for a more detailed instrument description).

To indicate the positions of the vector ion flux measurements relative to the previously studied structure in the plasma flow field, ion current density profiles, such as those described in previous experiments, were measured simultaneously. To simplify the experimental procedure, a set of measurements for different values of Φ_b were obtained with the test body fixed at each axial position. An example set of these profiles obtained at $Z/R_o \cong 11$ are shown in Figure 4-29. The scaling parameters for these data are $R_d \cong 1$ and $S \sim 7.5$. The test body potential, Φ_b, is varied and its values are indicated in the figure. Most of the DIFP data discussed in the remainder of this section apply to this set of profiles, although consistent results were obtained at several other axial positions. (In passing, it is interesting to note that the effect of Φ_b becoming increasingly negative is similar to a transition along the Z-axis; i.e., at $\Phi_b = -2.3$ the ion void is observed, while at $\Phi_b = -9.4$ the axial ion peak appears, and at $\Phi_b = -146$ the diverging streams of the far wake are seen.)

An example of the DIFP data is shown in Figure 4-30. These data were taken at a single position sufficiently off to the left of the Z-axis that at $\Phi_b = -2.3$, the DIFP was beyond the zone of disturbance and essentially monitored the ambient plasma stream. However, as Φ_b became more negative, the zone of disturbance grew so that at $\Phi_b = -16.6$, the axial peak began to affect the measurements which show two streams; the slightly deflected ambient stream from the left and a second stream deflected across the Z-axis from the right side of the body. These data will be discussed in detail later in this section.

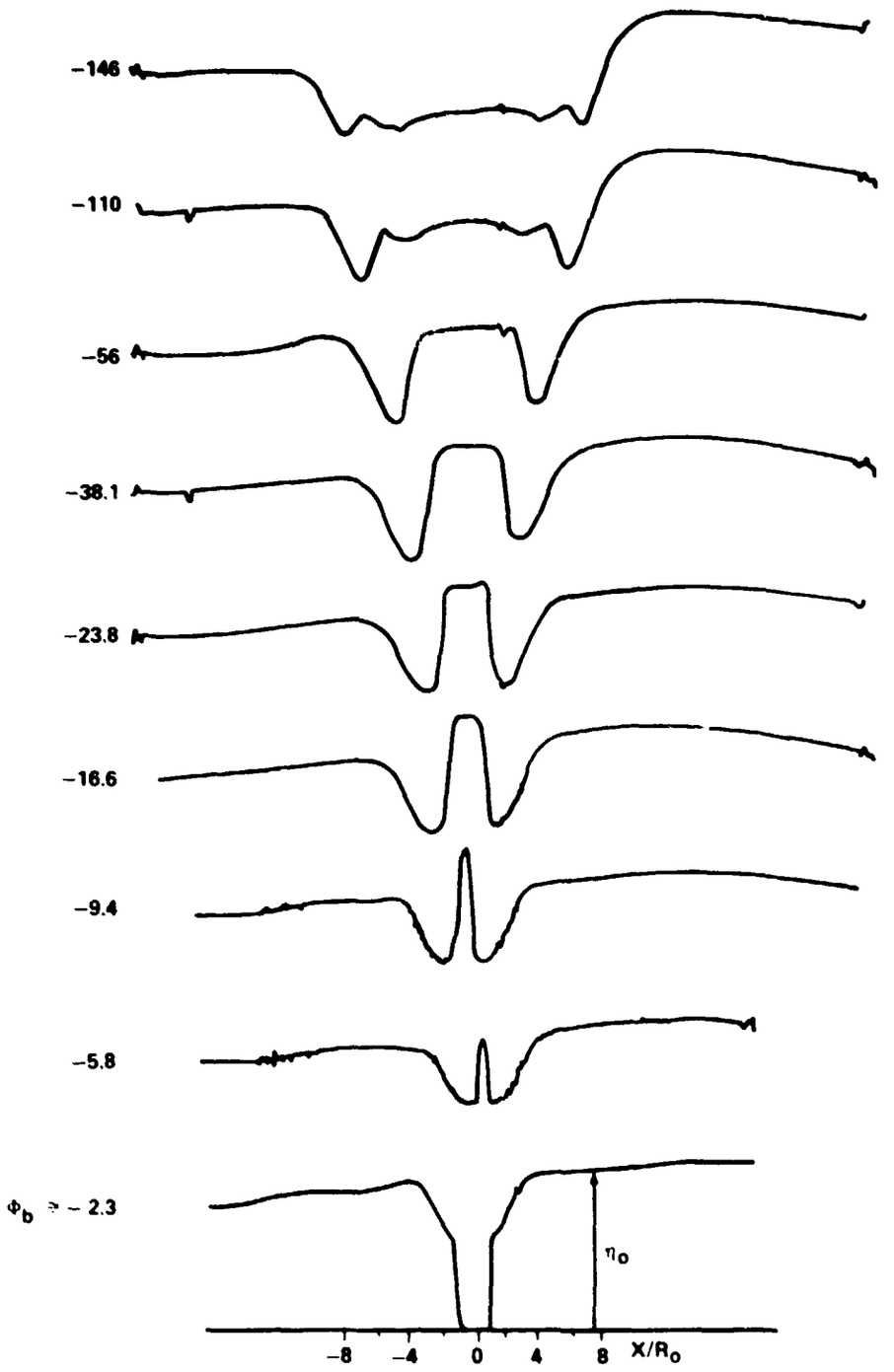

Figure 4-29. Ion current density profiles downstream from a long conducting cylinder for $R_d \approx 1$, $S \sim 7.5$, $2 R_o \sim 11$, and Φ_b as indicated. After Stone [99].

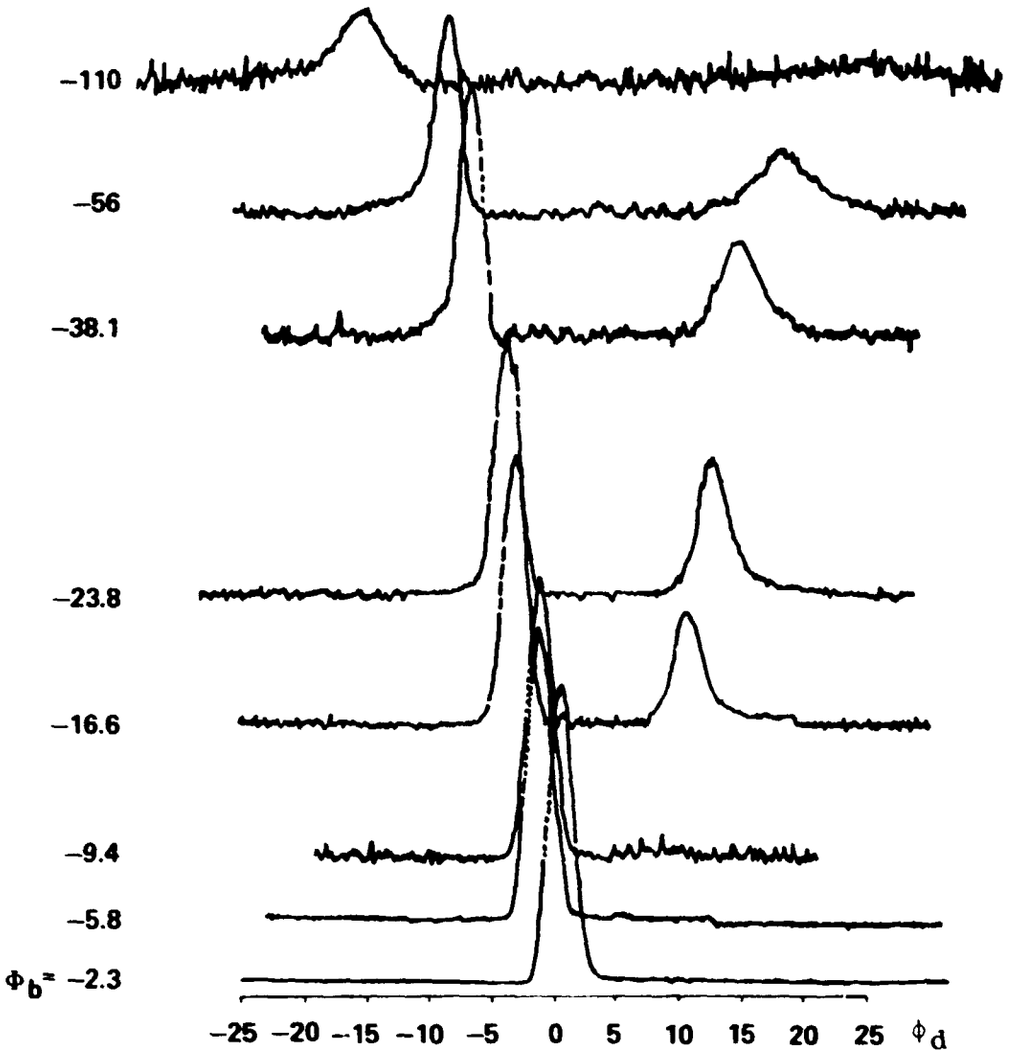

Figure 4-30. Example DIFP raw data. Profiles show current collected as a function of deflection voltage with no retarding potential, $J(\phi_d, \phi_r = 0)$. Data obtained off axis for the conditions of Figure 4-29 with Φ_b as indicated.
After Stone [99].

Figure 4-31(a) shows the axial variation of $[J/J_o]$ with Φ_b. The points connected by the curve were obtained from Figure 4-29. The squares represent values obtained from DIFP data by summing the amplitudes of all deflection peaks observed at a given value of Φ_b. These values are normalized by the peak height observed in the freestream. [The magnitude of the

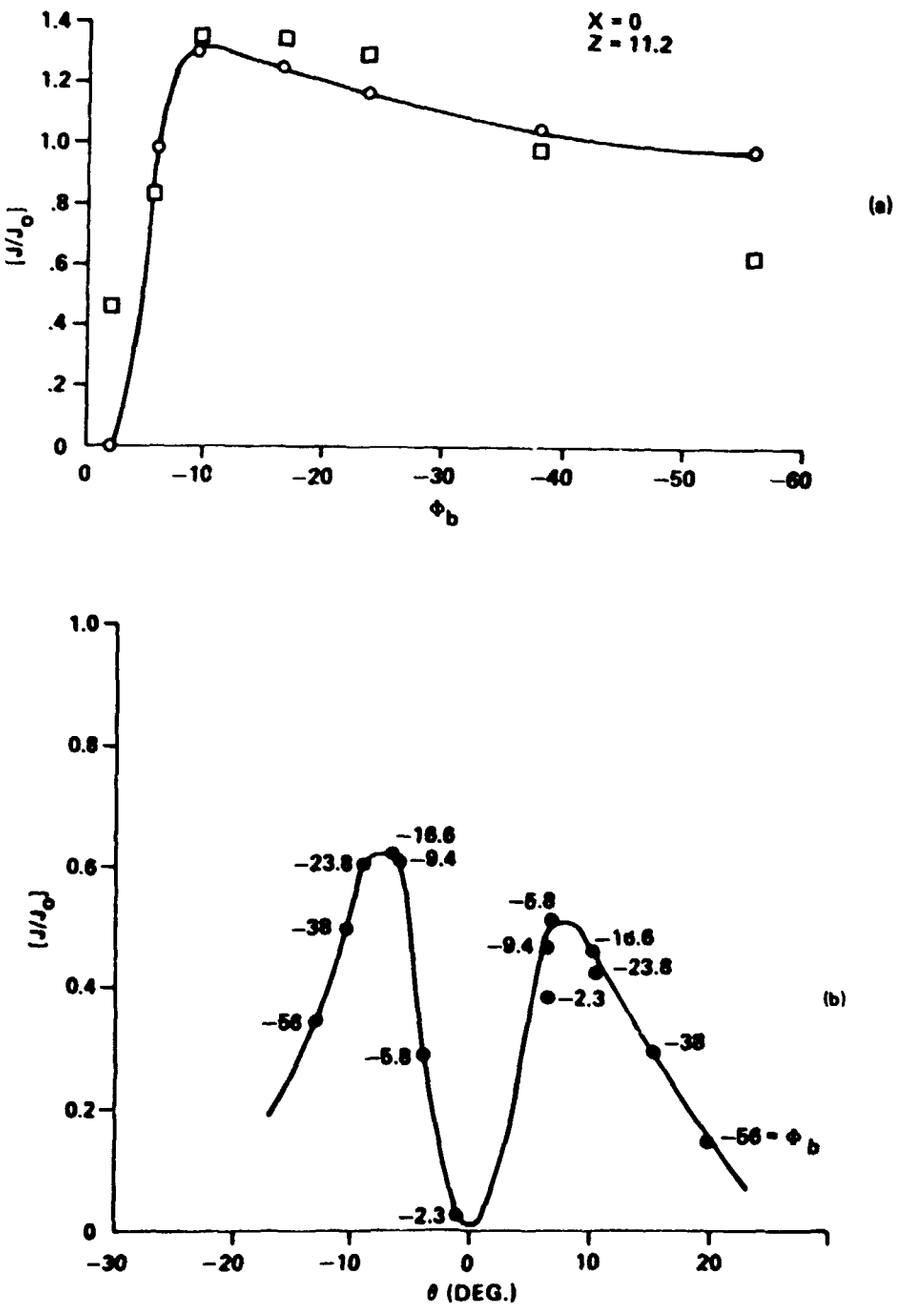

Figure 4-31. DIFP data showing: (a) normalized sum of peak currents obtained on axis at Z/R_o = 11.2 for various values of Φ_b, □, compared with Faraday cup data, O, from Figure 4-29; and (b) the angle and amplitudes of the peaks corresponding to the data in (a).
After Stone [99].

peak heights for the various Φ_b-values are shown in Figure 4-31(b)]. Note that the profiles in Figure 4-31(a) obtained from the Faraday cup and the DIFP agree reasonably well. The excess height of the point determined by the DIFP at $\Phi_b = -2.3$ is due to a displacement of the DIFP off the Z-axis. The point at $\Phi_b = -56$ is too low because the deflection peaks observed by the DIFP in this region became broad. Since, strictly speaking, the area under the deflection curves gives the total current and not the peak height, the use of peak height is a reasonably good approximation of total current density only when the peak is relatively narrow.

The data, given in Figure 4-31(b), show the dependence of the deflection peak heights on the angle of incidence for various values of Φ_b. These measurements were made on the wake axis at $Z/R_o \cong 11$. These data show, conclusively, the converging stream nature of the mid-wake axial ion peak; which could only be surmised previously from the scalar, current density measurements. Note that a slight (1 to 2°) mechanical misalignment added to a 4° inclination of the plasma stream, due to deflection by the geomagnetic field, caused the DIFP to be near the boundary of the void region for $\Phi_b = -2.3$. This is evident by the offset and the disparity between the two peaks obtained at this potential. For all other values of Φ_b, two streams were observed; one arriving from the left side of the body and one from the right. Further, the angles of the peaks to the probe face normal are significant and increase with increasingly negative Φ_b, in agreement with an expanding sheath. Both the left and right incident peaks rise in amplitude from near zero at $\Phi_b = -2.3$ to a maximum near $\Phi_b = -7.5$ and they decrease in amplitude with further decreases in Φ_b. This is the expected behavior of the converging VB streams observed in Experiment A of Section A.

Figure 4-32 shows the spatial variation of the incidence angle and amplitude of the ion streams corresponding to the current density profile obtained for $\Phi_b = -56$ (Figure 4-29). The locations at which the observations were made along the X-axis, relative to the current density profile, are shown in Figure 4-32(a).

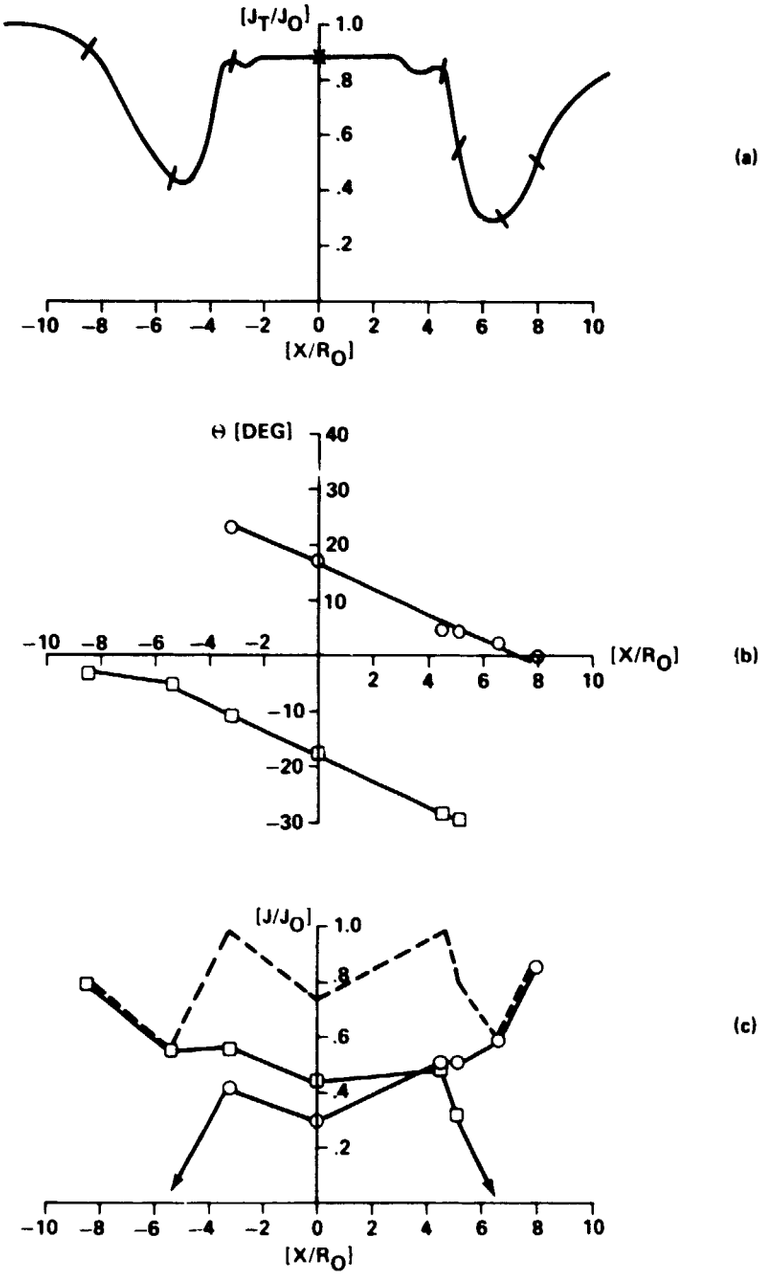

Figure 4-32. Transverse variation of θ and $[J_{peak}/J_o]$ for $Z/R_o \cong 11$, $\Phi_b = -56$: (a) current density profile from Figure 4-29; (b) angle of incidence, θ, variation for two converging streams; and (c) peak height variation.
After Stone [99].

Figure 4-32(b) shows the angle of incidence of the ion streams at various positions on the X-axis. (The angles in this figure have been corrected for the ambient stream inclination.) Figure 4-32(c) shows the corresponding peak amplitudes normalized by the freestream current density. Again, the two converging streams are apparent. Notice the almost linear variation in angle of the streams, beginning with zero deflection near either side of the disturbed zone (where the peak amplitude is near ambient) and increasing in magnitude until the deflected streams vanish on the opposite side of the Z-axis. (Note that this is not equivalent to following a single stream line.) The points at which the deflected streams vanish should correspond to the leading edges of the VB streams observed in Experiment A of Section A.

Note that there is no evidence of any ion stream deflection in the data of Figure 4-32 other than within the plasma sheath. The observed angular dependence can be explained fully in terms of the simple stream line pattern predicted by Call (Figure C-7(a) of Appendix C).

The variation of the incident angle of the converging ion streams along the Z-axis is shown in Figure 4-33. Since the angles of the left and right incident streams are approximately equal, their average value is plotted, rather than the two separate angles, which vary slightly due to small errors in the placement of the DIFP. The solid curve shows the variation of the geometric angle, while the average ion stream incidence angles are shown by data points for a number of Φ_b values at each axial position. Also shown is the ion acoustic Mach angle.

For $\Phi_b \leq -16.6$, all ion stream angles observed are greater than the geometric angle and are therefore explained by simple ion deflection within the plasma sheath and possibly some additional deflection (also toward the Z-axis) by the space charge potential in the ion void region. However, it is interesting to note the extent to which the plasma sheath grows as Φ_b becomes increasingly negative. The single point obtained at $Z/R_o \cong 11$ for $\Phi_b = -146$ implies that deflection occurred at approximately 6 radii from the center of the cylinder, based on a simple geometric extension of the angle

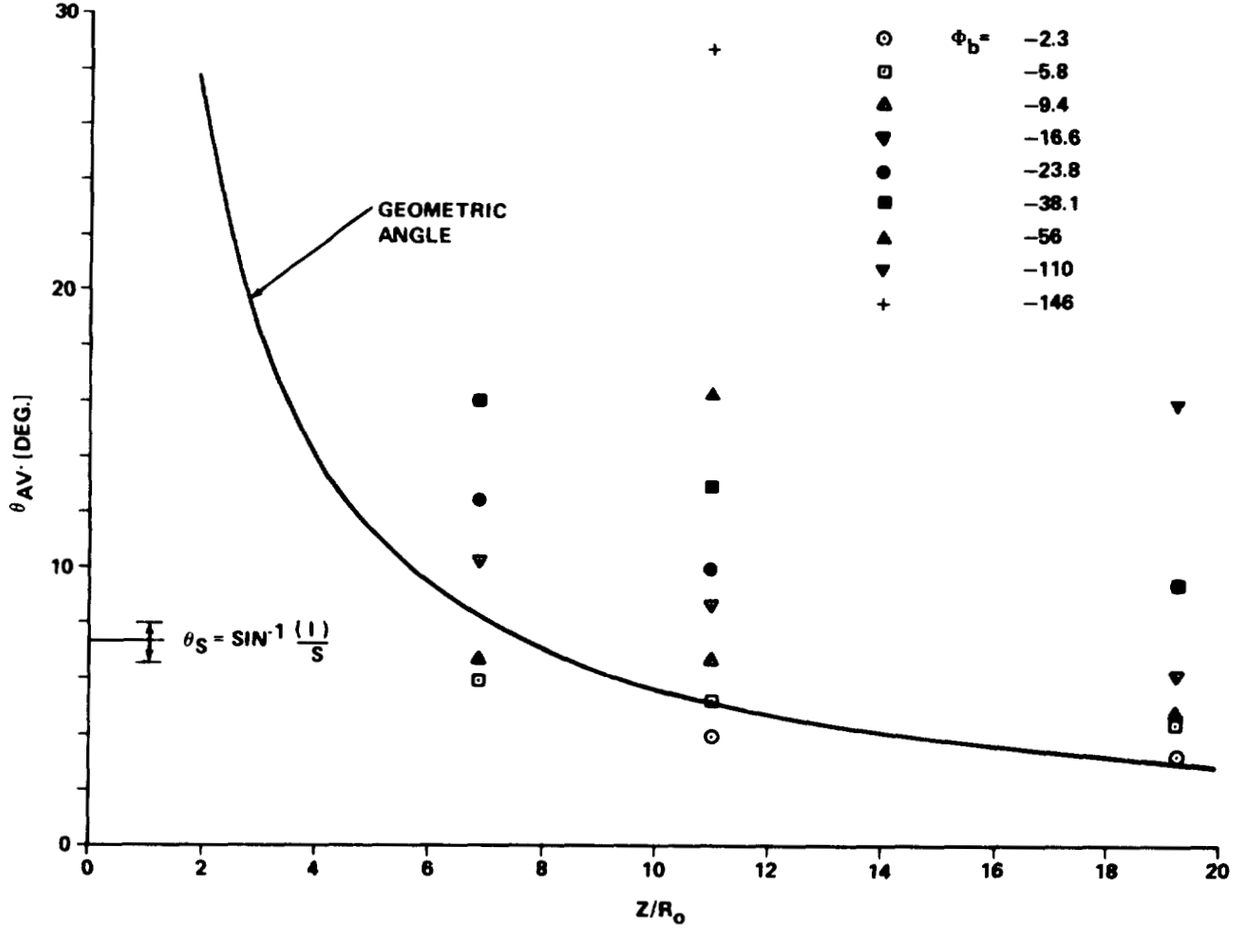

Figure 4-33. Variation of θ along Z-axis for the conditions of Figure 4-29. Solid line is the geometric angle subtended by the test body radius. After Stone [99].

of incidence. (Additional deflection by the negative space charge potential in the ion void region would tend to decrease this value, but this should be small compared with the deflection produced in the sheath for such a highly negative test body.)

As the body becomes less negative ($\Phi_b > -16.6$), several angles of incidence are observed to be less than the geometric angle; specifically, the points for $\Phi_b = -9.4$ and -5.8 at $Z/R_o \cong 6.9$ and $\Phi_b = -2.3$ at $Z/R_o \cong 11$. The stream lines corresponding to these angles of incidence cannot be explained in terms of the simple monotonic deflections predicted by Call in Figure C-7(a) of Appendix C. Although the present data are much too coarse to determine the detailed behavior of these stream lines, since any attractive force on the ions within the plasma sheath would result in angles greater than the geometric angle, it is definitely established that the stream lines undergo additional deflections some distance downstream from the body and are therefore of the type predicted by Call (Figure C-8(a) of Appendix C) and Maslennikov and Sigov (Figure C-2 of Appendix C).

The downstream deflection of ion streams was hypothesized by Hester and Sonin to explain the systematic variations they observed in ion current density profiles (Appendix E.1.g). However, with this exception, multiple deflected streams have received little attention and have never been directly observed before. The fact that they are found at this position only for small Φ_b values is consistent with the explanation given by Hester and Sonin; i.e., that the component of ion velocity normal to the Z-axis decreases with distance downstream and that the ions will be repelled from the Z-axis by the positive space charge potential associated with the axial ion peak when $1/2\, m_i V_\perp^2 = e\phi_s$ (Appendix E.1.g).

Angles of incidence smaller than the geometric angle have been consistently observed for a number of cases for small values of Φ_b. As predicted by Martin, this effect would be expected to be more pronounced for spherical, or at least axisymmetric, test bodies (Appendix C.7). However, the present DIFP is capable of measuring angles only in the plane normal to

its slit axis, whereas an instrument capable of measuring angles in orthogonal planes is needed to study axisymmetric problems (see Appendix G for more details).

Figure 4-34 shows the average angle of incidence of plasma streams on the wake axis as a function of ϕ_b and Z/R_o for two additional cases (not related to Figure 4-29, although the same test body was used). For Case I, where $S \cong 15.8$, note that the angles are consistently less (the ion streams are more rigid) than for Case II, where $S \cong 9.4$. All curves, obtained at fixed values of Z/R_o for large Φ_b, appear to have a $\Phi_b^{1/2}$ dependence, while those obtained for small values of Φ_b have an approximate linear dependence on Φ_b. Note also, that for most of these data and that of Figure 4-33, the angle of incidence depends strongly on Φ_b. However, far downstream (represented only by one case in Figure 4-34; i.e., $Z/R_o = 47.7$ for Case II), the angle does not vary with Φ_b. This is consistent with the results of Experiment A in Section A, where the VB streams were found to depend strongly on Φ_b while the far-wake TV streams were independent of the test body potential.

Figure 4-35(a) shows the ion stream incident angles, θ, as a function of Φ_b, while Figure 4-35(b) shows the stream line amplitudes (deflection peak heights) as a function of θ. These plots correspond to the raw data shown in Figure 4-30. A schematic of the indicated behavior of the stream lines is shown in Figure 4-36. Note that the DIFP, offset to the left of the Z-axis, measures essentially the slightly deflected freestream from the left at $\Phi_b = -2.3$, while no ions are found to be deflected across the Z-axis at this position downstream by this small negative body potential. At $\Phi_b = -16.8$, the sheath has expanded, resulting in a larger ion void which approaches ambient conditions at the position of the DIFP on the left side of the body. Ions are just beginning to be deflected across the Z-axis and into the DIFP from the right side of the body. At $\Phi_b = -23.8$, the void has expanded farther on the left, resulting in a further decrease in the left peak amplitude while the peak of VB stream, deflected across the Z-axis, is now approaching the DIFP. At higher values of Φ_b, the void continues to expand on the left and the left peak continues to diminish while the peak of the VB stream is deflected beyond the DIFP and therefore the right peak diminishes as well (see also Figure 4-30).

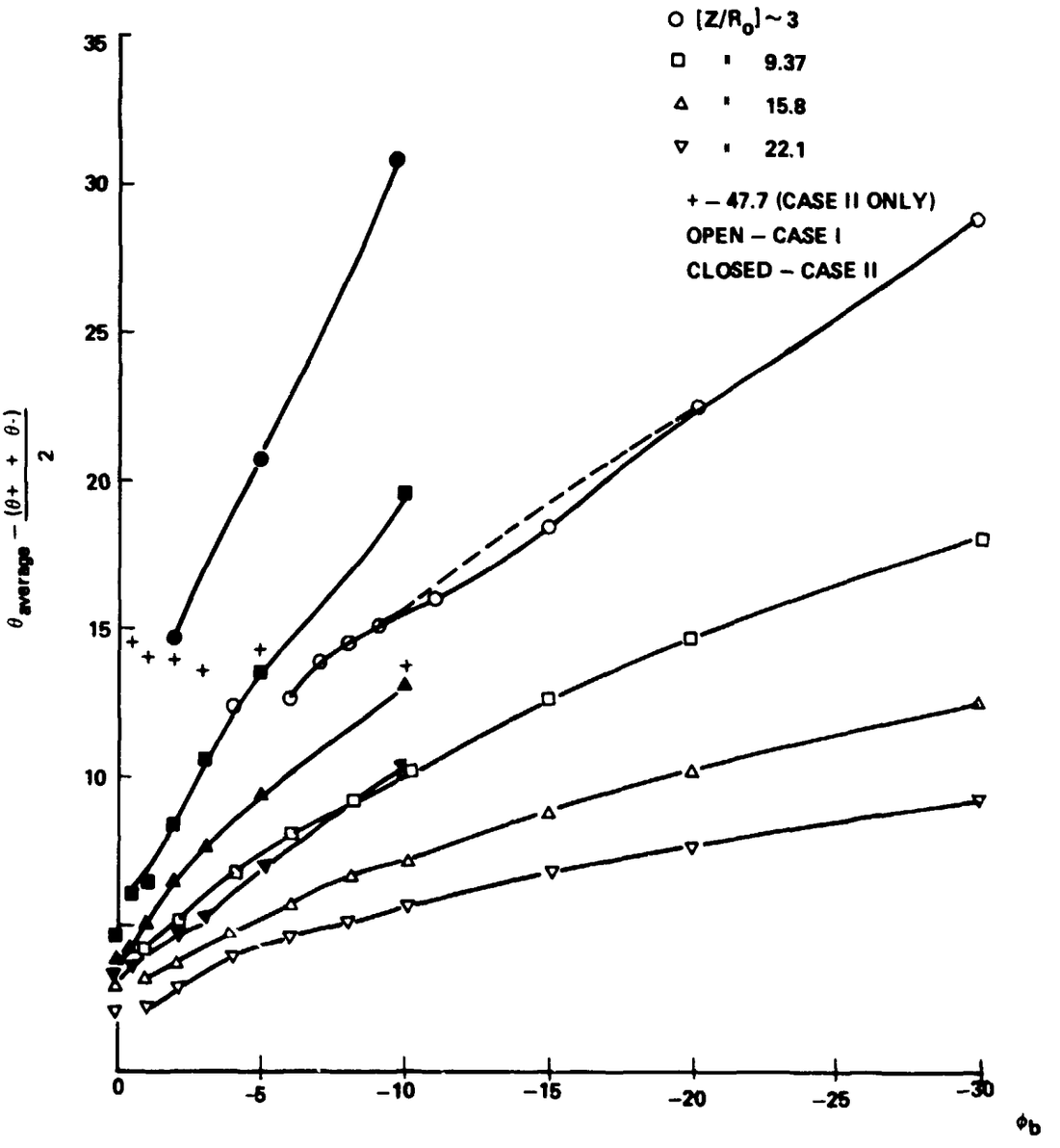

Figure 4-34. Variation of the average incidence angle, θ_{av}, with ϕ_b at various positions along the Z-axis for S ≅ 15.8 (Case I) and S ≅ 9.4 (Case II).

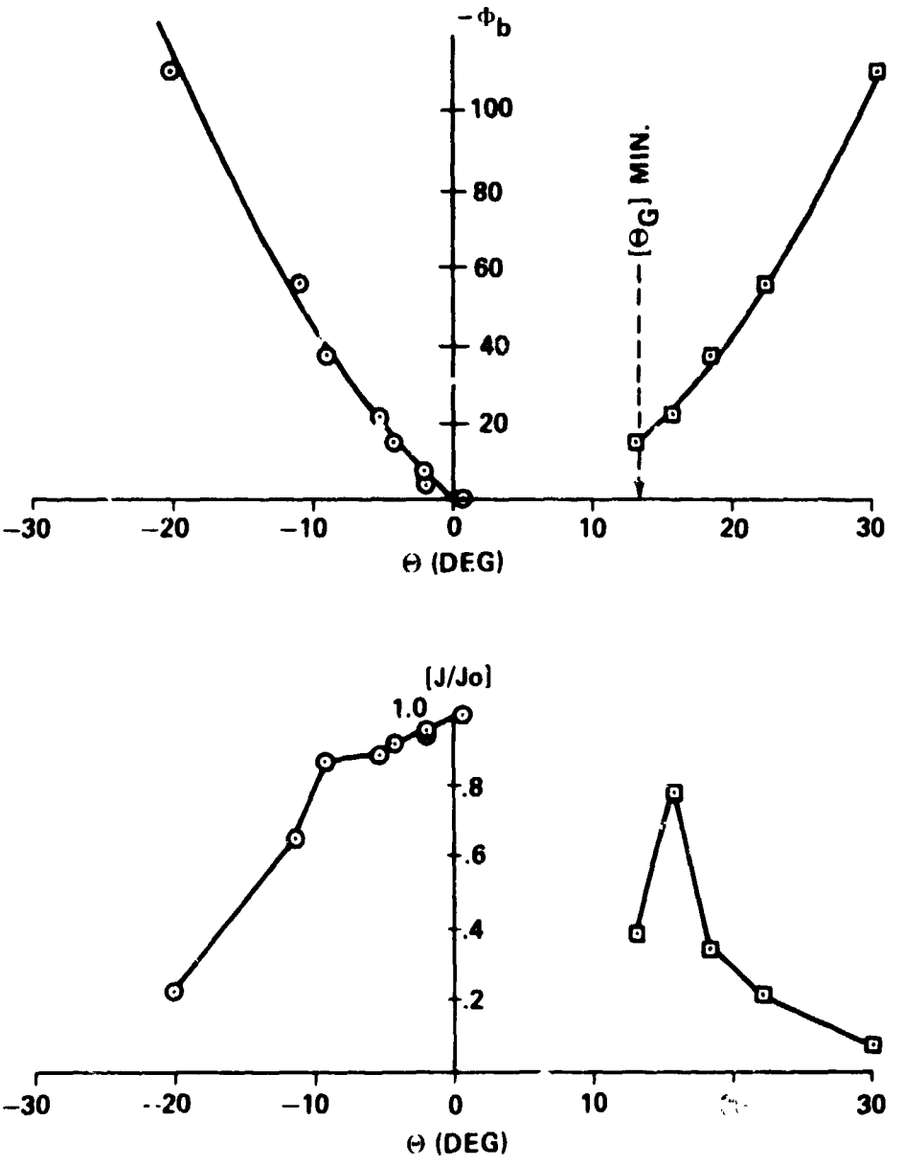

Figure 4-35. DIFP data corresponding to Figure 4-30: (a) variation of θ with Φ_b and (b) corresponding variations of peak amplitudes with θ.
After Stone [99].

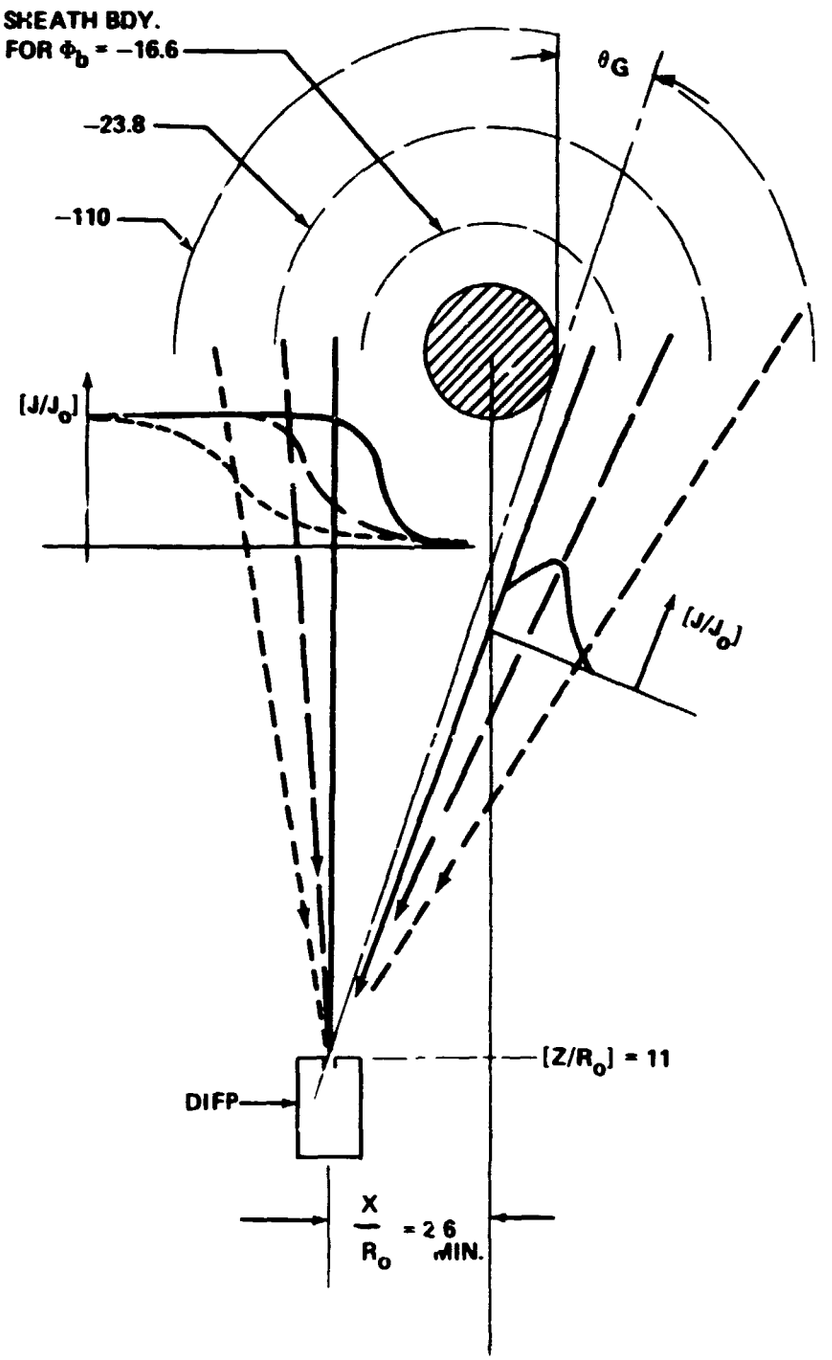

Figure 4-36. Schematic representation of the flow processes described by the data from Figures 4-30 and 4-35.
After Stone [99].

The DIFP measurements have allowed direct observation of ion streams deflected across the Z-axis by the potential gradients in the plasma sheath surrounding the body, have shown some detailed behavior of these streams as a function of Z, X and Φ_b, and have, for the first time, provided direct evidence of the deflection of the converging ion streams by potential wells or barriers downstream from the test body. However, in spite of this, the current measurements are sketchy and greater detail is needed along with two-dimensional measurements which would not be limited to long cylindrical test bodies. A two-dimensional version of the DIFP has been built and successfully tested. However, obtaining results from the DIFP involves the tedious reduction of copious amounts of raw data and the addition of a second dimension will only multiply this. It is, therefore, not practical to carry out a detailed study with hand-reduced data. Such a study must, of necessity, involve an automated data-handling capability. As mentioned in Section III, an automatic digital data recording system has been completed and work is progressing on the required software for data reduction.

CHAPTER V. CONCLUSION

A. Summary of Results and Conclusions

In the present study, the characteristics of the near- and mid-wake regions of disturbed plasma flow have been investigated downstream from conducting test bodies, primarily of spherical and cylindrical geometry. In this chapter, the results obtained will be summarized in the context of the physical processes involved, shown schematically in Figure 5-1. The primary case discussed will be for small bodies ($R_d \simeq 1$) for which most of the data were obtained. Extension to other values of R_d will then be made. For a discussion of the upstream and far-wake disturbances, the reader is referred to the work of Fournier [23] (Appendix C.6), Hester and Sonin [34] (Appendix E.1.g), and Woodroffe and Sonin [30] (Appendix C.8).

1. Disturbance Envelope. In the present investigation, the envelope of the zone of disturbance, defined by the boundary between freestream conditions ($J_i / J_{io} = 1$) and disturbed flow ($J_i / J_{io} \neq 1$), was found to depend on two factors: the initial width of the disturbance at the largest cross section of the test body, and the rate at which the disturbance propagates away from the Z-axis as it moves downstream. The initial radial extent of the disturbance, defined by the sum of the test body radius and the sheath thickness, was found to increase in direct proportion to the negative body potential, $-\Phi_b$ (Figure 4-22). It can also be expected to increase with the Debye length. The propagation of the disturbance boundary away from the wake axis was found to define a Mach cone, based on the ion acoustic Mach number, S (Figure 4-23). This result is in agreement with several theoretical treatments, including those of Rand [4,5] and Maslennikov and Sigov [17-19] which predict a Mach cone

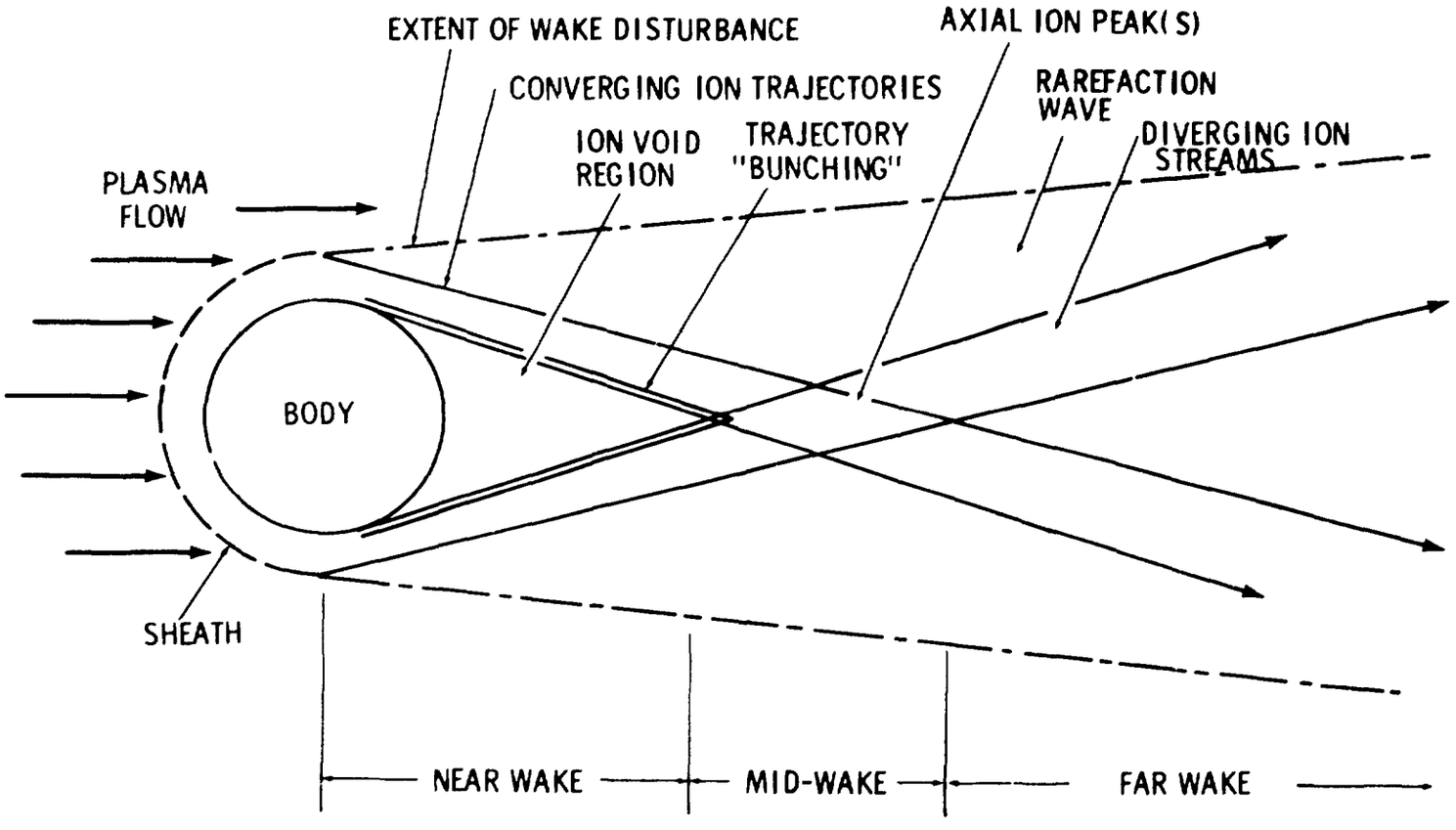

Figure 5-1. Ion behavior within disturbed zone.

structure for bodies with a small potential Φ_b (Appendices B and C). The rarefaction wave, which is the most spatially extensive characteristic of the disturbance, was found to decrease the ambient ion current density by as much as a factor of three at distance s great as $2(S \cdot R_o)$ downstream (Figure 4-24).

The above conclusions are based on the parameter range $R_d = 4$ to 6. $S \simeq 11$, and $\Phi_b = -3.8$ to -47. Measurements by Hester and Sonin [51-53] (Appendix E.1.g) show the existence of pseudowaves for $\Phi_b >> S$ (streams of ions deflected across the wake axis by the sheath fields) which overrun the rarefaction wave and expand the zone of disturbance beyond the Mach cone. However, this effect was small in amplitude and decayed rapidly. It was probably not observed in the present experiment due to the larger diameter plasma source and, hence, a greater ion temperature which would diffuse the streams more rapidly.

2. Ion Trajectory Focusing by the Plasma Sheath. The focusing of ion streams onto the wake axis by the electric field existing in the plasma sheath surrounding test bodies has long been inferred by the presence of diverging wave-like structures in the far-wake region. The present study provides the first direct observation of deflected ion streams and shows their angle of incidence to be proportional to Φ_b in the near wake for small body potentials (Figure 4-34).

A "bunching" of the ion trajectories was found to occur at the radial boundaries of the ion void region [Figures 4-1, 2, 4, and 31(b)]. This effect has not been discussed in previous theoretical or experimental studies, but is apparent in the theoretical results calculated by Maslennikov and Sigov [18] (Appendix C.2, Figure C-3).

The present experimental measurements are not sufficient to reveal the physical mechanism which produces the observed ion trajectory "bunching" in the near wake. Neither do the calculations of Maslennikov and Sigov allow an explanation; and the effect does not even occur in other theoretical treatments such as the one by Call [12], which predicts a "fanning out" of the

deflected ion trajectories (Appendix C.5, Figure C-7). The near-wake ion trajectory grouping could be produced either by a collective effect on the ions (possibly a result of instabilities set up by the large density gradient at the void voundary) or by the shape of the potential gradient in the plasma sheath. More detailed measurements in the void boundary region are needed to determine the casual mechanism.

3. Enhancement of Electron Temperature in the Near-Wake Ion Void Region. An apparent electron temperature enhancement, which coincided spatially with the ion void region, was observed in the MSFC No. 2 facility by Oran et al. [77], as shown in Figure 4-25. However, no physical explanation was given for the effect, which appeared to be similar to that observed in the wakes of the Explorer 31 satellite and the Gemini-Agena 10 spacecraft (Appendix D.2.b). In the present study, these data were re-evaluated. It was found that it could be partially explained by the effects expected to occur as a result of the existence of a potential well in the ion void region. However, all the available data can be explained in terms of a "two-stream" type instability predicted theoretically by Gurevich et al. [32] for plasmas of mixed ion composition. Although the experiments were not conducted in plasma streams of mixed composition, it is known that a population of slow ions existed in the chamber ($\geq 30\%$ of the stream concentration) and the same type instability can be expected to have occurred as a result of the disparity in their velocities.

If this explanation is correct, it means that the experimental results do not apply to the in situ observations where there is no appreciable slow ion population moving with the spacecraft. However, the results take on a new significance in that they indicate the existence of a wave particle interaction mechanism operative in the laboratory and point the way to experiments with mixed ion composition (and no appreciable slow ion population) which will apply directly to the in situ observations.

4. Axial Ion Peak. The general concept of an axial ion peak created in the mid-wake by converging ion streams has been predicted by a number of theoretical treatments (Appendix C) and observed in a large number of

experiments (Appendix E). The present study goes beyond qualitative observation of the axial ion peak and provides a detailed description of its parametric behavior.

The converging streams (VB streams), discussed in Chapter V.A.2, were found to create an initial ion peak on the wake axis. The position of this peak was found to depend on $[SR_d^{\alpha} / |\Phi_b|^{1/2}]$, where $\alpha = 0.02359$ (Figure 4-11). This result agrees closely in its S and Φ_b dependences with the theoretical predictions by Martin [13]. However, the experimental results do not agree with Martin in their R_d dependence (Appendix C.7).

It was also found that the axial ion peak may be created by more than one mechanism. The first peak to occur downstream is produced by the converging, grouped ion streams and has the behavior discussed previously. However, a second peak is also created, possibly by ion trajectories which are deflected, but not grouped, or possibly by the attractive space charge potential in the ion void. The two types of axial ion peaks normally are superpositioned for small Φ_b and cannot be distinguished from each other. However, they tend to separate at highly negative Φ_b values, indicating that the two casual mechanisms have different dependences on Φ_b (Figure 4-8).

The height and width of the axial ion peak at the location of its maximum amplitude were also investigated. The maximum peak height for spherical test bodies was found to be proportional to $[S/|\Phi_b|]^{1/2}$. The lack of any significant R_d dependence is surprising. Apparently, the expected proportionality to R_d, resulting from the R_o dependence of the cross-sectional area of the focused ion streams, is offset by ion stream diffusion which is proportional to the distance traveled in reaching the Z-axis and, therefore, also depends on R_o. The peak width (normalized by the test body radius, R_o) was found to depend only on $|\Phi_b|^{-1/2}$. This dependence is taken to represent a balance between the momentum the particles obtain due to deflection toward the Z-axis, produced by ϕ_b, and the magnitude of the space charge potential barrier on the Z-axis, which is proportional to kT_e. (Note that $\Phi_b = e\phi_b / kT_e$.)

The previous results were obtained for spherical test bodies and apply only to bodies with axial symmetry. It was found that the nature of the axial ion peak depends strongly on the cross-sectional geometry of the test body. For example, a square cross section produces multiple peaks or a broad plateau which spans across the Z-axis and which is usually less than the ambient current level, rather than a strong, single peak centered on-axis. Variations in the length of axisymmetric bodies along the Z-axis was found to affect the position and amplitude of the axial ion peak, but not its basic morphology.

It was found that the above geometric dependence of the axial ion peak can be explained simply by the behavior of the plasma sheath, which is directly proportional to Φ_b and inversely proportional to λ_D. For small Φ_b and for large R_d, the sheath is thin compared to the test body dimensions and conforms closely to its geometry. For a test body having a square cross section, the ion streams will be deflected onto orthogonal lines at the Z-axis which are approximately a body diameter in length. This produces a wider peak of lower amplitude. As Φ_b becomes large or R_d becomes small, the sheath becomes relatively thick, expands away from the body and acquires a more spherical shape. Hence, the ions will be deflected more toward a point on the Z-axis and the axial ion peak structure will take on a behavior more characteristic of spherical test bodies (Figure 4-16). For very long cylindrical test bodies, the sheath geometry would not be expected to change with sheath thickness. Therefore, the axial ion peak morphology would not change as the sheath expands. The experimental data for a long cylinder are consistent with this explanation in that the axial ion peak was found to depend strongly on S and, apparently, weakly on R_d (Figure 4-17).

Concerning the question as to the fundamental difference between the wakes of long, cylindrical and axisymmetric test bodies, the conclusion reached is that there is no fundamental difference; i.e., the same physical processes occur and produce the wake structure. However, it is apparent that the improved focusing effect of axial symmetry creates a much stronger

axial ion peak and therefore a much larger space charge potential. It then happens that, for some conditions, this stronger potential prevents effects, such as crossing ion streams (pseudowaves), which are observed for the cylindrical case. Therefore, the wake structure may appear fundamentally different.

Test bodies of complex, mixed geometry were studied in a preliminary manner. The data could be explained in terms of simple bodies, indicating that the wakes of geometrically complex bodies may be formed by a simple linear superposition of the wakes of the different geometric constituents.

Although the electron and ion densities are apparently not equal within the axial ion peak (since a positive space charge potential has been shown to exist there by Fournier [23], Maslennikov and Sigov [18] et al., see Appendix C), a smaller axial electron peak has been observed which correlates roughly with the spatial location and extent of the axial ion peak [77].

5. Deflection of Ion Trajectories in the Mid-Wake Region. The deflection of ion trajectories in the mid-wake region was first predicted theoretically by Maslennikov and Sigov [18] (Appendix C.2, Figure C-2) and later, by Call [12] although not to the same degree due to the limitations imposed by his flux tube technique (Appendix C.5, Figure C-8(a)). In both cases, the ion trajectories were found to be deflected away from the Z-axis by the positive space charge potential associated with the axial ion peak. This effect has been ignored in most studies although it was inferred by Hester and Sonin from the nature of the diverging wave-like structure they observed in the far wake (Appendix E.1.g). It can also be inferred from the lack of a consistent dependence on Φ_b of the maximum axial ion peak (only the section of the peak formed by the converging VB streams followed a $|\Phi_b|^{-1/2}$ dependence).

The present study offers the first direct observations of this type of deflection. It was found that the ion trajectory inclinations to the Z-axis changed from an approximately linear Φ_b dependence for small test body potentials, to an approximately $|\Phi_b|^{1/2}$ dependence for larger potentials (Figure 4-34). The deflection of the ion trajectories in the mid-wake is made even

more evident by the observation of ion streams with angles of inclination to the Z-axis which are smaller than the geometric angle defined by the radial extent of the test body (Figure 4-33). Since ion streams obviously cannot pass through the test body and do not originate on its surface, this is clear evidence that the streams have been focused toward the Z-axis by the plasma sheath fields at the body and have subsequently undergone an additional deflection away from the Z-axis somewhere downstream.

The present data, which are in the form of vector measurements at a few individual points, are not sufficient to determine where or over what distance the second deflection occurred. Additional measurements, made on a fine spatial grid, are needed to establish the overall flow field before this type question can be answered.

6. Diagnostic Applications of the Wake Structure. The present study has revealed a very clear parametric behavior of the ion void boundaries, the converging VB streams in the near wake and the initial point of the axial ion peak (the apex of the VB streams). These characteristics of the wake are easily observed and, therefore, offer unique diagnostic opportunities which can determine the parameters Φ_b and S from which several characteristics of the ambient plasma may be determined (i.e., T_e, m_i, and V_o).

This possibility is especially attractive in the laboratory or in regions of the ionosphere or magnetosphere where there is only one (or a very dominant) ion. However, further investigation is needed before it can be used confidently in plasmas of multiple ion constituents. The effects of ion thermal motion, discussed below, must also be considered.

7. Effects of Ion Thermal Motion. The experiments of the present study did not directly address the effects of the T_e/T_i ratio. However, it is clear that the general effect of ion thermal motion is to diffuse the detailed wake structure discussed above. The more quantitative question as to how effective this diffusion process is and at what T_e/T_i value the structure vanishes has not been satisfactorily resolved. An extensive experimental study of this effect was carried out by Fournier and Pigache (Appendix E.1.i)

and it has been studied theoretically by Taylor, Gurevich, et al. and Fournier (Appendix C.3, C.4, and C.6).

The calculations by Fournier for a long cylindrical body show the effect of ion thermal motion to oppose the focusing effect of Φ_b (Figure C-10). However, it is noteworthy that a nonmonotonic n_i distribution continued to exist in the wake for $\Phi_b \leq -2.75$ when $T_e/T_i = 2$ and for $\Phi_b \leq -6$ when $T_e/T_i = 1$ (Figures C-9 and C-10). The calculations by Taylor further substantiate these results and the calculations by Gurevich et al. [32] show an axial ion peak to exist in the wake of a disk for $T_e/T_i = 4$ but to vanish for $T_e/T_i = 1$. These results are generally supported by the experimental observations by Fournier and Pigache [58] which show the peak structure to completely vanish only for small Φ_b and $T_e/T_i \leq 1$.

It, therefore, appears that the opposing effects of Φ_b and T_e/T_i are such that for small Φ_b the axial ion peak vanishes for $T_e/T_i \simeq 1$ but can be recreated by a sufficiently negative value of Φ_b. Further, we may conclude from the above results that in the ionosphere, where $T_e/T_i \simeq 2$ and $\Phi_b \simeq -5$, the axial ion peak can be expected to occur to some extent. This conclusion is supported by the clear presence of an axial electron peak (which we find to be of less amplitude than the ion peak in laboratory studies) in the wakes of the Ariel I satellite and its spherical ion probe (Appendix D.2.a).

8. Effects of Large R_d Values. Laboratory and theoretical studies have been limited to R_d values less than 50 which only approach the R_d range for large space platforms. However, several parametric trends have been established by the present experiments and review which may be cautiously extrapolated to describe large bodies in earth orbit.

It was pointed out above that the amplitude of the axial ion peak significantly depended only on S and Φ_b and, further, that the peak width depended only on Φ_b. If these observations, made over a relatively small range of R_d, can be extrapolated to large R_d values, then, on this basis, the axial ion peak would be expected to maintain an approximately constant amplitude and width, relative to the body radius, as R_d increased arbitrarily.

The above conclusion is incomplete, however, without considering the effects of ion thermal motion. The tendency of this random motion to spread out and diminish the wake structure can be expected to increase with the distance traveled by the ions, and hence with R_d. Therefore, it becomes doubtful that the detailed wake structure discussed above would be observed for very large bodies in the ionosphere at floating potential. However, if the body potential became elevated (such as may occur in the case of the Space Shuttle orbiter when charged particle accelerators are fired) the structure may appear as a result of the opposing effect of Φ_b shown by Fournier.

The extension of the present results to large bodies, over a large range of the R_d parameter, is probably the most difficult to study in the laboratory as well as theoretically. Clearly, at the very least, good benchmark in situ results are required in this area of the investigation.

B. Suggestions for Future Research

A number of questions have been revealed which the available data and theoretical calculations either do not address or are insufficient to provide an unambiguous answer. Below, we discuss what appear to be the most significant problems remaining for the three avenues of approach to plasma flow interaction studies; i.e., theoretical, experimental and in situ.

1. Theoretical. The most important weakness of the theory at the present time is its inability to include ion thermal effects under realistic conditions; i.e., for $R_d \sim 10$ to 100, $S \sim 5$ to 10, and $\Phi_b \sim -5$. The best treatment available is by Fournier [23]. However, it is limited to infinite cylinders and, because of the geometric effects discussed in Chapter V.A.4, it does not adequately describe the disturbance created by satellites of spherical, cylindrical, or even more complex geometries. A treatment of the type developed by Fournier is needed which could handle at least spherical and short cylindrical geometries.

Secondly, few theories include the effect of the geomagnetic field. As discussed in Appendix E.2, this probably is not important for describing the near- and mid-wakes of small to intermediate bodies ($R_d < 100$) in the ionosphere. However, it may become important for very large space platforms such as the Space Shuttle or for the far wake of bodies in general.

The third major problem to be faced by theoretical treatments is that none of them provide a practical self-consistent solution throughout the zone of disturbance. Those which adequately treat the near wake, where large charge separation occurs and particles may not be Maxwellian, do not carry the solution sufficiently far downstream (at least not in a self-consistent way). The fluid type theoretical treatments are capable of providing solutions great distances from the test body, but allow only very small space charges and require Maxwellian electrons and therefore are unable to describe the near wake. An effective coupling between the two approaches needs to be established. This was done, in principle, by Taylor [20], but his calculations were carried out for only one interation and were therefore not self-consistent. Also, like the treatment by Fournier [23], Taylor's calculations are limited to infinitely long bodies.

2. Experimental. The most fundamental limitations of laboratory studies are the lack of Maxwellian ions and the nonuniformity of the plasma stream — expecially along the stream axis. Although effective ion thermal motions have been created by Fournier and Pigache [58] and improvements in stream divergence (and presumably in the axial variations of the plasma stream) have been made by Martin and Cox [60], it appears that these problems can only be minimized to some extent and not eliminated. However, there remain several questions which can be effectively studied within the existing constraints of the laboratory.

The most obvious extension of the present study is a detailed investigation using vector ion flux measurements made by a two-dimensional version of the DIFP on a fine spatial grid. This study would establish, for example, the parametric nature of the ion trajectory deflections downstream from the test

body, would reveal the existence and effects of a potential well in the ion void region, would show, explicitly, the effects of the space charge potential associated with the axial ion peak, and would determine the wave or stream nature of the far wake wave-like structures observed for very small cylinders. This type study will involve very large amounts of data and therefore requires some form of automatic data handling and reduction.

A second area which needs further investigation in the laboratory is the effect of multiple ion constituents on the near-wake void region. According to the theoretical treatment by Gurevich et al. [32], the existence of proper mixtures of heavy and light ions can result in instabilities at the ion void boundaries where large density gradients occur. To the author's knowledge, no experimental investigations have been carried out with multiple ion plasmas. The extension from present studies is straightforward, however, and could be very rewarding if such instabilities are found and, especially if they couple with the electrons to produce an enhanced electron temperature.

3. In Situ. In the past, most space missions have involved single satellites, which a priori could provide only very limited information on the satellite-generated plasma disturbance, if for no other reason than the limited spatial coverage possible. In the near future, however, this restriction will be lifted with the advent of the Space Shuttle. The Shuttle will eventually provide a wide range of capabilities such as tethered and free-flying subsatellites which can be effectively used for plasma flow studies as shown, for example, in Figure 5-2. In effect, the Shuttle will serve as a near-earth plasma laboratory and many of the problems faced in the laboratory, such as non-Maxwellian ions, nonparallel flow, charge exchange ions, and wall effects will be circumvented.

This does not imply that ground-based laboratory investigations will no longer be needed. To the contrary, the Shuttle will provide a new approach to the problem which will utilize both laboratory and theoretical investigations. Space experiments will always be inherently more expensive than ground-based studies and it is therefore not cost effective to carry out studies in space which

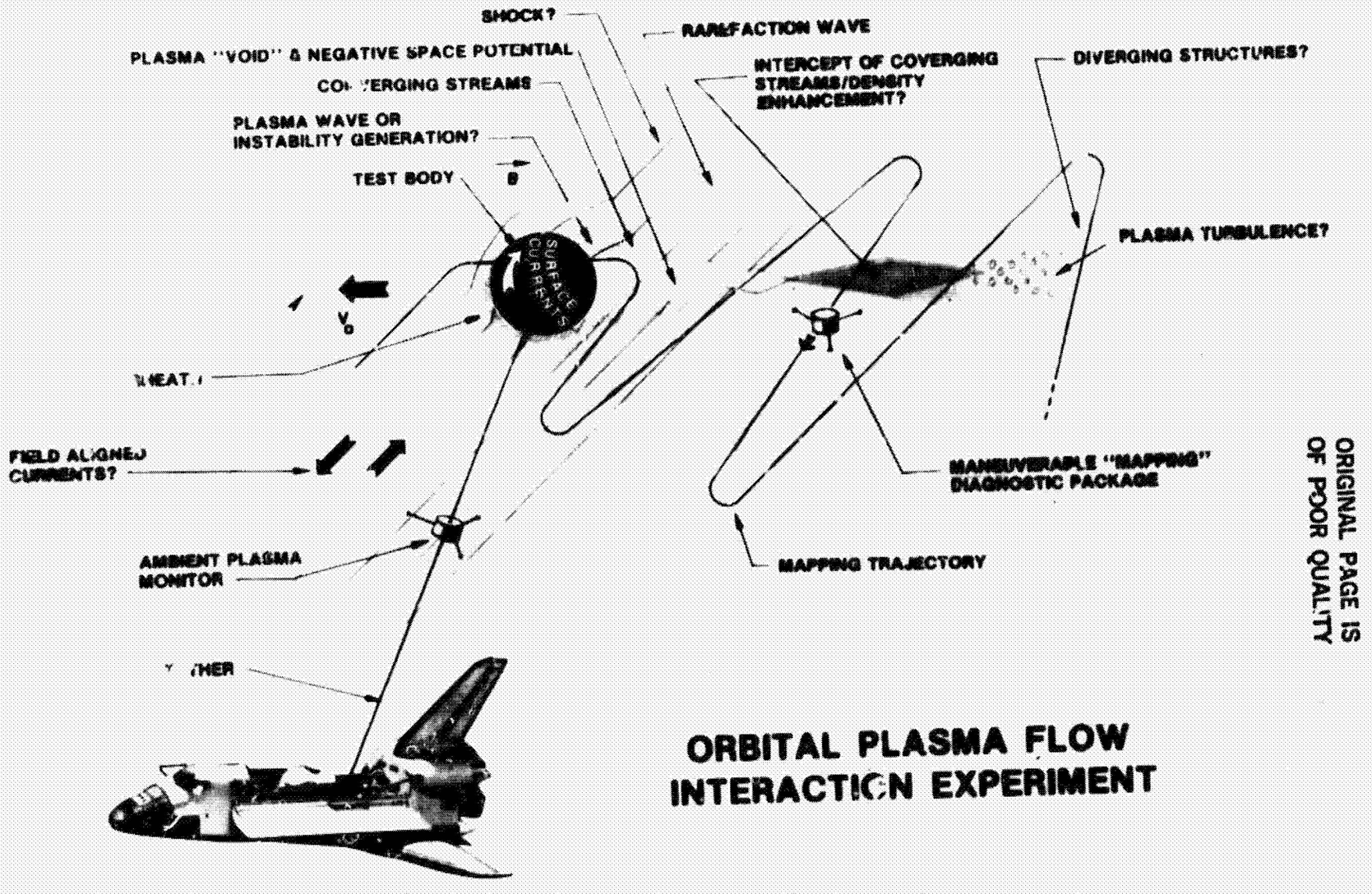

Figure 5-2. An example method for large body in situ plasma flow interaction studies utilizing the Space Shuttle. (Note that all effects shown would not be expected to occur under the same conditions and the existence of some has not been shown yet.) After Stone and Samir [101].

can be done in the laboratory. Even in the case where the study can be performed only in space, laboratory and theoretical results should be utilized to the extent possible to design the most effective flight experiment. We will therefore consider a few categories of experiments which can be performed effectively only in space.

First, using the methods of laboratory plasma physics in the natural plasma environment of the ionosphere affords a new range of parameter space not previously available. For example, in addition to the previously mentioned advantage of thermalized ions and the need to confirm ground-based studies under these conditions, scale sizes of the test bodies can be increased up to a factor of 10^3 greater than in the laboratory while still maintaining collisionless conditions. From the plasma physics point of view, this wide range of scale sizes makes possible, for example, the investigation of the relationship between the kinetic and continuum-MHD theories in the transition range where it is not clear which of the theoretical approaches applies [82]. From the ground-based experimental data, which can only approach this region of parameter space, it also appears that the nature of the interaction may change. This is not unreasonable since, unlike neutral gas flow where there is only one collision mean-free-path-length and hence one Knudsen number, in a plasma there are several additional effects which produce deflections of the charged particles including electrostatic coulomb collisions for which the Debye ratio, R_d, applies (as used herein) and magnetic deflections characterized by the Larmor radii for electrons and ions for which the ratios [R_o/R_L(ie)] would be appropriate.

Probably the most interesting type of ionospheric experiment involves an extension of the qualitative modeling concept formerly used in the laboratory to study the interaction of the ionosphere with artificial satellites. With this concept, certain plasma flow interactions occurring naturally in the solar system can be qualitatively modeled with test bodies in the ionosphere. A notable example is the interaction of the Jovian satellite, Io, with its environmental magnetospheric plasma, for which an almost complete qualitative scaling can be achieved, as shown by Table 5-1.

It is realized that natural phenomenon, such as the earth's magnetosphere, have been modeled in the laboratory. However, there are competing scaling requirements which make it difficult, if not impossible, to achieve even a proper qualitative scaling of these phenomena in ground-based laboratories and therefore the utility of these studies is limited (although specific processes can be effectively studied). Further, in reducing the scale size of solar system phenomenon to the laboratory scale, collisional effects usually become significant and boundary layers become too small to be probed. However, in the ionosphere, due to the large scale size possible, perturbations from diagnostic instruments can be minimized, measurements can be made in boundary layers formerly too small for probing, and collisional effects become insignificant.

The limitations of modeling are well known and experiments of this type will never eliminate the need for in situ observations by planetary probes. However, they may provide the best information available on what physical processes are likely to be operative and where and how to look for them. Such information would be invaluable in planning subsequent planetary missions.

TABLE 5-1. PLASMA PROPERTIES AND SCALING PARAMETERS
(After Stone and Samir [101])

PARAMETER	LABORATORY	IONOSPHERE @ 300 km	JOVIAN MAGNETOSPHERE @ Io
$N_{i,e}$ [cm^{-3}]	10^3 10^6	5×10^5	2×10^2
T_e [K°]	10^3 10^4	2.5×10^3	$\sim 10^5$
T_i [K°]	T_e	1.5×10^3	10^5
B [G]		0.5	2×10^2
V_o [km sec]	6	7.7	5.6×10^1
R_o (effective) [km]	10^5 10^4	0.1	3.3×10^3
M_i (AV) [AMU]	2 28	20	1
$S = (M_i V_o^2 / 2kT_e)^{1/2}$	~ 3	6	1.4
$M_A = (4\pi N_i M_i)^{1/2} V_o / B$		5×10^3	2×10^2
$M_N = V_o \left[\frac{5k(T_e + T_i)}{3M_i} + \frac{B^2}{4\pi N_i M_i} \right]^{-1/2}$		5×10^3	2×10^2
$\beta = N_i k (T_e + T_i) / B^2$		3×10^5	2×10^4
$R_{mag} = 4\pi R_o V_o / c^2$		6×10^7	6×10^7
[illegible]		4×10^3	7×10^5
[illegible]		2×10^1	2×10^4
[illegible]	0.4 40	2×10^4	2×10^4
[illegible]	10^8 10^7	2×10^1	3×10^3
$\rho_{ion} = R_o$ (effective) V_o	10^{11} 10^{12}	5×10^5	5×10^7
ρ_i	10^9 10^{11}	3×10^3	1×10^6
ω_i		1×10^5	2×10^7
ω_i		3	1×10^4

APPENDIX A. DERIVATION OF THE FLUID EQUATIONS

In Chapter II.A.1.b., the assumptions required in deriving the continuity and momentum transfer equations from the Boltzmann equation were discussed. Here, some details of the derivation of these two equations are given.

The Boltzmann equation can be written in the form:

$$\frac{\partial f}{\partial t} + \vec{v} \cdot \nabla_{\mathbf{x}} f + \vec{a} \cdot \nabla_{v} f = \left(\frac{\delta f}{\delta t}\right)_c \tag{A-1}$$

where

$$\vec{a} = \frac{q}{m} [\vec{E} + \vec{v} \times \vec{B}/C] \quad .$$

To simplify the notation, we have dropped the subscript used to designate the constituent; however, a set of conservation equations will be required for each type of particle. Multiplying equation (A-1) by any function of particle velocity $Q(\vec{v})$ and integrating over all velocity space bring us to

$$\int Q \frac{\partial f}{\partial t} d^3v + \int Q \vec{v} \cdot \nabla_{\mathbf{x}} f \, d^3v + \int Q \vec{a} \cdot \nabla_{v} f \, d^3v = \int Q \left(\frac{\delta f}{\delta t}\right)_c d^3v \quad . \tag{A-2}$$

Assuming Q is not a function of time, the first integral of equation (A-2) is simply:

$$\int Q \frac{\partial f}{\partial t} d^3v = \frac{\partial}{\partial t} \int Qf \, d^3v = \frac{\partial}{\partial t} [n \overline{Q}] \quad , \tag{A-3}$$

where the bar indicates the average value, defined as:

$$\overline{Q} = \frac{1}{n} \int Qf \, d^3v \quad .$$

In the second integral, since $\vec{x}$ and $\vec{v}$ are independent variables, the spatial gradient operator can be removed from the integral, giving:

$$\int Q\vec{v} \cdot \nabla_x f \, dv^3 = \int [\nabla_x \cdot (Q\vec{v}f) - f\nabla_x \cdot (Q\vec{v})] \, dv^3 = \nabla_x \cdot [n\overline{(Q\vec{v})}] \tag{A-4}$$

Note that $\nabla_x \cdot (Q\vec{v}) = 0$ since Q and $\vec{v}$ are not functions of $\vec{x}$.

Evaluating the third integral we have:

$$\int Q\vec{a} \cdot \nabla_v f \, dv^3 = \int [\nabla_v \cdot (Q\vec{a}f) - Qf\nabla_v \cdot \vec{a} - f\vec{a} \cdot \nabla_v Q] \, dv^3$$

$$= \int \nabla_v \cdot (Q\vec{a}f) \, dv^3 - \int Qf\nabla_v \cdot \left[\frac{q}{m}(\vec{E} + \vec{v} \times \vec{B}/C)\right] dv^3$$

$$- \int f\vec{a} \cdot \nabla_v Q \, dv^3$$

$$= \oint_s (Q\vec{a}f) \cdot d\vec{s} - \frac{q}{m} \int Qf\nabla_v \cdot (\vec{v} \times \vec{B}/C) \, dv^3$$

$$- n\overline{(\vec{a} \cdot \nabla_v Q)}$$

$$\int Q\vec{a} \cdot \nabla_v f \, dv^3 = -n\overline{(\vec{a} \cdot \nabla_v Q)} \quad . \tag{A-5}$$

Note that in the above evaluation, the surface of integration for the surface integral is a sphere of radius v and its area is proportional to v^2. This integral vanishes if $(Q\vec{a}f) \to 0$ faster than v^{-2} as $v \to \infty$, which must be the case for any distribution with finite energy; i.e., for $\alpha \neq 0$, $v^\beta \exp[-\alpha v^2] \to 0$ as $v \to \infty$ if β is finite. The second integral is simplified by the fact that the electric field is not a function of velocity and hence $\nabla_v \cdot \vec{E} = 0$. The velocity gradient of the $\vec{v} \times \vec{B}$ term is zero since $\vec{v} \times \vec{B}$ is a vector normal to $\vec{v}$ and hence ∇_v. The integral on the right-hand side of equation (A-2) is expressed as:

$$\int Q\left(\frac{\delta f}{\delta t}\right)_c dv^3 \rightarrow \overline{[Q(\delta f/\delta t)_c]} \quad , \tag{A-6}$$

and is taken to represent the rate of change of $(n\overline{Q})$ due to discrete collisions. This seems reasonable since $(\delta f/\delta t)_c$ represents the rate of change of f resulting from this type of collision. Substituting relations (A-3) through (A-6) into equation (A-2) yields,

$$\frac{\partial}{\partial t}[n\overline{Q}] + \nabla_x \cdot [n\overline{(Q\vec{v})}] - n\overline{(\vec{a} \cdot \nabla_v Q)} = \overline{[Q(\delta f/\delta t)_c]} \tag{A-7}$$

which is the general continuum equation used in Chapter II.A.1.b.

If $Q(\vec{v}) = 1$, then equation (A-7) becomes:

$$\frac{\partial n}{\partial t} + \nabla_x \cdot (n\vec{u}) = 0 \quad , \tag{A-8}$$

which is the continuity equation. Note that $u = \overline{(\vec{v})}$ and $\overline{(\delta f/\delta t)_c} = 0$ since collisions cannot change the total number of particles of a given type in an elemental volume of real space if we assume that no creation or annihilation of charge occurs and there is no chemical reaction.

If $Q(\vec{v}) = m\vec{v}$, equation (A-7) becomes

$$\frac{\partial}{\partial t}(mn\vec{u}) + \nabla_x \cdot (nm\overline{\vec{v}\vec{v}}) - n\overline{[\vec{a} \cdot \nabla_v(m\vec{v})]} = \overline{\left[m\vec{v}\left(\frac{\partial f}{\partial t}\right)_c\right]} \quad . \tag{A-9}$$

If we set $\vec{v} = \vec{u} + \vec{c}$ where $\vec{u}$ is the average (or drift) velocity and $\vec{c}$ is the random (or thermal) velocity, then $\overline{(\vec{c})} = 0$ and

$$\overline{\vec{v}\vec{v}} = \vec{u}\vec{u} + \overline{\vec{c}\vec{c}} \quad .$$

Therefore, the second term of equation (A-9) is

$$\nabla_x \cdot (nm\overline{\vec{v}\vec{v}}) = \nabla_x \cdot (nm\vec{u}\vec{u}) + \nabla_x \cdot (nm\overline{\vec{c}\vec{c}}) \quad .$$

If the plasma is assumed to be isotropic, then

$$\overrightarrow{c\,c} = \begin{bmatrix} c_x^2 & 0 & 0 \\ 0 & c_y^2 & 0 \\ 0 & 0 & c_z^2 \end{bmatrix}$$

and

$$\overline{c_x^2} = \overline{c_y^2} = \overline{c_z^2} = \overline{c^2}/3 \ .$$

Then

$$\nabla_x \cdot (nm\,\overline{\overrightarrow{c\,c}}) = \nabla_x (nm\,\overline{c^2}/3) = \nabla_x P \quad , \tag{A-10}$$

where P is scalar pressure. Note that

$$P = \int (m v_x)\,(v_x)\, f(\vec{v})\, dv^3 = mn \int v_x^2 f\, dv^3 = mn\,\overline{v_x^2} \ .$$

Then

$$P = nm\,\overline{c^2}/3 \ .$$

The remaining term can be written as:

$$\nabla_x (nm\,\overrightarrow{u\,u}) = m\vec{u}\,\nabla_x \cdot (n\vec{u}) + nm(\vec{u} \cdot \nabla_x)\,\vec{u} \quad . \tag{A-11}$$

We now assume that the momentum transfer resulting from discrete collisions can be expressed as

$$\overline{[Q(\delta f/\delta t)_c]} = -mn\,\nu_c\,\vec{u} \tag{A-12}$$

where ν_c is an effective collision frequency. (This presentation effectively assumes the average velocity of the target particles to be zero. If this cannot be assumed, then the relative velocity between the two particle populations, $[\vec{u} - \vec{u}_o]$ must be used.)

Substituting relations (A-10) through (A-12) into equation (A-9) gives:

$$mn\frac{\partial \vec{u}}{\partial t} + m\vec{u}\left[\frac{\partial n}{\partial t} + \nabla_x \cdot (n\vec{u})\right] + mn(\vec{u}\cdot\nabla_x)\vec{u} + \nabla_x P$$

$$- mn(\vec{a}) = - mn\nu_c \vec{u} \quad .$$

Note that the term in square brackets is the continuity relation and therefore vanishes. After dividing by (nm) and rearranging terms, we have the momentum transfer equation; i.e.,

$$\frac{D\vec{u}}{Dt} = -\frac{\nabla_x P}{mn} + \frac{q}{m}[\vec{E} + \vec{u}\times\vec{B}/C] - \nu_c\vec{u} \qquad \text{(A-13)}$$

where

$$D/Dt = [\partial/\partial t + \vec{u}\cdot\nabla_x] \quad .$$

APPENDIX B. A CRITICAL REVIEW OF THE RESULTS FROM FLUID TREATMENTS

Since one of the objectives of this study is to investigate the conditions under which the more easily solved fluid formulation holds, we will discuss the results of fluid calculations separately from the more extensive results of kinetic theory.

1. Kraus and Watson (1958)

Some of the earliest theoretical calculations were made by Kraus and Watson [3]. They investigated plasma flow past a negatively charged body in the limits of both a collision dominated and a collisionless medium. In both cases, magnetic effects were ignored, a steady state flow field was assumed, and the body was considered to be small compared to the Debye length; i.e., $R_o/\lambda_D \ll 1$ (the direct impact of particles on the body was therefore not considered).

In the limit of high gas density, the additional assumptions were made that (1) the plasma remained in thermodynamic equilibrium everywhere and hence $n_e = n_o \exp[e\phi/kT_e]$, which effectively assumes $V_o \ll \hat{c}_e$, (2) perturbations created by the body were small, allowing the fluid equations of motion to be linearized, and (3) the flow was assumed supersonic with respect to the mean thermal speed of ions.

The continuity and momentum transfer equations were used in conjunction with the Poisson equation. Subject to the above assumptions, this approach produced the following effects and conclusions:

(1) A trailing "Mach cone" disturbance is created behind the body of half angle, θ, given by:

$$\theta = \tan^{-1}\left[\left(\frac{V_o}{A}\right)^2 - 1\right]^{-1/2}$$

where

$$A^2 = (\hat{c}_i^{\,2} + \lambda_D^{\,2}\omega_{pi}^{\,2}) = a_i^{\,2}(T_i/T_e + 1/2) \quad .$$

ω_{pi} is the ion plasma frequency, $\hat{c}_i$ is the most probable thermal speed and a_i is the acoustic speed. Note that this result predicts that the Mach angle should decrease with T_e/T_i. For $T_e/T_i >> 1$ (which is generally the case in laboratory investigations) A reduces to the ion acoustic speed; i.e.,

$$A \cong (2kT_e/m_i)^{1/2}/\sqrt{2} \quad .$$

(2) An increase in charge density was found to occur within the Mach cone and is given by:

$$\left(\frac{n_e'}{n_o}\right) = \frac{eQ}{\lambda_D(\theta_e + \theta_i)\left[(V_o/A)^2 - 1\right]^{1/2}}$$

where,

n_e' is the electron densith within the Mach cone.

n_o is the undisturbed electron or ion density.

Q is the total charge on the body.

$\theta_{i,e}$ is ion or electron temperature in eV.

(3) It was concluded that the above effects resulted when the small ($R_o << \lambda_D$) negatively charged body moving supersonically ($V_o > \hat{c}_i$) excited collective motion in the plasma which resulted in the generation of a wake structure.

For the low density (collisionless) limit, Kraus and Watson resorted to a kinetic treatment, using Boltzmann equations for ions and electrons (ultimately assuming the electrons to be Maxwellian) and Poisson's equation.

Unfortunately, it was assumed that $V_o >> \hat{c}_e$, which is unacceptable for ionospheric applications. Therefore, the results obtained in the low density limit are not of interest, except to note that when the Landau damping term is negligible (tantamount to $T_e/T_i \gg 1$) the results are essentially the same as those achieved via the fluid formulation.

There are several short comings of the above analysis which should be pointed out. According to Alpert, et al. [25], the second order terms in potential (omitted by the linearized equations) become dominant in the far wake region. On the other hand, we note that the assumption of small perturbations (and possibly that of a Maxwellian electron distribution) does not hold in the near and mid-wake regions; i.e., where strong density gradients occur. Therefore, the spatial range of validity of this theory is very limited. Although it is useful for comparison with the results from some laboratory investigations, the assumption of a very small body ($R_o/\lambda_D << 1$) is not applicable to the interaction of satellites with the ionosphere. Finally, this study lacks detailed numerical calculations of the flow field.

2. Rand (1960)

Rand investigated the wakes behind negatively charged bodies in a mesosonic ($\hat{c}_i << V_o << \hat{c}_e$), low density plasma stream [4,5]. The bodies considered were a small diameter ($R_o/\lambda_D << 1$) cylinder and a large diameter ($R_o/\lambda_D >> 1$) disk, both oriented normal to the flow direction. The electrons were considered to be in equilibrium while a drifting Maxwellian distribution was assumed for the ions. The distribution functions were integrated to determine number densities (assuming no surface interaction with the small cylinder while the disk absorbed all incident ions). Conservation of energy was used to attain a tractable integral for ion density. The space potential was then found by substituting the particle density expressions into the linearized Poisson equation (i.e., assuming $e\phi/kT_e << 1$).

The solutions were obtained in two steps. First, the wakes of both bodies were analyzed assuming small scattering angles for ions ($e\phi/m_i V_o^2 << 1$), which is tantamount to excluding particles "trapped" by potential gradients [4]. In the second step, the small scatter assumption was relaxed and the effect of the "trapped" particles investigated [5].

For the case of the small cylinder it was assumed that the body presented no physical obstacle to the flow; i.e., particles interacted only with the electric field around the body; in effect, the body was treated as a line charge. Under the small scattering assumption, the analysis produced the following predictions and conclusions:

(1) Both electron and ion densities are enhanced along plane slabs extending back from the cylinder.

(2) The increase in electron density above ambient is given by:

$$\frac{n_e'}{n_o} = \frac{eq}{(kT_i m_i V_o^2)^{1/2}} \approx \frac{e\phi_b}{(kT_i m_i V_o^2)^{1/2} \ell n(L/R_o)} ,$$

where

q is the charge per unit length.

L is the cylinder length.

R_o is the cylinder radius.

(3) The half angle, θ, for the planes of density enhancement was given as:

$$\theta = \sin^{-1}\left[\frac{1 + (2T_i/T_e)}{(m_i V_o^2/kT_e) - 1}\right]^{1/2} \simeq \sin^{-1}\left(\frac{kT_e}{m_i V_o^2}\right)^{1/2} \quad \text{for } \frac{T_e}{T_i} >> 1 ,$$

where θ is measured with respect to the flow direction.

(4) Transverse profiles of $\phi(y, z = \text{const.})$ were calculated (Figure B-1). Unfortunately, these profiles were obtained for the case $T_e/T_i << 1$, which is of no practicle significance. However, for $T_e/T_i >> 1$ and $y = 0$ (on the wake axis) the expression derived by Rand reduces to:

$$\phi(0,z) = 2\pi\left(\frac{kT_e}{m_i V_o^2}\right)^{1/2} q\, J_1(\omega_{pi}\, Z/V_o) \quad ,$$

where

q = charge per unit length.

ω_{pi} = ion plasma frequency.

J_1 = first order Bessel function of the first kind.

This expression predicts that the space potential will oscillate along the wake axis with a period proportional to ω_{pi}/V_o. This is in reasonable agreement with the experimental results of Hester and Sonin (Appendix E.1.g).

For the case of the disk, it was assumed that $R_o/\lambda_D >> 1$ so that ions deflected by the electric field at the edge of the disk would not be affected by its curvature. Only the near wake was considered so that, in fact, the problem is actually that of a semi-infinite plane. With the exception of the body size and the absorption of incident charge on its surface, the same assumptions were used as for the cylinder. Under the small scattering assumption, the following results were achieved:

(1) For $T_e/T_i << 1$, the ions passing near the edge of the half-plane are deflected through the angle:

$$\theta = \sin^{-1}\left[\left(\frac{kT_i}{2m_i V_o^2}\right)^{1/2}\right] \quad .$$

(2) Two perturbation planes are created by the deflection: one inclined toward the half-plane at an angle θ_1 and the other inclined into the ambient plasma at θ_2 where

$$\theta\begin{Bmatrix}1\\2\end{Bmatrix} = \left[\frac{k\left(T_i + T_e\right)}{2m_i V_o^2}\right]^{1/2} \cdot \begin{Bmatrix}+\\-\end{Bmatrix} \cdot \left[\frac{kT_i}{2m_i V_o^2}\right]^{1/2} \quad .$$

(3) Considering the circular disk, this would produce concentric cones; one inclined toward the wake axis at θ_1, and the other inclined away from the axis at θ_2.

(4) Assuming a uniform charge density on the body (a dielectric body), an increase in charge density occurs at each plane (cone) of disturbance over a thickness on the order of λ_D, and is given by:

$$\frac{n_e'}{n_o} = \frac{\pi}{2} \frac{e\sigma\lambda_D}{\left[2k(T_i + T_e) m_i V_o^2\right]^{1/2}} ,$$

where σ is the charge per unit area. After obtaining the particle number densities, Rand used the Poisson equation to find the electric potential, ϕ. Profiles of ϕ were calculated and are shown in Figure 5-2.

(5) For a conducting disk, the charge density is not uniform but tends to be more concentrated at the edges. This results in the perturbation charge density increasing by the factor $(2R_o/\lambda_D)^{1/2}$.

It should be remembered that the above results for the disk were achieved under the unrealistic assumption, $T_e/T_i << 1$, and therefore must be viewed with caution. (However, the general wake morphology of concentric cones of disturbance will be found to be generally correct even for $T_e/T_i >> 1$). Regarding both solutions, Alpert et al. [25] points out that Rand has neglected a term representing ion scattering in the near field of the body and therefore the solution is not accurate in the far wake. Inclusion of second order terms in ϕ would correct this deficiency.

With the inclusion of trapped particles [5], Rand investigated the effect of the T_e/T_i ratio on damping of the wake of the small cylinder. The conditions were as stated above with the additional assumptions that particles travel along straight-line trajectories between collisions and the plasma is quasi-neutral (small degree of charge separation).

In the previous analysis, Rand considered only ions which suffered small angle deflections; i.e., which were sufficiently energetic to pass over the potential barrier associated with wake perturbations with little deviation of their trajectories. In this section, a second class of ions are considered which have velocities near the phase velocity of the potential wave (barrier). These particles rebound from the potential barrier and therefore suffer large

angle deflections. Such particles may become trapped by the potential wave, thereby absorbing energy from it and contributing to its decay; i.e., Landau damping.

By calculating the density of trapped ions and the rate of energy transfer to them, Rand arrives at the following conclusions:

(1) Unless $T_e/T_i \geq 10$, damping will become significant at approximately a Mach number of Debye lengths downstream. (Within the ionosphere, where $T_e/T_i \simeq 2$, this would predict the wake to be smoothed within a meter).

(2) As T_e/T_i increases above a value of about 10, damping becomes rapidly insignificant.

(3) Once damping begins, the wake decreases as Z^{-2}.

(4) The degree of damping predicted should hold when the line charge is replaced with a large body ($R_o/\lambda_D > 1$), since damping depends on plasma parameters and the velocity but not the shape of the body.

Rand states that the results of this analysis may depend strongly on the form of the ion distribution function.

As a final comment on Rand's work, it should be pointed out that the analysis was carried out only to linear terms in potential and the assumption quasineutrality leads to a description of the wake as an ion-plasma oscillation; i.e., the wake results totally from collective plasma wave mechanisms. Therefore, effects which produce a large charge separation, such as the negative potential well in the ion void region immediately behind the body and ion streams deflected by the plasma sheath fields, are not allowed. In fact, Rand's prediction of trapped ions associated with potential waves is suggested as an explanation by Vaglio-Laurin and Miller [6], for the observation of "apparent" pseudowaves in cold plasma laboratory experiments (Appendix E.7). This explanation is shown to be unviable in Chapter IV.C.

3. Lam and Greenblatt (1964, 1965)

A general hydrodynamic theory was developed by Lam for the steady flow of a weakly ionized gas around an arbitrary solid body with a charge absorbing surface [7]. This theory is of limited use, however, since the fluid was required to be collision dominated and highly subsonic (to be incompressible). A less restrictive theory was developed by Lam and Greenblatt [8] in which the fluid is collisionless and the only necessary assumptions are that it is cold ($T_e/T_i >> 1$), steady, subsonic with respect to electrons ($V_o << \hat{c}_e$), behaves as a perfect gas and, the flow is laminar (no crossing ion trajectories). It must also be assumed that there are no magnetic fields and that the body absorbs all incident charge, that it is large ($R_o/\lambda_D >> 1$) and biased highly negative ($-e\phi_b/kT_e >> 1$).

From the continuity and momentum equations, expressions are obtained for the velocity potentials, $\psi_{i,e}$, of the form:

$$\nabla^2 \psi_{i,e} = \beta \nabla \psi_{i,e} \cdot \nabla \left(\frac{1}{2} \nabla \psi_{i,e} \cdot \nabla \psi_{i,e} \right) ,$$

where $\beta = (m_i u^2/kT_e)$. This is exactly the form of the governing equation for the irrotational, isothermal compressible flow of classical gas dynamics. (The fact that the plasma flow is irrotational is shown by taking the curl of the ion momentum equation which, for this case, has only $q/m_i \nabla\phi$ as a force term [equation (A-13)].

The boundary conditions consist of defining the electric potential to be a constant, Φ_b, at the surface of the body and zero in the ambient medium. However, the transition form Φ_b to $\Phi = 0$ occurs through two regions; i.e., a thin sheath region immediately adjacent to the body, in which $n_i \neq n_e$, and a quasineutral region beyond the sheath in which $n_i \simeq n_e$. In the outer, or ambient region, $\Phi = 0$ and $n_i = n_e = n_o$. A more detailed investigation of the sheath and quasineutral zones is presented in a second publication by Lam and Greenblatt [9].

Subject to the above assumptions, Lam and Greenblatt [8] arrive at the following results and conclusions:

(1) When there is no net charge flux to the body, the body potential is less than the potential at the edge of the sheath ($\Phi_b < \Phi_s$) and hence a sheath will always exist for this condition.

(2) The sheath vanishes for Φ_b less than a certain value of order unity (for $R_o/\lambda_D \gg 1$).

(3) If $\Phi_b = 0$, the potential distribution within the sheath will be nonmonotonic.

(4) A negatively charged body will create a region of positive space potential far down stream on the wake axis. The value of Φ in this region is $(m_i V_o^2/2kT_e) \equiv S^2$.

It should be mentioned that the theory of Lam and Greenblatt cannot be applied to the near wake because the condition of laminar flow (ion trajectories must not cross in order to be associated with streamlines of the fluid theory) is not met there. Similarly, it cannot account for effects in the mid- and far-wake zones if streamlines are crossed (e.g., pseudo waves consisting of ion beams passing through the ambient plasma). Further, the treatment assumes no significant absorption of electrons by the body (hence the requirement $-\Phi_b \ll 1$). Therefore, the flow interaction with bodies having potentials ranging from slightly negative to positive cannot be described.

4. Sanmartin and Lam (1971)

The fluid theory developed by Sanmartin and Lam is of interest because it gives the asymptotic structure of the far wake behind a charged body moving through a collisionless, uniform plasma. All perturbations are assumed small and a wave equation is derived from the linearized continuity and momentum equations and Poisson equation. A dispersion relation is then obtained and analyzed to determine the possible excitation of electrostatic ion waves and the evolution of wave fronts in the far wake. The assumptions required are:

(1) $\Phi \ll 1$.

(2) $T_e/T_i \gg 1$.

(3) $(T_i/ZT_e) \ll S^2 \ll (m_i/m_e)$.

(4) $R_o/\lambda_D \ll 1$.

(5) $V_o \ll \hat{c}_e$.

(6) The body is small compared to the width of the wave front; i.e., on the wake axis $(x/z = 0)$ $R_o/\lambda_D \gg z^{-1/2}$ while for $0 < x/z < \hat{x}$ where $\hat{x}$ is the wave front position, it is required that $R_o/\lambda_D \gg z^{-1/3}$.

Subject to the above assumptions, the Sanmartin-Lam theory produces the following results and conclusions:

(1) For $S > 1$, a steep wave front develops at an angle to the wake axis of $\theta = \tan^{-1}(S^{-1})$.

(2) Transversely, the wave front behaves as the derivative of the Airy function squared and has an amplitude of order Z^{-1} and grows in width as $Z^{1/3}$.

(3) Behind the wave front is a broad region where ion waves occur and decay as Z^{-1}.

(4) Near the axis, a second wave front develops with a transverse structure proportional to the Airy function times a sine function and of order $Z^{-5/6}$ in amplitude. The width of this wave also grows as $Z^{1/3}$ and the angle to the wake axis vanishes at $(T_i/T_e)^{3/4}$; i.e., this is a curved, divergent wave front.

(5) Between the trailing wave front and the wake axis, the plasma is quasineutral with a Z^{-2} decay law for ion plasma waves.

(6) Wave fronts may also develop for $S < 1$. The structure is similar to that for $S > 1$ with the addition of curved, transverse wave fronts behind the initial wave front.

(7) The results for $S > 1$ are readily extended to the hypersonic $(S \gg 1)$ case.

(8) The rate of damping of all waves is inversely proportional to S. For a warm plasma, ion Landau damping increases with wave number and is minimized at the Mach cone for $S > 1$.

(9) The trailing wave front is more strongly damped than the leading wave front.

The form of the wave fronts for a cold plasma is shown in Figure B-3(a) and (b), while the angle of the initial wave front as a function of Mach number is given in Figure B-3(c). The modification produced by warm ions is shown in Figure B-4.

It should be noted that in contrast with the theory of Lam and Greenblatt, the Sanmartin-Lam theory allows for crossing stream lines by inclusion of a pressure term in the ion momentum equation. They point out, however, that the results of this linear theory may be significantly modified by the inclusion of nonlinear terms. In three-dimensional flows, if the linear wave front is valid, it will always remain so; however, in two-dimensional flows, nonlinear terms can grow to the same order as the linear terms and hence the linear wave front structure breaks down.

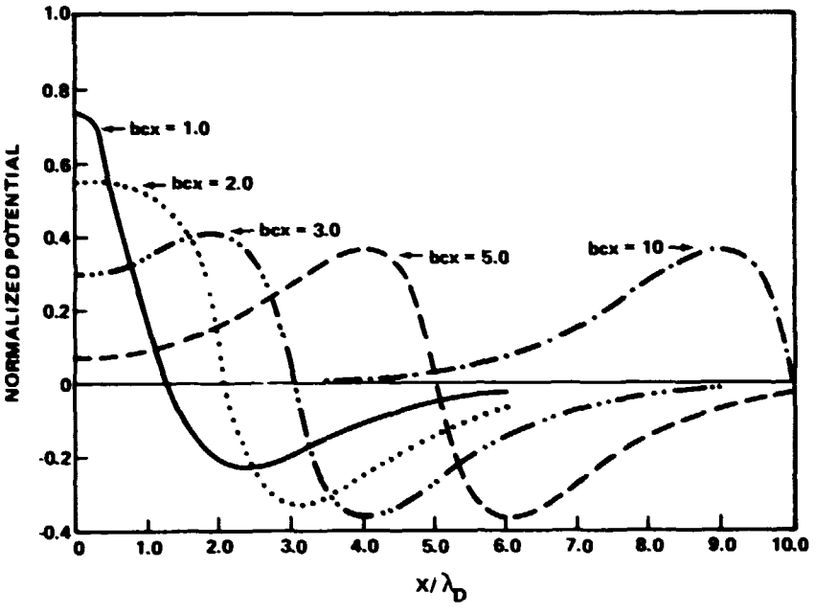

Figure B-1. Potential profiles at various distances downstream from a small cylinder for $T_i >> T_e$. Note: $b_c z = (z/\lambda_D)\ (T_i/T_e)^{1/2}/S$, after Rand [4].

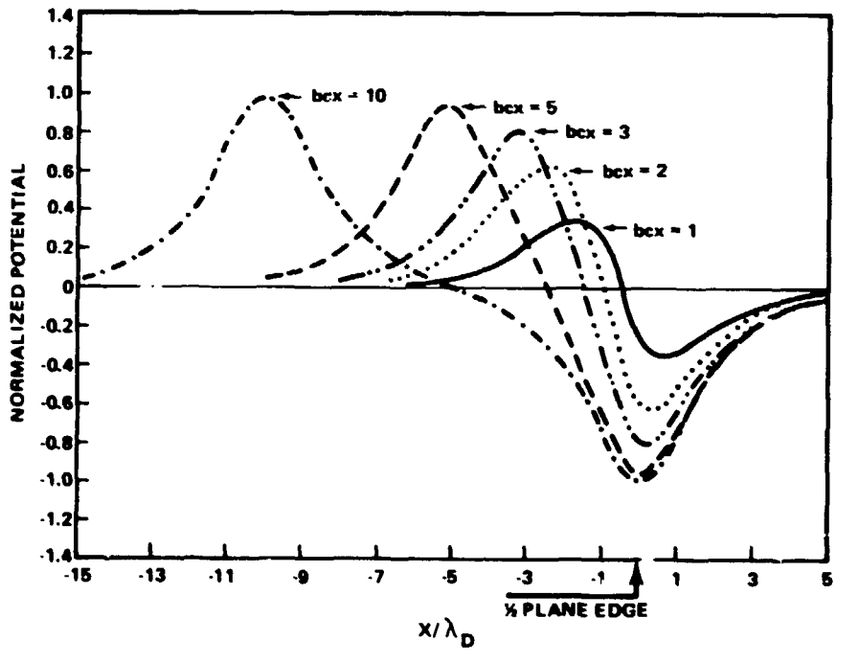

Figure B-2. Transverse potential profiles as above, in Figure B-1, but for a half plane, after Rand [4].

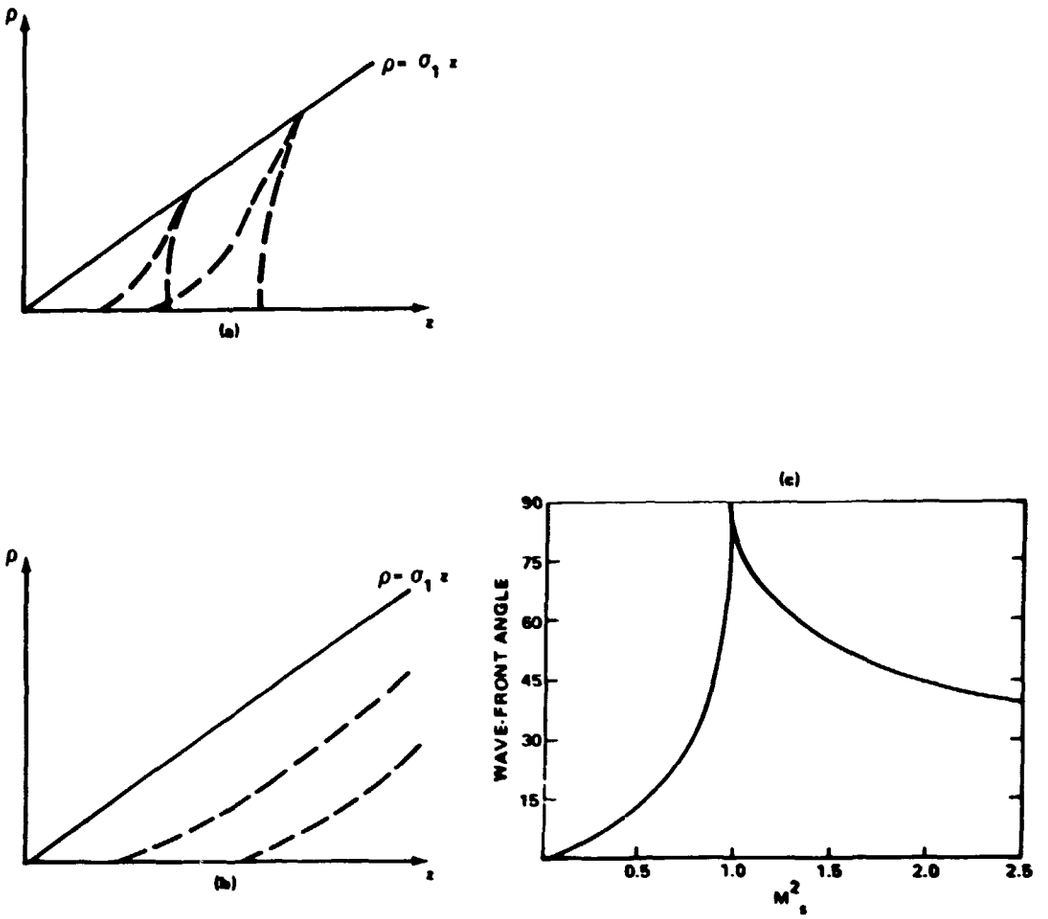

Figure B-3. Steady-state wave patterns for $T_e/T_i \gg 1$ and (a) $S < 1$; (b) $S > 1$; (c) leading wave front angle versus S with $T_e/T_i \gg 1$, after Sanmartin and Lam [10].

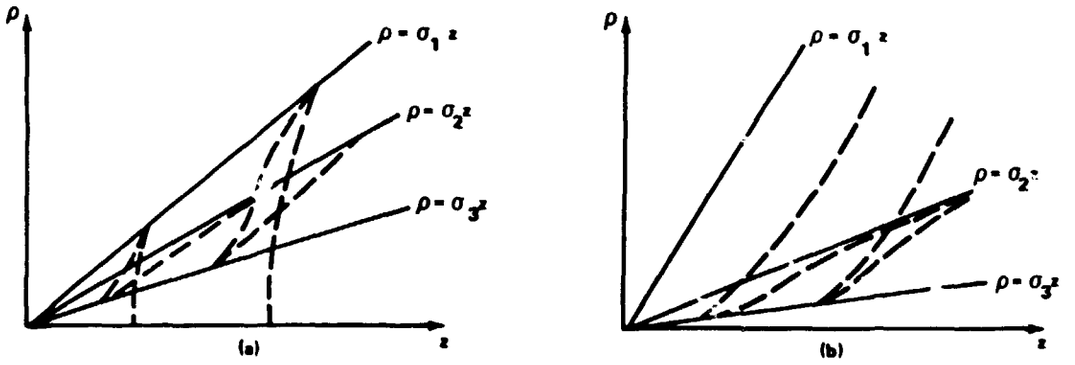

Figure B-4. Steady-state wave patterns with $T_e/T_i \ll 1$ for (a) $S < 1$ and (b) $S > 1$, after Sanmartin and Lam [10].

APPENDIX C. A CRITICAL REVIEW OF THE RESULTS FROM KINETIC TREATMENTS

In Appendix B, we have seen that continuum calculations are, almost without exception, limited to the solution of linearized sets of equations. Inclusion of nonlinear terms, while possible, would prevent uncoupling of the equations and therefore require solution by numerical techniques. The advantages of a closed, analytical solution would then be lost and the more exact kinetic theory may as well be used.

In this Appendix, we will consider only those theories which provide results in a useful parameter range and in a form which lends itself to comparison with experimental measurements. There are a number of other calculations available; however, due to the extreme complexity of the numerical programs involved, the results of these calculations are not easily altered to obtain a more meaningful solution (as was done with Rands theory, for example). It is therefore necessary to accept the results as they are given.

The techniques applied in kinetic theory make use of the fact that the characteristics of the Vlasov equation, on which the distribution function, f, remains constant, coincide with the trajectories of single ions. The numerical approaches can be divided into two basic groups: (1) the "outside-in" method, which follows the ions in time from the undisturbed medium upstream of the body, through the region of disturbance and (2) the "inside-out" method, which follows the ions from a point of interest within the disturbed zone, back upstream to the undisturbed medium.

The outside-in method is of two types: the "fluxtube" technique and the "super particle" technique. The fluxtube technique assumes the flux of

particles in a small tube, defined by two neighboring ion trajectories, to be constant. Since the two trajectories (characteristics of the Vlasov equation) define the cross-sectional area of the tube and the ion velocity is known along the trajectories, the ion density can be calculated anywhere within the flux tube. This technique has been used by Davis and Harris [11], Call [12], Martin [13], and McDonald and Smetana [12]. It has the advantage of greatly reducing the number of trajectory calculations required, and hence computational time. However, it does not allow for crossing trajectories and is therefore not realistic in all regions of the plasma wake; it is suitable orly for cold ion streams, and a distribution function must be assumed for the electrons.

In the super particle (or weighted deposition) technique, the plasma flowing into the region of interest is divided into a large number of discrete packets containing many particles. Each packet is assigned the total mass and charge of the particles it contains and is treated as a single super particle. The trajectories of the super particles are followed through the region of interest which is divided into spatial cells. When the trajectory of a super particle passes through a cell, its density and charge are considered to occupy the entire cell uniformly and are weighted by the amount of time the super particle spends in the cell. By considering the contribution of all trajectories to each cell, the complete number density distribution in the region of interest can be constructed. This technique accounts for the possibility of crossing trajectories and is adaptable to time-dependent computer simulation. However, many trajectories are required to obtain good statistics and the technique is therefore time consuming. This technique has been used by Parker [15], Maslennikov and Sigov [16,17,18] and Maslennikov, et al. [19]. Again, a Maxwellian distribution function must be assumed for the electrons.

The inside-out method was developed by Parker [15]. It is very flexible and has the advantages that the points to be evaluated can be chosen and only trajectories intersecting these points need be calculated; it is suitable for either ions or electrons, and it accounts for crossing trajectories. However, information carried by the trajectories is lost from point-to-point and

the process is therefore very time consuming. This technique has been used by Taylor [20], Parker [21], Parker and Whipple [22], Fournier [23], and Grabowski and Fischer [24] (who assumed quasineutrality).

Although some simplifying assumptions will be used in each case discussed in this appendix, the kinetic approach is not restricted by any fundamental underlying assumptions of the type which were necessary to obtain the fluid equations in Chapter II.A.1.b. The usual simplifying assumptions are:

(1) Steady state conditions, i.e., $\partial/\partial t \equiv 0$.

(2) A collisionless medium, i.e., $\lambda >> R_o$.

(3) No magnetic effects.

(4) A perfectly absorbing body surface.

(5) A uniform negative surface potential on the body.

(6) A Maxwell-Boltzmann electron distribution; i.e., $n_e = n_o \exp[\alpha \phi]$.

(7) $T_e/T_i >> 1$.

(8) $V_o << \hat{c}_e$.

(9) Axial or cylindrical symmetry.

Additional assumptions or exceptions to these usual assumptions will be pointed out in the discussion below.

1. Davis and Harris (1961)

The calculations by Davis and Harris are of interest because they represent the first attempt to include the electric potential in a self-consistent way [11]. The numerical solution made use of the usual assumptions to calculate the ion density and electric space potential around spherical bodies of $R_d = 10$ and 25 with the surface potential (left as a parameter) ranging from -20 to $-10^3\ kT_e$.

The numerical method used consists of following ions along trajectories beginning in the undisturbed plasma and passing into the disturbed zone (outside-in method). The process proceeds by assuming an arbitrary ion density distribution, calculating the space potential from the Poisson equation,

following ions along trajectories passing through the region of interest to determine the velocity distribution, and, finally, calculating a new density by using the continuity equation. This process is iterated until the solution converges.

The predicted effects of bodies of $R_d = 10$ and 25 include:

(1) The body is almost surrounded by a positively charged sheath produced primarily by repulsion of electrons.

(2) The shielding distance of such highly biased bodies may extent many Debye lengths into the medium.

(3) A low ion density occurs in most of the space downstream from the body.

(4) This rarefied zone may extend to a larger diameter than that of the body.

(5) Near the axis, there exists a region of high positive space charge density which extends far downstream (resulting from ions focused onto the axis by the highly attractive body potential).

(6) In the near wake a small region of negative space charge exists where the ions have been swept out by the bodies motion.

The results of the Davis-Harris calculations are subject to large error due to the coarseness of the grid size used and therefore must be taken only as a very qualitative indication of the processes involved.

2. Maslennikov and Sigov (1965, 1967, 1968, 1969)

A numerical solution using the super particle technique was developed by Maslennikov and Sigov for axially symmetric bodies in a rarefied plasma flow [16]. This treatment makes the usual assumptions, given above, and provides a self-consistent electric potential field. The potential on the body is left as a parameter. The numerical iterations are very similar to those of Davis and Harris, discussed above.

Collisionless plasma flow around spherical bodies was investigated in their first paper [16] for the conditions $S = 4.4$, $R_d = 1$, $\Phi_b = 0$, and $S = 1.1$, $R_d = 1$ and $\Phi_b = 0$. These results are shown in Figures C-1(b) and (c). It is interesting to note that, although no magnetic effects are considered, the space potential oscillates in the wake for both cases. The wavelength of these oscillations is obviously proportional to S. Their amplitude decreases with Z. The region of positive space potential would appear to agree qualitatively with the ion current peaks predicted by the fluid theory of Lam and Greenblatt [9]. However, the locations of these regions do not appear to agree with the results of kinetic treatments by Taylor [20], Call [12], and Martin [13], who also predicts axial enhancement of ion current and potential.

The most detailed results of the Maslennikov-Sigov theory are given in a 1967 paper [17]. These results, all obtained for spherical bodies, are shown in Figures C-1, C-2, and C-3. Figure C-1 gives space potential profiles on the XZ-plane for a variety of conditions. The following observations were made:

(1) For $\Phi_b = 0$, a region exists immediately behind the body which is void of ions but which remains populated by electrons. The depth of the potential well thus created depends on $(kT_e/m_iV_o^2)$ and R_o.

(2) Oscillations of ρ_c and Φ are observed to some extent for all values of Φ_b, but particularly for $\Phi_b = 0$ and $R_d = 1$ (Figure C-1(c)). The amplitude of these oscillations depends on $(kT_e/m_iV_o^2)$, Φ_b, and R_o.

(3) For $\Phi_b < 0$, the focusing of the ions by the attractive body force dominates the wake so that the ion void region is replaced by an axial ion peak. A corresponding change occurs in the Φ-field (Figure C-1(d) and (f)).

Figure C-2 shows the perturbed ion trajectories in the flow field surrounding the body for a variety of conditions. Note that the data for Figure C-2(a) and (b) correspond to the potential profiles shown in Figure C-1(c) and (d), respectively. Maslennikov and Sigov point out the very obvious occurrence of orbital ions (or quasifinite trajectories). Recall that the majority of theoretical studies do not allow crossing trajectories and therefore

do not show this effect. The orbital ions occur for $\Phi_b << -1$ and can be associated with an impact parameter δ ; i.e., trajectories passing within a critical range of distance from the body. This effect occurs for the cases shown in Figure C-2(b) and (c). Figure C-2(d) provides an expanded view of the critical trajectories of Figure C-2(c).

Although not discussed by Maslennikov and Sigov, an additional property of the ion trajectories is very apparent in their data. The ions passing near the body are deflected through a relatively large angle and cross the axis in the near wake. The velocity component normal to the wake axis, $v_\perp$, for these ions is sufficiently large so that the resulting kinetic energy is greater than the potential barrier on the wake axis; i.e., $1/2\ m_i v_\perp^2 > e\phi$. However, the ions passing farther from the body experience a smaller attractive force, are deflected through a smaller angle and intersect the wake axis farther downstream. It is apparent then that since there are regions of positive space potential on the wake axis (Figure C-1) that at some point down stream, the condition $1/2\ m_i v_\perp^2 \leq e\phi$ will arise. At this point, the ions will be repelled from the axis and travel back into the ambient medium. This effect is shown clearly by Figures C-2(a), (b), and (c), and graphically illustrates the explanation given by Hester and Sonin [34,52] for the repeated occurrence of trailing shock type structures in the wakes of small cylinders (this is discussed in Appendix E.g.1).

Figure C-3 shows ion current profiles calculated at $z = 1.4\ R_o$ downstream from a spherical body with $R_d = 0.08$ and $S = 1.4$. The calculations were carried out for a variety of body potentials and presented in the same format as the data by Hall, Kemp, and Sellen [46] (Figure E-4, Appendix E.1.c.). For $\Phi_b << -1$, in addition to the dominant axial ion peak, two additional ion peaks begin to appear off axis. This was observed experimentally by Hall, Kemp, and Sellen [46], but even more clearly by Hester and Sonin [34, 51-53] (Figure E-13(b) of Appendix E.1.g). Hall, Kemp, and Sellen did not provide the necessary measurements to evaluate scaling parameters; however, the splitting off of the two additional peaks in the

Hester-Sonin experiment occurred at $z/R_o < 7$ for $\Phi_b = -20$. The calculations of Figure C-3 are carried out at $Z/R_o = 17.5$ and the division occurs for $\Phi_b = -24$ and -38.6. Therefore the comparison is quite good.

3. Taylor (1967)

Taylor calculated potential and ion density profiles downstream from an infinitely long, rectangular cylinder oriented with its axis normal to the plasma flow direction [20]. All of the usual assumptions were made with the exception that the thermal motion of the ions was considered with $T_i = T_e$.

A closed zeroth-order solution of number density, $n_j^{(0)}$ and potential $\Phi^{(0)}$, was obtained for neutral ions (i.e., no E-field effects for ions) with $T_i = T_e$. A first-order ion distribution function was then found by the inside-out method. The first-order distribution function was integrated at a number of points to obtain the $n_i^{(1)}(x,z)$ profiles. The potential, $\Phi^{(1)}$, was then obtained from Poisson's equation.

The main results of Taylor's calculations are as follows.

(1) In the frontal region, $n_i^{(1)} < n_i^{(0)}$. This is explained by the fact that the E-field accelerates the ions, increasing their speed, and hence decreasing their density according to the continuity equation. There is no contribution from reflected particles due to the total absorption assumption. (This effect was also found by Stone and Sheldon [2].)

(2) The first-order solution, $n_i^{(1)}$, fills the ion void region, swept out by the body, faster than $n_i^{(0)}$, resulting in the region becoming shorter but wider. This is shown by the transverse profiles in Figure C-4. Note also that there is no change in $n_i^{(0)}$ at the geometric wake edge as a function of Z. This agrees with Rand's results for the large disk when they are altered for $T_i = 0$.

(3) A potential well occurs in the wake. The location of this potential minimum moves toward the body as Φ_b becomes more negative and seems to attach to the rear surface of the body for $\Phi_b = -1$.

(4) An axial $n_i^{(1)}$ peak occurs in the wake, for small $\Phi_b < 0$, beginning approximately at $Z = S R_o$ [Figure C-5(a)]. This is attributed to a focusing effect for ions produced by the attractive potential on the body. This explanation is supported by the fact that the strength of the focusing effect is proportional to $-\Phi_b$. By increasing the negative bias to $\Phi_b = -14$, the axial ion current peak was drawn sufficiently close to the body to observe its overall nature [Figure C-5(b)]. It was found to reach a maximum value of $0.9\, n_o$ (for $T_i = T_e$) and divide into a trailing "V" structure further down stream. The apex of the trailing V was located at $S R_o$ (where the axial ion peak begins to grow). Its half angle was $\simeq 10°$ [which is approximately $\sin^{-1}(1/s)$] and its thickness was on the order of a Debye length.

It should be pointed out that Taylor carried out the iteration procedure only to first order. There is, therefore, no indication of whether the solution is convergent and the electric potential is not self-consistent. However, in spite of this, his results agree well with other theoretical treatments of the problem. In fact, the trailing V structure is also found in the results of Maslennikov and Sigov [17,18] and Alpert, et al. [25]. The important contribution of Taylor's calculations is to show that this effect remains very much in evidence for $T_i = T_e$ and is therefore not restricted to cold plasma flows.

4. Gurevich, Pitaevskii, and Smirnova (1969)

In addition to the usual assumptions, the calculations by Gurevich, et al. [26] assume quasineutrality, that both ion and electron distributions are proportional to a Boltzmann factor, and that the axial (in the flow direction) component of ion velocity is constant. Note that the effect of assuming quasineutrality is to ignore the sheath region and therefore the ion attractive body potential. As a result of these assumptions, the Gurevich, et al. calculations are very restrictive and of limited use. However, they provide results for different temperature ratios, T_e/T_i, and a unique calculation of the form of the ion distribution function downstream from a long plate with its surface oriented normal to the flow direction.

The effect of the temperature ratio was investigated for the case of a disk oriented normal to the flow direction. For $T_e/T_i = 1$, the results show a monotonic filling of the ion void region with increasing distance downstream. However, for $T_e/T_i = 4$, some enhancement of n_i occurred, centered on the wake axis. It was stated that the amplitude of the axial n_i = enhancement increased proportional to $(T_e/T_i)^{1/2}$ for $T_e/T_i > 1$. The regions of minimum ion concentration existing on either side of the axial n_i enhancement were said to diverge at the angle given by $\sin^{-1}(1/s)$, analogous to the Mach cone in hydrodynamics.

The ion distribution function was given in the disturbed region downstream from a long conducting plate at the transverse position $x/R_o \simeq 0.4$ ($x/R_o = 0 \equiv$ center of the plate) and a variety of axial distances Z/R_o. The resulting "two-peak" distributions (Figure C-6) will be discussed in a later section in conjunction with experimental observations.

5. Call (1969)

The calculations by Call [12] apply the usual assumptions to essentially the same kinetic approach used in the studies discussed above; i.e., ion trajectories are calculated to obtain a solution to the Vlassov equation and hence the ion density which in turn is used to obtain the electric potential through the Poisson equation. However, Call applied a more efficient numerical method which makes use of the flux tube concept of parallel flow in classical gas dynamics. The flux tube method requires only 2 to 5 trajectories per cell to obtain an accuracy of 5%. This is an order of magnitude better accuracy per unit of computer time than obtained by the super particle technique used by Maslennikov and Sigov. The main disadvantage of the flux tube method is that it does not allow trajectories to cross flux tube boundaries; i.e., adjacent ion trajectories cannot merge or cross and no reversal of the velocity component in the flow direction, v_z, is allowed. The result is that none of the semi-infinite trajectories found by Maslennikov and Sigov would be allowed to occur.

The parameter range investigated by Call includes $0.2 \leq R_d \leq 25$ $-40 \leq \Phi_b \leq 0$ and $1.1 \leq S \leq 6$. The body potential, Φ_b, is treated as a parameter although, according to Call, the floating potential can be estimated by $\Phi_{bf} \cong \ell n[(2\pi)^{1/2} V_o A/S]$, where A is the cross-sectional area and S is the total surface area of the body.

The most important results of the study are as follows:

(1) The length of the ion void region behind the body is determined by the point on the Z-axis where the trajectories, which just graze the body, cross. Assuming $T_i = 0$, $\Phi_b = 0$, and $\Phi = 1$, within the void region, this point is given by: $(z_{min}/\lambda_D) = 2(R_o/\lambda_D)^{1/2} (m_i V_o/2kT_e)^{1/2}$.

(2) The ion void region is almost void of electrons as well. Therefore, the local Debye length is greatly increased.

(3) For cylindrical or planar bodies oriented normal to the flow with $R_d \sim 1$, ions which are deflected by the sheath electric field, cross at the wake axis, and create a positive space potential. The crossing ion trajectories are focused by this perturbed field and emerge on the other side of the axis as narrow beams which are distinct from the two broad streams covering the remainder of the wake (Figure C-7).

(4) The ion beams occurred in all solutions for $R_d \sim 1$ and it was observed that their width, density, and angle to the flow direction increased with Φ_b [Figures C-7(b) and (c)]. For $R_d = 0.21$, $S = 3.2$, and $\Phi_b = -9$, Call found the angle of the ion beams (0.35 radian), to compare well with the diverging V structure (0.34 radian) obscured by Hester and Sonin (Appendix E.1.g).

(5) The beams were absent in the wakes of large bodies ($R_d \sim 25$). This presumably results from smaller ion density gradients, which allow electrons to neutralize any potential disturbance and, hence, no focusing of the ion trajectories occurs.

(6) In the case of axially symmetric bodies, the wakes of a sphere and disc are essentially the same except very near the body. This observation has been confirmed by experimental studies [78] and allowed a considerable simplification to Call's calculations.

(7) Compared to the two-dimensional problem (i.e., a long flat plate or cylindrical body), the axial symmetry produces additional ion compression as trajectories converge on the wake axis. This creates a much stronger axial ion enhancement.

(8) A region of positive space potential is created by the axial ion peak, which repells ions from the wake axis and creates a second ion void region farther downstream with a corresponding negative space potential. This region attracts ions, creating a second ion enhancement still farther downstream. This oscillating behavior continues along the wake axis, decreasing in amplitude with increasing Z [Figure C-8(b)]. This effect seems analogous to the multiple wave fronts generated along the wake axis for small body in the theory of Sanmartin and Lam discussed in Section B.4 above.

(9) The amplitude of the potential oscillations along the wake axis are on the order of $-0.4 \leq \Phi \leq 0.4$.

(10) According to Call, the oscillitory structure does not occur for the two-dimensional case (i.e., long plate or cylindrical bodies) and indicates a fundamental difference in flows with and without axial symmetry [Figure C-8(c)]. However, this observation is not in agreement with the results of either Rand [4] (Section B.2), Fournier (Section C.6), or Hester and Sonin [34] (Appendix E.1.g), which show the same type of oscillatory structure in the wake of a long cylinder.

The implications of the flow fields shown in Figures C-7(a) and C-8(a) will be discussed in a later section in the context of experimental measurements. Call also included the effects of a magnetic field in some of the calculations. His conclusions are in agreement with those arrived at in this study on the basis of experimental results discussed in Appendix E.2; namely, that when the magnitude of B is appropriate with respect to ionospheric conditions, then $B_{\perp}$ has no effect on the near and intermediate wake regions and $B_{\parallel}$ has very little.

Call assumes steady flow conditions as do all of the treatments discussed (with the exception of Stone and Sheldon, discussed in Section 8 below). However, Call incorrectly justifies this assumption based on the apparent observation of steady-state conditions in experimental studies. It was shown

in Chapter III that the available experimental observations do not, by any means means, indicate steady-state conditions. It should also be remembered that the Call results are based on the assumptions of parallel flow (no crossing or reversing ion trajectories) and cold ions ($T_i = 0$).

G. Fournier (1971)

The calculations by Fournier [23] utilize what may be called a hybrid technique. The problem addressed is the usual Poisson-Vlasov system of equations and Fournier used the digital inside-out method of computation, developed by Parker [15], to solve the Vlasov problem for ions. However, the electric potential was obtained by solving the Poisson equation on an analog computer. When electrons could be considered to have a Maxwell-Boltzmann distribution, the electron density was obtained on the analog machine as well. This hybrid approach has the advantage that the potential and electron density, which constitute a time-consuming "minor" iterate in a purely numerical computation, are obtained without iterating and are supplied to the digital computer as parameters for the numerical ion density computation. Major iterates, in which the ion distribution is obtained (usually only two to five were required) were carried out between the two machines until the solution converged.

The usual assumptions are made (body geometry is limited to an infinitely long circular cylinder) with the exceptions that (1) $V_o << \hat{c}_e$ is not required, although most results fall into this range, (2) there is, in principle, no restriction on the temperature ratio, T_e/T_i, which is varied from 1 to 10, and (3) a Maxwell-Boltzmann electron distribution is not essential. Although the last assumption is used when permissible, for economic reasons, the electron Vlasov problem can be solved by inside-out trajectory analysis, just as the ion problem, in regions where the electrons are significantly disturbed.

The boundary conditions are obtained by inverting real space to a unit circle; i.e., $X \equiv (\rho/R_o)^{-1}$, where ρ is the real space radial distance. With this transformation, the boundary conditions become:

(1) $\Phi = \Phi_b$ (a constant) on the unit circle, $X = 1$, corresponding to the body's surface.

(2) $\Phi = 0$ on the circle $X = X_o < 1$, corresponding to distant points in real space beyond the zone of disturbance.

(3) $\partial\Phi/\partial\theta = 0$ for $\theta = 0$ or π, corresponding to the wake axis, which constitutes a boundary since it is only necessary to evaluate conditions at points in a half plane.

The results of Fournier's calculations provide additional insight into the effect of the parameters R_d, S, Φ_b, and T_e/T_i on the behavior of the space potential, Φ, and the charged-particle densities n_i and n_e. Specifically, the following conclusions are obtained:

(1) For $\Phi_b < 0$, the sheath thickness upstream (defined by $\Phi/\Phi_b = 0.1$) may be decreased by as much as four times from its value for a quiescent plasma by the supersonic nature of the ion flow.

(2) As Φ_b becomes increasingly negative, the contours of constant, Φ, which are elongated downstream for less negative values of Φ_b, become more circular (Figure C-9). This agrees with the experimental observations of Hall, Kemp, and Sellen (see Appendix E.1.c).

(3) When Φ_b becomes positive with respect to the floating potential, the upstream sheath vanishes and the body potential field extends far into the plasma (Figure C-9). This apparently results from extensive absorption of electrons by the body. This being the case, it should also be noted that the Boltzmann assumption for electrons ($n_e = n_o \exp[\Phi]$) is no longer valid for this condition.

(4) A potential well ($\Phi < \Phi_b$) was found to exist in the near wake for three cases evaluated by Fournier [see Figure C-9 for $\Phi_b = +3$ and 0 and Figure C-11 (b)]. It was concluded that the necessary conditions for the existence of a potential well are $R_d > 10$ when $\Phi_b < -2$ and $R_d \gtrsim 1$ when $\Phi_b > -2$. This observation was made by independently varying Φ_b (Figure C-9) and R_d (Figure C-11) and also agrees with the theoretical results of Call [12],

Jew [83] and Parker (Section C.8). To the authors knowledge, there has been no experimental verification of the existence of a potential well.

(5) The development of deflected ion streams passing through the wake and diverging into the ambient medium is apparent in Figure C-9, for sufficiently negative body potentials. This occurs, then, for small bodies (R_d = 1.5) even though ion thermal effects are included ($T_i = T_e$).

(6) The effect of the T_e/T_i ratio is shown in Figure C-10. All other parameters being the same, ion thermal motion is seen to have the opposite effect of the negative body potential; i.e., as T_e/T_i decreases, the equipotential contours become elongated downstream. Similarly, the rather complex ion density contours which occur for $T_e/T_i = 10$ are smoothed as T_e/T_i decreases. It should be noted, however, that ion density profiles are still non-monotonic for $T_e/T_i = 2$, which is approximately the ratio occurring in the lower ionosphere (300 to 1000 km altitude).

In addition to the above findings, Fournier also corroborates Calls prediction (Section C.5) of an oscillating structure on the downstream wake axis for small bodies at low Mach numbers. However, where Call gave potential contours for $T_i = 0$, Fournier gives n_i contours for $T_e/T_i = 1$.

Finally, it should be pointed out that while the calculations by Fournier are the most general so far in regards to the restrictions on the plasma conditions, they are restricted to a two-dimensional problem; i.e., an infinitely long, cylindrical body. Also, there are areas of disagreement; e.g., Fournier concludes that the mid-wake structure for cylindrical bodies is significantly different from that of a long flat plate normal to the flow. This is not in agreement with the findings of Call [12].

7. Martin (1974)

The calculations made by Martin [13] use the numerical technique developed by Call [12] and are subject to the same assumptions (see Section 5 above). Therefore, the results of Martins calculations serve to extend those obtained by Call to provide additional insight into the electrostatic nature of

plasma flow interactions with two-dimensional (long plate) and axisymmetric (disk) conducting bodies. Transverse ion density profiles at a variety of axial positions downstream from both bodies were calculated for $R_d = 1$ and 0.2 with $S = 3.5$ and $\Phi_b = -5$. Additional calculations were made for a variety of conditions and are presented in the context of a parametric study. The main results are shown in Figures C-12 through C-16.

Figures C-12(b) and C-12(c) give the transverse ion density profiles for the plate and disk respectively under the conditions $R_d = 1$, $S = 3.5$, and $\Phi_b = -5$. Part (a) shows the wake structure observed schematically. Notice the two types of wave structure found (indicated with "d" and "w"). Apparently the d peaks result from ion trajectories deflected across the wake by the electric field in the sheath while the w peaks consist of ion trajectories which have been deflected less by the sheath field and, therefore, having a smaller transverse component of velocity, are redeflected away from the wake axis by the space potential associated with the dominant axial ion enhancement. [See the discussion of the Maslennikov and Sigov calculations in Section (C.2) above.] The axial ion peak is much greater for an axisymmetric body than a plate (proportional to $2\pi R_o n_o$ rather than $2n_o$) and, hence, a larger space charge potential develops. Therefore, fewer ions are able to penetrate the wake and contribute to the d peak for an axisymmetric body, most of them being deflected to create a strong w peak. For the two-dimensional case of the long plate, the opposite is true. The space potential on the axis is weaker, allowing most of the particles to penetrate and form a strong d peak while few ions are deflected from the axis to form a w peak. This can be seen by the relative peak heights shown in Figure C-12(b) and C-12(c).

Figure C-13 shows the effect of the ion acoustic Mach number, S, on the axial crossing point for the most strongly deflected ion trajectories, Z_d, and two wave angles θ_d and θ_w [see Figure C-12(a) for definition of terms]. The crossing point is clearly proportional to S while the angle, θ_w, follows the Mach angle closely. However, the angle θ_d, is not well defined in terms of S for small values.

Figure C-14 shows the effect of Φ_b on Z_d and the angles θ_d and θ_w. Again, θ_w strictly follows the Mach angle and is unaffected by Φ_b. Note that θ_d is linearly dependent on Φ_b, while Z_d appears to have a $\Phi_b^{-1/2}$ dependence.

Transverse profiles of ion density are shown for both bodies in Figure C-15 for the conditions: $R_d = 0.2$, $S = 3.5$, and $\Phi_b = -5$. Note that the strength of the wake perturbations is greater than for $R_d = 1$ (Figure C-12). Also, no Mach cone (θ_w) structure is evident, although this may be concealed by the large axial enhancement. The other striking difference is the large increase in the strength of the d peak for the disc, indicating a greater number of ions are able to cross the wake axis. Also note that the angle of the d peak is reduced for both bodies in Figure C-15, indicating θ_d is proportional to R_d.

Details of the influence of R_d on Z_d and θ_d are shown in Figure C-16. The crossing point, Z_d, is not proportional to $R_d^{1/2}$ as stated by Martin, but depends more closely on $R_d^{0.66}$ (determined empirically from the data points of Figure C-16).

By assuming the electric field, E, to be constant in the ion void region and proportional to Φ_b acting over some distance r, Martin arrived at an approximate expression for Z_d; i.e.,

$$Z_d = (2S^2 R_d/E)^{1/2} \sim S(R_d/\Phi_b)^{1/2} \quad .$$

However, this expression omits the distance, r, over which Φ_b acts and thereby gives the incorrect $R_d^{1/2}$ dependence for Figure C-16. One would expect r to depend on R_d in some way. If we assume the electric field to be given by $C\Phi_b/R_d^{\xi}$, where C and ξ are constants, then substitute this into the above formula and equate it to an empirical fit of the points given for Z_d in Figure C-16 we have:

$$Z_d = \left(2S^2 R_d^{1+\xi}/C\Phi_b\right)^{1/2} = 3.16\, R_d^{0.66} \quad .$$

Then

$$Z_d \cong SR_d^{0.66}/(2\Phi_b)^{1/2} \quad .$$

The S and Φ_b dependence indicated in this formula are confirmed by the results given in Figures C-13 and C-14 while the R_d dependence has been tailored to the results shown in Figure C-16. It is interesting that the results of such a complex calculation agree so well with such a simple formula based on physical arguments. This expression is discussed further in Chapter IV.A.3 in the context of experimental results.

The same qualifying statements made concerning Call's results in Section (C.5) apply to the above results obtained by Martin. In addition, it should be mentioned that some of Martin's results do not seem consistent; i.e., it is stated that the deflected ion beams create a corresponding perturbation of the potential field for $R_d = 1$ but that no such perturbation of the potential field occurs for $R_d = 0.2$. Yet, the ion density profiles of the two cases indicate the density of the deflected ion beams to be greatest for $R_d = 0.2$. No explanation is given for this apparent inconsistency, which may indicate that the solution is not entirely self-consistent.

8. Other Calculations

The following calculations will be mentioned only briefly to indicate their contribution to the above discussion. Again, only aspects applicable to the present study will be discussed.

In a 1969 paper by Liu [27], calculations are made by assuming energy, angular momentum, and the component of ion velocity in the flow direction to be invariants and solving the resulting system of nonlinear integro-differential equations by numerical techniques. The near wakes of a large sphere and a large cylinder, oriented normal to the flow, were investigated. The results do not indicate any focusing of ions. However, the body potential was only slightly negative in all cases ($\Phi_b = -1$) and the solution was only carried

downstream to $Z = S \cdot R_o/2$, which is insufficient to observe mid-wake structure. Liu's calculations indicate the existence of a potential well for both bodies in hypersonic flow with $\Phi_b = -1$ and $R_d = 20$, which is consistent with the above results of Fournier.

The calculations by Liu and Hung [28,29] treat the far-wake distances created in a hypersonic plasma, first by a large axially symmetric body and, second, by two large axially symmetric bodies aligned with V_o and traveling some distance apart. This treatment assumes quasineutrality and small perturbations to linearize the Poisson equation and simplify the Vlasov equation. The resulting equations are solved by Fournier transformation techniques. With the exception of a difference in sign (which results in ion density rarefaction, rather than condensation, waves) the results for a single body are in qualitative agreement with the experimental results of Hester and Sonin (Appendix E). The effect of the second body traveling in the wake of the first is to enhance the density gradients associated with the wake disturbance. In both cases (single body and two bodies aligned with V_o) the effect of increasing T_e/T_i is to enhance the disturbance amplitude. Further, T_e/T_i is seen to affect the disturbance cone half angle since this is defined by $\theta = \sin^{-1}(1/S)$ for both cases.

Calculations have been made by Woodroffe and Sonin [30] which specifically treat the case of a long, very small diameter cylinder studied experimentally by Hester and Sonin (Appendix E). These calculations include the effects of Φ_b in a region near the body. Far downstream, the potential, Φ, is assumed small and the linearized Poisson equation used. The transition between the two solutions occurs when the potentials calculated by the Poisson and linearized Poisson equations are equal. The ion density in both regions is inferred from ion trajectory analysis (outside-in method). The far-wake solution is not iterated and should therefore not be self-consistent. This, coupled with the assumption of a cold ion stream ($T_i = 0$), may explain the unusually sharp potential and density gradients far downstream and the

general lack of dispersion. However, with this exception, the results compare very well with the experimental results of Hester and Sonin and appear to be physically reasonable.

The calculations by Stone and Sheldon [2] address the time-dependent hypersonic plasma flow interaction problem in one dimension; i.e., the body consisted of an infinite plate oriented normal to the flow direction. The inclusion of time dependence in this problem necessitated a simplified body geometry. However, the problem has application to the frontal region at the axis of symmetry of very large spacecraft and, to the author's knowledge, is the only time-dependent treatment of the spacecraft-space plasma interaction problem. The ion stream was assumed cold ($T_i = 0$) and the electrons were given a Maxwell-Boltzmann distribution. The resulting integro-differential equations were solved numerically. Two cases were treated: Case I — The body was grounded and then allowed to seek equilibrium conditions corresponding to the ionosphere at 200 km altitude, and Case II — starting with the equilibrium conditions of Case I, the plasma parameters were instantaneously changed to those corresponding to the ionosphere at 3000 km and new equilibrium conditions approached. The following results were obtained from these calculations:

(1) Equilibrium was reached from a grounded body (Case I) in 1.42 μsec while the transition from equilibrium conditions at 200 km to those at 3000 km (Case II) required 30.5 μsec.

(2) The surface charge density and sheath potential were found to overshoot early in Case II (at $t = 0.4$ μsec) and decrease monotonically to their equilibrium values (indicating the delayed response of the ion population).

(3) The equilibrium sheath thicknesses at 200 and 3000 km were 0.3 and 0.7 cm, respectively.

(4) The equilibrium floating potentials were 0.06 volts at 200 km and 0.5 volts at 3000 km.

(5) A depletion in ion density occurred in the sheath region for both cases (consistent with Taylor, Section C.3 above). The sheath thickness and floating potential values are low because the value of T_e used was a factor of 3 too small.

The most recent and, seemingly, the most general steady-state treatment of the plasma flow interaction problem was developed by Parker in 1976 [21]. This numerical program uses the inside-out method for ion as well as electron trajectory analysis (although electrons are considered Maxwell-Boltzmann where possible). It is not limited to a cylindrical body (as are the Fournier calculations) and should permit all possible physical effects (such as crossing trajectories and a variety of boundary conditions on the body; i.e., particle emission, finite conductive, etc.). The main drawback of this approach seems to be the extensive computer time required. To minimize this, Parker limited the ion trajectory analysis to 10 speeds, 10 radial angles, and 10 azimuthal angles and the boundaries of the region treated to $0 \leq r/R_o \leq 2.5$ and $0 \leq z/R_o \leq 6$ [31]. Unfortunately, this made the results too course to clearly observe any detailed mid-wake structure and, in addition, convergence in this region was poor. However the results generally comply with those to be expected in the near wake; i.e., a potential well is found for $R_d = 100$ and $\Phi_b = -4$ (consistent with Fournier, Section C.6 above).

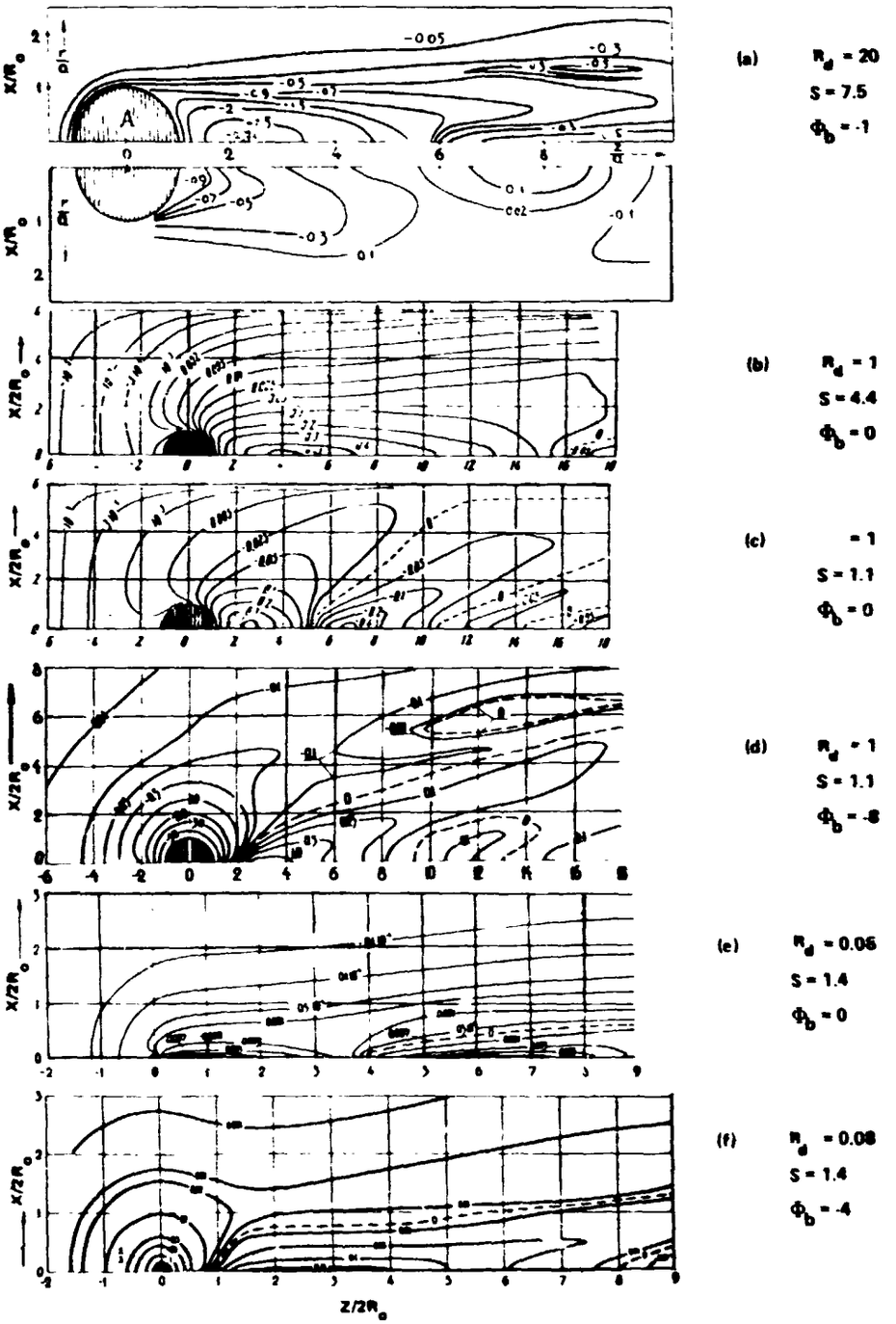

Figure C-1. Potential field in the vicinity of spherical bodies in a collisionless plasma. All axes are normalized by λ_D except (a) which is normalized by R_o, after Maslennikov and Sigov [16-18].

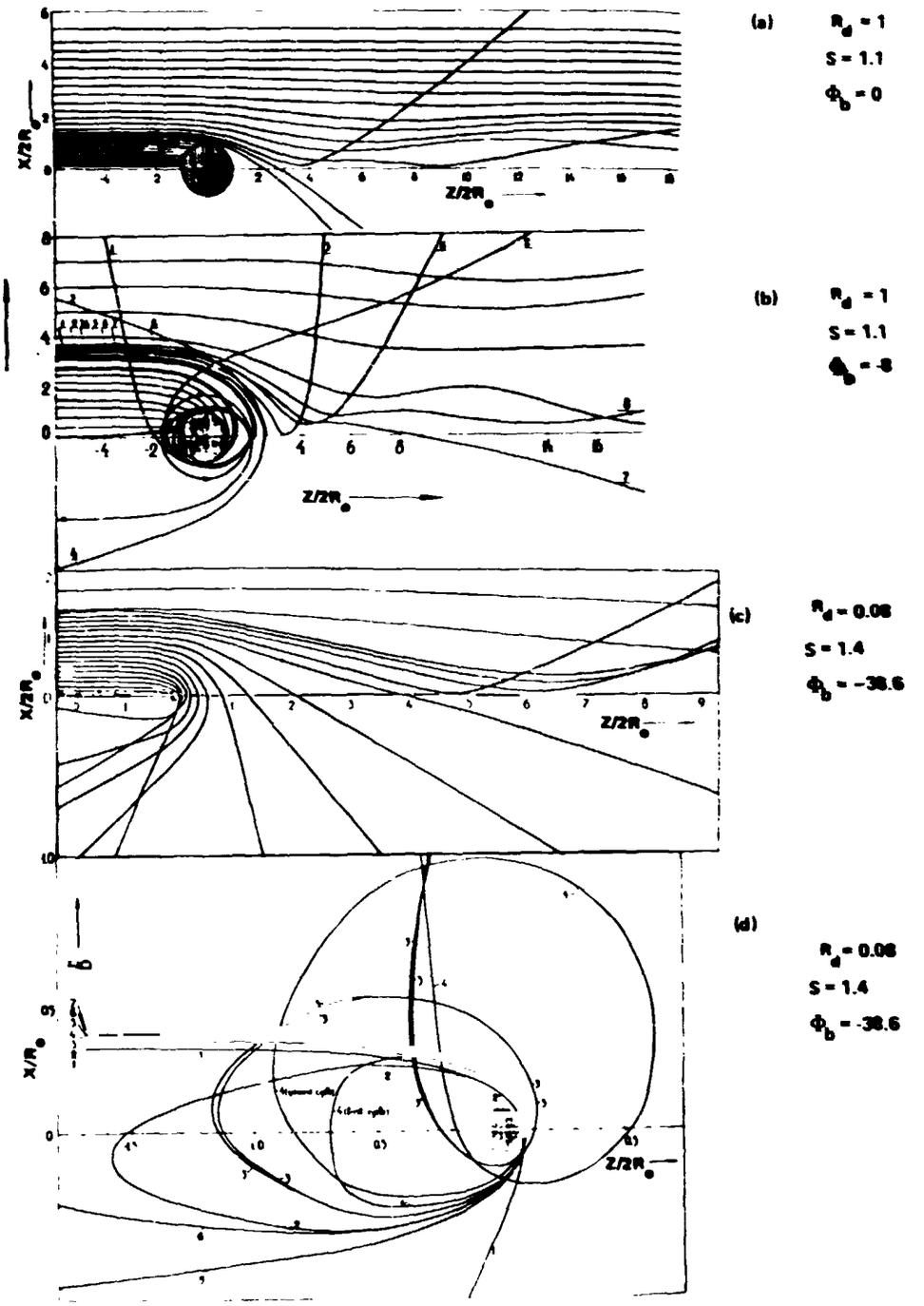

Figure C-2. Ion trajectories in the vicinity of spherical bodies. Note that (d) is an expansion of some trajectories of (c). All distances are normalized by λ_D, after Maslennikov and Sigov [17].

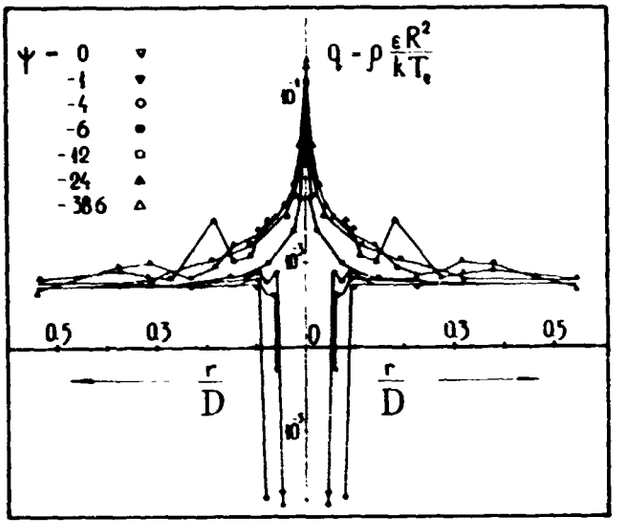

Figure C-3. Ion density profiles in the plane $Z/R_o = 1.4$ behind a spherical body with $R_d = 0.08$, $S = 1.4$, and Φ_b as shown, after Maslennikov and Sigov [17].

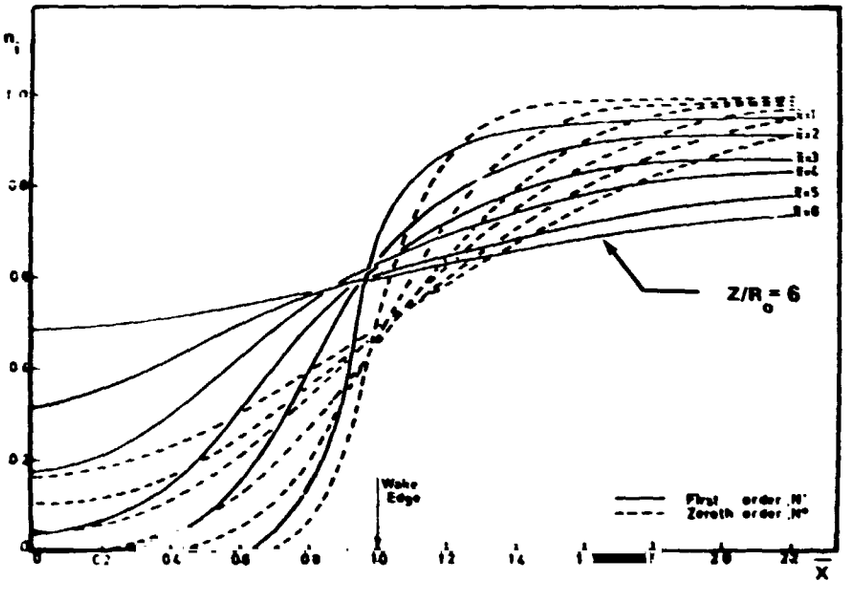

Figure C-4. Transverse ion density profiles downstream from a long rectangular cylinder for the conditions: $R_d = 1.5$, $S = 6$, $\Phi_b = -2.75$, $X = x/R_o$. Solid lines are first order solutions, $n_i^{(1)}$, while dashed lines are $n_i^{(0)}$ solutions, after Taylor [20].

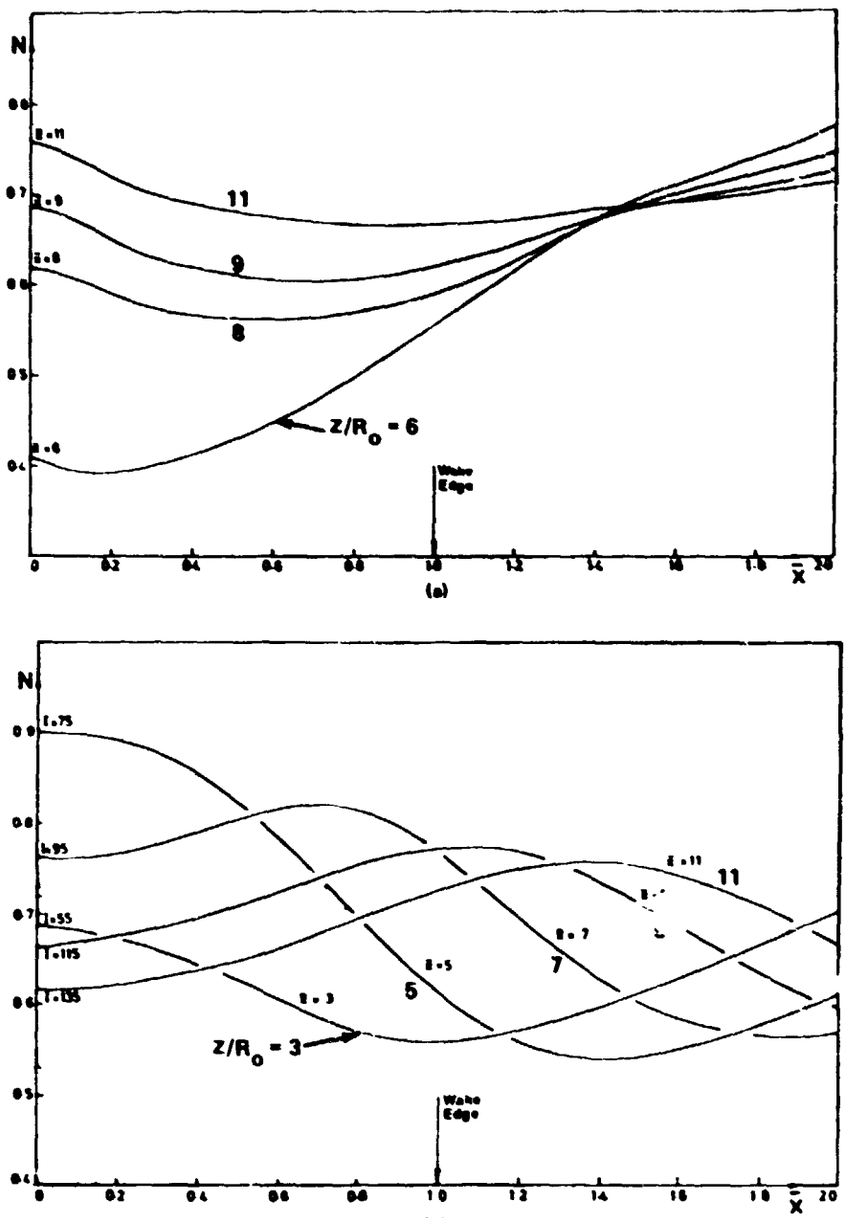

Figure C-5. Ion density profiles for the conditions of Figure C-4. $R_d = 1.5$, $S = 6$, (a) $\Phi_b = -2.75$, (b) $\Phi_b = -14$. All profiles are first order, normalized by n_o, after Taylor [20].

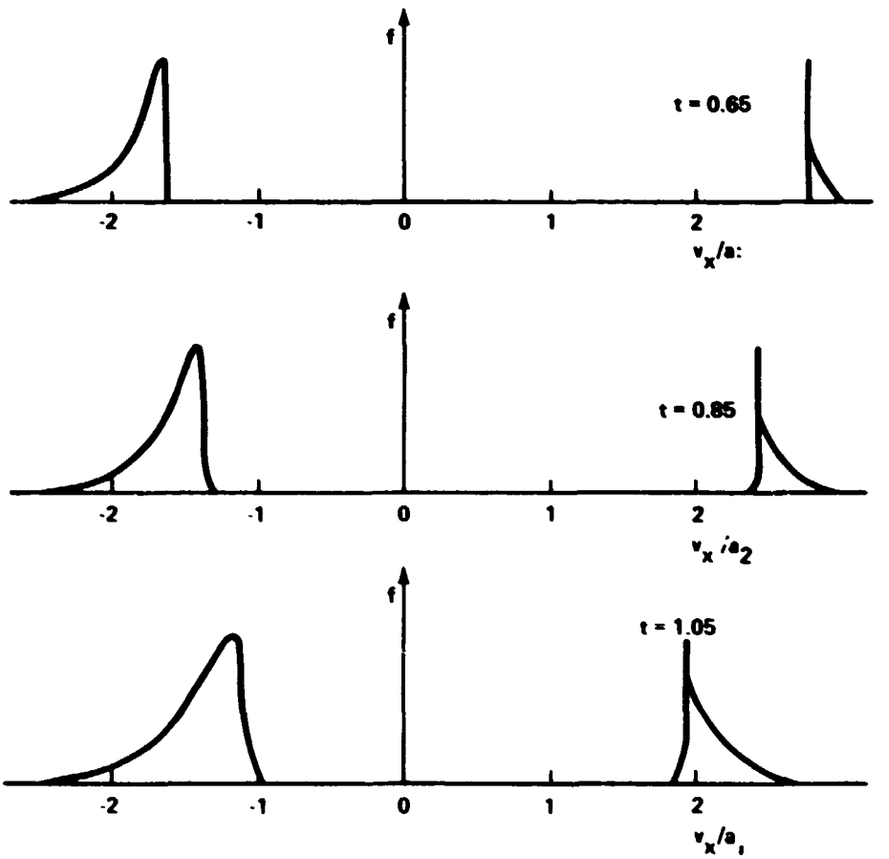

Figure C-6. Ion distribution function, $f\ (v_x/a_i)$, behind a long plate at $X/R_o \sim 0.4$ and various values of $t = z/S{\cdot}R_o$, $T_e/T_i = 1$, after Gurevich, et al. [26].

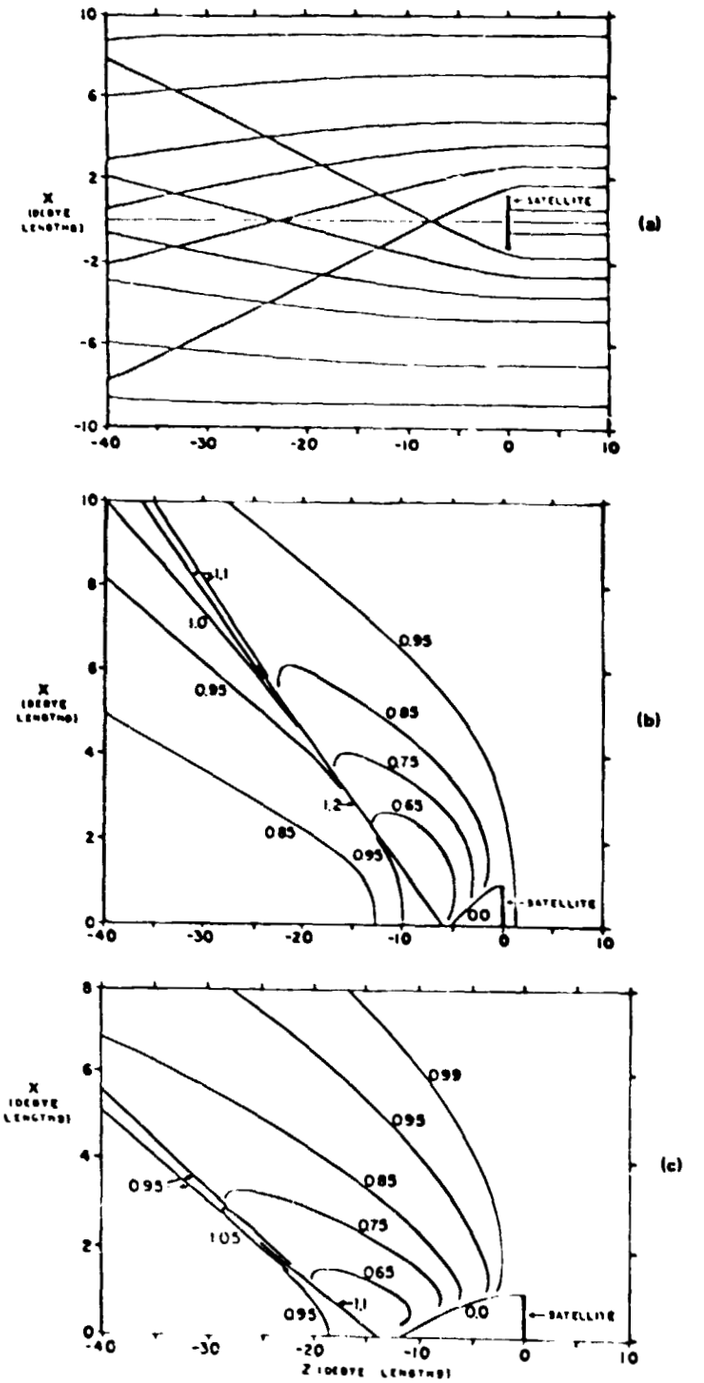

Figure C-7. Ion trajectories (a) and density profiles (b) for $R_d = 1$, $S = 3.5$, and $\Phi_b = -5$, and density contours for $\Phi_b = 0$ (c), long plate body, after Call [12].

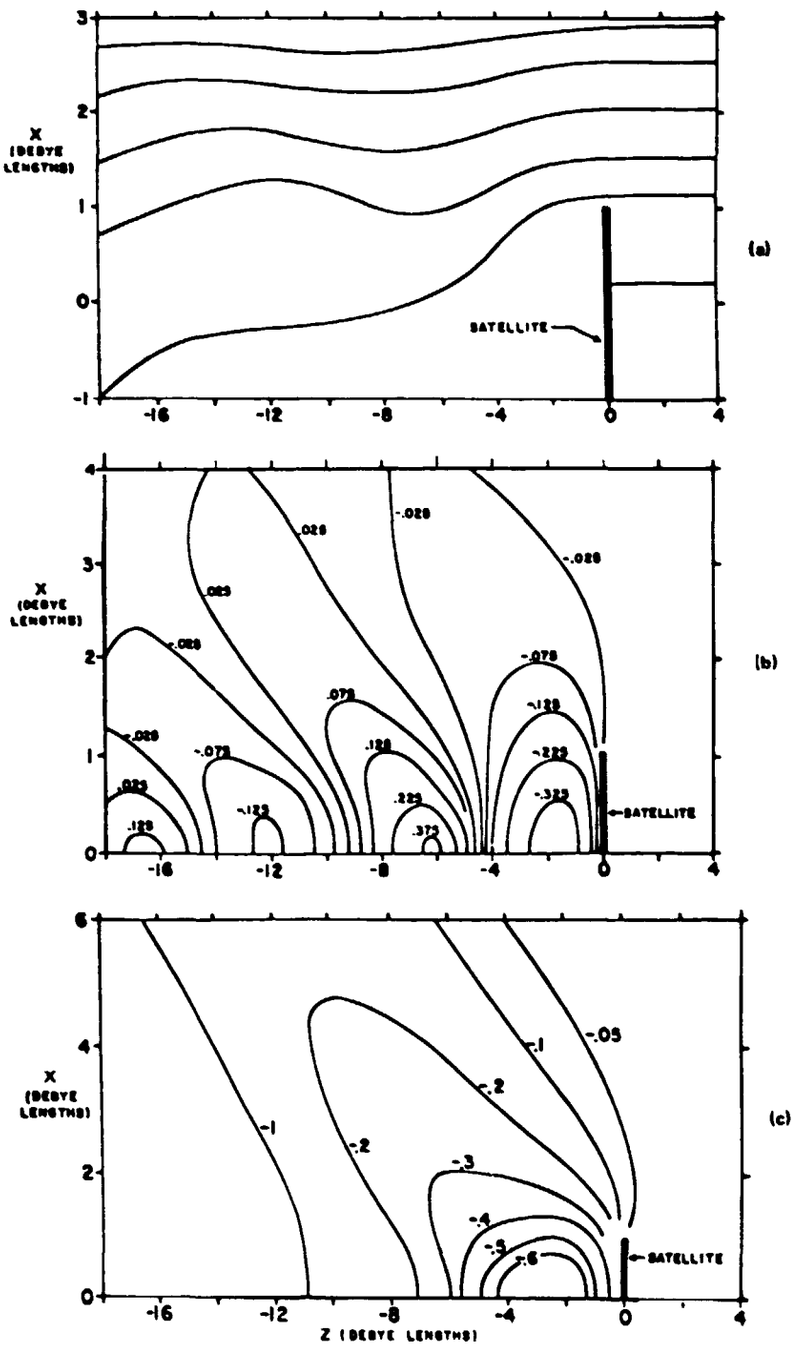

Figure C-8. Ion trajectories (a) and potential contours (b), for a disk with $R_d = 1$, $S = 1.1$, and $\Phi_b = 0$, and (c) potential profiles for a long plate under same conditions, after Call [12].

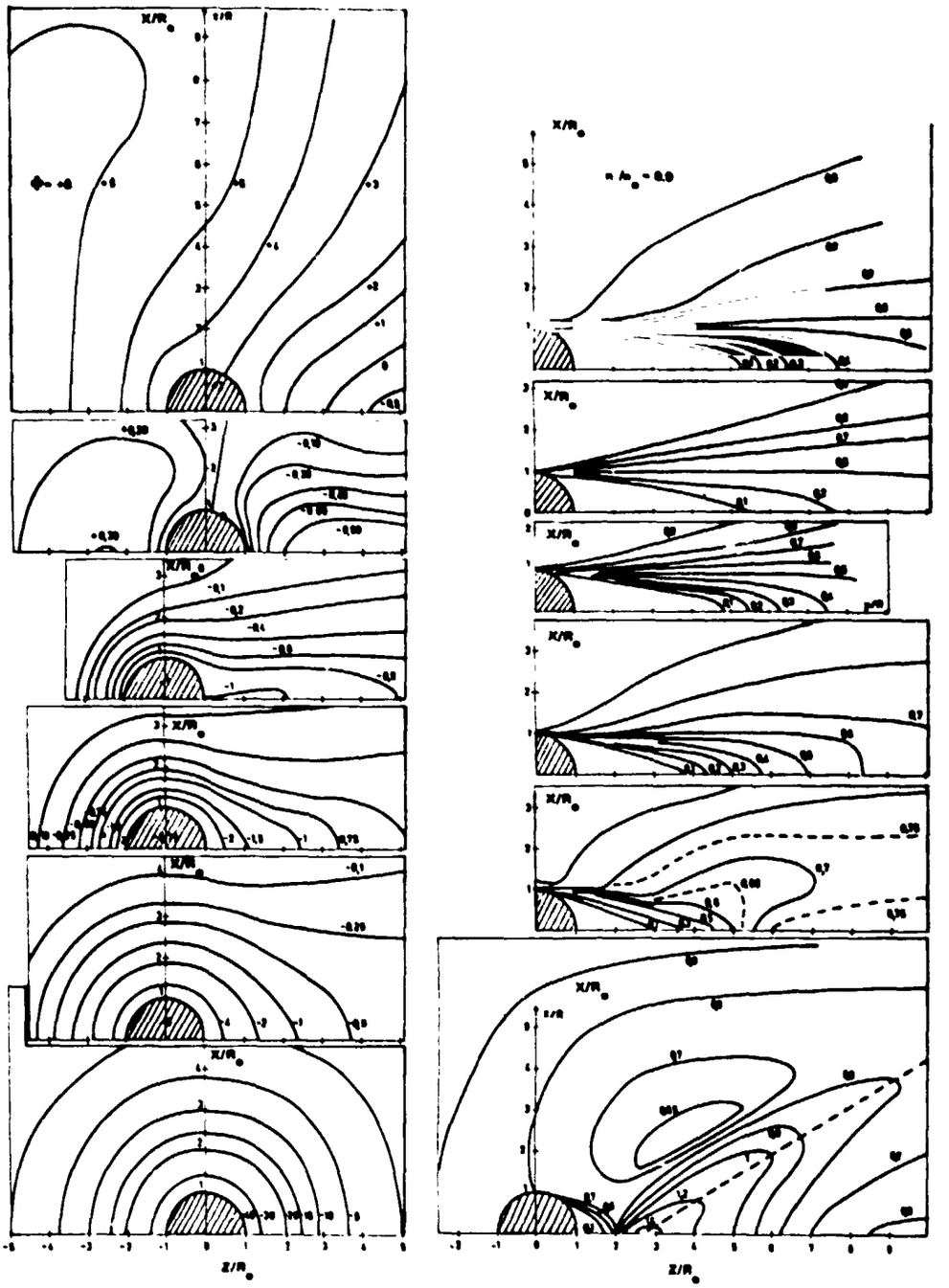

Figure C-9. Equipotential (left) and ion density (right) contours for $R_d = 1.5$, $S = 6$, $T_e/T_i = 1$ and (top to bottom), $\Phi_b = +3$, 0, -1, -2.75, -6, and -40, after Fournier [23].

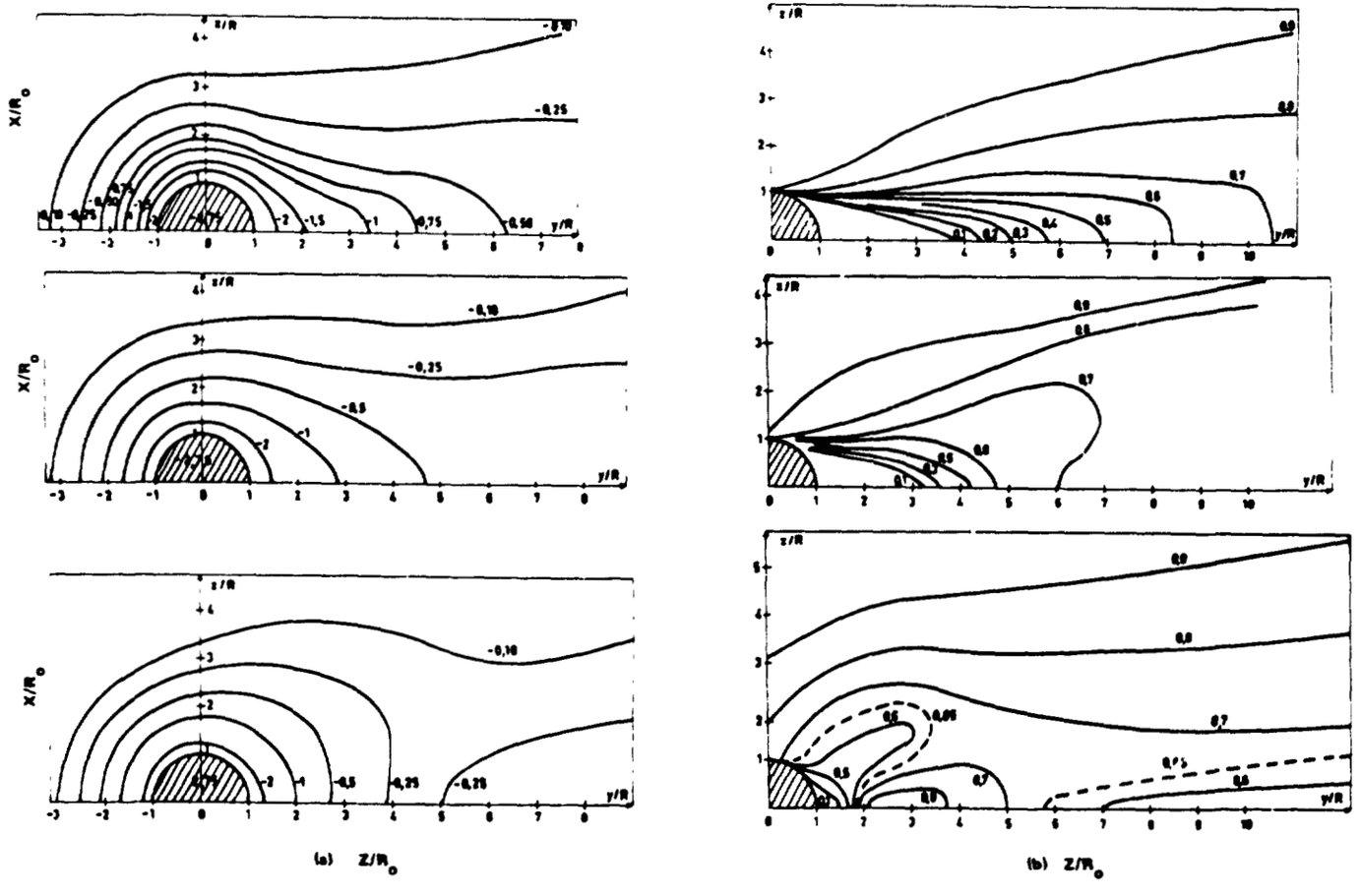

Figure C-10. Equipotential (a) and ion density (b) contours for $R_d = 1.5$, $S = 6$, $\Phi_b = -2.75$, and (top to bottom) $T_e/T_i = 1, 2, 10$, after Fournier [23].

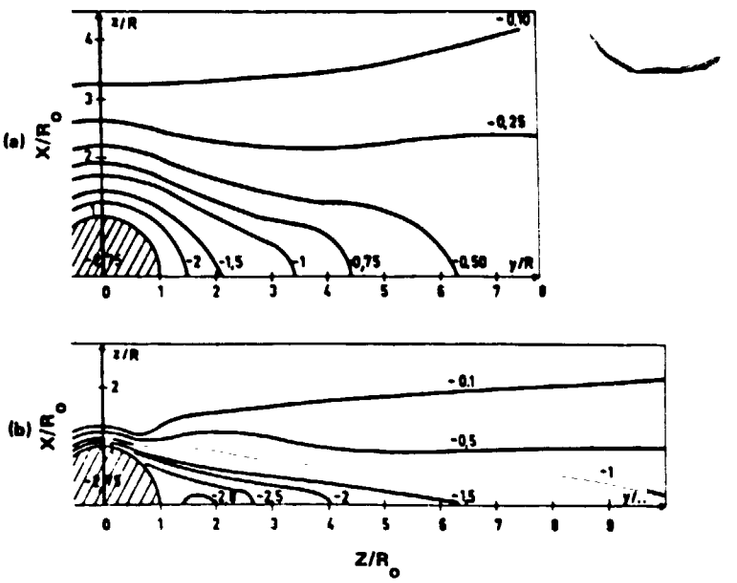

Figure C-11. Equipotential contours for S = 6, Φ_b = -2.75, T_e/T_i = 1, and (a) R_d = 1.5 and (b) R_d = 10, after Fournier [23].

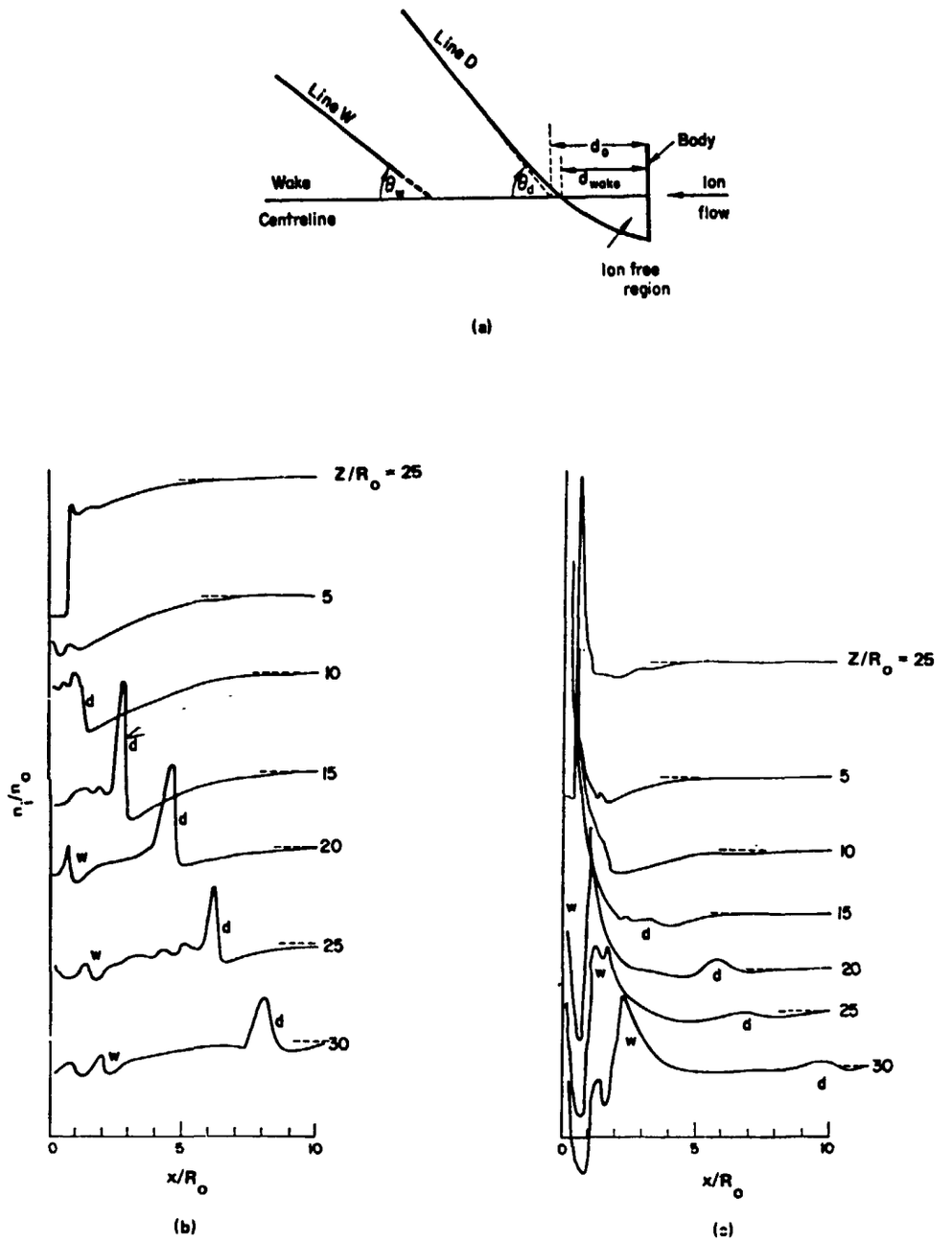

Figure C-12. Transverse ion density profiles for $R_d = 1$, $S = 3.5$, and $\Phi_b = -5$ for (b) a plate and (c) a disk. (a) shows behavior schematically, after Martin [13].

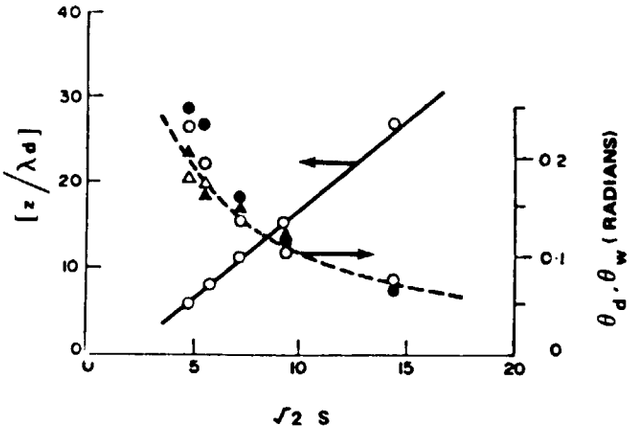

Figure C-13. Variation of Z_d (open circles), θ_d (triangles-open → plate, closed → disk), and θ_w (circles, open → plate, closed → disk) with S. Dashed line shows Mach angle, after Martin [13].

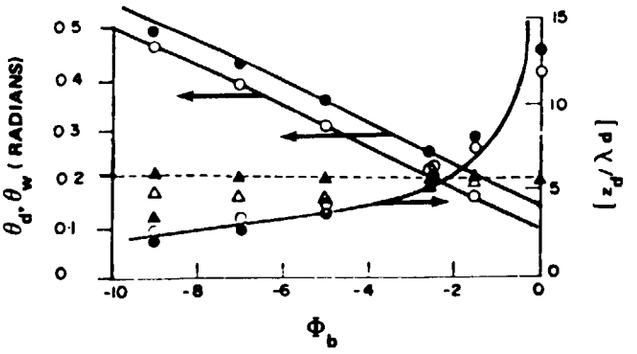

Figure C-14. Effect of Φ_b on Z_d (circles), θ_d (circles), and θ_w (triangles) open → plate, closed → disk. Dashed line shows the Mach angle, after Martin [13].

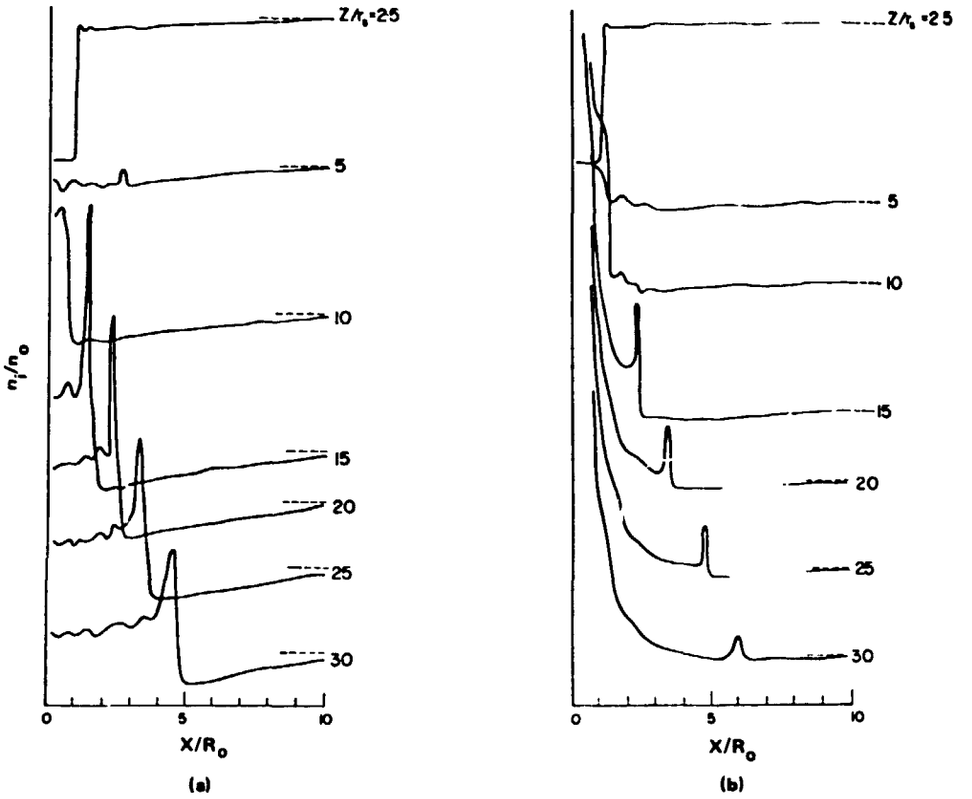

Figure C-15. Transverse ion density profiles for $R_d = 0.2$, $S = 3.5$, and $\Phi_b = -5$. (a) Plate, (b) disk, after Martin [13].

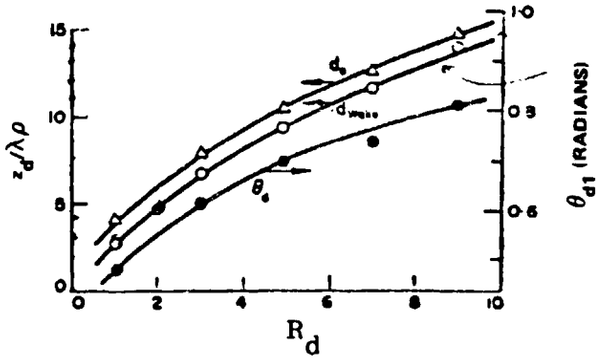

Figure C-16. Effect of R_d on Z_d and θ_d for $S = 3.5$ and $\Phi_6 = -9$, after Martin [13].

APPENDIX D. A CRITICAL REVIEW OF THE RESULTS FROM THE AVAILABLE SATELLITE DATA

1. Spacecraft, Instruments, and Mission Parameters

The basic geometry of the Ariel I, Explorer 31, AE-C, and Gemini-Agena 10 spacecraft, the location of instruments, and important dimensions are shown in Figure D-1. The various mission parameters and other necessary data are given in Table D-1. The most common instruments used were: (1) the retarding potential analyzer (RPA), (2) the cylindrical or the planar, guarded Langmuir probe, and (3) the spherical ion trap. The RPA and the Langmuir probe techniques are discussed in Appendix F. The spherical ion trap on Ariel I and Fxplorer 31 was mounted on a short stem ($r \simeq 2R_o$ from center) on the spin axis and consisted of a 9 cm diameter spherical collector enclosed by a concentric spherical grid 10 cm in diameter. The grid was biased to repell electrons (-6 volts on Ariel I).

On the Ariel I satellite, the boom and base probes were planar Langmuir probes, each consisting of a 2 cm diameter disc collector surrounded by a 1 cm wide guard ring. The boom probe was mounted at $r = 5\ R_o$ from the center of the satellite with the instrument face normal to the satellite spin axis and facing the opposite direction from the base (surface mounted) probe. The base probe was mounted on the spin axis.

The stem mounted probes on Explorer 31 were cylindrical Langmuir probes which made measurements over a length of 23 cm centered at $r \simeq 2\ R_o$ from the center of the satellite. A planar RPA was also used on the Explorer 31 and was located in a position similar to that of the surface-mounted planar Langmuir probe shown in Figure D-1(b). The ion and electron sensors

(planar RPA's) on the Agena vehicle were mounted near the docking cone, even with the skin of the booster, and facing outward, normal to its axis of symmetry.

2. Results Obtained from Insitu Data

a. Electron and Ion Current Variations in the Near Wake. The variation of electron flux at the Ariel I surface with angle of attack is shown in Figure D-2. The current at the surface was measured by the base probe and normalized by the current to the boom-mounted probe (assumed to be ambient). This normalization was necessary since the satellite spin axis was fixed in space and therefore the base probe rotated through the wake only once per orbit and ionospheric conditions could be expected to have varied significantly over the time and distances involved. From these data, it was concluded that (1) in the altitude range of 400 to 700 km (where 0^+ is the major ion constituent), the near wake electron flux is depleted by a factor of 10^{-2} below the ambient value, (2) no enhancement occurs in the frontal region, and (3) the current collected by the boom probe was apparently not significantly reduced when in its own wake [89]. The third conclusion may appear peculiar in light of the first, and the numerous other theoretical predictions and experimental observations of the ion and electron depletion region in the near wake. However, it should be noted that, while the satellite (which did create an electron depletion in its near wake) was at a negative floating potential, the probe was biased very near plasma potential when the currents were measured. As a result, electrons of all kinetic energies would be absorbed at the probe surface, therefore preventing the build up of a large negative space charge (see Fournier, Appendix C.3). If the measurements were made slightly into the electron acceleration region of the probe characteristic (slightly positive with respect to plasma potential), the electron flux would tend to become even more isotropic. The effects of wake will, in this way, be minimized for electrons and only a small reduction in electron flux would be expected.

Figure D-3 shows the electron current collected by the Ariel I boom probe (at $r = 5\,R_o$) as a function of angle of attack (averaged over 10° intervals). The currents, in this case, were not determined with the probe near plasma potential, as in Figure D-2, but were obtained from the modulation depth of the first derivative, $dI_e/d\phi_p$, in the acceleration region (positive with respect to plasma potential). Note that the Ariel I spin axis rotated with respect to the velocity vector and as a result, the boom probe passed through the disturbance created by various parts of the satellite. The two curves given show the disturbances created by the spherical ion probe (part a) and the main body (part b). It was concluded from this and similar data that (1) the width of the wakes of both the ion probe and the main body were wider than the corresponding geometric wakes, (2) both wakes show an enhancement at the center ($\theta \simeq 180°$), and (3) the wake due to the spherical ion probe was very similar to that of the main body in extent and amplitude, even though the ratio of the effective radii of the two bodies was about 6 [36]. It was pointed out, however, that the spherical ion probe was biased 6 volts negative with respect to the main body, which was, in turn, floating between 0 and 1 volt negative with respect to the ambient plasma. This could be expected to enlarge the disturbed zone considerably (Chapter IV).

Figure D-4 shows electron current profiles as a function of angle of attack taken at the surface of the Explorer 31 satellite. This satellite had a highly elliptical orbit (Table D-2) which allowed the electron depletion to be observed as a function of altitude. The measurements were made with a surface-mounted, planar-guarded Langmuir probe (Figure D-1). The current densities were obtained when the probe was at the plasma potential. Note that the amount of depletion in the wake region ($\theta \simeq 180°$) decreased with increasing altitude; i.e., n_e (wake)/n_e (front) ranges from 0.01 at 500 to 600 km to 1.0 at 3000 km [37]. The low altitude depletion is in agreement with the value obtained from the Ariel I measurements over a similar altitude range (400 to 700 km). The plasma density, temperature, and ion constituents change significantly over this altitude range. However, the average ion mass was

found to be the dominant parameter affecting the variation of the electron current depletion. The dependence of $\delta_e = [n_e \text{ (wake)}]_{av} / [n_e \text{ (front)}]$ on $[M_i]_{av}$ shown in Figure D-5 [38]. Note that δ_e is determined from profiles similar to those of Figure D-4 and is plotted against the average ionic mass measured at the appropriate altitudes by the spherical ion mass spectrometer [37] (referred to as "spherical ion trap" in Figure D-1).

The behavior of the ion density measured by the spherical ion trap at about 2 R_o from the center of the Ariel I satellite (Figure D-1) is shown as a function of angle of attack in Figure D-6. The ion density measurements have been normalized by the electron density measured at the same time by the boom probe (assumed to be the ambient plasma density). Some form of normalization was necessary since each rotation of the spherical ion trap required one complete orbit and ionospheric conditions could be expected to have varied significantly, as previously noted. The authors [39] note that the ion density depletion observed was not as great as the electron depletion under comparable conditions; i.e., ~ 3 compared to $\sim 10^{-2}$ (Figure D-2). This was explained by the difference in radial distances ($r \simeq 2\ R_o$ for the ion probe compared to $r = R_o$ for the electron probe) which, in turn, was taken to indicate that the maximum ion depletion is confined to an axial distance of $Z \sim 2\ R_o$ [39]. However, this explanation is not in agreement with other, more recent theoretical and experimental results which predict the ion void region (maximum depletion) to extend down stream to about $Z \simeq S_o R_o$ [20]. For the altitudes of 100 to 1200 km, $S \geq 3$ so that one would not expect to see the void begin to fill until $Z \geq 3\ R_o$. In retrospect, possibly a more plausible explanation is the effect of the probe being biased 6 to 7 volts negative with respect to plasma potential, which could possibly have attracted ions from the wake boundaries when the probe rotated into the void region.

Although no explanation has been given for the ion enhancements occurring between 90° and 120° on either side of the wake [39, 84], it seems appropriate to comment on their possible origin in light of the numerous studies reviewed herein. First, it seems unlikely that such an effect could

result from the satellite itself since its surface was a conductor and all studies (theoretical and experimental) failed to reveal any structure in this location (at 120°, Z = 1 R_o, and X = 1.7 R_o) for this type surface However, Figure D-1 shows that when the spherical ion trap was oriented at 120° to the flow direction, the solar petals were located upstream. Solar cells have insulating surfaces of uncertain characteristics and the petals, themselves, may have regions biased at a relatively high potential exposed to the plasma (Figure D-1). In either case, the assumption that all charge is absorbed at the body surface (Appendix B) may not apply. The conditions of the theoretical and experimental studies would not be met in such a case and their results would no longer strictly apply. Therefore, the possibility that ion acoustic type shock fronts were created by the solar petals cannot be ruled out. On the other hand, there are good reasons to suspect that the effect may be instrumental. Note that the electron current collected by the surface mounted planar Langmuir probe on Explorer 31 (Figure D-4) had typically not reached ambient (maximum frontal) value at $\theta \geq 60°$. If the same effect can be assumed to have occurred for the base probe on Ariel I, then Figure D-2 indicates that, while the boom probe current did not decrease by orders of magnitude in its self wake (as discussed following Figure D-2), it must have decreased ~50% between 60° and 120° since the ratio, n_e (base)/n_e (boom), remained unity over this range. The enhancements of n_i/n_e (boom) shown in Figure D-6 may therefore indicate that n_i remained constant while n_e (boom) decreased 40% over the angular range $90° \leq \theta \leq 120°$. As stated above, this ion behavior is consistent with the results of other studies. Unfortunately, neither possibility can be evaluated with the published data.

The behavior of both electron and ion currents at the surface of the Explorer 31 satellite is shown as a function of angle of attack in Figure D-7. (All curves are normalized by the appropriate current measured in the frontal direction.) The electron currents were obtained from the surface mounted Langmuir probe, as above [38,85], while the ion currents were measured by a planar RPA [86] mounted in a similar position (Figure D-1). The

dimensionless parameters for each set of ion and electron current curves are given in Table D-2. These values were obtained by averaging the parameters over a range of altitudes where they remain relatively constant, as indicated in the table. The authors concluded that the ion density is less than the electron density for $\theta > 90°$ and that this difference increases as θ approaches 180° (i.e., approaches the wake axis) [86]. We may also point out that the ion current profiles drop in amplitude at any given angle as the ion Mach number, S, increases. The Debye ratio, R_d, also increases but less dramatically while Φ_b fluxuates over the three cases. It can therefore be concluded that, in these cases, S is the dominant parameter (at least of the four parameters considered) controlling wake filling by ions very near the body. For electron filling, a different dependence emerges; i.e., the only case in which I_e decreased appreciably, involves a large increase in R_d. Note that S also increased to some extent and may have contributed to the observed depletion.

The main objective of the Gemini-Agena 10 experiment was to attempt an axial mapping of the wake produced by the Gemini capsule [89]. This was to be accomplished by aligning the Gemini-Agena system with the orbital velocity vector and moving the Gemini upstream (Figure D-1). The currents measured by the outboard ion and electron sensors during this maneuver are shown in Figure D-8(a). It must be pointed out that the distances shown are separation distances between the two craft, determined by thruster firing data [43], and are not necessarily aligned with the flow direction; i.e., the angle between the line connecting the two vehicles and the flow direction could not be determined accurately. Hence, it is possible that the Gemini moved significantly off the Z-axis [75,84]. The possible effects of this ambiguity are discussed in Chapter IV. It can be concluded from these data, however, that in the near wake (within a few radii of the Gemini) there is a depletion of both ions and electrons with a net negative space charge remaining. This is consistent with the above observations from the Ariel I and Explorer 31 satellites.

Figure D-8(b) shows the currents measured by the outboard electron and ion sensors during a yaw maneuver of the Agena. This effectively shows

a self-mapping of the Agena similar to the measurements by the base probes on the Ariel I and Explorer 31 satellites. Beginning at orientation A, with the sensors facing into the flow, the Agena rotated to position B where the sensors faced downstream into the wake of the docking cone. In between, the wake of the main body was observed, which is indicated by the abrupt dip and subsequent rise in electron current. The authors [43] conclude from these data that while the electron current decreased by about two orders of magnitude during the maneuver and the ion current decreased by at least four orders (5×15^{-11} A was the lower limit of the sensors). It was also noted that the ion depletion is comparable to that measured on the Ariel I and Explorer 31 satellites, at the appropriate altitude, even though the geometry of the Agena differed considerably. This was taken to indicate that the ion mass, m_i, and Debye ratio, R_d, are more important in the wake. near the trailing surface, than the geometrical configuration of the spacecraft.

The variation of electron current and density with angle of attack was also investigated using the Explorer 31 stem-mounted, cylindrical Langmuir probes [87,88]. These probes provide measurements at $r \sim 2 R_o$ from the center of the satellite, which was roughly the radial position of the spherical ion trap on the Ariel I. The electron density measurements in the wake of the Explorer 31 agree well with the ion densities measured in the wake of the Ariel I. However, cylindrical Langmuir probe measurements are subject to the same type of limitations discussed above for the spherical ion trap; i.e., they were made with the probe biased highly positive which could be expected to have attracted electrons from a large region of the near wake where the charged particle density is low and, therefore, the Debye length is long. Also note that the cylindrical probes collect current over a range in r of approximately $R_o/2$ (which would tend to smear out any fine structure) and are influenced by the orientation of the geomagnetic field [12].

More recent investigations have been made of both ion and electron currents, using an improved version of the cylindrical Langmuir probe, on the Atmospheric Explorer C satellite [40,41]. The basic satellite geometry

and probe orientations are shown in Figure D-1. These probes provide measurements at $r \sim 1.6\ R_o$ from the center of the satellite. The collector is only 7.5 cm long as compared to 23 cm for the Explorer 31 instrument. Therefore, measurements should be confined to a smaller spatial region. Unfortunately, the currents and densities were still measured in either the ion or the electron acceleration portion of the probe current-voltage characteristic, and the effect of relatively high potentials on the collection area is difficult to assess within the wake region. However, ion density measurements made by the cylindrical Langmuir probes compared well with those obtained from a planar RPA. The basic findings of these studies are:

(1) The variation of ion density with angle of attach, $n_i(\theta)$ has an exponential dependence on the Debye ratio in the wake region; i.e., n_i (wake) $\sim$ exp (R_d).

(2) The ion density in the wake region depends linearly on S; i.e., n (wake) $\sim$ S.

(3) The presence of hydrogen ions greatly accelerates the wake-filling process; i.e., for $(n_H+/n_O+) \ll 1$, n_i (wake) $n_{io} \cong 10^{-2}$ and 30 for T_e = 1000°K and 3000°K, respectively, whereas for $(n_H+/n_o+) \sim 1$, n_i (wake) / $n_{io} \cong 6$ at T_e = 1000°K, and 2.3 at T_e = 3000°K (where n_h+ is the hydrogen ion concentration and n_o+, the atomic oxygen ion concentration). These results demonstrate the contribution of both temperature and relative hydrogen-atomic oxygen ion concentrations to the wake filling process.

b. Electron Temperature Variations in the Near Wake. Two investigations of the variation of electron temperature with angle of attack have been carried out. The first makes use of data from the Explorer 31 surface-mounted planar Langmuir probe [80] while the second makes use of additional data from the Explorer 31 surface mounted planar RPA [42]. Both of these investigations revealed a significant increase in T_e within the spacecraft wake.

In the first investigation [80], two well documented examples of large electron temperature enhancements in the wake region are given; i.e., T_e (wake) $/T_e$ (front) ≥ 1.8. The results, shown in Figure D-9 and

characterized by the parameters given in Table D-3, were obtained from the surface mounted Langmuir probe. The data were analyzed by the Druyvesteyn technique (Appendix F). In the wake, the collected current was too low to properly test the distribution for Maxwellianality and the authors note that the distribution may have deviated from a Maxwellian and, therefore, the concept of temperature must be used with this understanding.

The T_e enhancement was found to occur at a large number of locations and times for altitudes below 2000 km. Figure D-10 shows T_e (front) and T_e (wake) as a function of altitude between 500 and 750 km. For altitudes above 2000 km the enhancement became less obvious. It was also noted that the same probe, mounted on the boom at 2 R_o on Ariel I, did not reveal any T_e enhancement in the wake. It was, therefore, concluded that the enhancement must be limited to the near wake. (Laboratory measurements show the region of T_e enhancement to conform roughly to the ion void region; see Chapter IV).

The possible influence of the geomagnetic field on T_e was also discussed. Figure D-11 shows two cases of T_e as a function of the angle between the geomagnetic field direction and the probe normal with the region of the wake indicated for each case. Although some magnetic effects appear, they are clearly dominated in these cases by the enhancement associated with the wake.

The second investigation [42] used data from the surface-mounted RPA in addition to the data used in the investigation discussed above [80]. The RPA determined T_e to an accuracy of ±50° or better. In addition, the data were subjected to a rigid screening process to eliminate spurrious effects which may occur when the sun shines into the instrument and poor quality data that did not submit to a good, reliable fit by theoretical probe characteristics. A very large amount of electron temperature data obtained at altitudes ranging from 500 to 3000 km was screened and those found admissible were plotted against the angle between the probe normal and the flow direction. The data were found to fall into four general categories, illustrated by the example data in Figure D-12, which depend primarily on the average ionic mass, $[m_i]_{av}$. For $[m_i]_{av} \simeq 1.1$ and with the satellite in the earth's shadow,

no enhancement of T_e was found as shown in Figure D-12(a). For $[m_i]_{av} \simeq$ 1.6 and 3.3 with the satellite in the sunlight [Figure D-12(b) and (c)], a T_e minimum occurred in the forward direction (assumed ambient) and a definite T_e enhancement occurred in the wake. In the fourth class [Figure D-12(d)], the satellite was illuminated by the sun and the average ionic mass was 4.4. Notice that for this class of data, the T_e maximum and minimum values show a definite offset from $\theta = 180°$ and $\theta = 0°$. Almost all data fell into one of the above classes. It was also stated that the types of enhancements were repeatable under similar ionospheric conditions.

Statistically, it was found that 62% of the data was anisotropic with respect to the angle between the probe normal and the magnetic field direction. However, 52% of these cases were T_e enhancements while 48% were depletions, indicating no clear dependence on the magnetic field. When the data were related to the angle between the probe normal and the flow direction, 67% of the T_e (θ) curves were anisotropic, of which 88% were T_e enhancements. Eleven percent of the enhancements were greater than 1000°K and 46% were greater than 500°K. Statistically, a clear dependence on angle of attack is indicated. Similar considerations did not reveal any clear correlation with ionic mass existed.

Since the electron temperature was obtained by fitting all data from a sweep with theoretical curves and local plasma potential was determined by the position of the maximum value of $d^2I/d\phi_p^2$, the T_e enhancements observed cannot be explained by a truncated Maxwellian produced by a shift in the space charge potential as suggested by Illiano and Story (Appendix E.1.i). Similar T_e enhancements were found in the Gemini-Agena 10 data [43].

Two mechanisms were offered as possible explanations of the effect: (1) the existence of a three-dimensional potential barrier in the near wake, which would selectively repel electrons of different energies, depending on their trajectory angle, and (2) the existence of wave-particle interactions associated with either a potential well in the near wake and/or the steep density gradients at the wake boundary. Unfortunately, the investigation was unable to uniquely test either alternative.

c. Evidence of Plasma Oscillations in the Near Wake. The oscillations discussed here refer to temporal variations of the plasma in the spacecraft frame of reference as opposed to oscillations in the plasma reference frame, which appear as standing waves when viewed from the moving spacecraft. Temporal oscillations of this type, generated by the spacecraft motion, have never been directly observed, primarily because the necessary type of measurements were not made. However, the boom-mounted planar Langmuir probe on the Ariel I satellite exhibited a peculiar behavior at certain distinct angles of attack which corresponded to the times when the probe moved across the wake boundaries [39].

The Ariel I Langmuir probe data were analyzed by the Druyvesteyn technique which makes use of the first and second derivatives of the probe current with respect to the probe potential; i.e., $dI/d\phi_p$ and $d^2I/d\phi_p^2$ (Appendix F). These derivatives were obtained directly from the Ariel I probes by using the AC mode of operation in which the main sweep voltage was modulated by two small amplitude oscillations of 500 Hz and 3.2 kHz. The first and second derivatives were then directly proportional to the amplitude of the current variations at these frequencies.

When the probe rotated into the wake region, the total collected current dropped below the sensitivity of the instrument. In this case, the modulated currents, obtained by appropriate filtering of the total current, should have approached the noise level. However, as the probe passed through the wake boundaries, even though the total current was below the instrument sensitivity, as expected, the modulation amplitude was well above the noise level. While this does not constitute a direct observation of oscillations, the authors state that the behavior can be explained by the existence of ion plasma oscillations occurring within the steep density gradients at the wake boundary. The plasma frequency was within the band pass of the 3.2 kHz filter and would, therefore, have created the observed modulation current.

This explanation is supported by the fact that the effect was very repeatable and only occurred at the location of the wake boundaries. It should

also be pointed out that oscillations of this type, occurring in a region of highly disturbed plasma flow, are not unexpected from the theoretical point of view [27,32]. Their existence could also help explain the electron temperature enhancements, discussed above, which were observed in the same region.

TABLE D-1. SOME DETAILS ON THE ARIEL 1, EXPLORER 31, AND GEMINI-AGENA 10 SPACECRAFT, AFTER SAMIR [89]

ITEM	ARIEL I	EXPLORER 31	GEMINI-AGENA 10 SYSTEM
DATE OF LAUNCH	APRIL 1962	NOVEMBER 1965	JULY 1966
APOGEE (km)	1200	3000	1400
PERIGEE (km)	400	500	300[a]
INCLINATION (°)	54	80	29
SATELLITE DIAMETER (cm)	≈ 60	≈ 70	SEE FIGURE D-1(c)
EXPERIMENTAL TECHNIQUE/METHOD	RETARDING POTENTIAL DRUYVESTEYN-MODULATION FIRST AND SECOND DERIVATIVES.	RETARDING POTENTIAL (i) LANGMUIR (ii) DRUYVESTEYN RPA (MULTIGRID)	MULTIGRID COLLECTORS, RPA LANGMUIR
PROBE LOCATION	ON SATELLITE SURFACE AND TWO BOOMS OF DIFFERENT LENGTH	ON SATELLITE SURFACE AND ON A BOOM (ONE PROBE)	ON THE SURFACE OF THE AGENA
MEASURED QUANTITIES	$n_e; n_+; T_e; T_+; \phi_s; M_+$	$n_e; n_+; T_e; T_+; \phi_s; M_+$	$I_e(n_e), I_+(n_+), T_e, \phi_s$

SUFFIXES (e) AND (+) REFER TO ELECTRONS AND IONS RESPECTIVELY:
n = NUMBER DENSITY (CONCENTRATION);
T = TEMPERATURE;
M_+ = IONIC MASS;
ϕ_s = SATELLITE POTENTIAL.
a. THE DATA PRESENTED IN THIS PAPER WAS TAKEN AT AN ALTITUDE OF ≈400 km.

TABLE D-2. PARAMETERS FOR FIGURE D-7

SYMBOL	X	+	Δ
PASS NO.	393	482	683
R_d	20.3 (7.8)	18.9 (9.5)	65.6 (43)
S	4.8 (3.6)	3.9 (3.7)	5.8 (5.6)
Φ_b	−4.6 (−5.5)	−3.2 (−3.8)	−3.6 (−5.1)
T_e/T_i	1.1	1.06	1.23
ALT. RANGE	695–786 km	592–909 km	519–567 km

NOTE: UNBRACKETED VALUES FOR IONS, BRACKETED ARE FOR ELECTRONS.

TABLE D-3. PARAMETERS FOR FIGURE D-9, AFTER [80]

	T_e (FRONT) (°K)	n_e (FRONT) (cm^{-3})	$[M_i]_{AV}$ (a.m.u.)	Φ_b	S	R_d
a	1740	1.2×10^4	12	-8.4	5	15
b	1950	1.1×10^3	1	-7.2	1.1	4.3

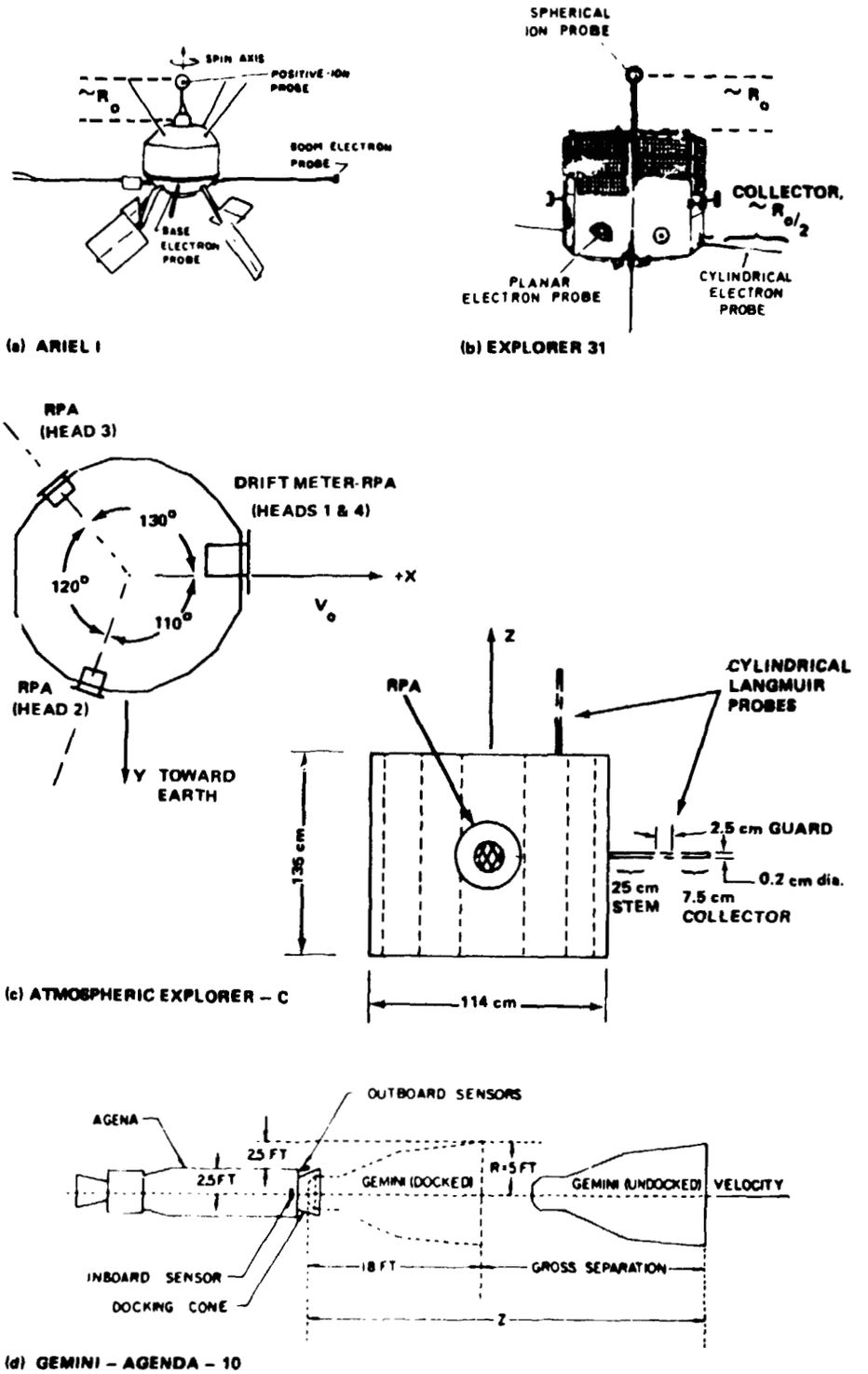

Figure D-1. Spacecraft geometry, dimensions, and instrument locations.

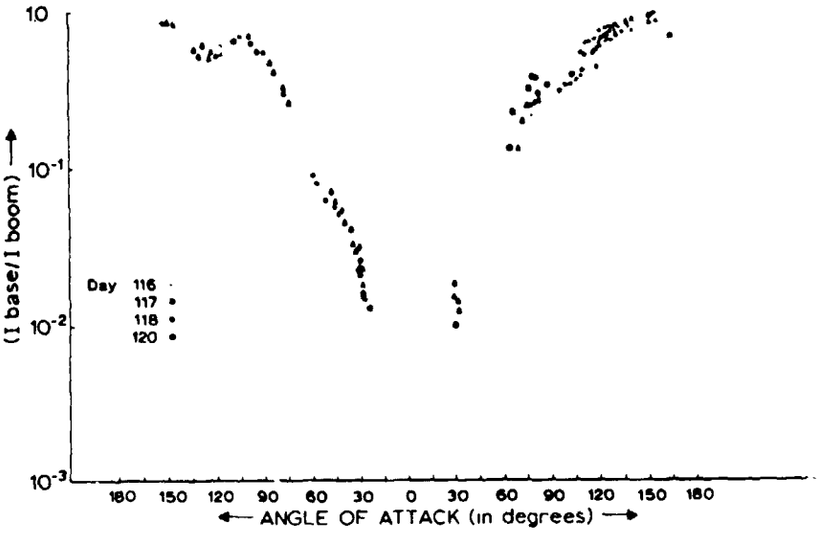

Figure D-2. Variation of electron current with angle of attack. Ariel I data from days 116, 117, 118, and 120 in 1962. (Note: Ram direction = 180° in this figure.) After Samir [89].

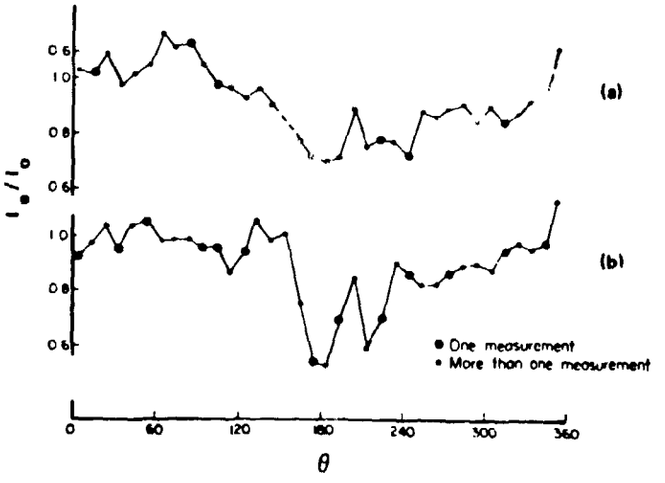

Figure D-3. Normalized electron current, I_e/I_o, as a function of angle of attack between the probe normal and the flow direction, θ, for (a) probe in the wake created by the spherical ion probe, and (b) probe in the wake created by the main body of the satellite, after Henderson and Samir [36].

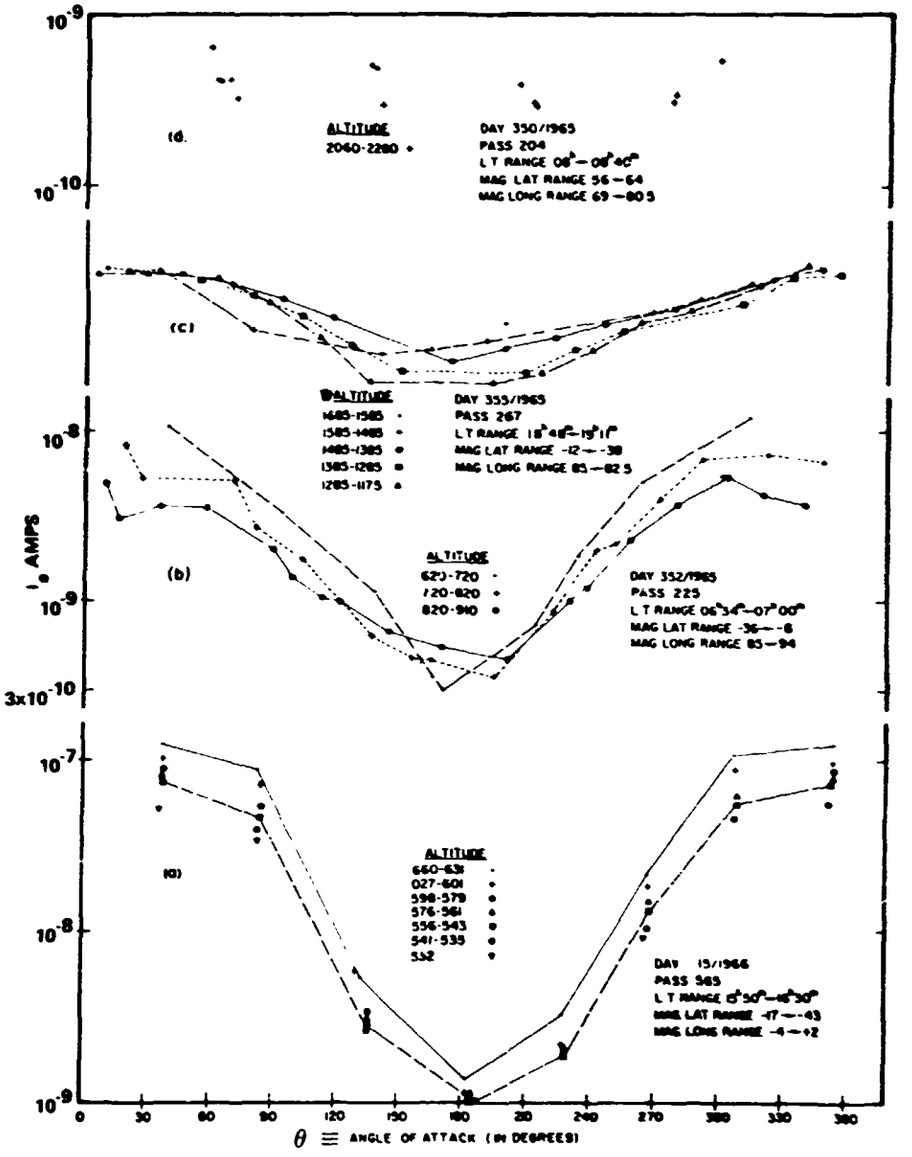

Figure D-4. Variation of electron current, I_e, collected with the probe at space potential, as a function of angle of attack. Explorer 31 data obtained with the surface mounted planar Langmuir probe, after Samir and Wrenn [37].

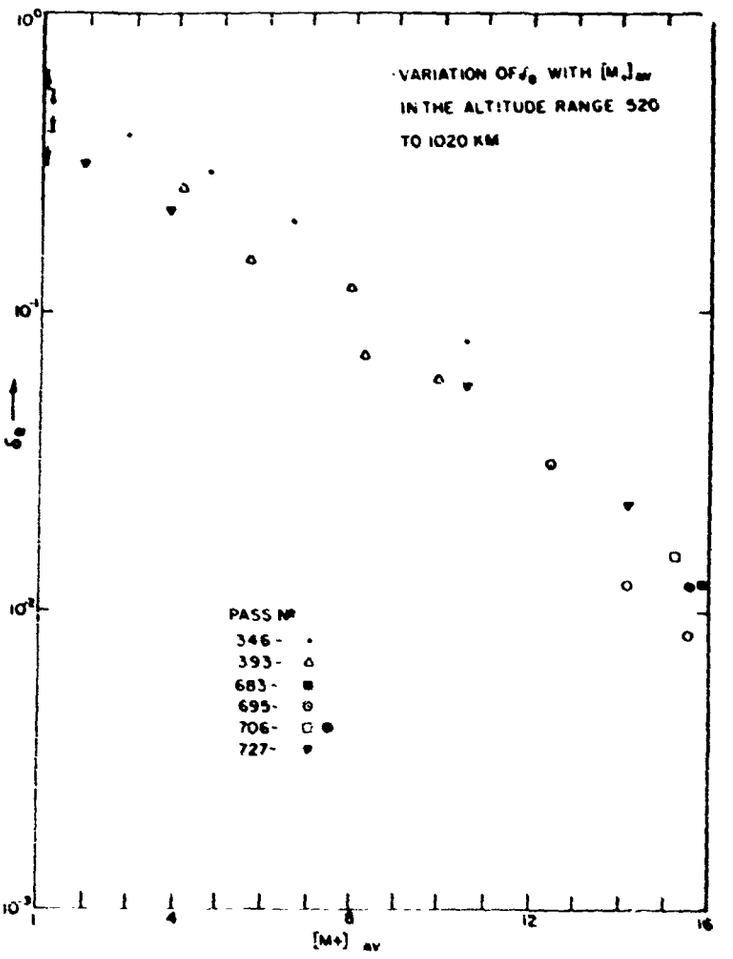

Figure D-5. Variation of $\delta_e \equiv n_e$ (wake) $/ n_e$ (front) with average ionic mass, $[m_i]_{av}$, over the altitude range 520 to 1020 km; data from Explorer 31, after Samir [38].

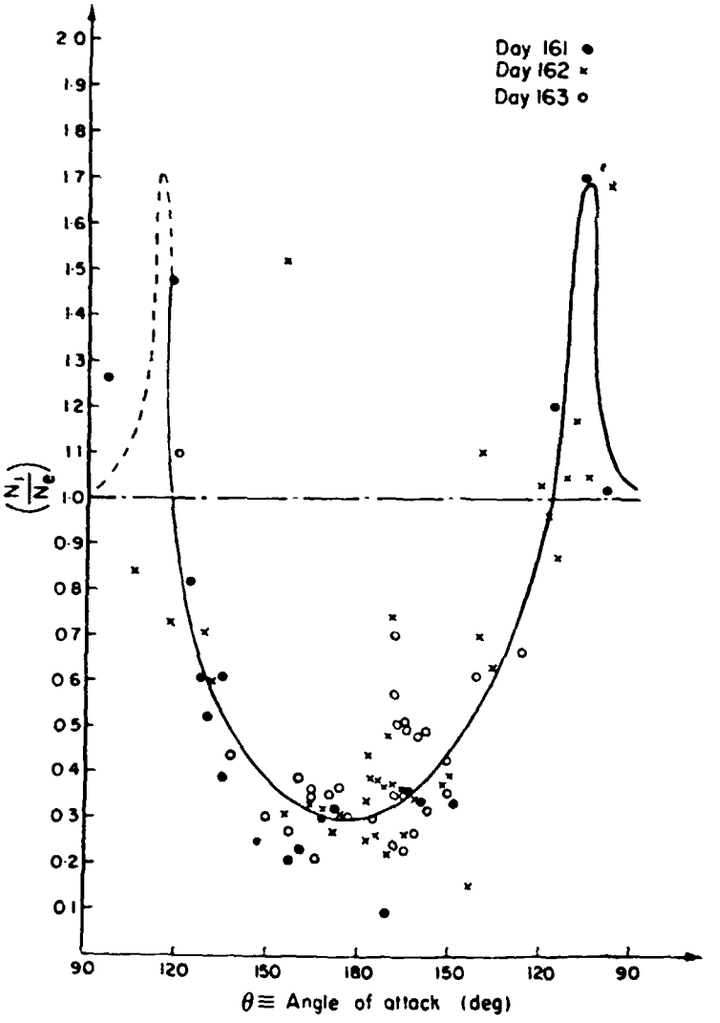

Figure D-6. Variation of normalized ion density with angle of attack. Measurements of n_i obtained from spherical ion probe; n_e, from the boom-mounted Langmuir probe on Ariel I, after Samir and Willmore [39].

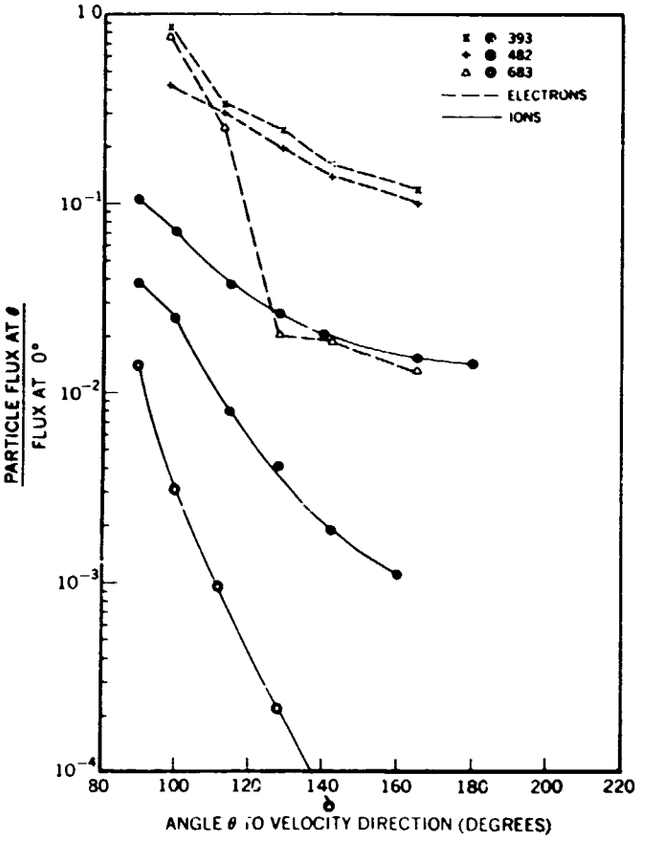

Figure D-7. Variation of normalized current, $I_i(\theta)/I_i(\theta=0)$ (solid lines), and normalized electron current (dashed lines) as functions of angle of attack, θ, over the altitude ranges, 700 to 930 km (pass 393); 900 to 600 km (pass 482); and 570 to 520 km (pass 683); Explorer 31 data, after Samir, et al. [86].

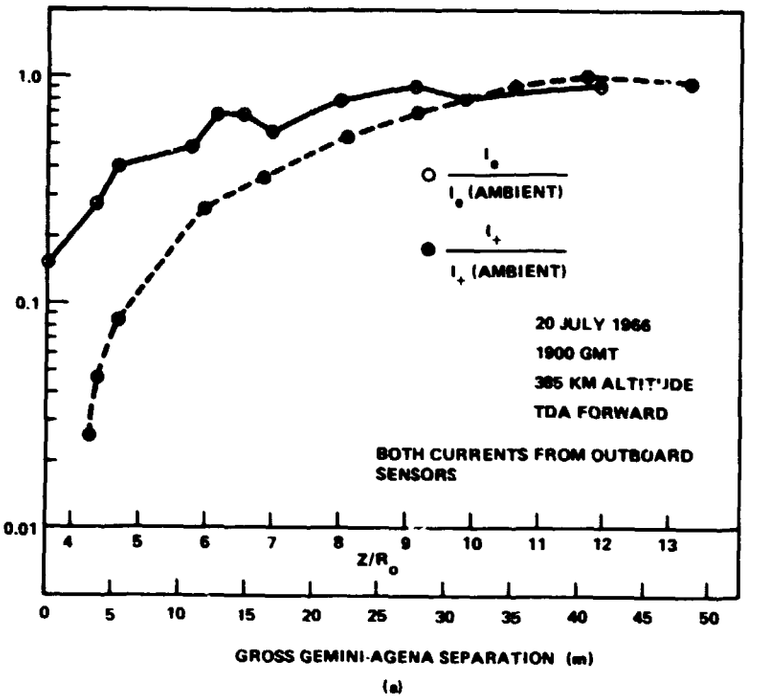

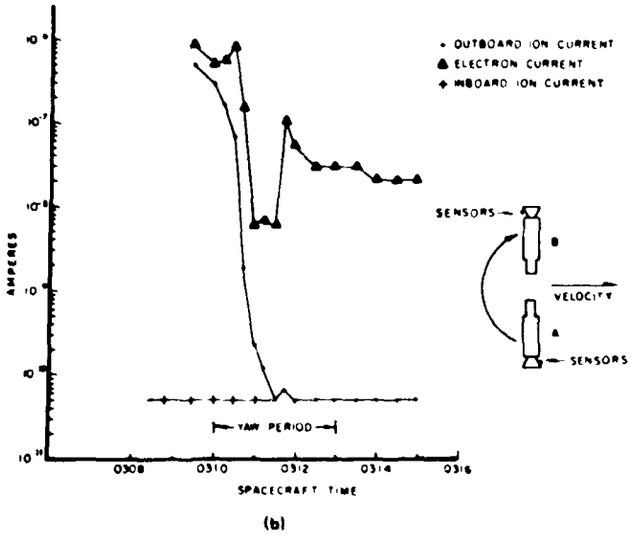

Figure D-8. Ion and electron currents collected during the Gemini-Agena 10 maneuvers. (a) Normalized currents (ambient current only approximated) as a function of the separation distance, and (b) currents collected during the Agena yaw maneuver, after Troy, et al. [43].

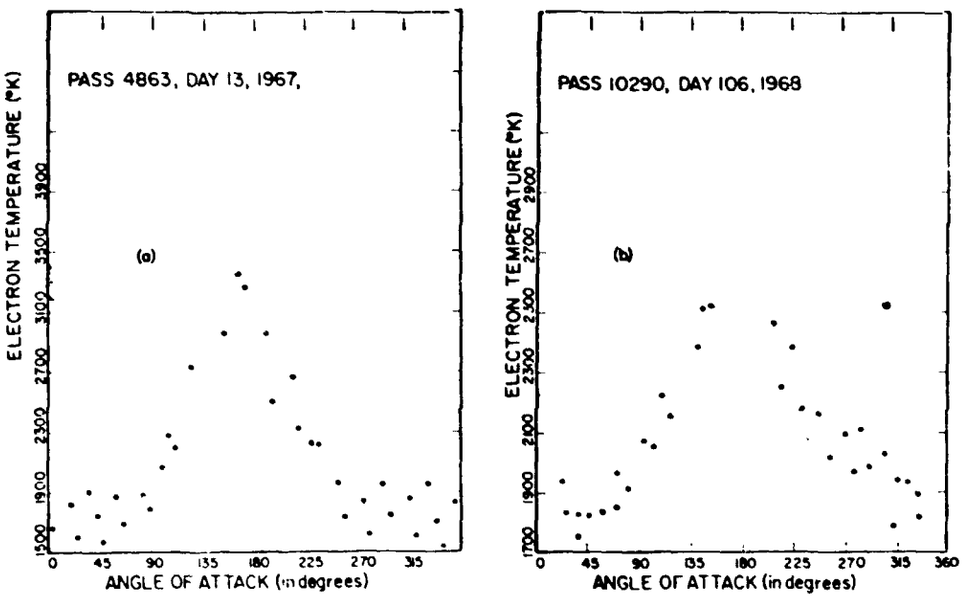

Figure D-9. Variation of T_e with angle of attack for (a) an O^+-plasma and (b) an H^+-plasma for conditions shown in Table D-3, after Samir and Wrenn [80].

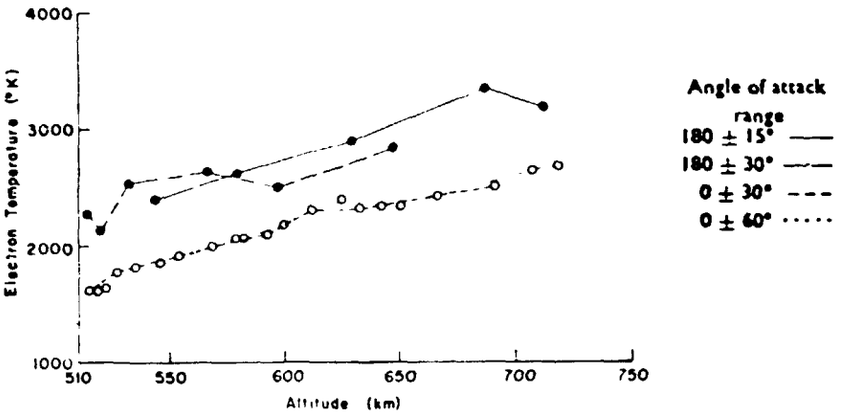

Figure D-10. Variation of electron temperature in the frontal region (open circles) and wake region (closed circles) as a function of altitude, after Samir and Wrenn [80].

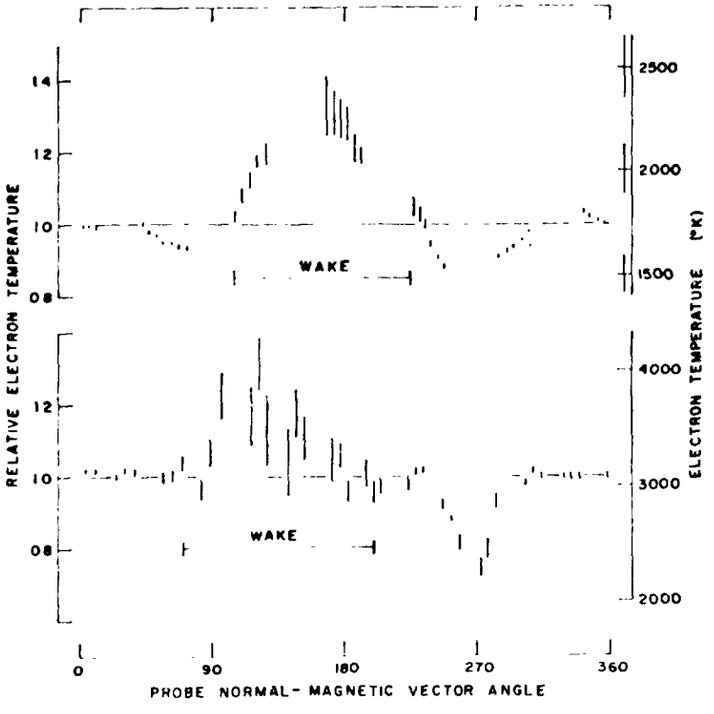

Figure D-11. Normalized electron temperature, $T_e(\theta_e)/T_e(\theta=0)$ as a function of angle between the probe normal and $\vec{B}$, θ_B, for two relative orientations between $\vec{V}_o$ and $\vec{B}$; after Samir and Wrenn [80].

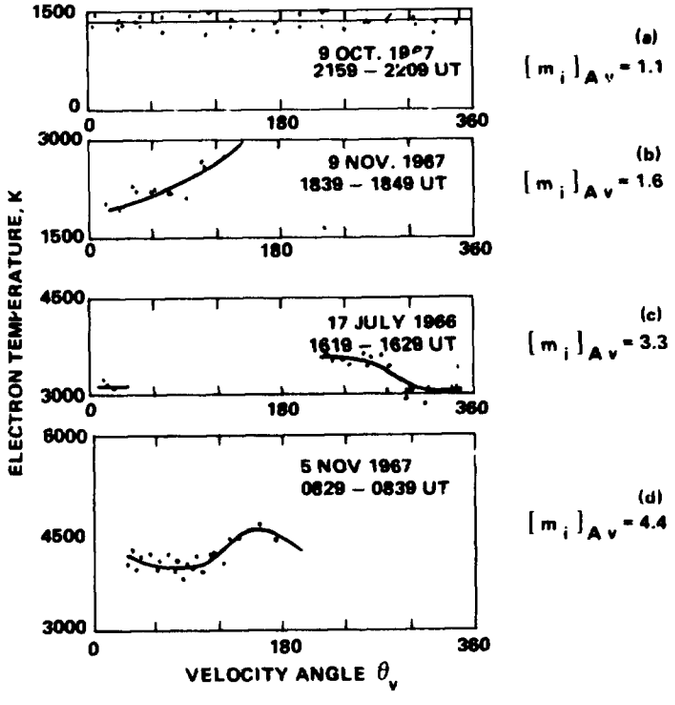

Figure D-12. Examples of the classes of angular dependence of electron temperature on angle of attack; (a) at 2700 km altitude with $[m_i]_{av}$ = 1.1, (b) at 1600 km altitude with $[m_i]_{av}$ = 1.6, (c) at 800 km altitude with $[m_i]_{av}$ = 3.3, and (d) at 2400 km altitude with $[m_i]_{av}$ = 4.4; all cases in sunlight except (a); after Troy, et al. [42].

APPENDIX E. A CRITICAL REVIEW OF THE RESULTS FROM PREVIOUS EXPERIMENTAL INVESTIGATIONS

The following review of other experimental work will be made in order of research groups. This will permit a grouping of all results produced in the same experimental facility and, therefore, subject to the same limitations. In addition, the investigations are divided into those involving only electrostatic forces and those which include a magnetic field within the plasma. This division is a natural one in view of the different scaling laws (discussed in Chapter III) and the facilities required.

For a more detailed discussion of diagnostic techniques, the reader is referred to Appendix F. A discussion of experimental requirements and facilities is given in Chapter III.

1. The Electrostatic Interaction (No B-Field)

a. Convair (1961). One of the first experimental studies of the interaction of a streaming plasma with conducting bodies was reported by Meckel [44]. A drifting plasma was created by a pool-type mercury arc discharge from which ions were extracted and accelerated into a drift tube by a biased mesh grid exposed to the discharge plasma on one side. The space charge was neutralized by electrons produced by an emissive electrode emersed in the ion stream near the acceleration grid. The drift chamber in which experiments were conducted was a 4.5 cm diameter by 15 cm long cylinder. The ion stream was reasonably parallel; however, background pressure ranged from 5 to 10^{-3} torr. Charged particle densities ranged up to 2×10^{11} cm^{-3}. As shown in Table E-1, the electron temperature was not measured; therefore, it is not

possible to determine the simulation parameters for this set of experiments. The results of this study are therefore of limited, very qualitative value.

The experiments conducted include the observation of current collected by a thin disk, positioned in the flow, as a function of angle of attack (Figure E-1). An enhancement of the current collected by the disk occurred when the disk was oriented parallel to the flow. This is apparently similar to the end effect noted in later publications for cylindrical Langmuir probes [51]. Although not explained in this work, this effect occurs as a result of two independent mechanisms for current collection; i.e., the direct impact of free-stream ions and the impact of ions deflected by electric fields in the plasma sheath. When the disk is normal to the flow ($\theta = 90°$), only the ions physically swept up in the geometric cross-section of the disk are collected. Those deflected by the sheath pass into the wake and are not collected. As the angle of attack is decreased, the cross-sectional area of the disk, and hence the magnitude of the current collected by direct impact, decreases. The total current therefore decreases until θ approaches zero (parallel to the flow), when the ions deflected by the sheath begin to be collected by the portion of the disk extending into the wake. This effect increases the current and is maximized when the disk is parallel. If the disk is small compared to the sheath size, $R_o \leq \lambda_D$, then the deflected ion current will be greater than the direct impact ion current. Since no temperature measurements were provided, no assessment of the relative size of the body in these experiments can be made. However, the above explanation, which has been subsequently verified [51], together with the data would indicate that $R_d \lesssim 1$.

A second experiment consisted of total current measurements by an electrostatic probe in the wake of a cylinder. These measurements show a central ion void region which is occupied by electrons. The void is flanked by regions of ion current enhancement which are, in turn, flanked by regions of slight ion current rarefaction. These observations are in qualitative agreement with the theoretical description by Rand [4] (Appendix B). However, no quantitative assessment can be made, since R_d, Φ, and S cannot be

determined. The measurements were repeated for ϕ_b = -4, 0, and +5 volts. The negative bias created a current peak in the center of the wake approximately equal to the ambient current density. The zero and 5-volt bias cases show only a void of ion current. This suggests a focusing of ions into the wake axis by the electric fields created in the sheath around the cylinder, which is born out by the work of other experimenters described below.

b. RARDE, Halstead, G. B. (1964). Experiments in which the flows past satellites and rocket plumes were simulated have been reported by Cox [45]. The experiments were carried out in an arc-generated (or discharge) plasma. The spacecraft-space plasma interaction is considered to be divisible into several regions as shown in Figure E-2. The parameters for these experiments, shown in Table E-1, indicate that they were conducted in region 1 (i.e., $R_o > \lambda_{nn}$ and λ_{ii}), whereas all other studies discussed are carried out in the region where $R_o << \lambda_{ii}$ and λ_{nn} and $R_d << 1$ to $R_d \gtrsim 1$. Of particular interest is the observation of enhanced charged particle density associated with a neutral bow shock. The increase of n_o associated with the shock produces an increase in n_i by collisional coupling. A corresponding increase in n_e then occurs as a result of the space charge set up by the ions.

It should be noted that since $R_o > \lambda_{nn}$ and λ_{ii}, the charged particles (ions and electrons) can be expected to be Maxwellian in this case.

The observations include electron current along the axis ahead of a disk and a spherical body and transverse profiles at three positions downstream from the sphere. The frontal axial profiles are proportional to n_e and show a slight enhancement in the shock region. The transverse profiles in the rear show a depletion of n_e ($\sim$75%) at the nearest position ($Z/R_o < 2$). At the next position ($Z/R_o \simeq 2$), the void region was found to have partially filled and an electron density peak (below ambient) occurred at the center. At the third position ($Z/R_o \gtrsim 5$) the peak does not occur and the depletion in the wake is only slightly below ambient and has increased in width (Figure E-3).

c. TRW - STL (1964). These studies, reported by Hall, Kemp, and Sellen [46], were conducted in a large plasma wind tunnel which used a contact

ionization, Cesium ion accelerator with subsequent emissive electrode neutralization to create a drifting plasma stream. This facility is similar to the Marshall Space Flight Center (MSFC) No. 1 facility used for the present investigation. The ion stream, 2.5 cm in diameter at the source, was accelerated through a 90-volt potential drop into a 1.2 m diameter by 2.4 m long cylindrical vacuum chamber. Stream divergence was determined to be 3 to 4° and the ratio of slow (charge exchange) ions to fast (stream) ions should have been negligible since chamber pressure was held at 2×10^{-6} torr during operation.

Experimental measurements were made of the space potential in the vicinity of a 0.94 cm radius sphere in a 7.7 km/sec ion stream. Measurements were made in the frontal, side, and rear regions with a variety of potentials applied to the sphere, ranging from -5 to -100 volts. Ambient ion density for these experiments was 1.3×10^{6} cm^{-3}. These data show that at the sides of thc sphere, the dimension of the sheath was slightly greater than in the frontal region for all potentials. The sheath was found to be elongated toward the downstream side for small negative potentials on the sphere, while for large negative potentials, the sheath became thin in the rear, creating an oval configuration with the major axis aligned normal to the flow.

The second type of experiment conducted consisted of ion current density measurements downstream from a sphere with a 2.54 cm radius. For these measurements, the plasma stream characteristics were $V_o = 11$ km/s and $n_i = (0.32 \text{ or } 5) \times 10^{-6}$ cm^{-3} while the bias on the sphere was varied from 0 to -307 volts. Data were taken downstream at $Z/R_o = 4$ and 7. These data show the first experimental evidence for focusing of the ion trajectories into the wake axis by the electric fields in the plasma sheath (Figure E-4). This result is qualitatively similar to the theoretical results of Davis and Harris [11], Taylor [20], and Call [12]. Unfortunately, no temperature measurements are given so that the simulation parameters R_d, S, and Φ_b, discussed in Chapter III.C.1, cannot be obtained, and hence, no direct comparison with theory can be made.

Finally, the effect of plasma screening on the electric fields within the sheath was investigated by measuring the charge deposition rate on a button collector mounted on the equator of the sphere.

This technique is based on the fact that in the absence of the plasma stream, the field at the surface of the sphere is given by $E_o = \phi_b/R_o$, where ϕ_b is the potential on the sphere. From Gauss' law, the total charge on the button is $Q_{bo} = \epsilon_o E_o A$, where A is the botton collector area. With the sphere emersed in the plasma stream, the charge on the button will be $Q_{b1} = \epsilon_o E_1 A$. Then,

$$E_1 = \frac{Q_{b1}}{\epsilon_o A} = \frac{Q_{bo} + \Delta Q}{\epsilon_o A} = E_o + \frac{\Delta Q}{\epsilon_o A} \quad .$$

The enhancement of the field, $\gamma = E_1/E_o$, is therefore given by

$$\gamma = 1 + \frac{R_o}{\epsilon_o A} \frac{\Delta Q}{\phi_b} \quad .$$

The plasma stream was pulsed so that $i = \Delta Q/\Delta t$. The results of these measurements are shown in Figure E-5. The knee which occurs at $n_i \sim 10^7$ cm^{-3} was not explained.

The butte probe was also used to determine the ion flux to the sphere as a function of angle of attack; i.e., $j_i(r = R_o, \phi = 90°, \theta)$. From these measurements, it was determined that:

(1) $j_i(R_o, 90, \theta) = 0$ for $90° \leq \theta \leq 180°$ and $\phi_b \leq \phi_s$.

(2) $j(R,\theta)$ increases over the range $90° \leq \theta \leq 180$ as ϕ_b becomes more negative. $j_i(R_o,\theta)_{max}$ occurs at $\theta = 180°$.

(3) For $n_i \cong 10^7$ cm^{-3}, $j_i(R_o,180) \geq j_i(R_o,0)$ for $\phi_b = -150$ V.

(4) As n_i decreases, $j_i(R_o,180)$, becomes minimized for $n_i \simeq 3$ 10^6 cm^{-3}.

Unfortunately, no data are presented in the publication to substantiate the above statements and, again, no simulation parameters are available.

d. RARDE, Halstead, G. B. (1965). The second plasma wind tunnel built at RARDE consists of an electron bombardment ion souce which uses argon as the working gas and is neutralized by electrons from an emissive electrode emersed in the ion stream. The general characteristics of the plasma stream generated by this device are shown in Table E-'. The experiments conducted in this facility are reported by Clayden and Hurdle [47] and include measurements of total ion flux collected by conical bodies and measurements of normalized ion current density in the wakes of a 15° cone and a sphere. The total current measurements are not of interest except to note that for a given body, it is reported that preserving the ratio $e\phi_b/\frac{1}{2} m_i V_o^2 = \Phi_b/S^2$ reduces current versus potential profiles, obtained with various values of S and E, to a single curve. Therefore, Φ_b/S^2 is an important scaling parameter for total ion flux to a body.

The wakes of the cone and sphere were studied for a number of different values of body potential and positions downstream. Ion current was measured by a small (1 mm diameter) spherical electrostatic probe with a slightly negative bias. The current density in the wake was normalized to the current density measured in the ion stream with the body removed. Data are given for $-3 \leq \Phi_b/S^2 \leq +0.9$ at $Z/R_o = 1, 5, 9$, and 19 for both bodies.

The wakes behind both bodies are similar, as shown in Figure E-6, when a negative potential was applied to either body, a strong enhancement in ion flux, several times the ambient value, was observed on the wake axis beginning at the body and extending beyond 10 radii downstream. However, no current peak was observed when either body was biased positively or allowed to float. It was also noted that while the wakes for the two bodies are similar for low potentials, when the body is biased at large negative values, the axial ion current enhancement in the wake of the sphere is up to 50% greater than that of the cone. However, the cone creates a wider disturbance. This is probably due to the fact that it extends further upstream from its base than does the forward half of the sphere, and hence collects more current from the stream. This explanation was confirmed by the total current measurements.

These measurements are found to be in reasonable agreement with Davis and Harris [11], and with the neutral ion approximation theory developed by Alpert, et al. [25]. However, these results must be viewed with caution due to the high ratio of slow ions present, the rather short mean-free-path for collisions, and the existence of non-uniformities in the ion stream.

e. USSR-Skvortsov and Nosachev (1968). The first detailed Russian experimental work to be published on this subject was by Skvortsov and Nosachev [48,49]. Their experiments were conducted using a gas discharge ion source operated with argon. The ion stream was accelerated through a 150-volt drop into a 0.5 m diameter by 2 m long cylindrical chamber. The ion stream was neutralized in the usual way with an emissive electrode immersed in the stream.

In these studies, stream conditions were monitored with an R.P.A. and a Langmuir probe while current measurements in the wakes of various bodies were made with plasma electrostatic probes. Thermal (emissive) probes were used to measure the potential distribution.

In the first set of experiments [48], measurements of normalized ion current density, j/j_o, were made in the wakes of 2 and 6 cm diameter spheres, and the space potential was measured downstream from the 2 cm sphere (Figure E-7). These data were shown as equal current density and potential contours. They show an axial current enhancement ($j/j_o = 1.8$) surrounded by a rarefaction cone. This structure was observed when the spheres were at floating potential as well as negatively biased. The cone angle for the maximum rarefaction in the wake is in agreement with that predicted by Alpert, et al. [25] for the case when the body is at floating potential. The plot of space potential revealed a positive potential barrier at the location of the axial ion current density peak, and regions of negative space potential corresponding to the regions of reduced ion current density. Hence, the spatial distributions of ion current density and space potential are correlated. The locations of both Φ_s and j/j_o peaks tend to move toward the body and their amplitude increases as Φ_b becomes more negative.

In the second set of experiments, the effect of various parameters on the wake structure of 1, 2, and 4 cm diameter spheres, 30° and 60° cones with 1 cm base diameters, and a 1 cm diameter by 0.05 cm thick disk was investigated. Measurements of normalized current, j/j_o, in the wakes of 1 and 2 cm diameter spheres, where the parameters S, R_d, and Φ_b were preserved (Figure E-8), are in good agreement, as expected. The range of parameters, however, is insufficient to establish this result in general. In fact, it is acknowledged that although the near- and far-wake zone seem to be reproduced very well, there is some uncertainty concerning the mid-wake region.

It has been suggested that in order to obtain similar flow fields it is only necessary to preserve the ratio $e\phi_b/\frac{1}{2} m_i V_o^2 = \Phi_b/S^2$ rather than Φ_b and S separately. However, when j/j_o measurements were made downstream from the 2 cm diameter sphere while holding $[e\phi_b/\frac{1}{2} mV_o^2]$ constant, it was found that for $\phi_b \sim \phi_s$, a change in T_e from 1 to 3.5 eV produced marked changes in the wake structure. At $Z/R_o = 6$, $R_d = 8$, and $\phi_b = -6.5$ V, no axial ion current enhancement was observed for $T_e = 1$ eV but a very distinct peak appeared when $T_e = 3.1$ eV (Figure E-9). For these cases, $[e\phi_b/\frac{1}{2} m_i V_o^2]$ remained constant; however, for $T_e = 1$ eV, S = 11, and $\Phi_b = -6.5$ while for $T_e = 3.1$ eV, S = 6.6, and $\Phi_b \simeq -2.1$. It is apparent then that for these conditions Φ_b and S must be maintained independently. At large negative values of ϕ_b, changes in T_e become unimportant and preservation of the combined parameter Φ_b/S^2 would be sufficient.

f. California Institute of Technology (1969). The facility at Cal-Tech consists of an electron bombardment ion source which operates with argon gas. The ions were extracted through a single grid of either 2.54 or 30 cm diameter and neutralized by an emissive electrode. The experiments were conducted in a 0.5 m diameter by 1 m long chamber. The general characteristics of this facility are shown in Table E-1.

The experiments performed in this facility are reported by Sajben and Blumenthal [50]. Two rough theories are developed to help describe their results, both of which are of interest.

A theory is developed to predict the density of the slow, charge exchange ions in the plasma stream. A lower limit is established by considering only hard sphere type collisions. An upper limit is established by assuming all collisions to result in charge exchange while no momentum transfer occurs. This upper limit is given by

$$\left[\frac{n_s}{n_i}\right] = \frac{1}{2\pi} \frac{V_o r_s n_o Q_c}{(8kT_e/\pi m_o)^{1/2}} = \frac{1}{4} \frac{V_o}{(2\pi kT_e/m_o)^{1/2}} \frac{r_s}{\lambda_c}$$

where

r_s = plasma stream radius

n_s = slow ion density

n_f = stream ion density

Q_c = charge exchange cross-section

λ_c = charge exchange mean-free-path length.

The experimental results were found to fall between the predicted max and min values.

In addition to obvious effects such as neutralizing the space charge in the void region behind bodies, the slow ions, which have no preferred direction, were shown to affect plasma wave propagation; i.e.,

$$C = \left[\frac{T_f}{T_e} + \frac{1-\beta}{\beta + (T_s/T_e)} \cdot \frac{T_s}{T_e}\right]^{1/2} \left(\frac{kT_e}{m_i}\right)^{1/2}$$

where $\beta = n_{s\infty} / n_{e\infty}$, and C = propagation speed. The effect of $\beta > 0$ is to decrease C and therefore the speed ratio, S, will increase.

A second, very rudimentary theory was developed to predict the crossing point of deflected ion streams on the wake axis. It is assumed that the electric field at the largest diameter of the body is dominant to the extent that the field associated with all other regions of the body can be neglected. At the

largest diameter, the field is assumed to be uniform over some finite band of length L in the Z direction, and to fall off as $\exp[-(r-R)/\lambda_D]$ in the r-direction. The basic geometry is shown in Figure E-10. The crossing point, Z_o, is given by:

$$Z_o/R_o = \frac{L}{\lambda_D} (Y_o \tan Y_o/2)^{-1}$$

where

$$Y = \sqrt{\frac{2e\phi_b}{m_i V_o^2}} \frac{L}{\lambda_D} \exp[-R_o/2\lambda_D]$$

and

$$Y_o = \frac{L}{\lambda_D} [2e\phi_b/m_i V_o^2]^{1/2} \cos (Y_o/2) \quad .$$

In order to test the basic assumption in this theory (that only the potential on the band of width L is important) a sphere was constructed with a band around its equator which could be biased independent of the remaining two hemispheres. Figure E-10 shows axial current density profiles taken behind this segmented sphere with the entire sphere biased ($\alpha = 0.61$), the entire sphere floating, and with only the band biased and the remaining two hemospheres floating ($\alpha = 0.52$). Although the general morphology of the axial profile is unchanged, the biasing of the whole sphere resulted in the peak moving upstream. Therefore, it seems obvious that biasing the remaining two hemispheres, while possibly less important than the biasing band (no data were given for biasing the hemisphere and not the band), does significantly affect the crossing point location. Therefore, this theory will provide only a rough approximation of the crossing point location.

g. Massachusetts Institute of Technology (1969-70). The facility at MIT, as reported by Hester and Sonin [34, 51-53], uses an electron bombardment ion source which operates on argon gas. The ion beam was accelerated into a 0.5 m diameter by 1.2 m long cylindrical chamber and neutralized by

electrons emitted from a hot filament in the stream. The general characteristics of this facility are given in Table E-1.

Hester and Sonin studied, in detail, the wake structures formed by small cylindrical bodies with $5 \cdot 10^{-3} \leq R_d \leq 40$, spheres with $1.8 \leq R_d \leq 46$, and a flat strip with $R_d \simeq 40$ [51]. In these investigations, the speed ratio, S, and normalized body potential, Φ_b, were also varied. In addition, some analysis was made of the temperature of the ions and existence of slow, charge exchange ions.

The transverse ion temperature was considered to result from a finite (20 cm) accelerator diameter which did not produce a source like flow. Making the assumption that ions emitted from any point on the accelerator grid are equally likely to arrive at some point in the chamber, the distribution function was determined to be:

$$f_i(v) = \frac{4}{\pi}\left[1 - \left|\frac{v_\perp(Z)}{v_{max}}\right|^2\right]^{1/2}$$

where

$f_i(v)\,dv$ = fraction of ions at point Z with $v_\perp'$ between $v_\perp$ and $v_\perp + dv_\perp$.

Then

$$\bar{c} = \frac{4}{3\pi}(R_s/Z)\,V_o$$

where

$\bar{c}$ = mean thermal speed

V_o = drift velocity of the stream

R_s = source (accelerator and) diameter.

Hester and Sonin used $\bar{c}$ to characterize the transverse ion motion when it was considered.

The slow ion population was measured by a shielded collector disk oriented perpendicular to the stream. The slow ion current to the collector is

$I_s = en_s (kT_e/m_i)^{1/2} A$, where I_s and n_s are the slow ion current and number density, respectively, and A is the disk area.

Considering the wake structure behind the small diameter but very long cylinders $R_d << 1$ with Φ_b [illegible], the following observations are reported [34]:

(1) No ion void region was observed immediately behind the body. Since $R_o << \lambda_D$, the number of ions swept out by impact on the cylinder is very small compared with those deflected by the electric fields in the plasma sheath, which extends many radii out from the cylinder.

(2) The deflected ions form a region of ion flux enhancement when they cross the wake axis, as discussed previously. However, in addition to this initial peak, observed by previous experimenters, several other peaks occurred farther downstream at regular intervals of ω_{pi}/V_o (ω_{pi} = ion plasma frequency). This observation is shown clearly in Figure E-11. The first of these ion flux peaks is clearly the result of the deflection of ion streams from both sides of the cylinder and their subsequent addition when they intersect at the wake axis. It is not at all clear how the remaining current peaks are created from a physical point of view, although axial ion current oscillations were predicted to occur at the ion plasma frequency, ω_{pi}, in the theory developed by Rand [4]. The observation on the ion flux peaks at intervals of ω_{pi}/V_o is therefore in agreement with this prediction.

(3) The deflection of ions across the wake by the sheath fields create an ion rarefaction region on each side of the cylinder which propagates out from the wake axis at the ion acoustic speed, forming a Mach angle with the flow direction; i.e., $\theta = \sin^{-1}(1/S)$. This is also in agreement with the theoretical predictions by Rand [4].

(4) A wave-like structure is observed to originate at the axial ion flux peaks and propagate out from the wake axis. The term "wave like" is used because these disturbances do not propagate at the ion acoustic speed. At highly negative values of Φ_b, the disturbance originating at the first ion flux peak is clearly a pseudo wave, created by streams of ions which are deflected toward

the wake at the sheath on each side of the cylinder, pass through the ion flux enhancement at the wake axis, and continue on, traveling away from the wake axis and into the undisturbed flow. This interpretation is verified by the fact that the angle formed by these disturbances is equal to the maximum deflection angle for ions in the sheath surrounding the body (Figure E-12). At small negative values of Φ_b, the angle formed by the disturbances still depends on Φ_b, but is not equal to the maximum deflection angle, thereby indicating some interaction between the ion streams at the axial ion flux peak.

The nature of the disturbances originating at the remaining ion flux peaks is not understood. Their propagation speed depends on both Φ_b and R_o/λ_D. Therefore, they are not collective plasma phenomena such as ion acoustic waves. However, neither can they be explained by the deflection of ion streams at the body, as was the first set of disturbances. With the exception that an ion void appeared in the near wake, applying a small positive potential to the cylindrical bodies resulted in a far-wake structure very similar to that shown in Figure E-11 for negative biases.

Concerning the experiments performed with intermediate sized bodies ($R_o/\lambda_D \gtrsim 1$), the following observations were made [52,53].

First, for a cylinder with $R_d = 1.6$, a void was observed immediately behind the body and repopulation was dominated by the deflection of ions by the sheath fields. Streams of ions deflected through the wake intersected at the wake axis, formed an ion current peak, and continued on into the undisturbed flow field, thereby creating pseudo waves; i.e., a stream of ions traveling through the ambient medium which give the appearance of a wave. The behavior of the deflected ion streams is similar to that for very small cylinders discussed above and qualitatively similar to theoretical predictions by Taylor [20] and Call [12]. However, in this case, the additional ion flux peaks which occurred periodically in the wake of small cylinders are hardly perceptible. The wakes of spheres for which $1.8 \leq R_d \leq 7$ show that an ion void forms immediately behind the body and the deflection of ions in the sheath occurs as for cylindrical bodies [Figure E-13(a)]. However, the amplitude

of the axial ion current enhancement formed by the deflected ion streams is extraordinarily high due to the axial symmetry of the body (ions are focused to a point rather than to a line as with the cylinder). The peak divides to form a cone of enhancement as in the case of the cylinder. Also evident is an ion rarefaction wave which propagates out from the wake axis at the ion acoustic speed. This behavior is in agreement with the theory for a spherical body developed by Maslennikov and Sigov [17,18,19]. When a strong negative bias is placed on the sphere, a second cone of enhancement emerges from the peak and travels away from the axis at a greater speed [Figure E-13(b)]. This appears to be a pseudo wave created by deflected ions as described previously. The main peak splitting, occurring farther downstream, is thought to result from the deflection of ions by the positive space charge associated with the very large ion current peak. The ions reaching the wake axis farther downstream have been deflected less at the sheath and therefore possess a smaller component of velocity normal to the axis. At the point where $1/2\ m_i V_\perp^2 = e\phi_s$, the ions will be deflected away from the axis and the peak will appear to split. Although plausible, this explanation cannot be confirmed by the data. Note that while the wave like disturbance divides off axis, no oscillatory behavior on the axis was observed as for small cylinders.

Concerning very large bodies ($R_o/\lambda_D >> 1$), it was found that the wake formed by a cylinder with $R_d = 39$ has no axial structure for $\Phi_b = 0$ (floating) but does possess a small axial ion flux peak (much lower than the ambient flux level) when $\Phi_b = -50$ [51,53]. However, a small ion flux peak occurred in the wake of a large sphere ($R_d = 46$) with only a small negative bias of $\Phi_b = -3.5$ (Figure E-14). The effect of a simulated ion temperature (the motion of the ions was not Maxwellian) is also included in these data, as indicated.

This work points out a fundamental difference between the wakes created by cylindrical and spherical bodies. The wakes of cylinders are dominated by deflected ions which pass through the axial current peak and form pseudo waves. However, the wakes of spheres, while filled primarily by deflected ions (identically to the cylinder wakes) form axial current

enhancements which are too strong for the ion streams to pass through unaffected. Therefore, the far-wake structure of spheres is considerably different. It is also noted that while the axial ion current oscillations in the wake of the cylinder decay rapidly, the wave-like structure that propagates out from these oscillations is damped very little. This is also true of the diverging structure downstream from spherical bodies [Figures E-13 and E-11(c)].

h. ESTEC - Netherlands (1970). The ESTEC facility consists of an electron bombardment ion source which operates with argon gas and is neutralized by electron emissions from a hot filament immersed in the ion stream. The stream is approximately 1.6 cm in diameter at the plasma source and diverges to 10° to 13° as it is injected into a 0.5 m diameter by 1.7 m long cylindrical chamber.

Experiments conducted in this facility, involving the wake structure downstream from a thin disk and a long cylindrical body, oriented perpendicular to the flow, are reported by Knott and Pedersen [54]. The approximate conditions for these experiments are given in Table E-1. Unfortunately, conditions were not measured for each experimental run so that it must be assumed that they remained relatively constant from one run to the next. It should also be pointed out that no temperature measurements were made so that the simulation parameters cannot be evaluated. The results of these experiments must, therefore, be considered in a very qualitative light.

In the two experiments, the wakes created by a disk (R_o = 2.5 cm) and a cylinder (R_o = 3 cm) were studied with various potentials applied to the bodies ranging between 0 and -100 volts. Measurements were made for beam energies (ion drift velocities) of 40 and 80 eV for the disk at Z/R_o = 1.6 and beam energies of 40, 60, and 80 eV for the cylinder at Z/R_o = 2, where Z is measured from the center of the bodies.

The main findings of these studies were: (1) The axial ion current enhancement is maximized when the potential applied to the body corresponds to the kinetic energy of the plasma stream ions ($1/2\ m_i u_o^2 = e\phi_b$), which is shown in Figure E-15. This is in qualitative agreement with the implications of the Maslennikov and Sigov theory [17-19], and (2) it was determined that

the maximizing of the axial ion current density peak when the potential on the body is equal to the kinetic energy of the ions is most pronounced when measured at $Z/R_o = 2$ (no data were shown to verify this observation).

i. ONERA (1972, 1973, 1974, 1975, and 1977). The facility at ONERA is described in detail by Fournier and Pigache [55]. This facility uses argon gas in an electron bombardment ion source. The ion stream is neutralized by electrons emitted from a hot filament within the ion stream. The beam is accelerated into a cylindrical chamber 3 m in diameter by 5 m long. The general characteristics of this facility are shown in Table E-1.

A number of publications have resulted from the work carried out at this facility. Most of the data important to plasma flow interactions is presented in one paper by Fournier and Pigache [58]. The most important difference between this work and previous studies is an extensive effort to simulate and diagnose a proper scaling of the random ion motion. This was accomplished by placing a biased wire mesh (1 mm wire spaced at 7.5 mm) in the plasma stream 1.25 m from the source. A very low T_i ($\sim 700°K$) was achieved when the grid was allowed to float. With the grid biased at -20 volts, the effective ion temperature was determined to be $\approx 1900°K$. It must be emphasized, however, that while some transverse motion was induced in the formerly parallel ion flow, the motion was not Maxwellian and therefore the distribution was not, in fact, characterized by a temperature. The result of the experiments must therefore be considered qualitative in nature.

The first publication [55] described the experimental techniques and diagnostics used to study the behavior of the ion population in the plasma stream and shows an example of transverse ion current profiles in the wake of a cylinder at $Z/R_o = 7.5$. The body potential for these data was -20 volts and the plasma conditions were characterized by $R_d = 10$ and $S = 16$. A small peak (much below ambient) occurred on the wake axis for a cold plasma stream but was smoothed out when some (simulated) thermal motion was imposed on the ions of the plasma stream ($T_i = 700°K$ and $1900°K$). This result appears to be contradicted by results reported in a later paper [58], where extensive wake measurements were made for a variety of plasma flow conditions and the

axial ion current enhancement was very much in evidence for body potentials of only $\Phi_b = -3$, and grew as the body potential became more negative (Figure E-16, y-axis).

A 1975 publication by Fournier and Pigache [58] deals with an extensive investigation of the importance of the T_e/T_i ratio. The wakes created by the interaction of the synthesized, streaming plasma with conducting spherical bodies are studied to determine the effect of varying T_e/T_i from $>>1$ to $\simeq 1$ for a variety of plasma flow conditions.

The first set of data is for the conditions, $T_e/T_i \simeq 100$, $R_d = 16$, $S = 10.7$, and $\Phi_b = -3$. The wake structure corroborates the earlier work by Hester and Sonin (E.1.g) in which the wakes behind spheres in a cold plasma stream were studied, i.e., the ion streams deflected by the plasma sheath fields cross the wake and form an axial ion current density enhancement which divides further downstream and travels away from the axis forming a conical disturbance. The conical disturbance subsequently divides and at the most remote measurement downstream, a total of six ion current density peaks are observed (Figure E-16, x-axis). It is noted that the division of the conical disturbance into multiple wave packets was not predicted theoretically.

For the case when $T_e/T_i \simeq 10$, the resulting wake structure is studied for $S \simeq 10$, $\Phi = -3$ (floating), and $R_d = 6.5$, ~ 23, and 45 (Figure E-16, Z_1-axis). In all three cases, an axial ion current density peak is observed. In all cases, the magnitude of this peak is approximately equal to the ambient ion current density. For the smaller bodies, $R_d = 6.5$ and 23, the peak is found to divide into a trailing conical disturbance which subsequently divides into multiple wave packets. The primary difference between these data and those discussed above for $T_e/T_i \simeq 100$ is that the structure is less distinct; i.e., the disturbance far downstream is less sharp and of smaller amplitude (Figure E-16, x-axis). The large body wake ($R_d = 45$) does not show the axial ion current density peak to divide into a conical disturbance. However, due to the limited volume of the experiment, measurements were made to axial distances of only 25 R_o. Reference to the above small body data, in which the peak did

divide, shows that the division occurred further downstream than this (at $\sim 40\ R_o$ for $T_e/T_o \simeq 100$ and 40 to 80 R_o for $T_e/T_i = 10$). Therefore, the absence of this effect cannot be taken as conclusive evidence that it does not occur for large bodies. Finally, the case for $T_e/T_i = 10$ and $R_d = 6.5$ was repeated with $\Phi_b = -100$. The effect of the large ion attracting potential on the body was to produce an enormous increase in the amplitude of the axial ion current density enhancement ($\sim 9\ j_o$) (Figure E-16, y-axis).

The last set of data reported was recorded for the case $T_e/T_i \sim 1$, $S \simeq 5.6, \Phi_b = -3$ (floating) and $R_d = 1.6$, 7, 26, and 45 (Figure E-16, Z_2-axis). It is significant that, with the exception of the data for $R_d = 7$, no axial ion current density peak or conical disturbances occurred in these wakes. For the $R_d = 7$ case, there is only a slight hint of the axial ion current density peak. It is therefore declared that if the plasma ions are sufficiently warm, the structure in the wake will be smoothed out, leaving only the initial void region which fills in a manner very similar to wakes in neutral gases.

The data for $R_d = 1.6$ were obtained behind a cylindrical body and compares very well with the theoretical calculations for a cylinder by Fournier [23]. The remaining data were obtained in the wakes of spherical bodies and compare well with theoretical calculations by Jew [83] and Gurevich, et al. [26].

Three points should be made about this experiment which limit its applicability to the spacecraft-ionospheric interaction. First, as discussed previously, the heated ion population did not possess a Maxwellian distribution and therefore any temperatures quoted are effective temperatures; i.e., transverse motion of the ions was created in the plasma stream, but was not random and therefore was improperly characterized by a temperature. Secondly, the effective temperatures were actually greater than the electron temperatures by 20 to 40%, whereas, in the ionosphere, T_i is typically a factor of 2 less than T_e. Therefore, although there is no doubt that the experiment shows that a sufficiently warm plasma will destroy the wake structure, it does not establish that this would be the case in the ionosphere. Thirdly, the data appear to show a persistence of the wake disturbances created by the wires of the mesh used to

generate the lateral ion motion. This is surprising since it persists for a large number of radii downstream while the structure of the large test body is smoothed. This would seem to indicate that the randomized motion actually consists of a number of streams of ions, created by deflection at the wires, which have propagated undisturbed, downstream. This behavior would be far from a Maxwellian distribution.

In a 1977 publication, Fournier and Pigache present ion current density data obtained in the wake of a spherical body for the conditions: $R_d = 7$, Φ_b = floating, $S = 8$, and $T_e/T_i = 0.7$ [59]. The data appear identical to those of Figure E-16 for the case $R_d = 6.5$, $\Phi = -3$ (floating), $S = 10.54$, and $T_e/T_i \cong 10$. It would appear that an error occurs in the quoted conditions of one of the data sets.

Finally, it is observed in both the 1975 and 1977 publications that the presence of slow (charge exchange) ions in the chamber tends, primarily, to smooth the structure in the plasma wake; i.e., decrease the amplitude of ion current density peaks and the depth of the ion rarefaction regions.

Illiano and Story have conducted a set of experiments in the ONERA facility in which the effects of the near wake on electron temperature measurements were studied [57]. The test body for these studies consisted of a conducting 6 cm diameter sphere which contained a surface-mounted button (Langmuir) probe at its equator. The probe had the same radius of curvature as the sphere and occupied 60° of solid angle. The experimental conditions were $n_i = 2.4 \times 10^4$ to 5×10^5 cm^{-3}, $V_o \cong 10$ km/sec. $\lambda_D = 0.2$ to 1.1 cm and T_e = 268 to 629°K. The resulting simulation parameters were, therefore, $S \cong 20$ to 30 and $R_d \simeq 3$ to 19. Φ_b cannot be determined since ϕ_b was not given.

The measurements consisted of $I_e - \phi_p$ curves taken with the button Langmuir probe as a function of angle of attack (0° = probe in ram direction). An example of the data is shown in Figure E-17. The ion current has been subtracted, leaving only the net electron current as a function of probe potential measured with respect to the space potential of the ambient plasma stream. The main findings of this experiment are (1) a depletion of electron current

(and hence density) in the void region, (2) an apparent enhancement of electron temperature if T_e is determined by the slope of $\ell n I_e$ - vs - ϕ_p near the plasma potential, and (3) the apparent existence of a negative potential well in the void region shown by the fact that the electron current is not a function of θ up to a certain potential, ϕ_w, but is depleted in the wake region for lower retarding potentials. This indicates that, for ϕ_p more negative than ϕ_w, the electrons that are able to overcome the retarding potential are also able to overcome the potential well and reach the probe regardless of its orientation. However, if ϕ_p is less retarding than ϕ_w, electrons will be collected in the frontal regions which are not sufficiently energetic to penetrate the potential well in the rear and will therefore not reach the button when it is rotated into the wake.

The conclusions drawn, while apparently correct, do not apply to the enhancement of electron temperature measured in situ for several reasons. First, the entire sphere was swept at ϕ_p (although current was collected only from the button), whereas the satellite remained at floating potential while the Langmuir probe or RPA grids were swept [84]. One would therefore expect an entirely difference disturbance to be created in the two cases. Secondly, in order to attain an enhancement of T_e when the button probe was in the wake, the slope of the $\ell n I_e$ ϕ_p curve was taken near $\phi_p = 0$ ($V_p = V_s$) where it was not linear. The in situ temperatures, on the other hand, were determined by fitting the entire $\ell n I_e - \phi_p$ curve with a theoretical expression, defining ϕ_p to occur where the curve first became non-linear and calculating T_e from the linear portion of the curve. The two measurements are therefore entirely different. Further, it can be seen from Figure E-17 that if the same procedure were used for the experiment as was used for the in situ measurements, the space potential would become a function of θ and the three curves at $\theta = 0°$, 90°, and 180° would all yield the same temperature.

j. <u>The City University England (1973)</u>. The facility used for the experimental work at City University is the RARDE facility used in work reported by Clayden and Hurdle in 1965 (Section d.). The ion source was

modified by replacing the single acceleration mesh by a pair of matching (screen and extraction) grids. The electrical circuits were also modified to allow the wire mesh, used to line the chamber walls, t ' be biased independently of the accelerator circuit. These two modifications permit effective control of the plasma stream divergence, which could be reduced to approximately 1° for a 40 eV ion stream. The general characteristics of this facility are given in Table E-1.

The most important finding in this work, reported by Martin and Cox [60], is the explicit demonstration of the effects of slow (charge exchange) ions and stream divergence on wake structure. Figure E-18 shows four transverse profiles of ion current density taken at the same axial position downstream and for the same plasma flow conditions with the exception that the residual gas pressure and hence slow ion number density, is varied. The variation in pressure from 7×10^{-4} to 7×10^{-5} torr corresponds to a normalized slow ion number density, n_s/n_f, variation from 0.06 to 0.02, where n_f is the ambient plasma stream ion concentration. These data show that (1) the axial ion current density peak decreases with decreasing slow ion concentration, (2) the depth of the ion void region increases with decreasing slow ion concentration, and (3) the slow ion population apparently has a negligible effect on wake structure when the concentration is reduced to 3% of the ion stream density. The plasma conditions for these data are not given.

A number of transverse profiles of normalized ion current density are shown over the range $1.3 \leq Z/R_o \leq 8.13$, under the conditions, $R_d = 3$, $S = 5.4$, and $\Phi_b = 3.8$, with divergence angles of 1°, 10°, and 20°. These data show that stream divergence tends to reduce the sharpness of wake structure (in particular the axial ion current density peak), stretch the ion void region further downstream, and cause the axial ion current density peak to occur further downstream. Although all three of these conclusions seem reasonable, the data do not clearly show the last two.

2. The Magnetogasdynamic Interac[illegible] (With B-Field)

The current investigation does not involve a magnetized plasma so that a detailed review of experimental work in this area is unnecessary. It is useful, however, to mention some of the basic differences observed between this and the electrodynamic case in order to assess the importance of the magnetic field under certain conditions and within certain regions of the disturbance created by spacecraft in the earth's ionosphere.

Experimental investigations in which the flowing plasma contains a magnetic field have almost all used single-ended Q-machines. This is a discharge type device in which ions (usually potassium) and electrons are produced by a hot tungsten ionizer. The ions are accelerated down a drift tube and absorbed by a cold electrode at the opposite end. The plasma, thus created, is contained near the center of the drift tube by a strong magnetic field aligned with the drift tube axis, and hence parallel to the plasma flow direction. The flow velocity, density, and electron and ion temperatures can be controlled by the potential and temperature of the anode and the pressure of the working vapor

Experimental work with magnetized plasma streams has been carried out at the P.N. Lebedev Physics Institute in the USSR and is reported by Bogashchenko, et al. [61] and Astrelin, et al. [62]. The main contribution of the Bogashchenko, et al. paper is the observation and study of oscillating wake structure which is related to the ion cyclotron frequency. Figure E-19 shows the distribution of normalized ion current density along the axis in the wake of a disk. The measurements were made with a small cylindrical electrostatic probe biased at -2 volts with respect to the plasma. The approximate experimental conditions were: $R_o/\lambda_D \sim 25$, $S \sim 2$, $R_o/R_{L(i)} \sim 1$, and $\Phi_b \sim 10$. (The potential on the body was not specified for any particular measurement but was usually of the order of -2 volts with respect to plasma potential.) Note that the primary difference in the data of Figure E-19(a) and (b) is the magnetic intensity. The locations of the relative maximums and minimums of

the normalized current density shown are replotted against the parameter $(Z\omega_{ci}/2\pi V_o)$ in Figure E-20. This shows that the ion flux depletions and enhancements occur in a regular oscillatory manner and that the frequency of these oscillations is approximately the ion cyclotron frequency, ω_{ci}.

This behavior is explained by the fact that under the influence of the magnetic field, the ions undergo a helical motion with radius of curvature $R_{L(i)}$ and frequency ω_{ci}. In the reference frame of the plasma, at time t = 0, the motion of the disk removes the ions within R_o of the Z-axis, creating a cylindrical hole in the plasma. The ions which were located at distances greater than R_o off the Z-axis at the time the disk passed then spiraled in and filled the void region. However, these ions are not free to remain at this location and when they spiral back out of the wake, the cylindrical hole reappears. The hole thus oscillates at the cyclotron frequency of the ions, ω_{ci}. It is then easy to see that in the reference frame moving with the body, the ion current density will have a cyclic behavior along the Z-axis with relative maxima occurring at regular intervals of $(2\pi V_o/\omega_{ci})$.

In the Astrelin, et al. paper, this effect is studied further. The data shown in Figure E-21(a) and (b) indicate that the amplitude of the axial ion current density maxima are inversely proportional to the magnetic field intensity parallel to the flow direction, $H_{\|}$, and the body radius, R_o, respectively. This occurs since the cyclotron radius of an ion must be greater than half the body radius in order for the ion to reach the wake axis; i.e., $2R_{L(i)} > R_o$. Since $R_{L(i)} = m_i V_\perp C/eH$, for fixed H, $2R_{L(i)} > R_o$ implies that ions with a normal component of velocity less than some critical (cut-off) value will not reach the wake axis. As R_o increases, so must $R_{L(i)}$ and hence the cut-off velocity, which leaves fewer ions with sufficient energy to reach axis and create a current density peak. Since $R_{L(i)}$ is inversely proportional to H, an increase in H will decrease $R_{L(i)}$, for a given velocity, and hence will also decrease the number of ions reaching the axis. Although not shown by the data, it is obvious that the number of ions able to reach the wake axis will increase

with the component of random velocity normal to the magnetic field lines of force, $V_{\perp}$. This in turn, is proportional to $T_{i\perp}$.

If this interpretation is correct, it should be possible to normalize the axial ion current peak amplitudes (i.e., reduce all curves for various values of R_o and H to a single curve) by preserving the dimensionless ratio $R_o/R_{L(i)}$. This is indeed found to be the case as shown in Figure E-21(c).

Additional work has been carried out in this area by a number of research groups, including Waldes and Marshall at Columbia University [63], who present a model which accounts for experimental ion stream nonuniformities, and J. P. M. Schmitt [64] (Ecole Polytechnique, Paris, France), who studied the effect of collisions, the parallel ion temperature, and plasma wave coupling on the axial oscillation amplitude and frequency. (An interesting finding by Schmitt is that the length of the test body in the flow direction is important since a thick body was found to absorb all ions deflected by the sheath and thus eliminate the complex electrostatic wake structure. This is contrary to the theoretical results of Taylor and Call in Chapter I.A.)

The experiments by Bogashchenko, et al. [61] and Astrelin, et al. [62], although not conducted under similitude conditions for the ionosphere, do establish the dimensionless parameters which govern the position and amplitude of the axial ion current oscillations which can occur in the presence of a magnetic field parallel to the flow direction. We can therefore scale these parameters to determine where and to what extent this process might be expected to occur in the wakes of bodies in earth orbit. This comparison is given in Table E-2.

The parameter $(2\pi V_o/\omega_{ci})$ shows that even though the first axial ion density peak occurs relatively close to the body in the laboratory as a result of the strong magnetic field, in the ionosphere where the field is much weaker, the first peak occurs much farther downstream. Figure E-20 shows that the first peak occurs at $Z/(2\pi V_o/\omega_{ci}) = 1/2$. Therefore, in the ionosphere, the first peak can be expected to occur ~ 100 m downstream from the body.

The second parameter, $R_o/R_{L(i)}$, is proportional to the amplitude of the ion current density oscillations. Therefore, the values given in Table E-2 indicate that the amplitudes observed in the laboratory experiments are 14 to 24 times greater than the amplitudes to be expected in the ionosphere.

We therefore arrive at the conclusion that the effects of a parallel magnetic field associated with the ambient plasma will produce relatively small perturbations at large distances from the spacecraft in the ionosphere. It therefore seems reasonable to neglect this effect in the remainder of the current investigation where we are primarily concerned with simulating plasma disturbances in the vicinity of spacecraft and diagnostic instruments in earth orbit.

TABLE E-1. EXPERIMENTAL CONDITIONS

Group	P (torr)	N_o (cm^{-3})	λ_{nn} (cm)	λ_{ii} (cm)	$\frac{n_e}{n_i}$	V_o (km/sec)	T_e (°K)	T_i (°K)	S	λ_D (cm)	R_o (cm)	J_o (A/cm^2)	m_i (AMU)	R_d	T_e/T_i	Beam Diverg. (deg)
Convair (1961)	5×10^{-3} to 10^{-6}	2×10^{11}	10^1 to 5×10^3			10						3×10^{-2}	Hg 200			Small
FARDE - (Cox 1964)	1.5×10^{-2}	$\sim 10^{11}$**	0.25	4×10^{-3}	est very high	1.1	2000	600	1.3	10^{-4}	Disc .62 Sphere .09	0.18	Ar 40	Disc: 6×10^2 sphere 9×10^2	3.3	
TRW - STI (1964)	2×10^{-4}	$2.1 - 5 \times 10^6$	$>>R_o$		est. very small	7.7 - 11					2.54 0.94	$3.7 - 8.6 \times 10^{-3}$	C_2 134			3 - 4
RARDE (Clayden-Hurdle 1966)		$\sim 10^8$	50	$\sim 10^4$	0.1	12 - 26	10^4	$\sim 10^4$ (⊥) $5 - 10^4$ (∥)	6 - 12	0.1	0.5		Ar 40	~10	~1	
USSR (Skvortsov-Nosachev)	2 to 4 $\times 10^{-5}$	$10^7 - 10^8$			est. high	25 - 26	1.16 4×10^4		7 - 8		2 6		Ar 40	10 30	Prob. >>1	Large
Cal-Tech (1969)	$> 10^{-5}$	$\sim 10^8 - 10^7$			est. high	~22	1 to 5 $\times 10^4$	$T_\parallel \sim 0$ $T_\perp \sim ?$	1 - 21		1.3 to 3.8		Ar 40	10 - 21	>>1	
MIT (1968-70)	$\sim 10^{-5}$	$10^6 - 10^9$	5×10^2	$>10^3$	~0.02	15 - 150	4×10^3 to 6×10^4		3.5 to 70	0.02 to 1	0.1 to 10		Ar 40	0.01 to 10^2	10^3 to 1	~10
ESTEC - Netherlands (1970)	5×10^{-5}	1 to 3 $\times 10^7$			est. high	10 - 20	.5 - 1.2×10^4	10 - 15? $\cdot FE_j(T_\parallel)$					Ar 40			10 - 13
City University	$>5 \times 10^{-4}$	10^7 to 10^9			0.02 to 0.07	14 to 22		$T_\parallel \sim 10^3 - 10^4$ $T_\perp \sim 10^4 - 10^5$	5.4 to 6.5				Ar 40	3 to 4.5		Controlled 1 min
ONERA	10^{-6} to 10^{-7}	$6 - 24 \times 10^5$			0.05 to 0.2*	10 to 17	500 to 2000	5 to 2000	5.6 to 28		.4 to 10		Ar 40	~ to 45	~1 to 100	>11°*

*Values given by Martin and Cox [60].
** Calculated from given λ_D and T_e values.

TABLE E-2. SCALE FACTORS FOR THE MAGNETOGASDYNAMIC INTERACTION

Parameter	Value	
	Ionosphere (400 km)	Laboratory [61,62]
$2\pi V_o/\omega_{ci}$ [cm]	2×10^4	3.4 — 4.4
$R_o/R_{L(i)}$	0.2 ($R_o \sim 10^2$ cm)	2.8 — 4.8

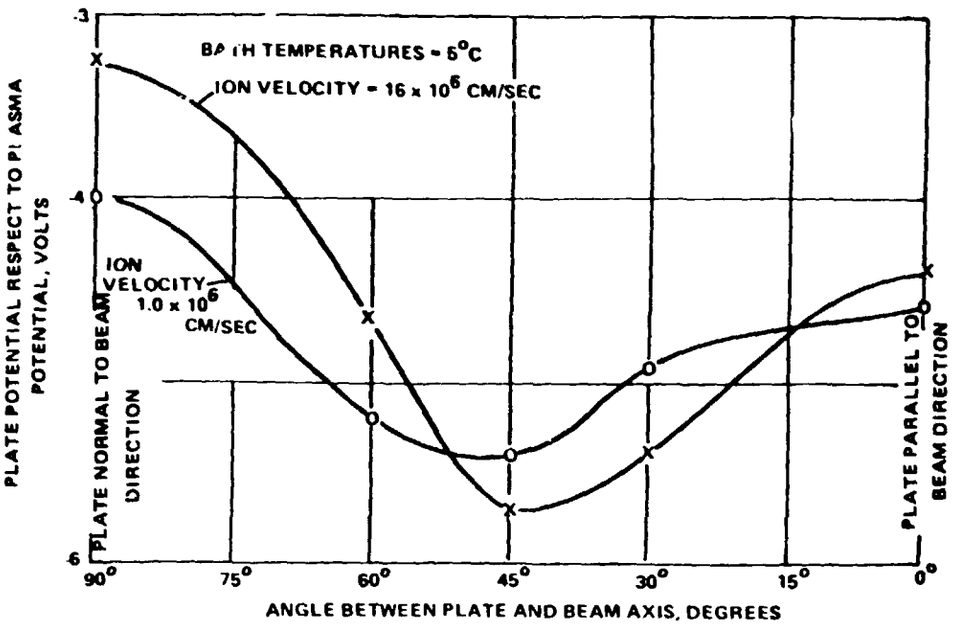

Figure E-1. Potential of a flat plate as a function of the angle between the plate and the plasma flow direction, after Meckel [44].

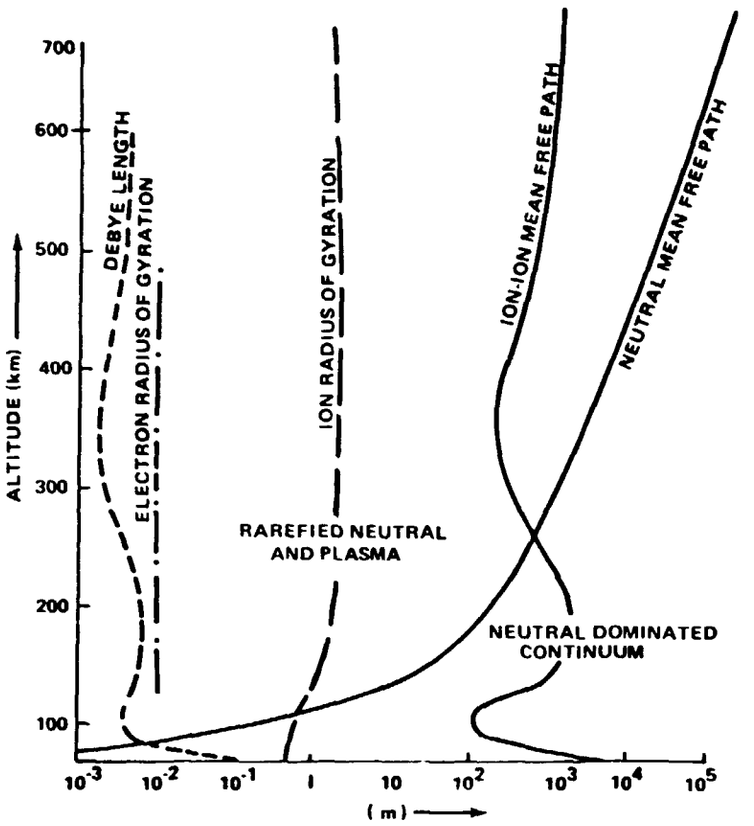

Figure F-2. Transition regions of the ionosphere, after Cox [45].

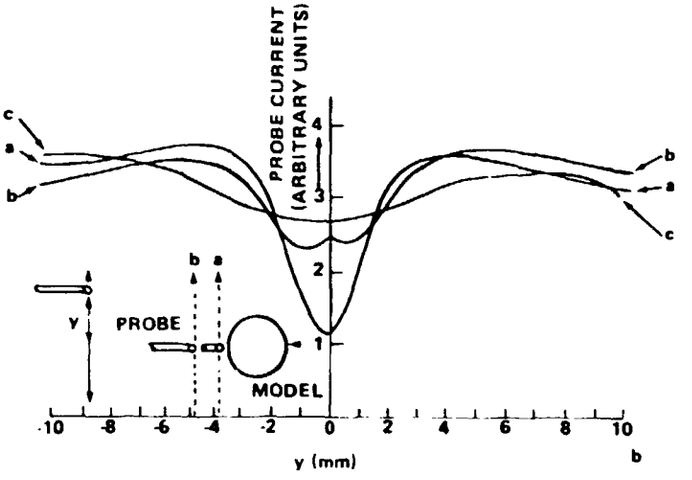

Figure F-3. Langmuir probe current in the wake of a conducting sphere for a collision dominated plasma, after Cox [45].

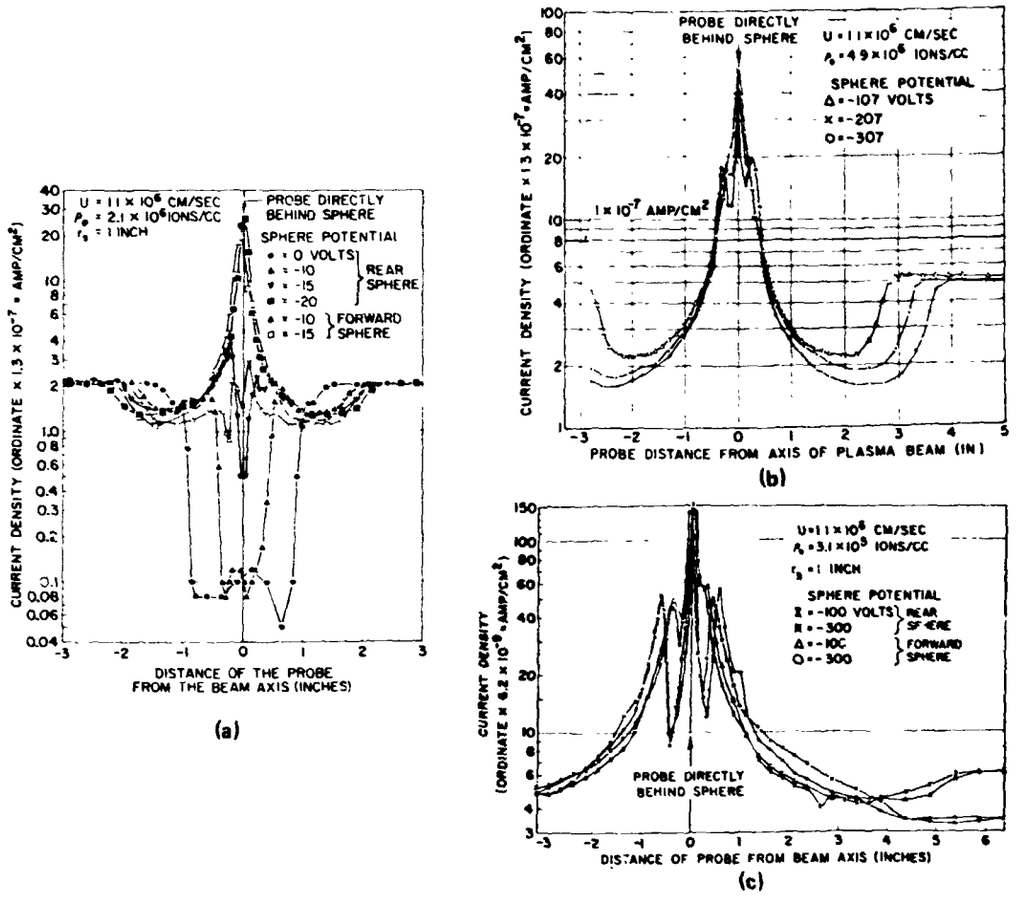

Figure E-4. Ion current density profiles downstream from a conducting sphere for several body potentials for a 90 eV ion stream; V_o = 11 km/sec, $n_i = 2.1 \times 10^6/cm^3$ (a); $4.9 \times 10^6/cm^3$ (b); and $3.1 \times 10^5/cm^3$ (c). $R_o = 2.54$ cm for all cases, after Hall, et al. [46].

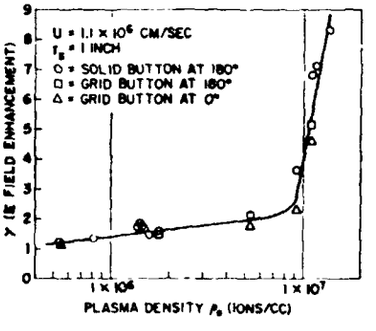

Figure E-5. Electric field enhancement by the sheath at front and rear of a conducting sphere as a function of ion density, data for a 90 eV ion stream, after Hall, et al. [46].

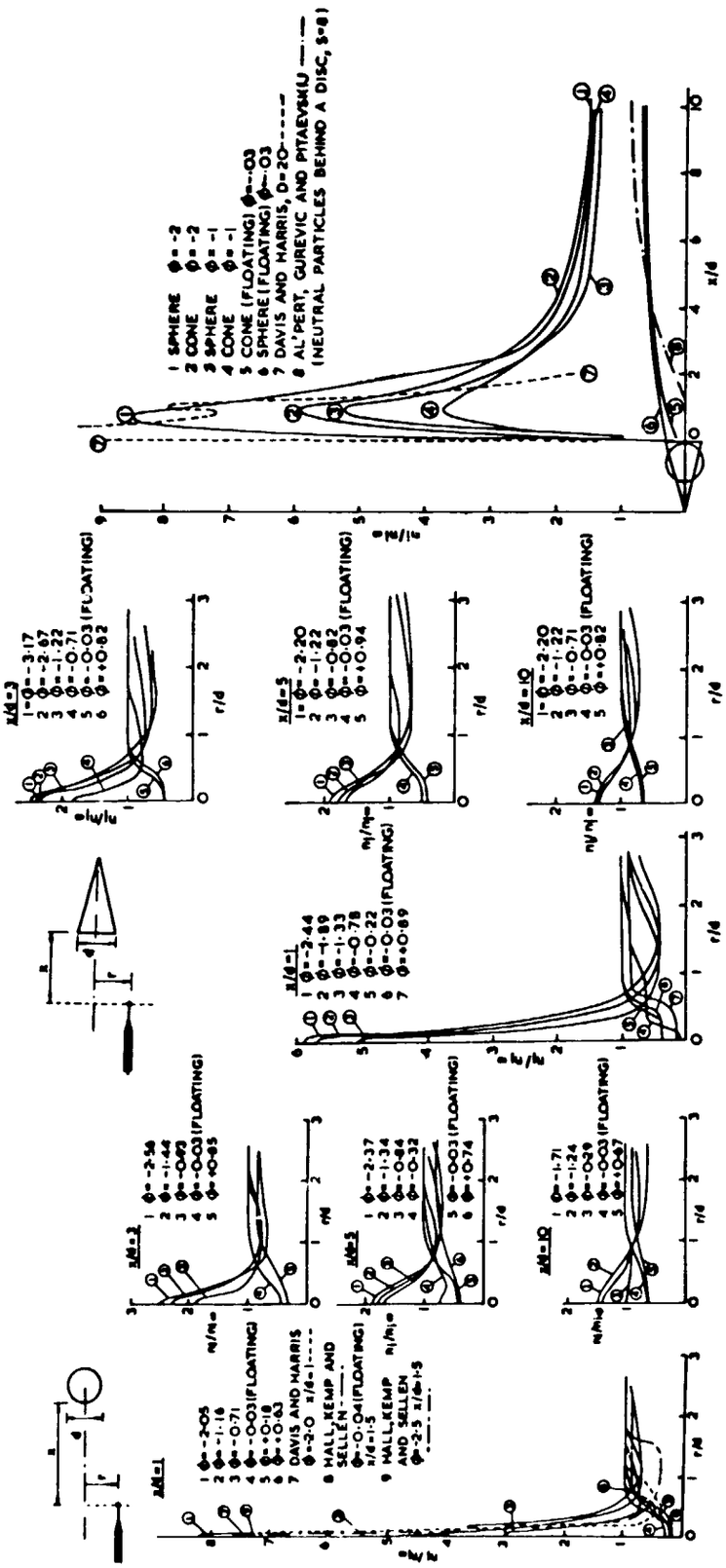

Figure E-6. Normalized ion density profiles downstream from a spherical test body and a conical test body with its apex into the flow. The cone angle was 15°. Data were obtained for a variety of test body potentials, as indicated, after Clayden and Hurdle [47].

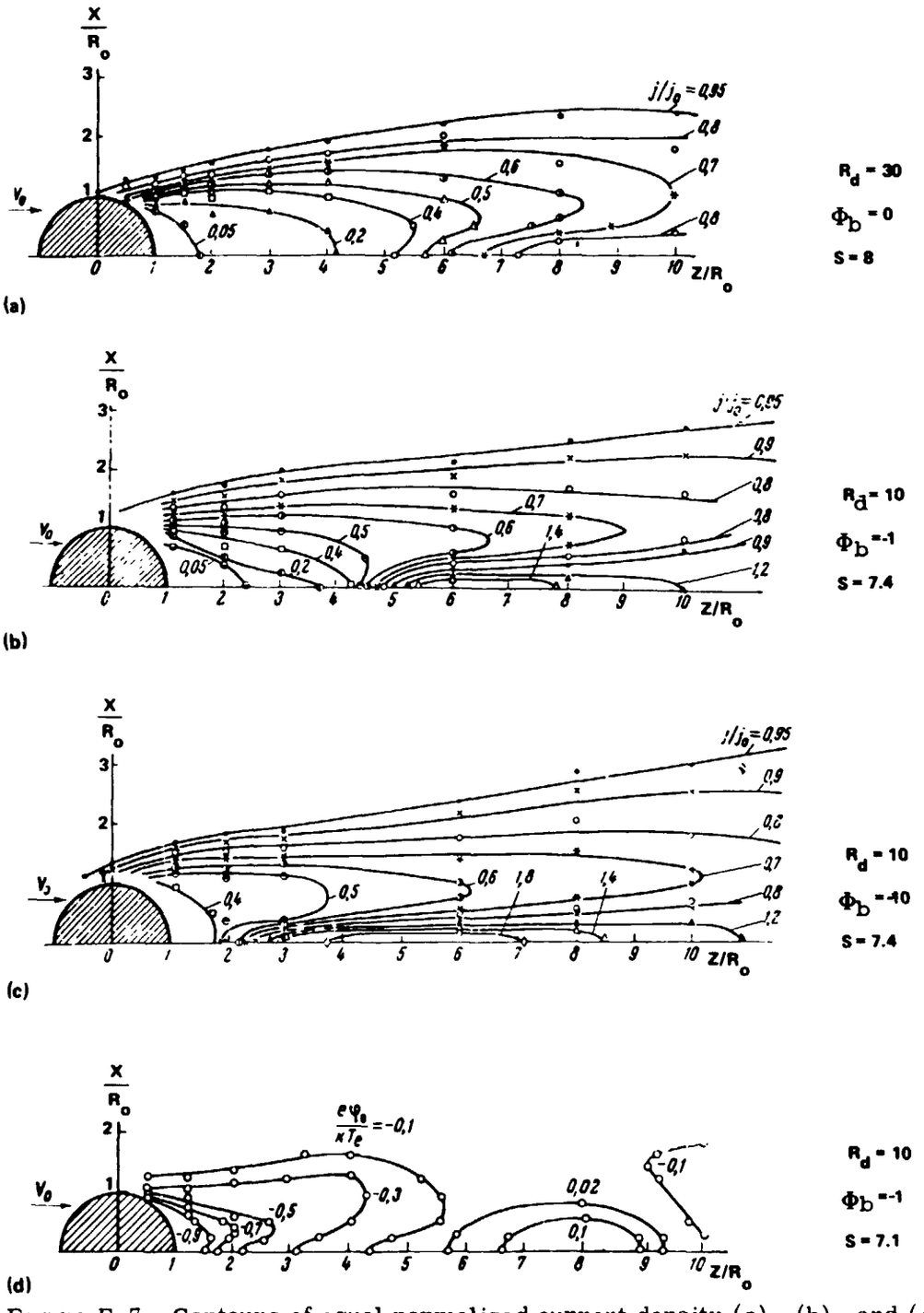

Figure E-7. Contours of equal normalized current density (a), (b), and (c) for the indicated conditions. Contours of equipotential, $\Phi = (e\phi/kT_e)$, for the indicated conditions, after Skvortsov and Nosachev [48].

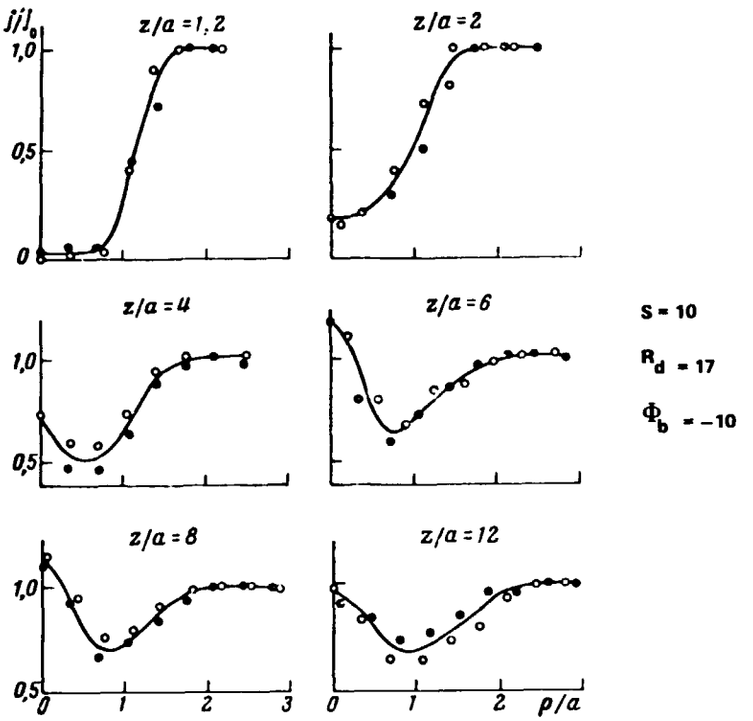

Figure E-8. Ion current density profiles (transverse) behind spherical test bodies of different diameters but the same Debye ratio, R_d, for the indicated conditions and distances downstream. Closed circles, R_o = 1 cm, open circles, R_o = 2 cm, after Skvortsov and Nosachev [49].

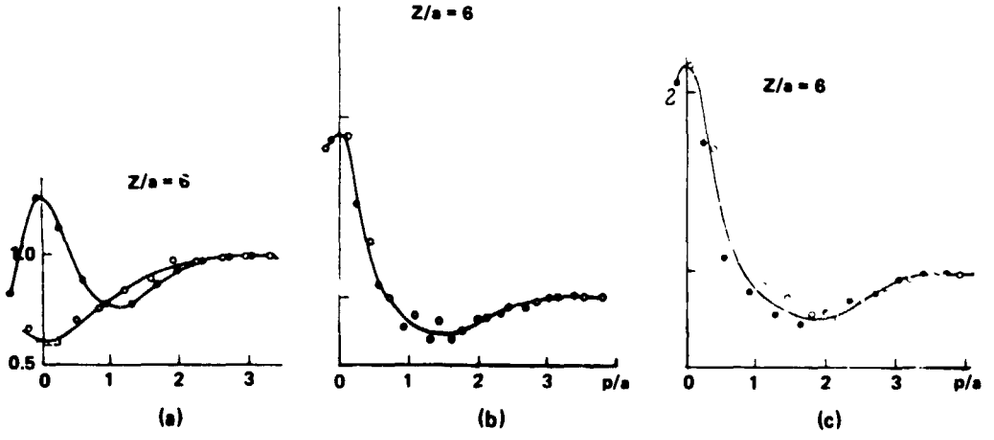

Figure E-9. Transverse profiles of normalized ion current for (a) Φ_b/S^2 = -0.05; (b) Φ_b/S^2 = -0.25; (c) Φ_b/S^2 = -0.5; open circles T_e = 1 eV, closed circles, T_e = 3.1 eV, after Skvortsov and Nosachev [49].

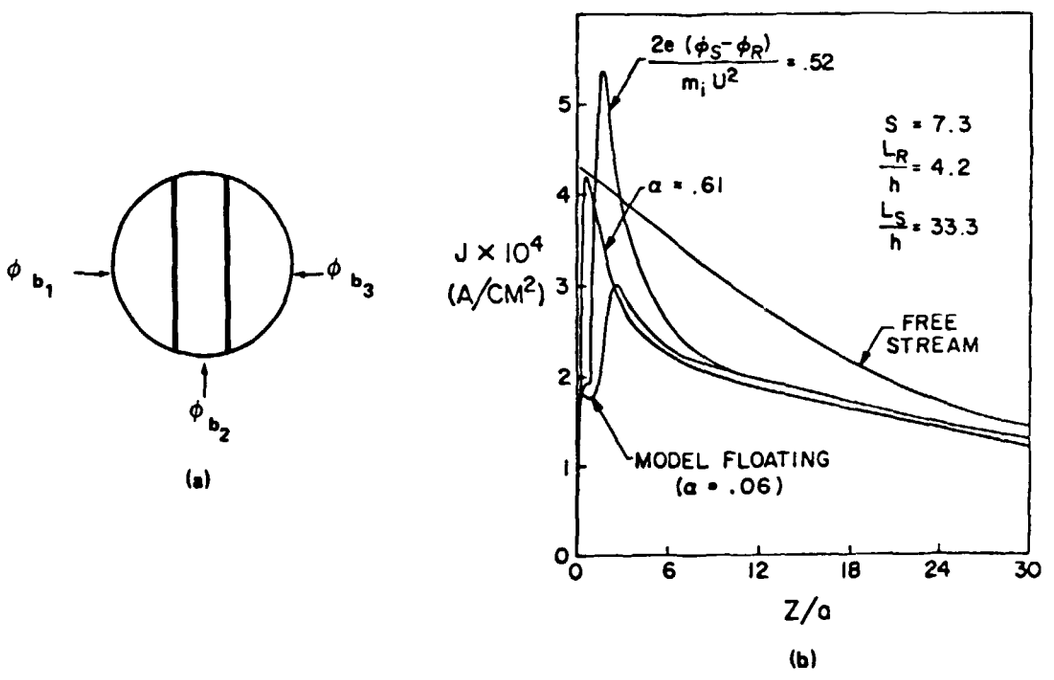

Figure E-10. Schematic of variable potential test body (a); ion current density profiles along the Z-axis (b), after Sajben and Blumenthal [50].

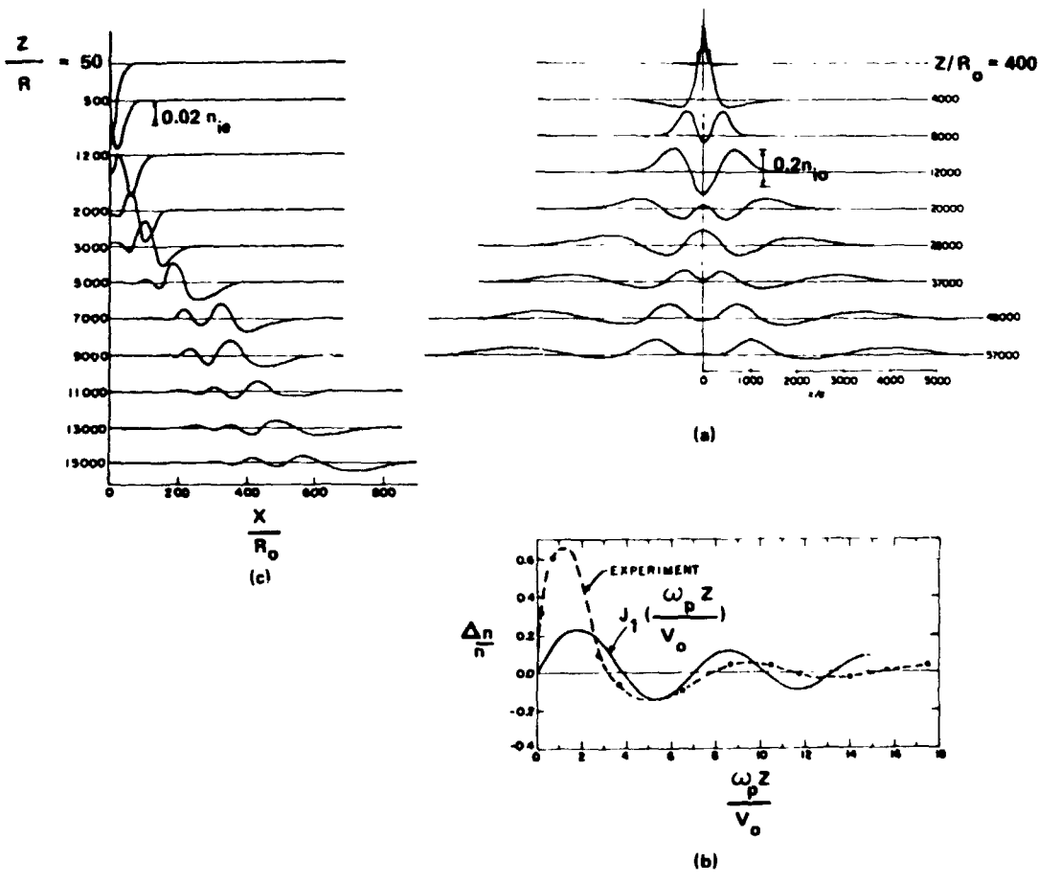

Figure E-11. Transverse profiles of ion current density downstream from a small cylindrical test body for S = 6, R_d = 0.005, and Φ_b = -3.5; (b) axial ion current density profile for same conditions as (a) compared with potential profile predicted by Rand [4]; and (c) transverse ion current density profiles for a small cylinder for S = 28, R_d = 0.2, and Φ_b = -3, after Hester and Sonin [34].

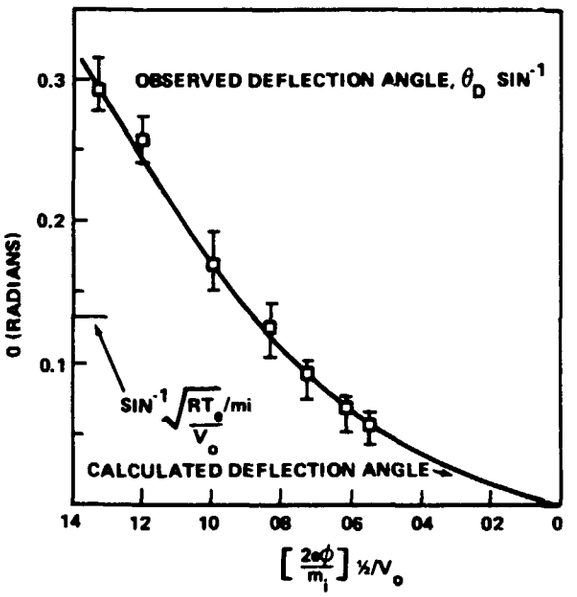

Figure E-12. Calculated and observed ion stream deflection produced by a small cylinder for S = 5.7, R_d = 0.005 and $\Phi_b^{1/2}/S$ as indicated, after Hester and Sonin [34].

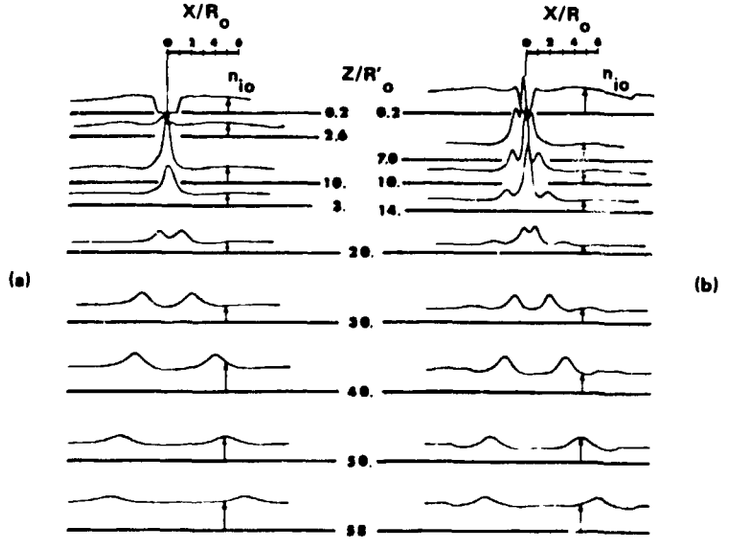

Figure E-13. The far wake ion current density distribution for a sphere at floating potential and negatively biased; S = 5.7, R_d = 1.8 (ox model), and 0.7 (at position of last trace due to axial variation of plasma stream) with Φ_b = -3.5 (left) and Φ_b = -20 (right), after Hester and Sonin [34].

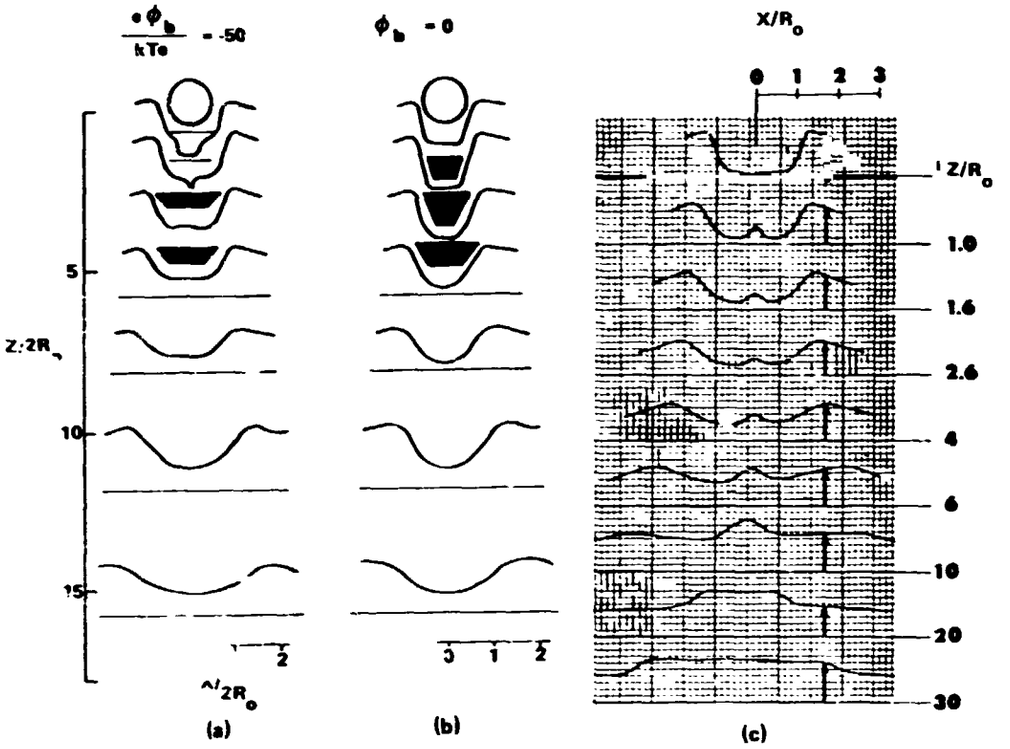

Figure E-14. Ion current density profiles in the wake of a large cylinder for S = 2.5, R_d = 39, and (a) Φ_b = -50 and (b) Φ_b = 0; and (c) a large sphere for S = 5, R_d = 46, and Φ_b = -3.5, after Hester and Sonin [51, 52].

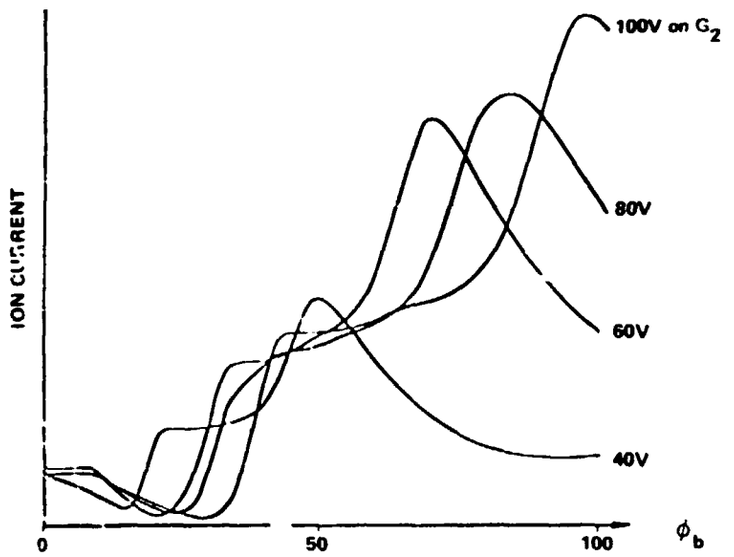

Figure E-15. Ion current density along the wake axis as a function of test body potential for various ion stream energies, after Knott and Petersen [54].

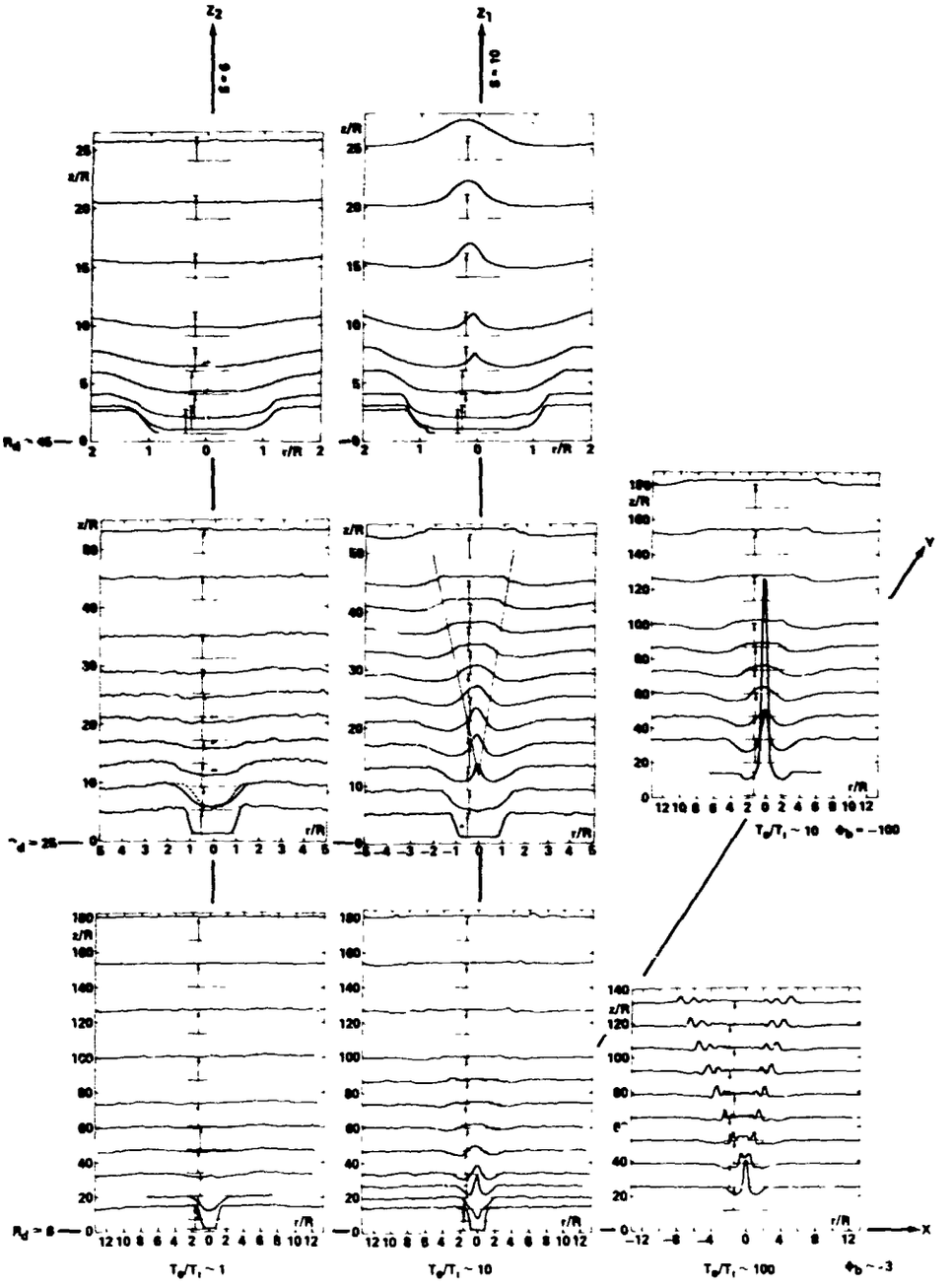

Figure E-16. The ion current density in the wakes of spherical test bodies for the indicated conditions, $P \cong 1.6 \times 10^{-7}$ torr, S = 10 (except under the Z_2-axis where S ~ 0), E_i = 20 eV, Γ_{eo} = 1400 to 2000°K, X-axis = $f(T_e/T_i)$, Y-axis = $f(\Phi_b)$ and Z-axis = $f(R_d)$, after Fournier and Pigache [58].

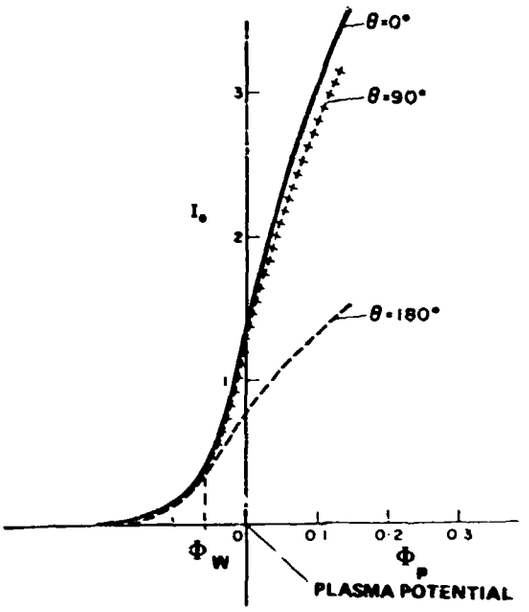

ELECTRON DENSITY N (m^{-2})	PLASMA CONDITIONS THERMAL ENERGY $\frac{kT_e}{e}$ (meV)	DEBYE LENGTH $\lambda\rho$ (mm)	APPARENT ELECTRON TEMPERATURE (°K) $\theta = 0°$	$\theta = 180°$	COMPLETE SPHERE
5×10^{11}	40	2·1	480	495	520
4×10^{11}	23	1·8	270	330	300
$2{\cdot}4 \times 10^{10}$	54	11	830	680	790

Figure E-17. Electron current, T_e, as a function of probe potential, Φ_p (with respect to plasma potential), after Illiano and Storey [57].

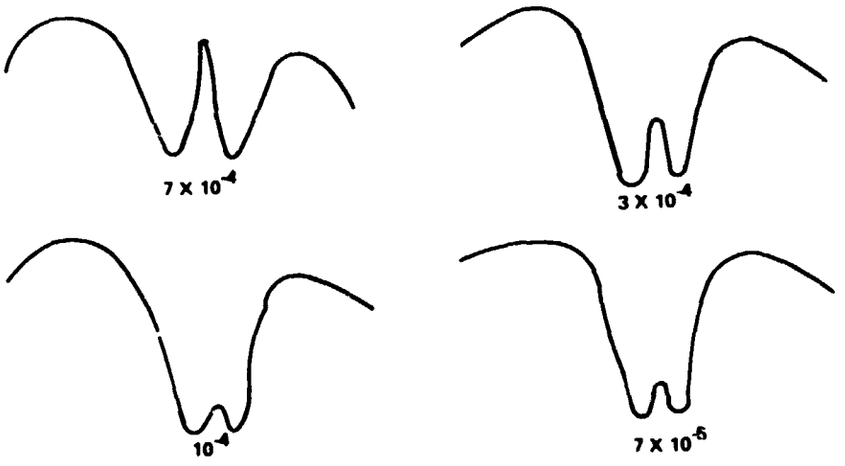

Figure E-18. Effects of slow ion concentration (proportional to chamber pressure indicated in the figure) on the near wake structure, after Martin and Cox [60].

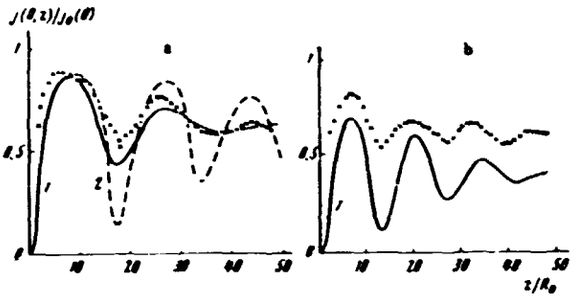

Figure E-19. Axial profiles of normalized ion current density for (a) H = 1100 O_e, T = 2700°K, J_o = 30 μA/cm^2 and $V_o/\hat{c}_i$ = 1.95; (b) H = 1900 O_e, J_o = 30 μA/cm^2, and $V_o/\hat{c}_i$ = 2.6. Points = experiment, line (1) = neutral approximation, line (2) = electric field included in theory, after Bogashchenko, et al. [61].

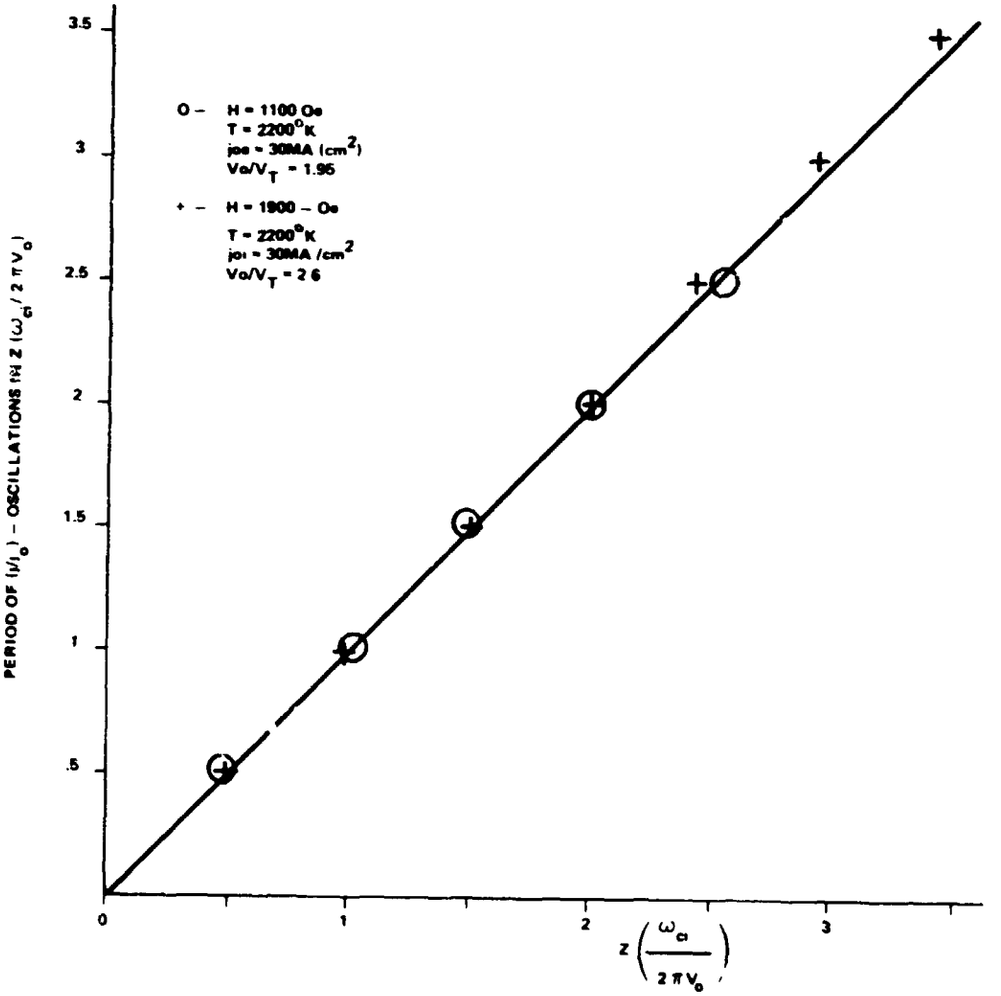

Figure E-20. Positions of relative [J/J_o]-extrema, data from Bogashchenko, et al. [61].

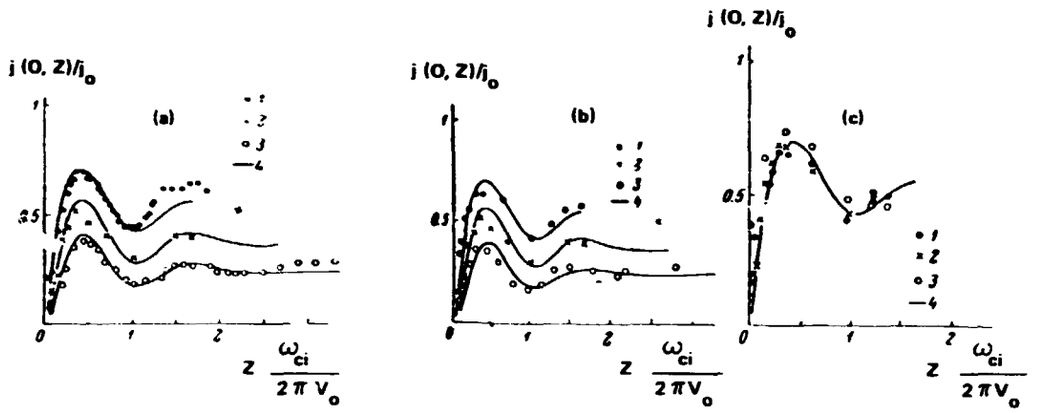

Figure E-21. Axial profiles of normalized ion current density downstream from a plate oriented normal to the plasma flow direction for (a) $V_o = 1.4 \times 10^3$ cm/sec, $V_o/\hat{c}_i = 1.4$ and H = 700 (1), 1100 (2), and 1500 O_e (3). (4) are calculated values; (b) $V_o = 1.4 \times 10^5$ cm/sec, $V_o/\hat{c}_i = 15$, H = 1100 O_e for $2R_o$ = 3.5 (1), 5 (2), and 7 mm (3) where (4) gives calculated values and (c) $V_o = 1.5 \times 10^5$ cm/sec, $V_o/\hat{c}_i = 1.5$, $R_c/R_{L(i)} = 0.45$ for $2R_o$ = 3.5 mm, H = 1000 O_e (1); 5 mm, 700 O_e (2); 7 mm, 500 O_e (3); and (4) giving calculated values, after Astrelin, et al. [62].

APPENDIX F. DIAGNOSTIC INSTRUMENTS AND ANALYSIS TECHNIQUES

This appendix is intended to provide a basic understanding of some of the commonly used diagnostic instruments and analysis techniques used in the present study and in some of the in situ and laboratory studies reviewed in Appendices D and E. It is not intended to be a detailed or comprehensive treatment of the subject. The reader interested in such detail is referred to several outstanding works already available [90,91,92].

1. The Langmuir Probe

The Langmuir probe, shown schematically in Figure F-1, is essentially a metallic electrode which is immersed in the plasma and swept by an applied potential ranging from a few volts above to a few volts below the plasma space potential. Note that, with the exception of probes with spherical geometry, all probes must be guarded to eliminate the effect of fringing fields. The electron current drawn from the plasma by the electrode as a function of applied voltage has the characteristic shown in Figure F-1. The Langmuir probe collects both ion and electron currents, depending on its potential with respect to the ambient plasma. The massive ions do not respond appreciably over small ranges of the voltage sweep and, therefore, the ion current remains relatively constant. The electron current, however, varies greatly. At the negative end of the sweep, all electrons will be repelled and the probe is said to be in the ion saturation region (region 1 in Figure F-1). As the probe potential becomes less negative, the more energetic electrons penetrate the potential barrier and the electron current begins to grow as the probe becomes more positive. This portion of the instrument characteristic is called the electron retarding region

(region 2 in Figure F-1). If the electrons have a Maxwellian energy distribution, an exponential I-V relation results, which is described by the equation

$$I = I_o \exp(e\Delta U/kT_e) \quad , \tag{F-1}$$

where ΔU is the potential difference between the probe and the plasma and I_o is the current collected when $\Delta U = 0$. Eventually, with further increases in the probe potential, electrons of all available energies will be collected. At this point the characteristic again changes since further increases of the electron current come from expansion of the plasma sheath (and therefore the effective collection area) and not the electron retarding process. This region of the curve is called the acceleration, or electron saturation region (shown as region 3 in Figure F-1).

If the electrons have a Maxwellian velocity distribution, then equation (F-1) describes the electron retarding region and a plot of $\ell n(j_e)$ against the probe voltage in this region takes the form shown in Figure F-2. The length and linearity of the straight section of the curve are measures of the degree of Maxwellianality of the electrons. The slope of the straight section is proportional to T_e, as shown. The break point (where the electron current deviates from an exponential dependence) is the point at which electrons of all energies reach the collector. This point is therefore taken to represent the plasma potential. Since there is no acceleration of the electrons at this point, their density is related to the current simply by:

$$I_o = -\frac{1}{4} e n_o \bar{c}_e A = -\frac{e n_o A}{4} \left(\frac{8kT_e}{\pi m_e}\right)^{1/2} \quad , \tag{F-2}$$

where A is the area of the probe.

The Druvystene analysis technique, which also applies to this type of probe, will be discussed in F.6.

Some of the experiments reviewed in Appendix E have used an electrode biased at a fixed, slightly negative potential to measure the relative ion current density. This assumes that, while the potential is sufficiently negative to repel

the electrons, the ions are not significantly affected. In terms of the above discussion, this is equivalent to operating a Langmuir probe in the ion saturation region.

2. The Emissive Probe

The emissive probe, which is used to determine the plasma or space potential, consists of a small, emissive tungsten wire loop. By measuring the total probe current at an emissive condition as a function of the applied potential and subtracting the usually small Langmuir current (which is determined at a non-emissive condition), the characteristic of the emitted electron current can be obtained. This curve is similar to an inverted Langmuir characteristic because the electron current flows into the plasma rather than being extracted from the plasma. The intersection of the emission-limited region of the curve with the Boltzmann region occurs at the plasma potential. This position may be determined more accurately than with a Langmuir probe as a result of a substantially higher probe current [93].

3. The Faraday Cup

The ion current density of the plasma beam is determined by Faraday cups, or ion traps, which consist of a collector and two grids (Figure F-3). The first grid shields the plasma from the negative potential applied to the second grid which repells electrons, allowing the cup to collect only the ion current. This is related to ion number density by the relation

$$I = \beta n_i Z_e V_o A \quad ,$$

where β is a transparency factor for the grids, n_i is the ion number density, Z_e is the electric charge per ion, V_o is the directed ion velocity, and A is the area of the Faraday cup aperture. Notice that the cup is designed with a deep collector and wedged bottom to minimize loss of secondary electrons, which would produce an artificially high ion current.

4. The Retarding Potential Analyzer

The RPA works on the same retarding principle as the Langmuir probe. However, in this case one species of particles is screened out and the retarding potential is applied to a grid rather than to the collector. A schematic of a planar, gridded RPA is shown in Figure F-4. The diaphragm limits the entrance area so that all ions, over the range of incident angles expected, reach the collector. The first grid shields the plasma from internal voltages. The second grid repells one type of particle (usually electrons). The third grid is swept from slightly below plasma potential (when all ions are collected) to some positive potential at which all ions are repelled. The fourth grid repels secondary electrons back into the collector.

The form of the collected current as a function of retarding potential is shown in Figure F-5(a). Note that it is the integral of the particle energy distribution (due to the component of velocity normal to the instrument face). Therefore, the derivative of the collected current gives the energy distribution, as shown in Figure F-5(b). In the present study, the average ion energy was of most concern and this was determined by the voltage corresponding to $I_o/2$ (an approximation of the inflection point).

If the data are digitized and analyzed on a computer, then a more eloquent analysis technique, which also yields the ion density and temperature, is to fit the data with the planar RPA equation:

$$I = \frac{1}{2}\beta v A e \sum_i n_i \left[1 + \text{erf}\,(\alpha_i v_i) + \frac{1}{\sqrt{\pi}\alpha v} \exp(-\alpha_i^2 v_i^2)\right] \qquad \text{(F-3)}$$

where

β = grid transmission factor

$v_i = V_i \cos\theta$

θ = angle of attack

A = area of aperture

$\alpha_i = (M_i/2kT_i)^{1/2}$

and the remaining symbols have the usual connotation. Note that for multicomponent plasma, either the velocity or mass of the constituents must be assumed. In the laboratory, the mass is always known, whereas, in the ionosphere, the orbital velocity is known (which is approximately the velocity of all constituents).

5. The 127° Electrostatic Energy Analyzer

The energy spectrum of ions in the plasma stream is determined by a 127° electrostatic analyzer. In the present study, the radius of the deflection channel, r_o, was chosen to be 50 mm with an electrode separation of 15 mm (Figure F-6). This produces the following ratio of deflection voltage to ion energy:

$$\frac{U_{defl}}{F} = (2/e)\ \ell n\ (r_1/r_2) = 0.6/e \quad . \tag{F-4}$$

This particular ratio provides accurate determination of ion energies ranging from a few eV to several hundred eV, which is the characteristic range for ionospheric simulation. The electrode separation limits the maximum and minimum radii of off-axis ion trajectories and it follows from the equation,

$$r_{max,\ min} = r_o\ (1 \pm \alpha_m/\sqrt{2}) \quad , \tag{F-5}$$

that the maximum vertical half angle, α_m, for which the ions are focused on the exit slot, is 11.5°. A collimator window at the entrance slot eliminates ions with larger incident angles.

The image width given by the relation $B = (4/3)\ \alpha^2 r_o$ is 2.7 mm. An exit slot of 2.0 mm was chosen to further improve resolution. The deflection radius and exit slot width imply a velocity resolution of $V/dV = 50$. Ions passing through the exit slot are detected by a Faraday cup or, for low density beams where higher sensitivity is required, by a Channeltron particle detector.

In the present study, current levels were high enough so that a simple cup collector was used instead of the electron multiplier. The output current characteristic as a function of plate voltage is very similar to the differentiated RPA curve shown in Figure F-5.

6. The Druyvesteyn Analysis Technique

The Druyvesteyn technique involves an analysis of the derivatives of the current collected by an electrical probe rather than the current itself, as was done in the above discussions. It applies to all types of retarding potential probes, including the Langmuir probe and planar, gridded RPA, discussed above. This technique has been used extensively by experimenters at University College, London [94,95]. There are a number of aspects to consider in its application. For example, the University College experiments use an ac probe in which the derivatives are obtained directly by applying a small (millivolt range) ac signal to the sweep voltage. This technique was applied to the Ariel I planar Langmuir probes as well as the spherical ion trap (or ion mass spectrometer) [96]. However, in this section, we wish only to introduce its elementary application to Maxwellian particle distributions.

Recall that the current collected in the electron retarding region was given by

$$I = I_o \exp\left[\frac{e\phi}{kT}\right] \quad . \tag{F-6}$$

This expression is based on the assumption $kT >> \frac{1}{2} mV_o^2$. It therefore applies to the electrons but not to the ions. The first and second derivatives of equation (F-6) with respect to ϕ are:

$$\frac{dI}{d\phi} = \frac{e}{kT} I_o \exp\left[\frac{e\phi}{kT}\right] \tag{F-7}$$

and

$$\frac{d^2I}{d\phi^2} = \left(\frac{e}{kT}\right)^2 I_o \exp\left[\frac{e\phi}{kT}\right] \quad . \tag{F-8}$$

Thus, the temperature of the particles is found simply from the ratio: $(dI/dT)/(d^2I/d\phi^2) = kT/e$. Once T is known, I_o can be calculated from $dI/d\phi$ at some known value of ϕ. Then the electron density is found simply by the expression:

$$I_o = \frac{1}{e} e n \bar{c} = \frac{1}{4} e n \left(\frac{8kT}{\pi m}\right)^{1/2} \quad . \tag{F-9}$$

The Druyvesteyn technique applies equally well to the analysis of the ion concentration [96] (related to $dI/d\phi$) and energy distribution (related to $d^2I/d\phi^2$) although the derivation is far more complicated since $1/2\ m_i V_o^2 \geq kT_i$ and, therefore, the ion kinetic energy must also be considered. Note that in the ionosphere, where $\bar{v}_i < V_o$ and, therefore, all ions may be considered to have a kinetic energy of $1/2\ m_i V_o^2$, the retarding analysis reveals differences in ionic mass. This is the basis for using the Ariel I spherical RPA (or ion trap) as a type of mass spectrometer.

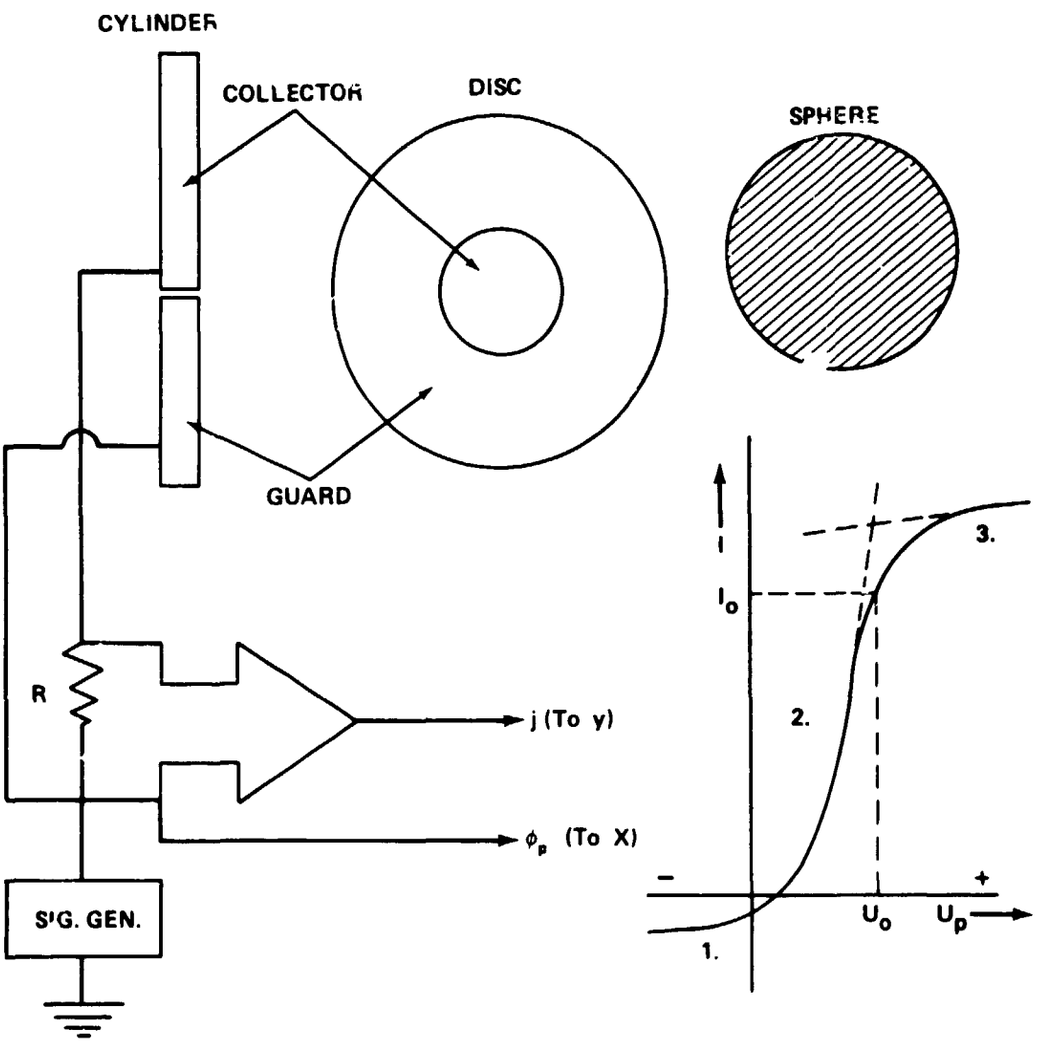

Figure F-1. Electrostatic (Langmuir) probe.

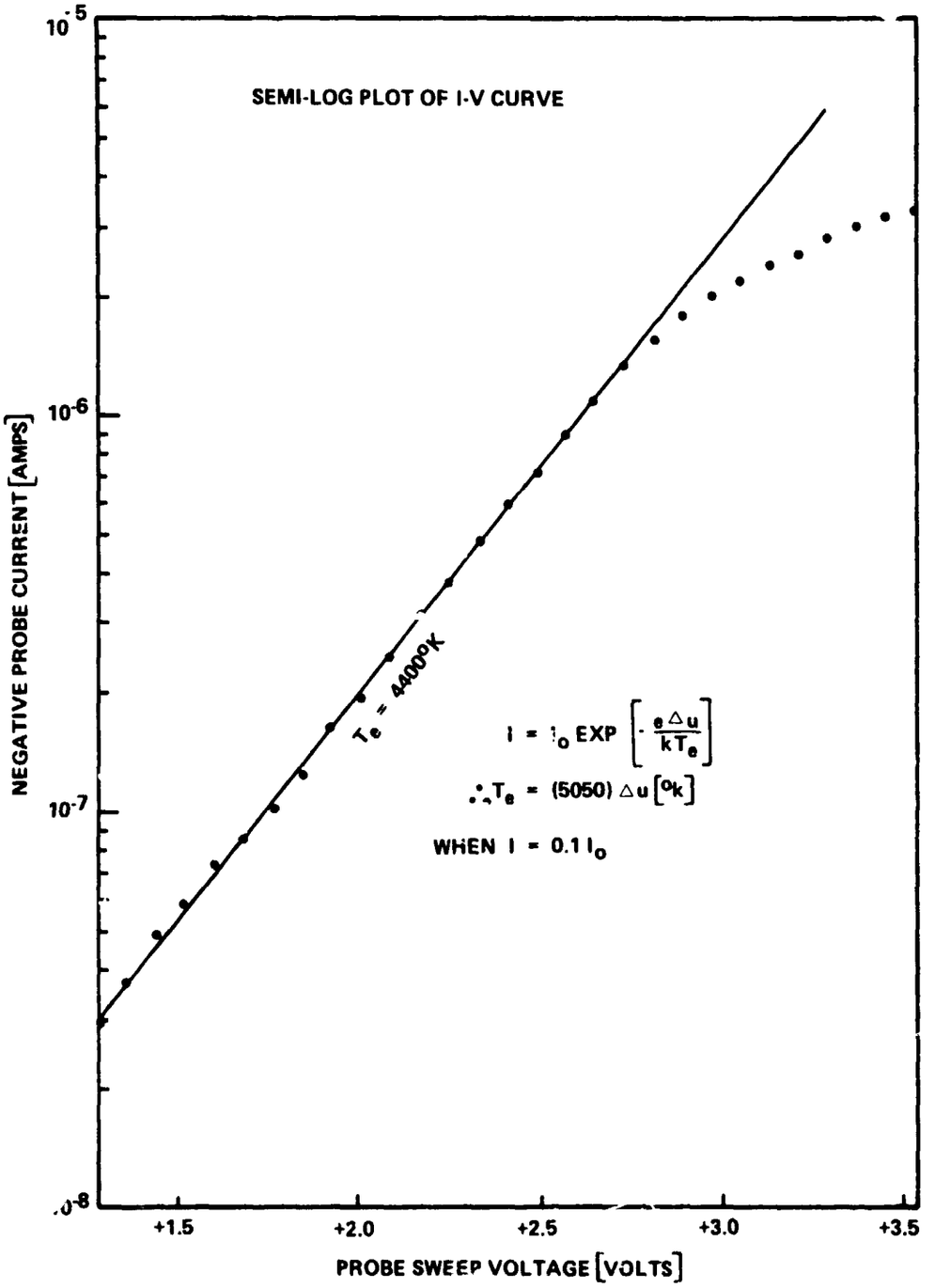

Figure F-2. Semi-log plot of I-V curve.

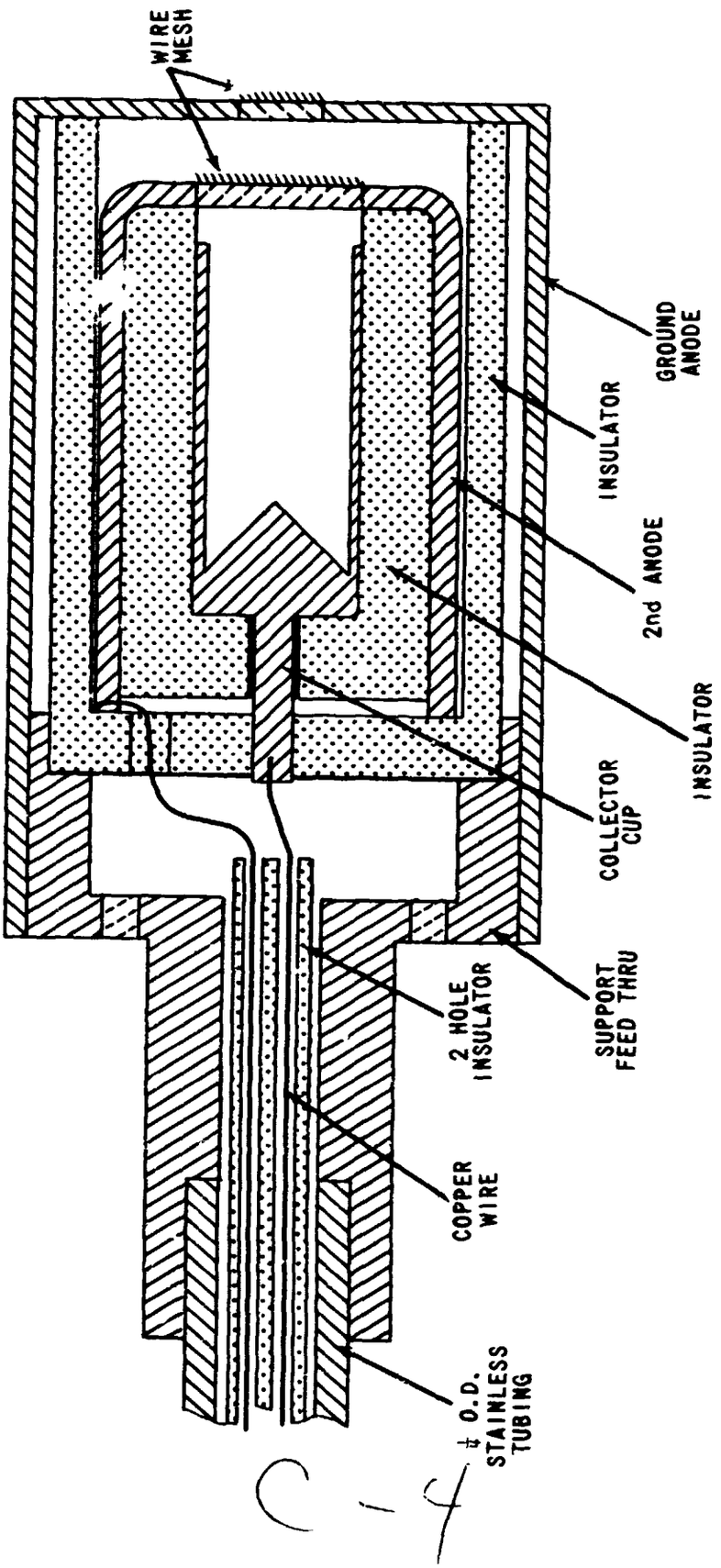

Figure F-3. Faraday cup assembly.

C-4

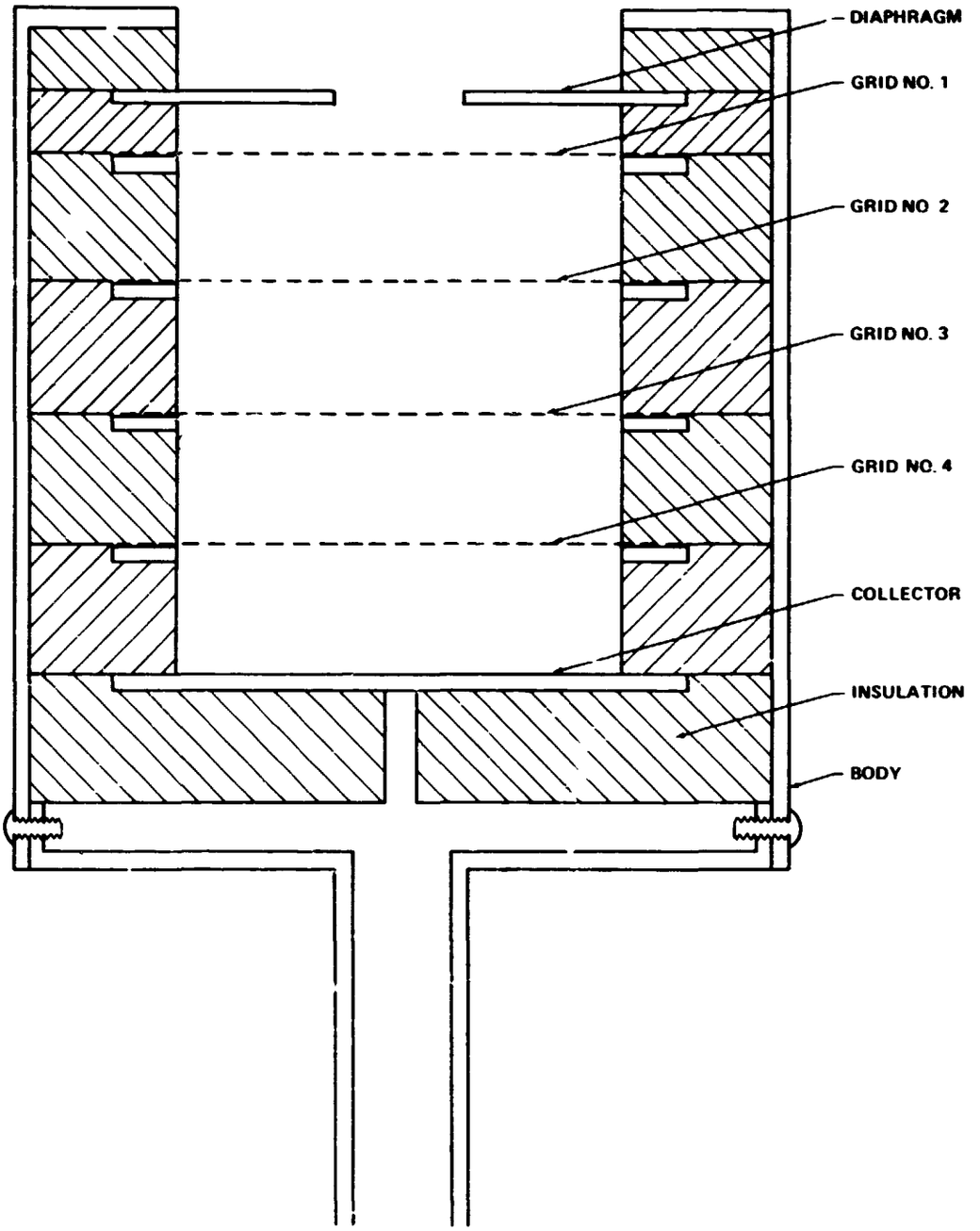

Figure F-4. RPA schematic.

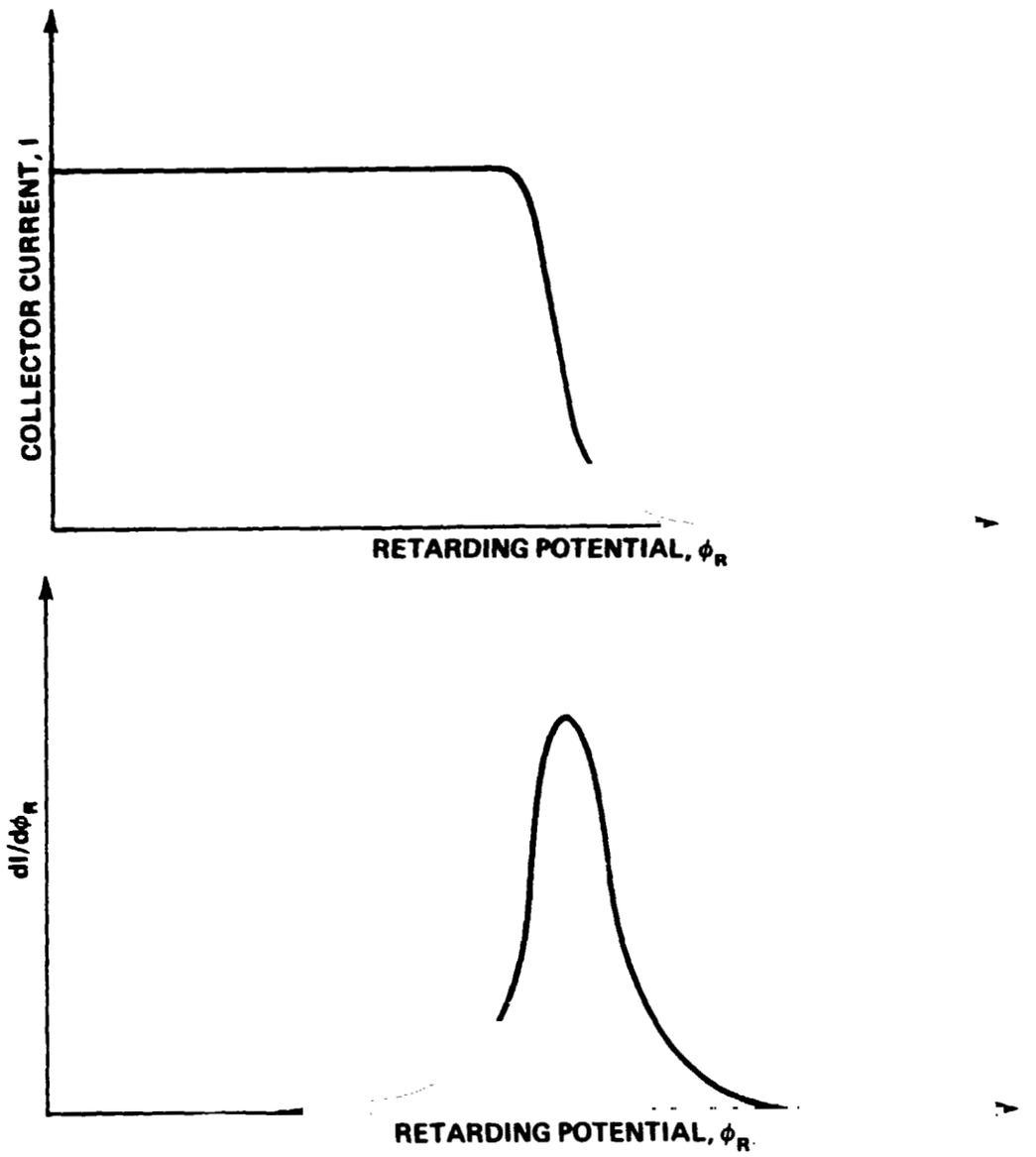

Figure F-5. RPA characteristic.

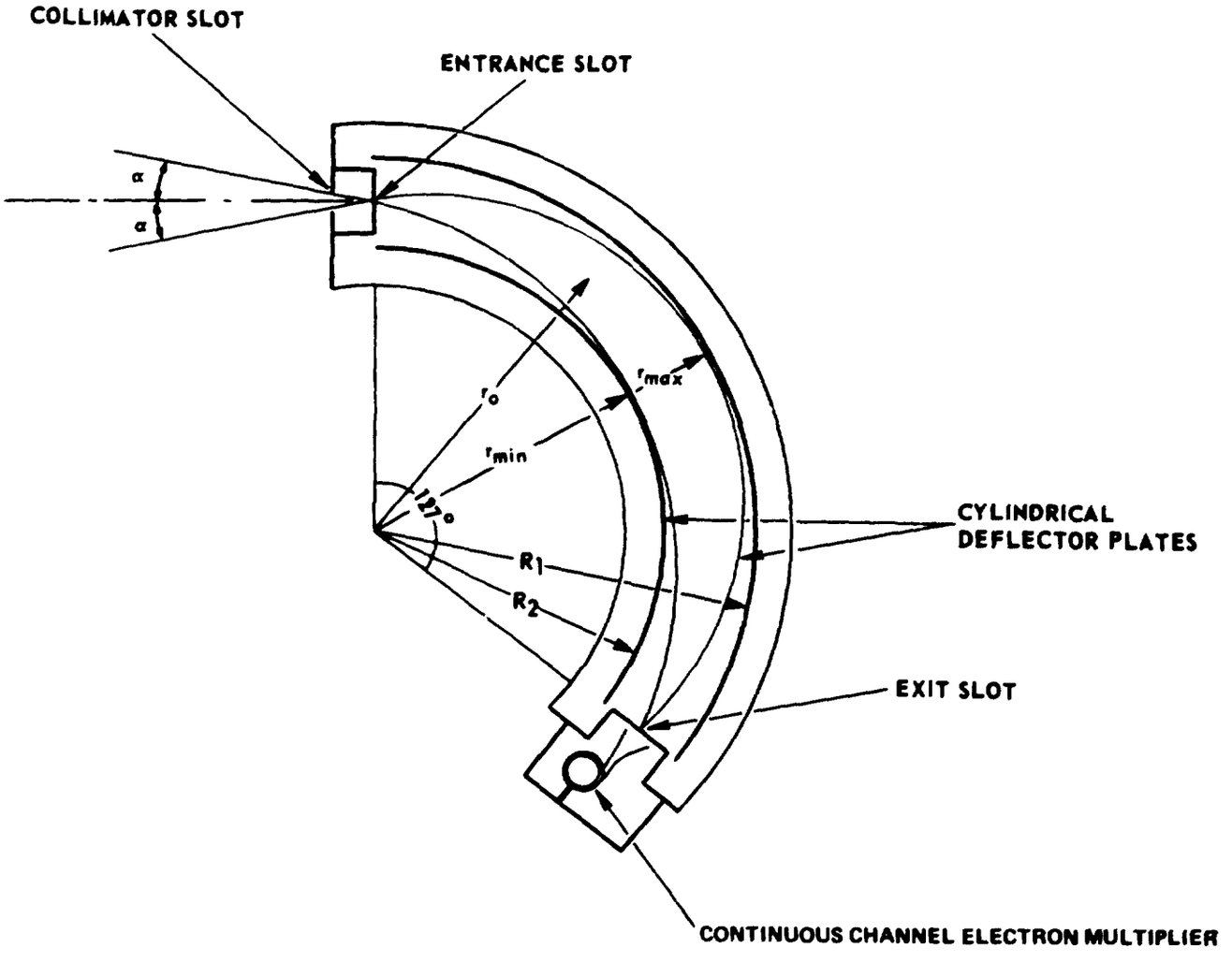

Figure F-6. Schematic of energy analyzer.

APPENDIX G. THE DIFFERENTIAL ION FLUX PROBE

The Differential Ion Flux Probe (DIFP), shown schematically in Figure G-1, consists of an electrostatic deflection system mounted on the front end of a standard planar RPA. This instrument allows direct measurement of the differential ion flux at a fixed region in space and in the presence of multiple ion streams. In other words, it gives the angle of incidence of an ion stream, the drift energy corresponding to the mean velocity of the stream, and the distribution of thermal motion superimposed on the drift.

The deflection system is made up of an entrance slit, which is flanked by two deflection plates and an exit slit. It functions much like similar devices in cathode ray tubes; i.e., a stream of ions entering the entrance slit at some angle to the normal, θ, and some kinetic energy corresponding to the mean velocity, E, will be deflected into the exit slit by applying some specified voltage, ϕ_d, of opposite polarity to the two deflection plates.

After passing through the deflection system, the ions enter the planar RPA. (In principle, this section may consist of any type of energy analyzer, although an integral instrument such as the planar RPA makes coupling with the differential deflection system easier.) The deflection voltage, ϕ_d, and the retarding potential, ϕ_r, provide two known variables that can be used to determine the two unknown characteristics of the ions, θ and E.

In practice, a ramp generator is used to apply a sweep voltage to one deflection plate while the inverted ramp is used to sweep the other plate. In this mode, the deflection system acts as an energy-angle filter. It has a characteristic "window" in θE-space. The size of the window is primarily determined geometrically by the width of the slits, the distance between them, and the angle of incidence of the ions. There is a slight additional variation in

window size, over the range of the instrument, which depends on the geometry of the deflection plates and the voltage applied to them.

For simplicity, we will assume for the moment that all ions have the same kinetic energy and differ only in their angle of incidence on the probe. In this case, when both deflection plates are at ground potential, no deflection takes place, and particles within $\Delta\theta/2$ of the normal will pass through the deflection system (Figure G-1). The angle, $\Delta\theta$, represents the characteristic window, which is now only in θ-space, since E is fixed.

As ϕ_d is swept, the window, $\Delta\theta$, moves through a range of incident angles, $0 \leq \theta \leq \Omega$. The window can be swept through the opposite range, $0 \geq \theta \geq -\Omega$, by reversing the polarity of the deflection plates. (For the data presented herein, $\Delta\theta \simeq 10°$ and $\Omega \simeq \pm 50°$.)

The current passing through the deflection system and into the RPA, $I(\phi_d, \phi_r)$, is measured as a function of deflection voltage by setting the retarding potential, ϕ_r, at ground and sweeping ϕ_d. If an ion stream is present, the collected current will display a spike at a critical value of the deflection voltage, $\phi_d{}^*$, which corresponds to the particular combination of kinetic energy, E, and angle of incidence, θ, of the stream. Some examples of the ion current collected in this mode are shown in Figure G-2. These data were obtained in th MSFC No. 1 plasma chamber. The DIFP was located 1.25 m downstream and could be rotated to provide different angles of attack to the plasma flow.

The plots of Figure G-2 show the current collected with the instrument at 10° intervals of angle of attack to the plasma stream. Figure G-2(a) gives the current response to a 10 eV ion stream, and Figure 2(b) the response to a 20 eV stream. In each case, instead of producing a simple spike (expected for a monoenergetic stream and perfect resolution), the current is spread around a maximum at $\phi_d{}^*$ as a result of finite instrument resolution and thermal motion of the ions. The variation in the amplitude of the current maxima with angle of attack will be discussed later.

At this point (after the ions have passed through the deflection system), neither the angle nor the energy of an incident ion stream is known. However, the pair (θ, E) must satisfy a known relationship:

$$f(\theta, E) = \phi_d^* \quad . \tag{G-1}$$

This relationship is characteristic of the deflection system and must be satisfied by any ion passing through it.

There is an obvious shift of the current peaks (Figure G-2) to higher values of deflection voltage with the increase in energy. This displacement of the ion current peaks with increasing kinetic energy of the ion stream is shown explicitly in Figure G-3 for a fixed angle of attack. The resulting dependence of the critical deflection voltage on the kinetic energy of the ion stream is given in Figure G-4 for ten-degree increments of the angle of incidence. This shows the energy dependence of the characteristic relationship (G-1) to be linear. It is therefore possible to normalize this function in terms of kineti. energy to obtain:

$$[\phi_d^*/E] = f(\theta, E)/E = g(\theta) = \beta \sin(\propto \theta) \tag{G-2}$$

where $\propto$ and β are empirically determined constants. This expression must also be satisfied by all admissible ions.

The normalized characteristic relation (G-2) is shown in Figure G-5 along with experimental values derived from calibration data (similar to that shown in Figure G-2) taken for ion drift energies ranging from 10 to 50 eV. With the exception of the data for the lowest energy (10 eV) ion stream, all data points fall essentially on the same curve as expected. The angular displacement of the data points corresponding to a 10-eV ion stream can be explained by the deflection of the ions in the earth's magnetic field. The gyro radius for more energetic ions is sufficiently large to produce a negligible deflection at the distances involved.

To determine the kinetic energy corresponding to the mean velocity of an ion stream, the instrument is operated with the deflection voltage fixed at ϕ_d^*, corresponding to the current peak, $I(\phi_d^*, \phi_r = 0)$, of a particular stream of ions. The kinetic energy of the stream is then determined in the standard way from the dependence of the collected current on the retarding potential, ϕ_r.

Having determined the kinetic energy of the ions and the critical deflection voltage, the angle of incidence of the corresponding ion stream can be obtained from the characteristic curve given in Figure G-5 [or from equation (G-2)].

We should note that these are first-order values. The value of E will generally be in error as a result of the ions entering the RPA section of the DIFP at some angle to the normal (given by α in Figure G-1).

The angle, α, will be non-zero for any ion stream that is not aligned with the probe axis. However, theoretical ray tracing indicates that it will be considerably smaller than the angle of incidence for the ion stream onto the deflection system aperture. Therefore, the accuracy of the kinetic energy of the ions, determined by the RPA section, should be improved by the deflection system.

Figure G-6 shows the experimentally determined error incurred in E_i as a function of angle of incidence. (The fact that the measured error for $\theta = 60°$ is less than 10% substantiates the claim, made above on the basis of theoretical ray tracing, that the angle α will be less than the initial angle of incidence.) A second-order (corrected) E can be found by using the correction factor from Figure G-6, corresponding to the first-order value of θ. This, in turn, allows a more accurate determination of θ from Figure G-5. This iterative procedure can be continued until the (θ, E) pair converge on the correct values.

If multiple ion streams are present, separate current peaks would normally be observed at different values of ϕ_d*, corresponding to each stream. However, the possibility exists that two or more ion streams could have energies and angles such that they all would pass through the deflection system for a common value of ϕ_d. As a result, the $I(\phi_d, \phi_r = 0)$ curve would have only a single peak. In such a case, the presence of the multiple streams would be readily detected by the corresponding RPA curve which would reveal multiple energy levels, one corresponding to each ion stream present.

If the ion stream is monoenergetic, as originally assumed, then we have completely determined one component of its velocity vector (assuming m_+ to be known). The remaining two components can be obtained by vector addition, using results from a second DIFP with its deflection system rotated 90°. However, if the ion population has some thermal motion superimposed on the drift motion, we still must determine the distribution of thermal motions for the stream. If the thermal motion is Maxwellian, then the temperature can be obtained from standard RPA analysis of $I(\phi_d^*, \phi_r)$. When the thermal motion is not Maxwellian, it appears that it may be possible to obtain the exact distribution function from the shape of $I(\theta_d, \phi_r = 0)$ current peaks such as those shown in Figure G-2. Additional work is required to evaluate this aspect of the technique.

In addition to the mean kinetic energy, the thermal energy distribution and the drift direction of a stream of ions, the full characterization of the stream requires the number density of ions, n_i. If the ion stream is normally incident on the DIFP, the deflection system acts as an aperture to the RPA section. When the retarding potential is at ground and thermal motion is neglected, the total ion current is related to the ion number density by the relation:

$$I_o = e n_i \beta A (2E/m_i)^{1/2} \quad , \tag{G-3}$$

where

I_o = Collected current for $\theta = 0$, $\phi_r = 0$, $\phi_d = 0$

e = Electronic charge

n_i = Ion number density

β = Grid transmission factor

A = slit area

E = Ion kinetic energy corresponding to the mean ion velocity

m_i = Ion mass.

The above expression is only valid when either the ion stream is monoenergetic ($qE = 1/2\ mU^2$), or the component of thermal motion normal to the flow direction, $(v_{th})_\perp$, is negligible; i.e., $U >> (v_{th})_\perp$. The later case occurs, for example, in certain types of laboratory synthesized plasma streams, where the ion generation and extraction processes can create streams having appreciable random ion motion only in the flow direction [97].

In the more general case, where $U >> (v_{th})_\perp$ cannot be assumed, one must consider the additional reduction in ion current produced at the second slit by dispersion of the ions after they pass through the first slit. This problem does not lend itself to a concise, analytical solution, is not necessary for the present laboratory application, and therefore will not be dealt with here.

The magnitude of the peak currents obtained over the angular range of the instrument for various ion beam energies is shown in Figure G-7. Each curve represents the amplitude envelope of the current peaks, $I(\phi_d{}^*, \phi_r = 0)$, obtained at a particular energy over a range of angles of incidence (e.g., the sets of current peaks shown in Figure G-2). For comparison, the curves have been normalized to the values at ±20°. This was necessary because a dip in the observed ion current occurs over the range $-20° < \theta < 20°$ for all curves corresponding to ion drift energies of 20 eV or greater. This apparently results from electron penetration of the screen grid (Figure G-1) which, due to the experimental setup, was biased at -15 V for all measurements. The electron penetration apparently did not occur at angles greater than ±20° as a result of the increasing value of ϕ_d which deflected them away from the exit slit.

The values of I_o, given by equation (G-3), correspond to the current peaks at $\theta = 0$.

If the DIFP is to provide a technique for measuring the differential ion flux (or the ion flux vector) in the plasma flow field around test bodies in the laboratory, it is essential that it be capable of measuring the differential ion flux in the presence of multiple ion streams; i.e., ion fluxes that differ in

direction and/or mean kinetic energy. This capability has been adequately demonstrated by preliminary laboratory data, some examples of which are discussed below.

The data shown in Figure G-8 were obtained with the instrument located 42 cm downstream from and directly behind a cylindrical body. The cylinder had a radius to Debye length ratio (R_o/λ_D) of ~ 20 and a length sufficient to ensure an essentially two-dimensional flow field. The deflection system of the DIFP was mounted with the collimating slits parallel to the cylinder axis (hence, analyzing ion flux in a plane normal to the cylinder axis).

Figure G-8 is a composite of $I(\phi_d, \phi_r = 0)$ curves obtained with different biases on the cylindrical body, as indicated. The polarity of the deflection plates was reversed in each case so that current peaks obtained at negative values of ϕ_d correspond to ion streams with negative angles of incidence; and those obtained at positive values of ϕ_d indicate positive angles of incidence.

In each case, at least two ion streams were observed as expected, one deflected from each side of the body by the potential gradient in the plasma sheath. With the body at floating potential (body bias = 0V) two streams were observed from each side of the body. (This may result from a non-monotonically decreasing sheath potential or possibly from additional deflections of the ions by potential gradients in the wake region.) Hence, the DIFP has clearly resolved up to four ion streams converging simultaneously to a single point. Also, the angular resolving power of the instrument is demonstrated by the two minor streams observed for the zero bias case, which are separated by only $\sim 3.5°$.

As discussed previously, the DIFP also allows one to correct the particle kinetic energy when the ion stream is not normally incident. This is especially important in plasma flow interaction studies where, due to electrostatic deflections within the plasma sheath, the angle of incidence to the normal may be large. A comparison of the deflection voltages, at which current peaks are observed in Figure G-8, with the calibration curves of

Figure G-2(b), shows that the deflection of ions by the sheath potential ranges from $\sim 10°$, for the dominant streams generated by a floating body, to $\sim 40°$ when a bias of -40 volts is applied. The present results show that both the ion kinetic energies and the ion number densities determined by a standard RPA could have resulted in sizable errors. As demonstrated by the data of Figure G-8, the DIFP is capable of making these types of measurements accurately, which will make possible meaningful comparisons with the distribution functions obtained from kinetic theory.

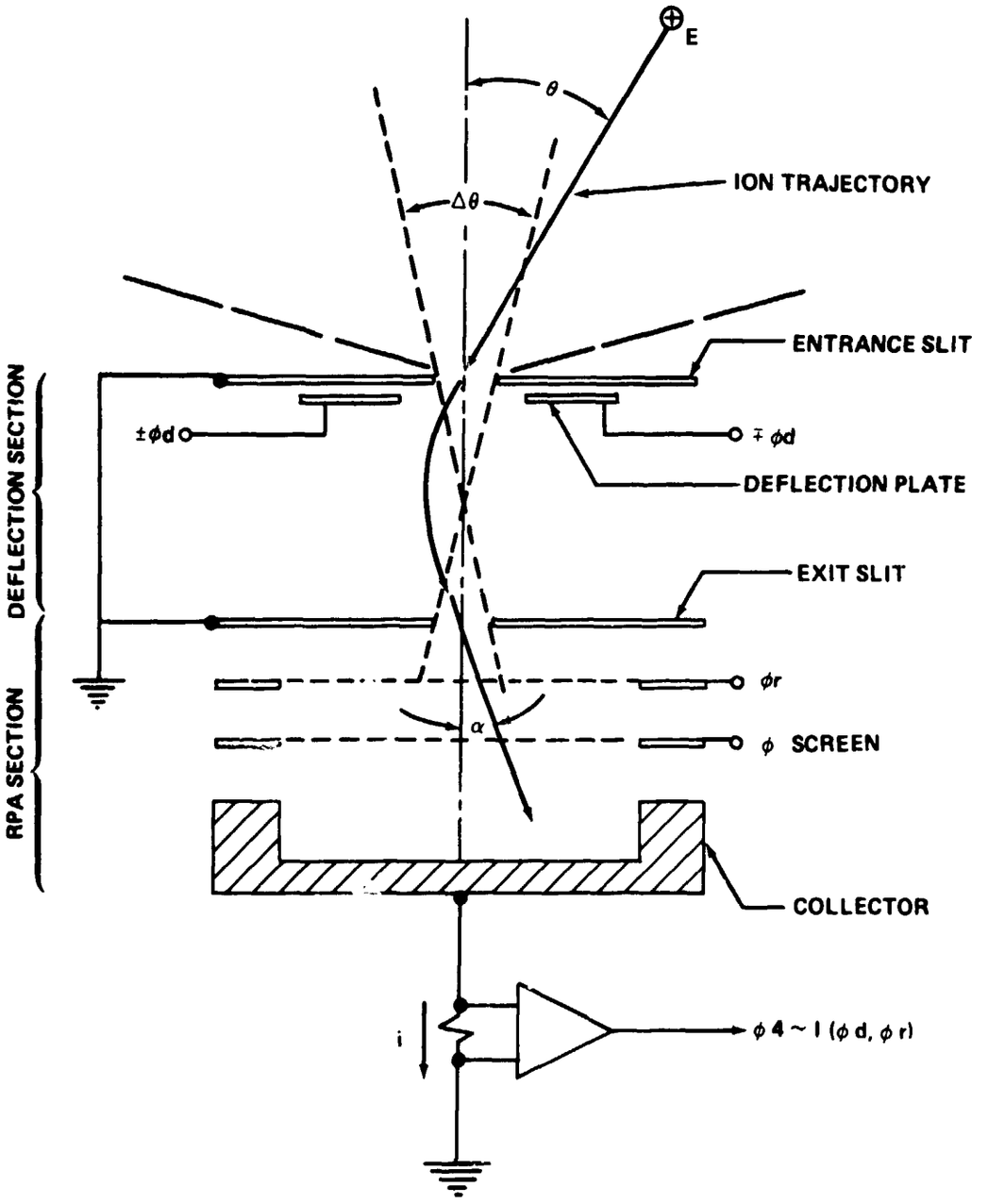

Figure G-1. Differential ion flux probe schematic (showing a cut through the instrument in a plane normal to the deflection system slits), after Stone [71].

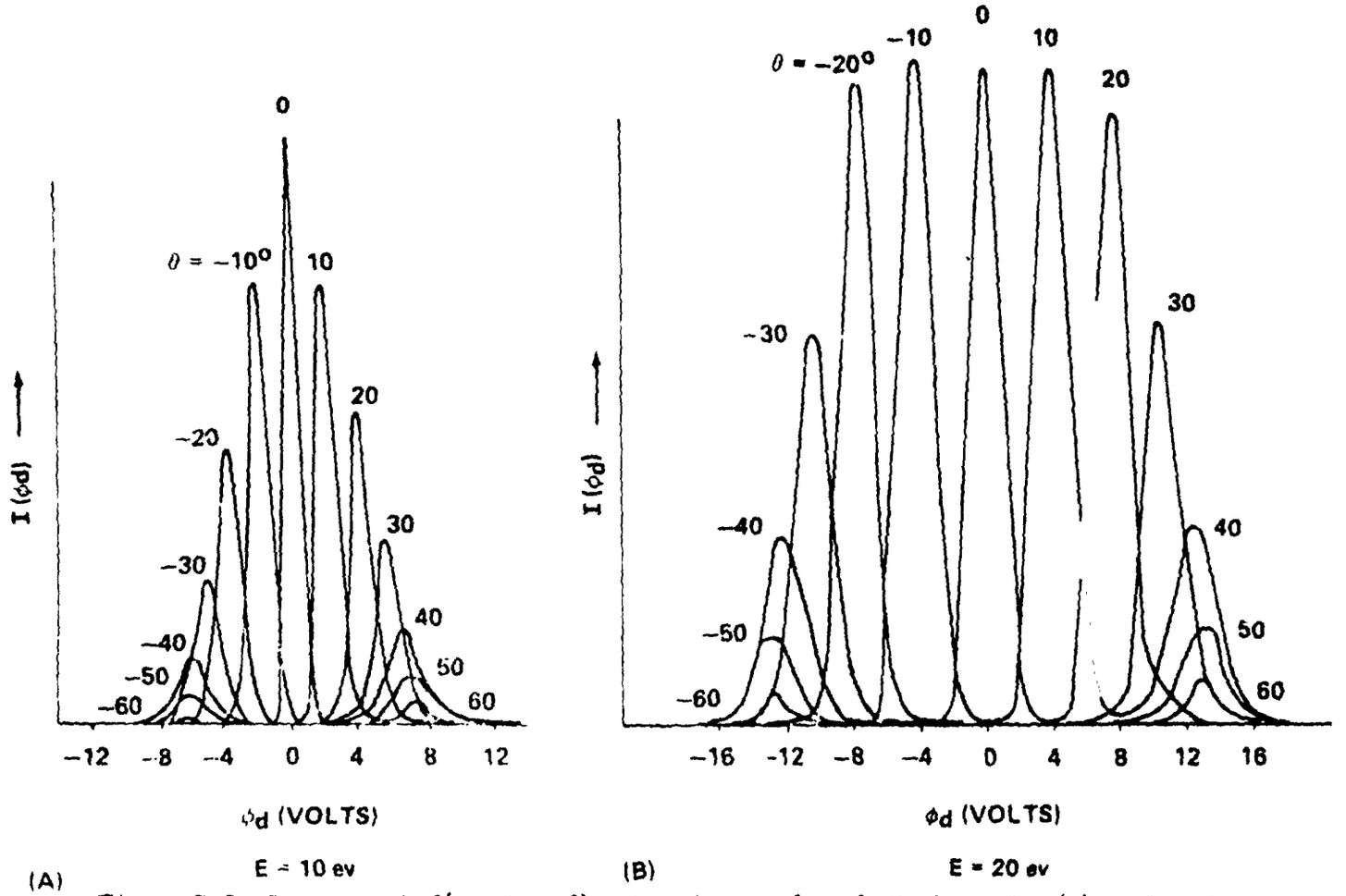

Figure G-2. Ion current, $I(\phi_d, \phi_r = 0)$, at various angles of attack, θ, for (a) a 10 eV ion stream, and (b) a 20 eV ion stream, after Stone [71].

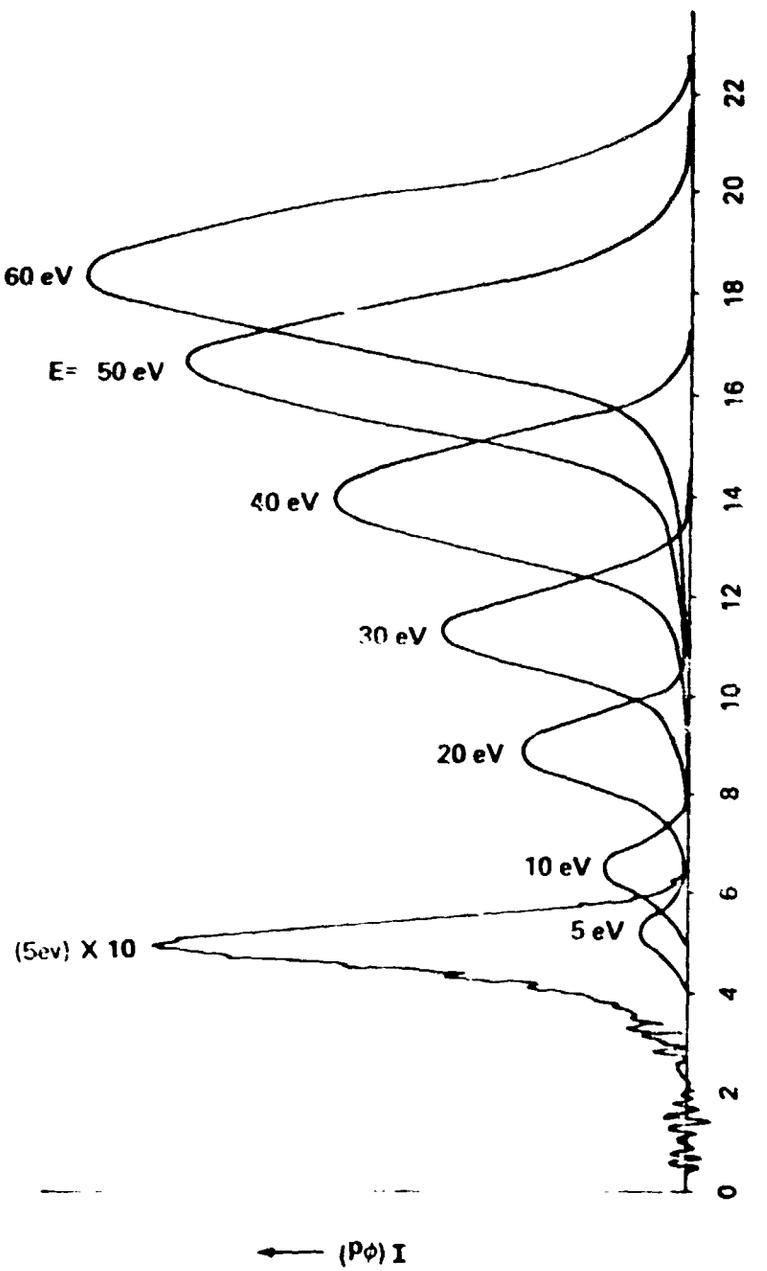

Figure G-3. Ion current, $I(\phi_d, \phi_r = 0)$, for a fixed angle of attack of 20° and various ion stream energies, E, after Stone [71].

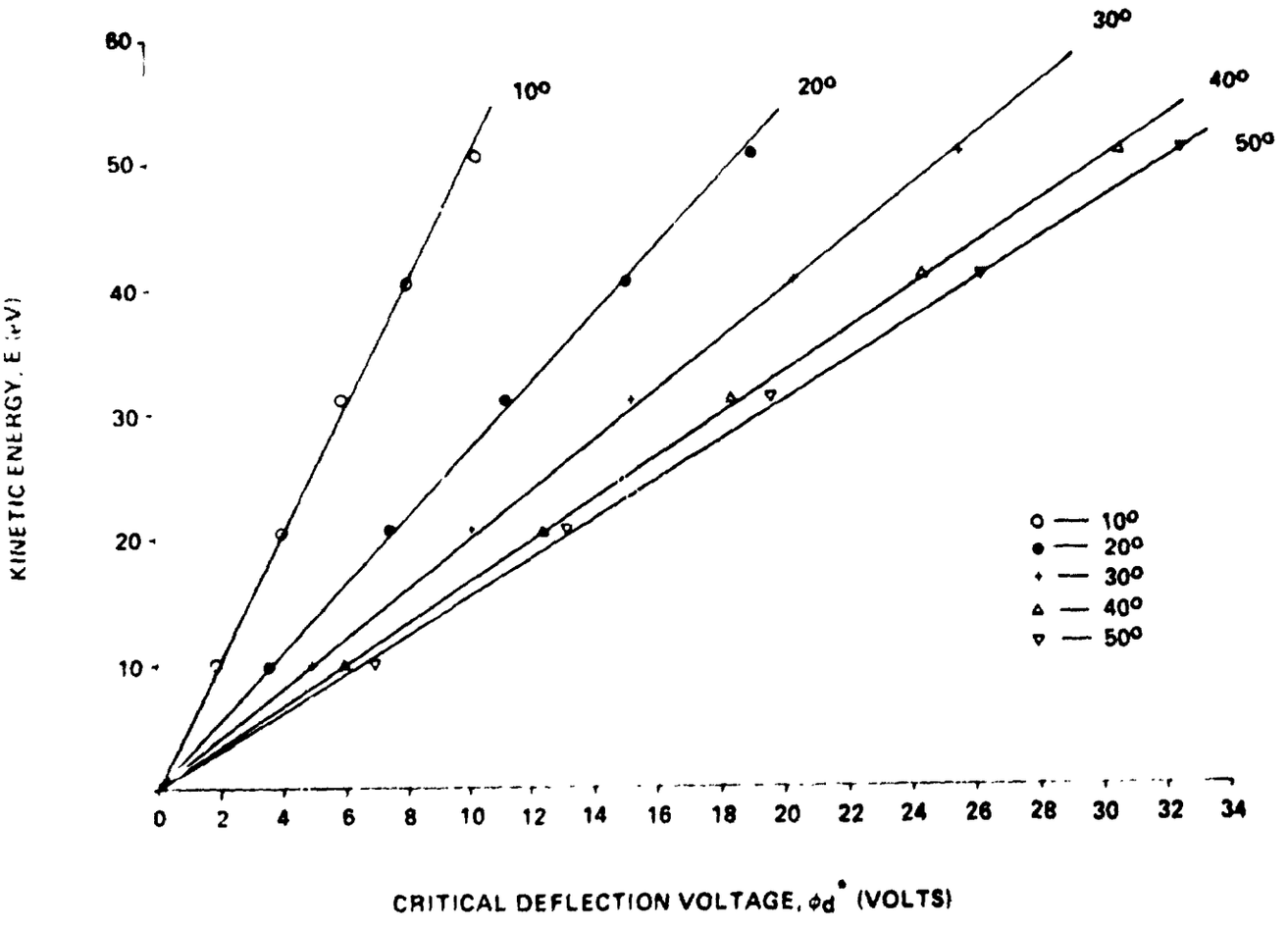

Figure G-4. Critical deflection voltage, ϕ_d^* (at which maximum ion current is collected), as a function of mean kinetic energy, E, at fixed angles of attack, after Stone [71].

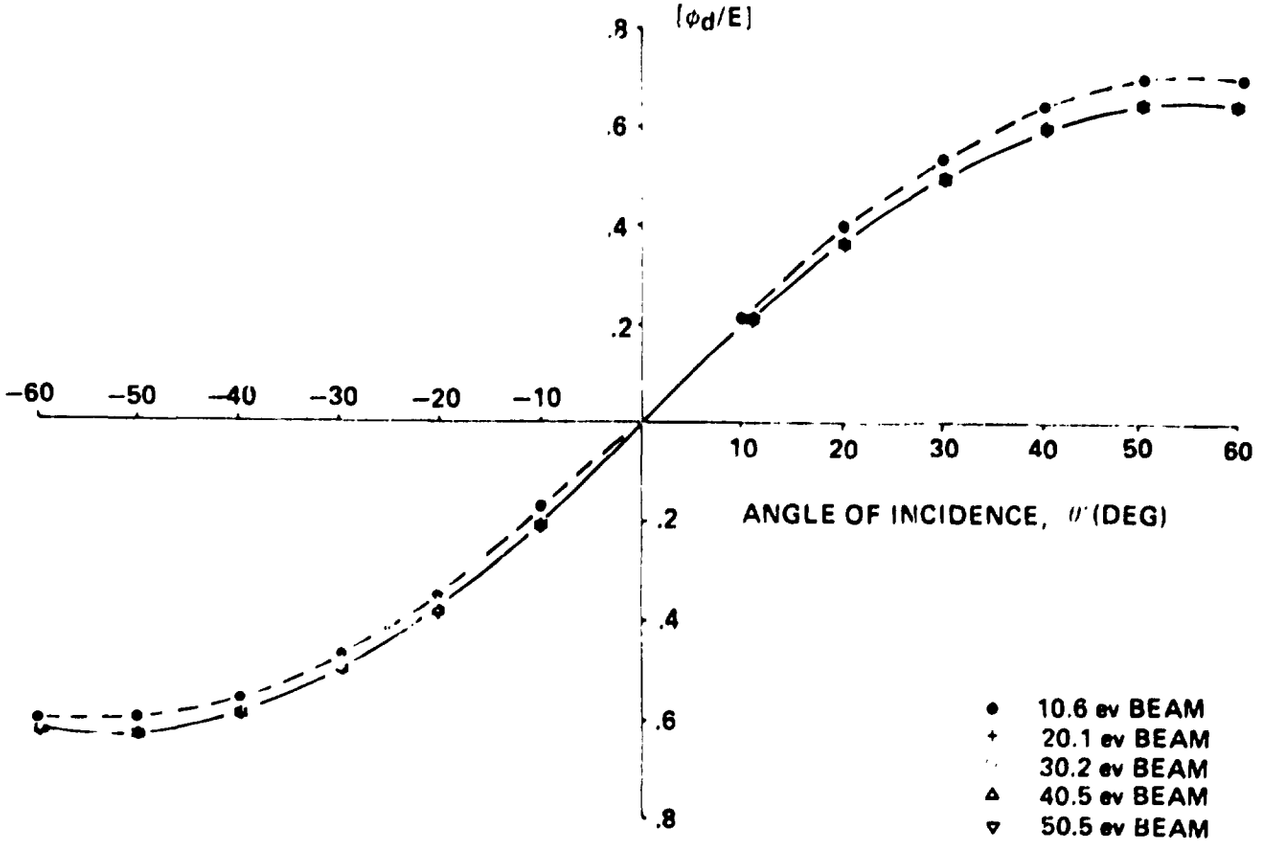

Figure G-5. Normalized critical deflection voltage, (ϕ_d^*/E), as a function at angle of attack θ, after Stone [71].

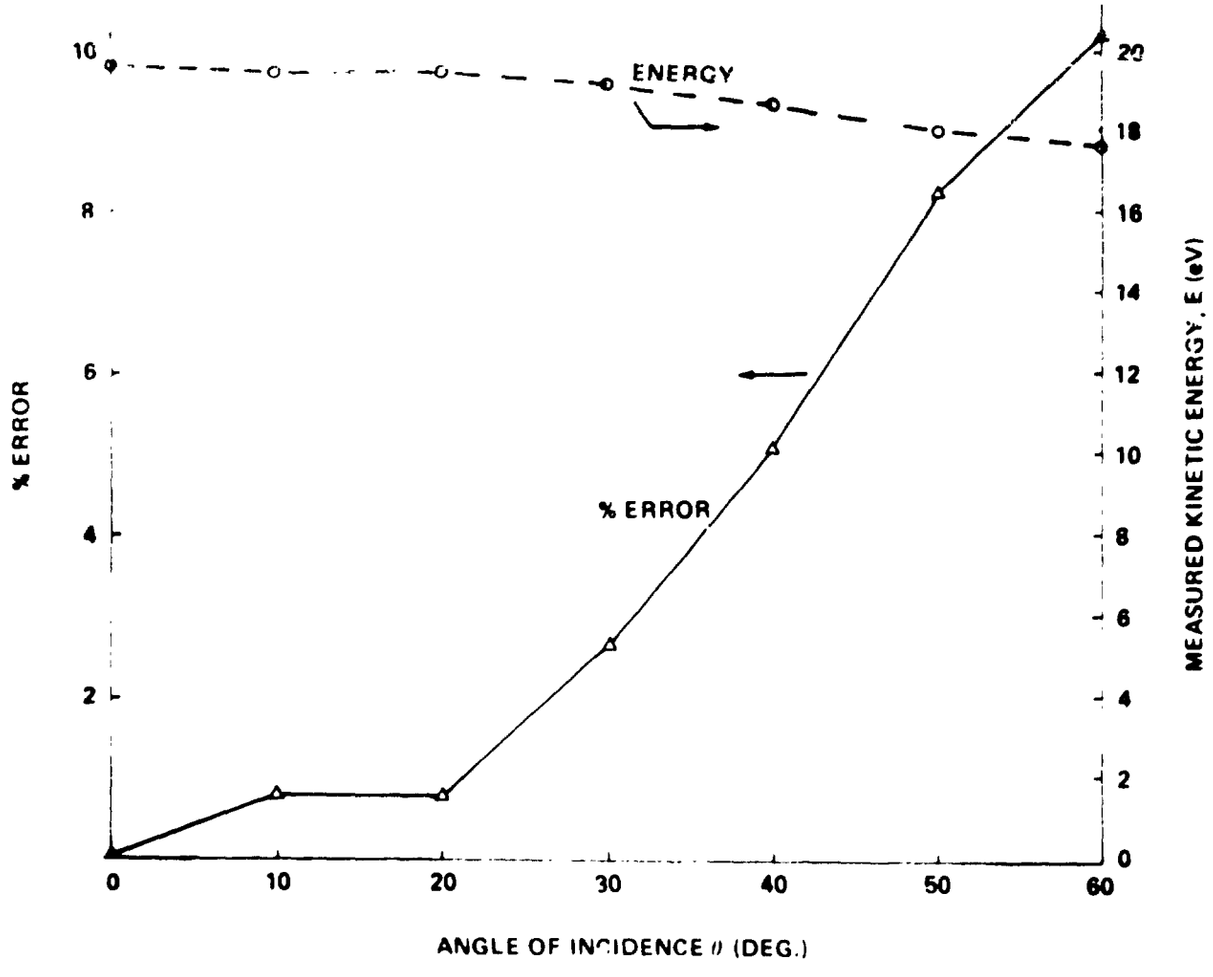

Figure G-6. Error incurred in determining ion kinetic energy as a function of angle of attack, after Stone [71].

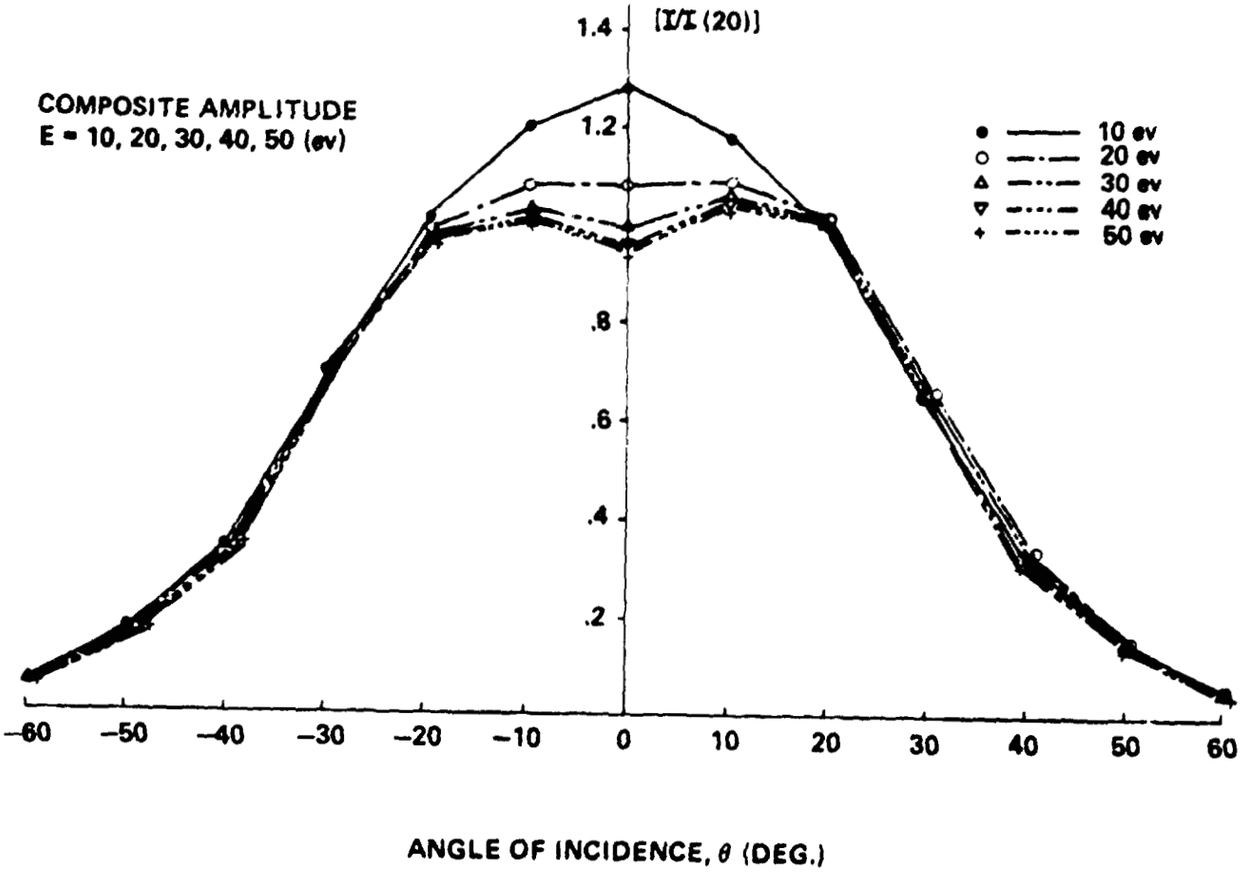

Figure G-7. Composite amplitude envelope for ion current peaks, $I(\phi_d^*, \phi_r = 0)$, as a function of angle of attack (normalized to the peak amplitude at $\theta = 20°$), after Stone [71].

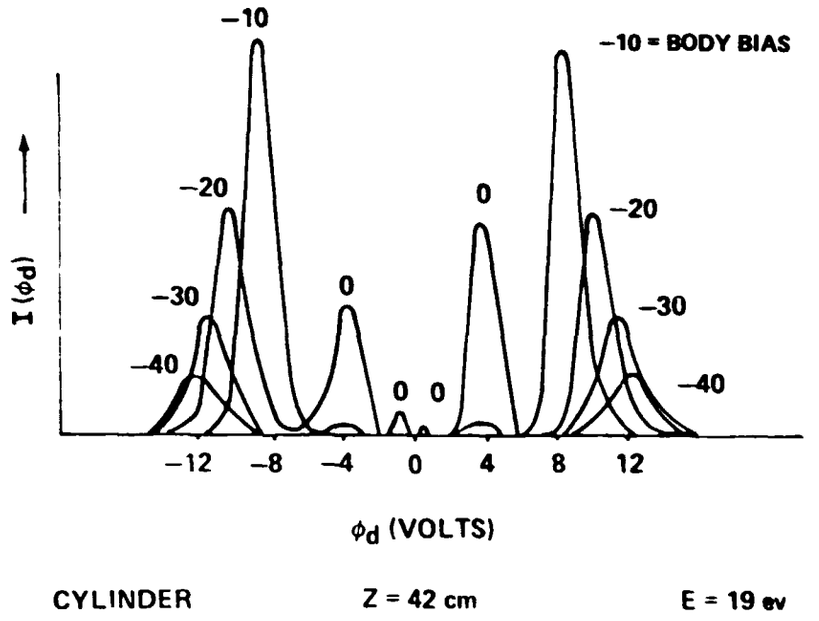

Figure G-8. Ion current, $I(\phi_d, \phi_r = 0)$, as a function of deflection voltage in the presence of multiple ion streams created by a long cylindrical body 42 cm upstream with E = 19 eV. (The zero bias voltage case is amplified by a factor of 10), after Stone [71].

REFERENCES

1. Liu, V. C.: On Ionospheric Aerodynamics. Prog. Aerospace Sci., 16, 273 (1975).

2. Stone, N. H. and Sheldon, J. W.: The One-Dimensional Time-Dependent Interaction of a Satellite with the Ionospheric Plasma. NASA TR-R-335 (1970).

3. Kraus, L. and Watson, K. N.: Plasma Motions Induced by Satellites in the Ionosphere. Phys. Fluids, 1, 480 (1958).

4. Rand, S.: Wake of a Satellite Traversing the Ionosphere. Phys. Fluids, 3, 265 (1960).

5. Rand, S.: Damping of the Satellite Wake in the Ionosphere. Phys. Fluids, 3, 588 (1960).

6. Vaglio-Laurin, R. and Miller, G.: Ionospheric Gas Dynamics Revisited. Paper presented at the 7th International Conference on Rarefied Gas Dynamics, Pisa, Italy, June 1970.

7. Lam, S. H.: A General Theory for the Flow of Weakly Ionized Gases. AIAA J., 2, 256 (1964).

8. Lam, S. H. and Greenblatt, M.: On the Interactions of a Solid Body with a Flowing Collisionless Plasma. RGD, 45 (1965).

9. Lam, S. H. and Greenblatt, M.: Flow of a Collisionless Plasma Over a Cone. AIAA J., 3, 1850 (1965).

10. Sanmartin, J. R. and Lam, S. H.: Far-Wake Structure in Rarefied Plasma Flows Past Charged Bodies. Phys. Fluids, 14, 62 (1971).

11. Davis, A. H. and Harris, I.: Interaction of a Charged Satellite with the Ionosphere. RGD, Sup 1, 691 (1961).

12. Call, S. M.: The Interaction of a Satellite with the Ionosphere. NASA CR-106555 (1969). Also Plasma Lab. Report No. 46, School of Engineering and Applied Science, Columbia University (1969).

13. Martin, A. R.: Numerical Solutions to the Problem of Charged Particle Flow Around an Ionospheric Spacecraft. Planet. Space Sci., 22, 121 (1974).

14. McDonald, P. W. and Smetana, F. O.: Results of a Numerical Experiment to Determine the Current Collected by a Charged Cylinder in a Collisionless Plasma Stream. RGD, 1627 (1969).

15. Parker, L. W.: Numerical Methods for Computing the Density of a Rarefied Gas About a Moving Object. Report for Air Force Cambridge Res. Labs., AFCRL-64-193 (1964).

16. Maslennikov, M. V. and Sigov, Yu S.: A Discrete Model for the Study of the Flow of a Rarefied Plasma About a Body. Soviet Phys Doklady, 9, 1063 (1965).

17. Maslennikov, M. V. and Sigov, Yu. S.: Discrete Model of Medium in a Problem on Rarefied Plasma Stream Interaction with a Charged Body. RGD, 2, 1657 (1967).

18. Maslennikov, M. V. and Sigov, Yu. S.: Rarefied Plasma Stream Interactions with Charged Bodies of Various Forms. RGD, 2, 1671 (1969).

19. Maslennikov, M. V., Sigov, Yu. S., and Charkina, G. P.: Numerical Experiments on Flow of a Rarefied Plasma Around Bodies of Various Shapes. Cosmic Res., 6, 184 (1968).

20. Taylor, J. C.: Disturbance of a Rarefied Plasma by a Supersonic Body on the Basis of the Poisson-Vlasov Equations — I and II. Planetary Space Sci., 15, 155 and 463 (1967).

21. Parker, L. W.: Computation of Collisionless Steady-State Plasma Flow Past a Charged Disk. Report, NASA CR-144159 (1976).

22. Parker, L. W. and Whipple, Jr., E.C.: Theory of Spacecraft Sheath Structure, Potential and Velocity Effects on Ion Measurements by Traps and Mass Spectrometers. JGR, 75, 4720 (1970).

23. Fournier, G.: Collisionless Plasma Flow Around a Cylinder in View of Applications to Ionospheric Probes. Publication No. 137, Office Nat. d' Etudes et de Rescherches Aerospatiales, Paris (1971).

24. Grabowski, R. and Fischer, T.: Theoretical Density Distribution of Plasma Streaming Around a Cylinder. Planet. Space Sci., 23, 287 (1975).

25. Al'pert, Ya. L., Gurevich, A. V., and Pitaevskii, L. P.: Space Physics with Artificial Satellies. Plenum Press, New York, 79 (1965).

26. Gurevich A. V., Pitaevskii, L. P., and Smirnova, V. V.: Ionospheric Aerodynamics. Space Sci. Rev., 9, 805 (1969).

27. Liu, V. C.: Ionospheric Gas Dynamics of Satellites and Diagnostic Probes. Space Sci. Rev., 9, 423 (1969).

28. Liu, V. C. and Hung, R. J.: Double Scattering of the Plasma Streams in a Bi-Thermal Ionosphere. Planet. Space Sci., 16, 845 (1968).

29. Liu, V. C. and Hung, R. J.: Further Remarks on the Double Scattering of the Plasma Stream in a Bi-Thermal Ionosphere. Planet. Space Sci., 19, 1020 (1971).

30. Woodroffe, J. A. and Sonin, A. A.: Calculation for the Wake of a Small Cylinder Under Ionospheric Satellite Conditions. Phys. Fluids, 17, 79 (1974).

31. Parker, L. W.: Personal communication (1979).

32. Gurevich, A. V., Paritskaya, L. V., and Pitaevskii, L. P.: Ion Acceleration Upon Expansion of a Rarefied Plasma. Soviet Phys. JETP, 36, 274 (1973).

33. Könemann, B.: The Collisionless Flow of Unmagnetized Plasma Around Bodies. J. Plas. Phys., 20, 17 (1978).

34. Hester, S. D. and Sonin, A. A.: Laboratory Study of the Wakes of Small Cylinders Under Ionospheric Satellite Conditions. Phys. Fluids, 13, 641 (1970).

35. Chopra, K. P.: Interactions of Rapidly Moving Bodies in Terrestrial Atmosphere. Rev. of Mod. Phys., 33, 153 (1961).

36. Henderson, C. L. and Samir, U.: Observations of the Disturbed Region Around an Ionospheric Spacecraft. Planet. Space Sci., 15, 1499 (1967).

37. Samir, U. and Wrenn, G. L.: The Dependence of Charge and Potential Distribution Around a Spacecraft on Ionic Composition. Planet. Space Sci., 17, 693 (1969).

38. Samir, U.: A Possible Explanation of an Order of Magnitude Discrepancy in Electron-Wake Measurements. JGR, 75, 855 (1970).

39. Samir, U. and Willmore, A. P.: The Distribution of Charged Particles Near a Moving Spacecraft. Planet. Space Sci., 13, 285 (1965).

40. Samir, U., Gorden, R., Brace, L. H., and Theis, R.: The Near-Wake Structure of the Atmosphere Explorer C (AE-C) Satellite, A Parametric Investigation. JGR, 84, 513 (1979).

41. Samir, U., Brace, L. H., and Brinton, H. C.: About the Influence of Electron Temperature and Relative Ionic Composition on Ion Depletion in the Wake of the AE-C Satellite. GRL, 6, 101 (1979).

42. Troy, Jr., B. E., Maier, E. J., and Samir, U.: Electron Temperatures in the Wake of an Ionospheric Satellite. JGR, 80, 993 (1975).

43. Troy, Jr., B. E., Medred, D. B., and Samir, U.: Some Wake Observations Obtained on the Gemini/Agena Two-Body System. J. Astronautical Sci., 18, 173 (1970).

44. Meckel, B. B.: Experimental Study of the Interaction of a Moving Body with a Plasma. RGD, Sup. 1, 701 (1961).

45. Cox, R. N.: Laboratory Simulation of the Perturbations of the Ionosphere by Space Vehicles. Astronautica Acta, 11, 183 (1965).

46. Hall, D. F., Kemp, R. E., and Sellen, Jr., J. M.: Plasma-Vehicle Interaction in a Plasma Stream. AIAA J., 2, 1032 (1964).

47. Clayden, W. A. and Hurdle, C. V.: An Experimental Study of Plasma-Vehicle Interaction. RGD, 2, 1717 (1966).

48. Skvortsov, V. V. and Nosachev, L. V.: The Structure of the Trail Behind a Spherical Model in a Stream of Rarefied Plasma. Cosmic Res., 6, 191 (1968).

49. Skvortsov V. V. and Nosachev, L. V.: Some Results on Disturbances Introduced by Extraneous Bodies into a Stream of Rarefied Plasma. Cosmic Res., 6, 718 (1968).

50. Sajben, M. and Blumenthal, D. L.: Experimental Study of a Rarefied Plasma Stream and Its Interaction with Simple Bodies. AIAA Paper No. 69-79 (Presented at AIAA 7th Aerospace Science Meeting, New York, January 1969).

51. Hester, S. D. and Sonin, A. A.: Some Results from a Laboratory Study of Satellite Wake Structure and Probe Response in Collisionless Plasma Flows. RGD, 2, 1659 (1969).

52. Hester, S. D. and Sonin, A. A.: A Laboratory Study of the Electrodynamic Influences on the Wakes of Ionospheric Satellites. AIAA Paper No. 69-673 (Presented at AIAA Fluid and Plasma Dynamics Conf., San Francisco, 1969).

53. Hester, S. D. and Sonin, A. A.: A Laboratory Study of the Wakes of Ionospheric Satellites. AIAA J., 8, 1090 (1970).

54. Knott, K. and Pedersen, A.: Wake Studies in an Argon Plasma Beam. Eldo-Cecles/ESRO-Cers Scient. and Tech. Rev., 2, 499 (1970).

55. Fournier, G. and Pigache, D.: Transverse Ion Temperature in an Ionospheric Wind Tunnel. J. Appl. Phys., 43, 4548 (1972).

56. Fournier, G.: Diagnostic D'un Faisceau De Plasma Autour D'un Corps Positif et Application a La Sonde De Sayers. Revue De Phys. App., 8, 341 (1973).

57. Illiano, J. M. and Storey, L. R. O.: Apparent Enhancement of Electron Temperature in the Wake of a Spherical Probe in a Flowing Plasma. Planet. Space Sci., 22, 873 (1974).

58. Fournier, G. and Pigache, D.: Wakes in Collisionless Plasma. Phys. of Fluids, 18, 1443 (1975).

59. Fournier, G. and Pigache, D.: Étude De Plasmas De Synthése Pour La Simulation Du Vol Ionosphérique. Revue De Phys. App., 12, 1063 (1977).

60. Martin, A. R. and Cox, R. N.: Simulation of Spacecraft Interactions with a Parallel-Streaming Plasma. AIAA/NASA/ASTM/IES 7th Space Simulation Conf., Los Angeles, November 1973, NASA SP-336, pp. 215-229.

61. Bogashchenko, I. A., Gurevich, A. V., Salimov, R. A., and Eidelman, Yu. I.: Flow of Rarefied Plasma Around a Body. Soviet Phys. JETP, 32, 841 (1971).

62. Astrel'n, V. T., Bogashchenko, I. A., Buchel'nikova, N. A., and Eidelman, Yu. I.: Flow of a Magnetized Plasma Around a Plate. Soviet Phys.-Tech. Phys., 17, 1369 (1973).

63. Waldes, J. and Marshall, T. C.: Flow of a Plasma Around a Disk in a Magnetic Field. Plasma Phys., 13, 837 (1971).

64. Schmitt, J. P. M.: Wake Past an Obstacle in a Magnetized Plasma Flow. Plasma Phys., 15, 677 (1973).

65. Fälthammar, C. G.: Laboratory Experiments of Magnetospheric Interest. Space Sci. Rev., 15, 803 (1974).

66. Reader, P. D.: The Operation of an Electron-Bombardment Ion Source With Various Gases. NASA TM X-52006 (1964).

67. LeVaguerese, P. and Pigache, D.: Etude d'une Source d'ions de basse Energie et a forte densite de courant. Revue De Physique Applique, 6, 325 (1971).

68. Stone, N. H. and Reihmann, W. K.: The Simulation of Ionospheric Conditions for Space Vehicles. NASA TN-D-5894 (1970).

69. Stone, N. H., Samir, U., and Oran, W. A.: Laboratory Simulation of the Structure of Disturbed Zones Around Bodies in Space. JATP, 253 (1974).

70. Sellen, Jr., J. M., Forbes, S. G., Kemp, R. F., Shelton, H., and Slattery, J. C.: Advanced Ion Beam Diagnostic Techniques. Am. Rocket Soc. Preprint No. 2067-61 (1961).

71. Stone, N. H.: Technique for Measuring the Differential Ion Flux Vector. Rev. Sci. Instrum., 48, 1458 (1977).

72. Martin, A. R. and Cox, R. N.: Simulation of Spacecraft Interations with a Parallel-Streaming Plasma. AIAA/NASA/ASTM/IES 7th Space Simulation Conf., Log Angeles, November 1973 (proc. pub. as NASA SP).

73. Stone, N. H., Samir, U., and Wright, Jr., K. H.: Plasma Disturbances Created by Probes in the Ionosphere and Their Potential Impact on Low-Energy Measurements Considered for Spacelab. JGR, 83, 1668 (1978).

74. Stone, N. H., Oran, W. A., and Samir, U.: Collisionless Plasma Flow Over a Conducting Sphere. Planet. Space Sci., 20, 1787 (1972).

75. Samir, U., Stone, N. H., and Oran, W. A.: Does a "Two-Stream" Flow Model Apply to Wakes of Large Bodies in Space? Astrophys and Space Sci., 31, L1 (1974).

76. Oran, W. A., Samir, U., and Stone, N. H.: Slow Ions in Plasma Wind Tunnels. AIAA J., 14, 1141 (1976).

77. Samir, U., Oran, W. A., and Stone, N. H.: Laboratory Simulation of Space Aerodynamic Phenomena: Satellite Wake Studies. Rarefied Gas Dyn., Proc. Int. Symp. 9th, 2, D11.1 (1974).

78. Oran, W. A., Stone, N. H., and Samir, U.: Parametric Study of Near-Wake Structure of Spherical and Cylindrical Bodies in the Laboratory. Planet. Space Sci., 22, 379 (1974).

79. Oran, W. A., Stone, N. H., and Samir, U.: The Effect of Body Geometry on the Structure in the Near Wake Zone of Bodies in a Flowing Plasma. JGR, 80, 207 (1975).

80. Samir, U. and Wrenn, G. L.: Experimental Evidence of an Electron Temperature Enhancement in the Wake of an Ionospheric Satellite. Planet. Space Sci., 20, 899 (1972).

81. Stone, N. H. and Samir, U.: The Tethered Subsatellite as a Tool for Large Body Plasma Flow Interaction Studies. Proc. UAH/NASA Workshop on the Uses of a Tethered Satellite System, Huntsville, May 1978.

82. Wu, S. T. and Dryer, M.: Kinetic Theory Analysis of Solar Wind Interaction with Planetary Objects. Photon and Particle Interactions with Surfaces in Space. D. Reidel Pub. Co., Holland (1973).

83. Jew, H.: Studies of the Rarefied-Plasma Interactions as Mesothermal Speeds. Ph.D. Thesis, University of Michigan, University Microfilms, Ann Arbor, Michigan (1968).

84. Samir, U.: Personal communication (1979).

85. Samir, U. and Jew, H.: Comparison of Theory with Experiment for Electron Density Distribution in the Near Wake of an Ionospheric Satellite. JGR, 77, 6819 (1972).

86. Samir, U., Maier, E. J., and Troy, Jr., B. E.: The Angular Distribution of Ion Flux Around an Ionospheric Satellite. JATP, 35, 513 (1973).

87. Miller, N. J.: Some Implications of Satellite Spin Effects in Cylindrical Probe Measurements. JGR, 77, 2851 (1972).

88. Brace, L. H. and Findlay, J. A.: Comparison of Cylindrical Electrostatic Probe Measurements on Alouette II and Exploere XXXI Satellites. Proc. IEEE, 57, 1054 (1969).

89. Samir, U.: Charged Particle Distribution in the Nearest Vicinity of Ionospheric Satellites — Comparison of the Main Results from the Ariel I, Explorer 31 and Gemini-Agena 10 Spacecraft. Photon and Particle Interactions with Surfaces in Space, (R. J. L. Grard, Ed.) pp. 193-219, D. Reidel Pub. Co., Dordrecht, Holland (1973).

90. Hudleston, R. H. and Leonard, S. L. (Ed.): Plasma Diagnostic Techniques. Academic Press, New York (1975).

91. Lochte-Holtgreven, W. (Ed.): Plasma Diagnostics. Wiley Interscience Div., John Wiley and Sons, Inc., New York (1968).

92. Swift, J. D.: Electrical Probes for Plasma Diagnostics. American Elsevier Pub. Co., Inc., New York (1969).

93. Kemp, R. F. and Sellen, Jr., J. M.: Plasma Potential Measurements by Electron Emissive Probes. Rev. Sci. Instrum., 37, 455 (1966).

94. Bowen, P. J., Boyd, R. L. F., Henderson, C. L., and Willmore, A. P.: Measurements of Electron Temperature and Concentration from a Spacecraft. Proc. Roy. Soc. A., 281, 514 (1964).

95. Bowen, P. J., Boyd, R. L. F., Raitt, W. J., and Willmore, A. P.: Ion Composition of the Upper F-Region. Proc. Roy. Soc. A, 281, 504 (1964).

96. Raitt, W. J.: Personal communication (1979).

97. Hall, D. F., Kemp, R. F., and Sellen, Jr., J. M.: Generation and Characteristics of Plasma Wind-Tunnel Streams. AIAA J., 3, 1490 (1965).

98. Oran, W. A., Samir, U., Stone, N. H., and Fontheim: Laboratory Observations of Electron Temperature in the Wake of a Sphere in a Streaming Plasma. Planet. Space Sci., 23, 1081 (1975).

99. Stone, N. H.: The Plasma Wake of Mesosonic Conducting Bodies. Part 1, An Experimental Parametric Study of Ion Focusing by the Plasma Sheath. J. Plasma Phys., 25, 351(1981).

100. Stone, N. H.: The Plasma Wake of Mesosonic Conducting Bodies. Part 2, An Experimental Parametric Study of the Mid-Wake Ion Density Peak. J. Plasma Phys., in press (1981).

101. Stone, N. H. and Samir, U.: Bodies in Flowing Plasmas: Laboratory Studies. Adv. Space Res., 1, 361 (1981).